Measuring the legacy of child abuse *pp. 1408 & 1480*

Overlooked trade-offs in biofuel versus food debates *p. 1420*

The mass difference between protons and neutrons *p. 1452*

Science

$10
27 MARCH 2015
sciencemag.org

AAAS

Gang of three

How dynactin, dynein, and Bicaudal-D2 motor together

p. 1441

CONTENTS

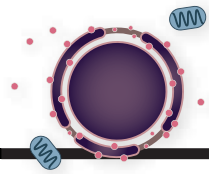

1414 Fighting fungal infections

27 MARCH 2015 • VOLUME 347 • ISSUE 6229

1410

NEWS

IN BRIEF

IN DEPTH

FEATURE

INSIGHTS

PERSPECTIVES

BOOKS *ET AL.*

1426

Published by AAAS

CONTENTS

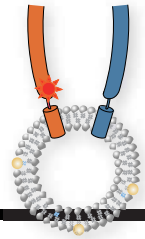

1485 Dissecting SNARE disassembly

27 MARCH 2015 • VOLUME 347 • ISSUE 6229

ON THE COVER

The cargo adaptor Bicaudal-D2 (orange) brings the dynein motor complex (yellow) together with its essential cofactor dynactin (red). This giant complex of 37 proteins drags cellular cargos for long distances along microtubules (blue). Cryo–electron microscopy provides insight into the structural assembly and operation of this supracomplex. See page 1441.
Illustration: Chris Bickel/Science

SCIENCE (ISSN 0036-8075) is published weekly on Friday, except the last week in December, by the American Association for the Advancement of Science, 1200 New York Avenue, NW, Washington, DC 20005. Periodicals mail postage (publication No. 484460) paid at Washington, DC, and additional mailing offices. Domestic individual membership and subscription (51 issues): $153 ($74 allocated to subscription). Domestic institutional subscription (51 issues): $1282; Foreign postage extra: Mexico, Caribbean (surface mail) $55; other countries (air assist delivery) $85. First class, airmail, student, and emeritus rates on request. Canadian rates with GST available upon request, GST #1254 88122. Publications Mail Agreement Number 1069624. **Printed in the U.S.A.**
Change of address: Allow 4 weeks, giving old and new addresses and 8-digit account number. **Postmaster:** Send change of address to AAAS, P.O. Box 96178, Washington, DC 20090–6178. **Single-copy sales:** $10.00 current issue, $15.00 back issue prepaid includes surface postage; bulk rates on request. *Science* is indexed in the *Reader's Guide to Periodical Literature* and in several specialized indexes.

Published by AAAS

Science
AAAS
1200 New York Avenue, NW, Washington, DC 20005
Bateman House, 82-88 Hills Road, Cambridge, UK CB2 1LQ

SUBSCRIPTION SERVICES For change of address, missing issues, new orders and renewals, and payment questions: 866-434-AAAS (2227) or 202-326-6417, FAX 202-842-1065. Mailing addresses: AAAS, P.O. Box 96178, Washington, DC 20090-6178 or AAAS Member Services, 1200 New York Avenue, NW, Washington, DC 20005

INSTITUTIONAL SITE LICENSES 202-326-6755 **REPRINTS:** Author Inquiries 800-635-7181 **COMMERCIAL INQUIRIES** 803-359-4578 **PERMISSIONS** 202-326-6765, permissions@aaas.org **AAAS Member Services** 202-326-6417 or http://membercentral.aaas.org/discounts

Science serves as a forum for discussion of important issues related to the advancement of science by publishing material on which a consensus has been reached as well as including the presentation of minority of conflicting points of view. Accordingly, all articles published in *Science*—including editorials, news and comment, and books reviews—are signed and reflect the individual views of the authors and not official points of view adopted by AAAS or the institutions with which the authors are affiliated.

INFORMATION FOR AUTHORS See pages 678 and 679 of the 6 February 2015 issue or access www.sciencemag.org/about/authors

Published by AAAS

EDITORIAL

Integrity—not just a federal issue

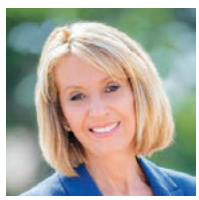

Marcia McNutt
Editor-in Chief
Science *Journals*

Few matters threaten the integrity of science more than scientists not being allowed to warn the public about legitimate hazards uncovered in the course of scientific research. Yet, this month, the issue was raised twice in the United States.

One instance involves the ~300-fold increase in earthquakes in Oklahoma since 2008, making it America's earthquake capital. Early on, investigations by the United States Geological Survey and academic scientists linked this departure from background levels to oil and gas industry activities, a position that the Oklahoma Geological Survey (OGS) had appeared to be willing to support in 2013. However, the position of the OGS took an about-face, coinciding with the state seismologist being called into the president's office at the University of Oklahoma (where the Survey is housed) for a pivotal meeting with billionaire oil man Harold Hamm, a major donor to the school.* E-mails associated with the meeting, just recently released through Oklahoma's Open Records Act, have prompted speculation that the OGS dialed back its willingness to link the seismicity to human activity because of potential impacts on the oil and gas industry.

"states should...enact integrity policies that protect...reporting of scientific findings."

The other instance involves a claim by employees at the Florida Department of Environmental Protection (DEP) that an "unwritten" policy, dating from the appointment of Herschel Vinyard Jr. as DEP director, forbids use of the terms "climate change," "global warming," and "sustainability" in any communications from the DEP.† Vinyard was appointed in 2011 by Florida Governor Rick Scott, a climate change denier. My quick scan of the DEP website for documents with the term "climate change" came up with more than 1600 hits, almost all dating from before Governor Scott's election to office in 2011. Only a small percentage of more recent documents mention climate change, such as a call for proposals to a federal-state partnership program (involving the U.S. National Oceanic and Atmospheric Administration) for resilient coastal communities (yes, Florida is the state with the lowest elevation). Although Governor Scott denies that such an unwritten policy exists, there is no scientific reason why climate change suddenly ceased to be an important issue for the DEP with Governor Scott's election.

In the mid-2000s, the U.S. Department of Interior Deputy Assistant Secretary Julie MacDonald, and other Interior Department officials with oversight of the U.S. Fish and Wildlife Service, repeatedly pressured agency scientists to alter their findings to circumvent the Endangered Species Act. The Union of Concerned Scientists and other groups demanded that integrity be restored to federal government research. In response, in 2009 President Obama issued a memorandum asking all federal agencies to reform their scientific integrity policies such that they would apply to all agency personnel, including political appointees, contractors, and nonscientists. These policies are now in place, including whistleblower protections, mechanisms for lodging complaints, and dispute resolution. While no policy is perfect, these policies do provide federal scientists clear recourse if they are urged to suppress or alter their scientific findings for political, economic, ideological, or other nonscientific reasons. However, these policies apply only to federal scientists.

Presidents of universities and research institutions should uphold the scientific integrity of their researchers, including those in affiliated state agencies, and ensure that they are not subjected to pressure from political, economic, or other interests in the conduct and reporting of their science. Governors should defend the integrity of all scientists in state agencies, universities, and research institutions. The incidents raised this month illustrate that the reality does not measure up to this ideal. I suggest that states should follow the federal example and enact integrity policies that protect state workers from interference in the conduct and reporting of scientific findings.

– Marcia McNutt

*www.eenews.net/stories/1060014342
†www.miamiherald.com/news/state/florida/article12983720.html

10.1126/science.aab1106

PHOTOS: (INSET) FL-PHOTOGRAPHY/ISTOCKPHOTO.COM; (RIGHT) STACEY PENTLAND PHOTOGRAPHY

NEWS

> “In the end, we did not know what words to use that would make the world wake up and realise how out of control the outbreak had truly become.”
>
> **Bart Janssens**, director of operations at Doctors Without Borders, in a critical report on the global response to the Ebola epidemic in West Africa, released this week.

IN BRIEF

Lopsided ice points to moon’s polar shift

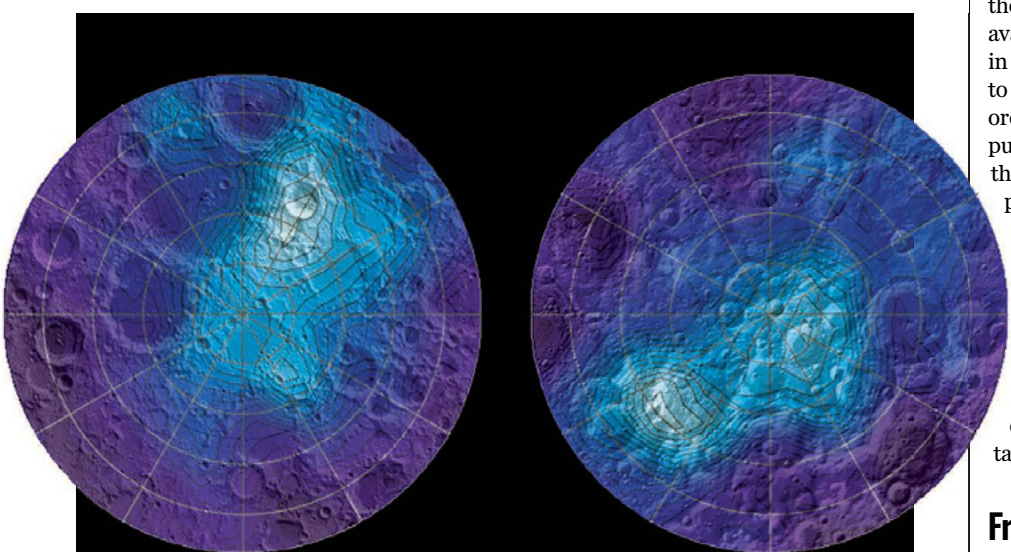

An off-axis abundance of water at the moon’s north pole (*left*) is matched symmetrically at the south pole (*right*).

Oddly, much of the moon’s ice is not found at its poles, but is buried below the surface in an area 5.5° away from the north pole and in a matching region 5.5° from the south pole, scientists announced last week at the Lunar and Planetary Science Conference in The Woodlands, Texas. The data came from NASA’s Lunar Prospector mission, which orbited the moon from 1998 to 1999 and measured neutrons emitted from the surface. Slower, less energetic neutrons indicate the amount of hydrogen—a proxy for water—lurking within a meter of the surface. The antipodal, off-axis location of the ice suggests that in the past, the moon’s axis of rotation—and hence its poles—shifted. The possible culprit: a 3.5-billion-year-old hot spot produced by high concentrations of radioactive elements. (The radioactive heat, and resulting lava, also formed the dark spot on the near side of the moon called Oceanus Procellarum.) The heat may have created a low-density lens in the moon’s mantle that would have caused the axis to wobble into today’s position. If so, the lopsided ice may mean the moon’s water is nearly as ancient as the orb itself. http://scim.ag/lopsidedice

AROUND THE WORLD

NSF to make papers free

ARLINGTON, VIRGINIA | The National Science Foundation (NSF) has released a policy that will require its grantees to make their peer-reviewed research papers freely available within 12 months of publication in a journal. The move comes in response to a February 2013 White House memo ordering science agencies to come up with public access policies similar to that of the National Institutes of Health, which posts grantees’ papers in the full-text PubMed Central archive. NSF will not follow that model, but will work with the Department of Energy to create an online index of papers that will link to full-text papers on journals’ own websites. Although open-access advocates prefer full-text archives, many publishers say NSF’s plan will minimize costs to taxpayers. http://scim.ag/NSFfree

Fracking rules for public land

WASHINGTON, D.C. | The Interior Department last week released the first federal regulations for oil and gas wells that use hydraulic fracturing. Intended to protect ground water, the rules tighten requirements for the cement casings of wells and for wastewater storage. Drillers must also release information about chemicals used. The rules apply to 283 million hectares of public land and 23 million hectares of American Indian land, but not private or state land, where much more fracking occurs. Alan Krupnick of Resources for the Future, a nonpartisan think tank in Washington, D.C., called the rules “a more thoughtful and more contemporary approach to regulation than we had before.” Environmental groups warned about loopholes, while energy groups immediately sued to have the regulations lifted.

U.K. science gets funding bump

LONDON | The United Kingdom’s budget contained few surprises for researchers—the core science budget is planned over 5 years—but did yield more than £240 million of additional funding. The extra

IMAGE: RICHARD MILLER/UNIVERSITY OF ALABAMA, HUNTSVILLE

Pangaea's monster amphibian

Before dinosaurs, this giant salamanderlike amphibian was a top predator in tropical areas of the supercontinent Pangaea. The newly discovered species *Metoposaurus algarvensis*, described this week in the *Journal of Vertebrate Paleontology*, was more than 2 meters long, weighed as much as 100 kilograms, and had a broad flat head the size and shape of a toilet seat. It lived between 220 million and 230 million years ago and was among the largest in a group of amphibians known as metoposaurs. Researchers unearthed hundreds of fossilized bones within a 4-square-meter area in southern Portugal, where they believe the creatures became concentrated and then died when the lake they inhabited dried up. Because the beasts had spindly limbs probably insufficient to support their weight, they likely remained in the water most of the time, feeding on fish but possibly snacking on small ancestors of dinosaurs or mammals that wandered too near the waterside.

Water-dwelling *Metoposaurus algarvensis* was bigger than a human.

money, announced 18 March, will be spent mostly on technology-related research, such as £100 million for R&D on driverless car technology and £40 million for R&D on the Internet of Things. "It is great to see the chancellor putting additional money into innovation and recognizing the value of science," says Naomi Weir, acting director of the Campaign for Science and Engineering, an advocacy group in the United Kingdom, which remains concerned about the effects of inflation on the flat budget for core funding. http://scim.ag/budgetUK

Gamma ray observatory opens

PUEBLA, MEXICO | On 20 March, Mexican and U.S. scientists gathered on the slopes of the Sierra Negra volcano to inaugurate the High-Altitude Water Cherenkov Gamma-Ray Observatory (HAWC). "It is the biggest astrophysics project there has ever been in Mexico," said Andrés Sandoval, HAWC's Mexican coordinator. Built at an altitude of 4100 meters, the $15 million observatory consists of 300 steel tanks, each containing 180,000 liters of pure water. Gamma rays that strike Earth's atmosphere create a shower of particles that hit the water in the tanks and emit a type of light known as Cherenkov radiation. Scientists can then trace the gamma rays back to their sources to study some of the universe's most extreme environments, including pulsars, supernovae, and the supermassive black holes at the centers of galaxies.

Mexico's High-Altitude Water Cherenkov Gamma-Ray Observatory.

EPA 'secret science' bills approved

WASHINGTON, D.C. | The U.S. House of Representatives last week approved two mostly Republican-backed bills that would change how the Environmental Protection Agency (EPA) uses scientific data and advice to write regulations. One would bar EPA from issuing regulations drawing on data that have not been made public in a way that allows for independent analysis. The other would change the membership and procedural requirements for the agency's federally chartered advisory panels. Backers say the bills would make EPA's regulatory processes more transparent and inclusive. Opponents claim they are designed to give regulated industries more influence and could force researchers to violate privacy rules. White House officials have said that they would advise President Barack Obama to veto the bills if they reached his desk in their present forms. http://scim.ag/EPAbills

Ukraine joins E.U. research club

KIEV | Ukraine has earned privileged access to competitive research funds from the European Union, bringing its science closer to the Western bloc. Under a deal signed on 20 March with the European Commission, Ukraine becomes an "associated country" to Horizon 2020, the European Union's €80 billion,

IMAGES: (TOP TO BOTTOM) JOANA BRUNO; MERCEDES RODRIGUEZ/INSTITUTO DE FÍSICA, UNAM

7-year research program. Until now, it was considered a "third country," meaning Ukraine-based researchers were not eligible for parts of the program, including coveted grants from the European Research Council. The upgrade puts Ukraine on par with other non-E.U. countries such as Israel and Norway—and it got a generous 95% rebate on the association fee. http://scim.ag/Ukraine2020

A boost for giant telescope

BRASÍLIA | Five years after Brazil committed to joining the European Southern Observatory (ESO), the country's House of Representatives approved the agreement on 19 March. ESO is relying on Brazil's contribution of €270 million, to be paid over a decade, to help build the 39-meter European Extremely Large Telescope (E-ELT) in Chile. Brazilian funding will allow ESO to begin the second phase of construction on the E-ELT, which is expected to see first light in 2024. After years of legislative limbo, the House's vote "brings the completion of the ratification process one step closer," says ESO Director General Tim de Zeeuw. The agreement will now go to the Brazilian Senate, and then the president, for ratification.

Mega–marine reserve announced

LONDON | The United Kingdom plans to create the world's largest fully protected marine reserve in South Pacific waters surrounding the Pitcairn Islands and will rely on satellites to help police it. The move, announced as part of the United Kingdom's 2015 budget last week, will bar commercial fishing, mining, and other extractive uses in the 834,334-square-kilometer reserve, which is home to at least 1249 species of marine mammals, seabirds, and fish and holds one of the deepest well-developed coral reef communities known. The U.K. government hopes to make agreements with nongovernmental organizations to monitor reserve users by satellite, and with regional port authorities to prevent the landing of illegal catch. http://scim.ag/UKreserve

Pitcairn Island waters are now protected.

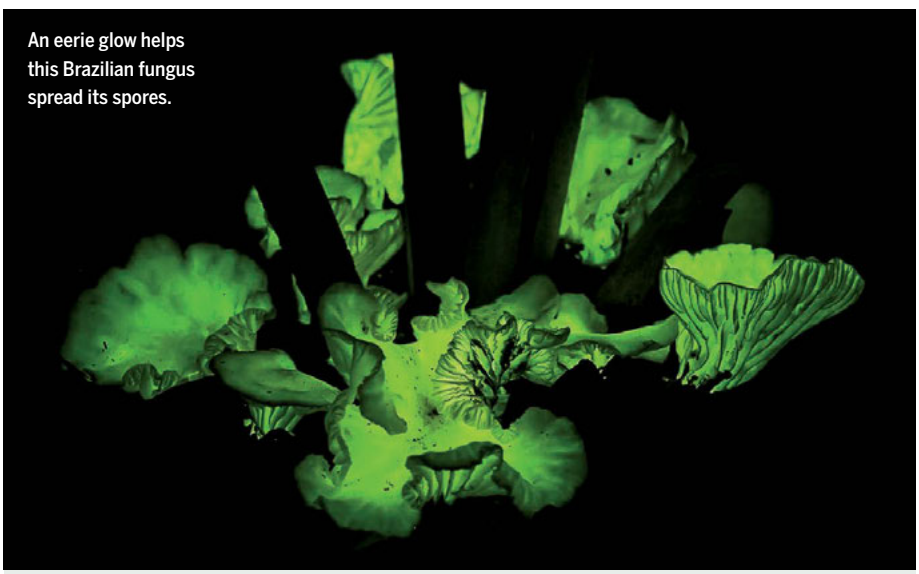

An eerie glow helps this Brazilian fungus spread its spores.

Luminous mushrooms entice winged visitors

It might look like something from a 1960s black-light poster, but the glowing fungus *Neonothopanus gardneri* grows at the base of palm trees in Brazilian forests. Its light show serves to attract insects that will spread its spores, according to a study published online last week in *Current Biology*. Scientists placed plastic mushroom decoys at the base of trees, some lit with green LEDs to mimic the bioluminescence of the real thing. Over 5 nights, they counted the insect visitors to each imitation mushroom and found that the LED light conferred an advantage: They collected a total of 12 insects from the dark mushrooms, compared with 42 from the glowing ones. In lab work, the researchers also showed that the mushrooms follow a daily rhythm, lighting up only when it's dark—presumably, an energy-conserving measure and another indication that their glow serves a purpose.

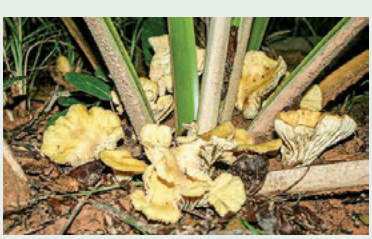

BY THE NUMBERS

14.54 million

Square kilometers, the maximum extent of Arctic sea ice in 2015—the lowest ever recorded, reports the U.S. National Snow and Ice Data Center.

67%

Projected global increase in the use of antibiotics in food animals between 2010 and 2030, according to a study in the *Proceedings of the National Academy of Sciences.*

38:11

Minutes and seconds it would take to fall through a borehole piercing Earth, based on a new estimate published in the *American Journal of Physics.*

PHOTOS: (TOP TO BOTTOM) © DOUGLAS PEEBLES PHOTOGRAPHY/ALAMY; MICHELE P. VERDERANE/IP-USP-2008 (2)

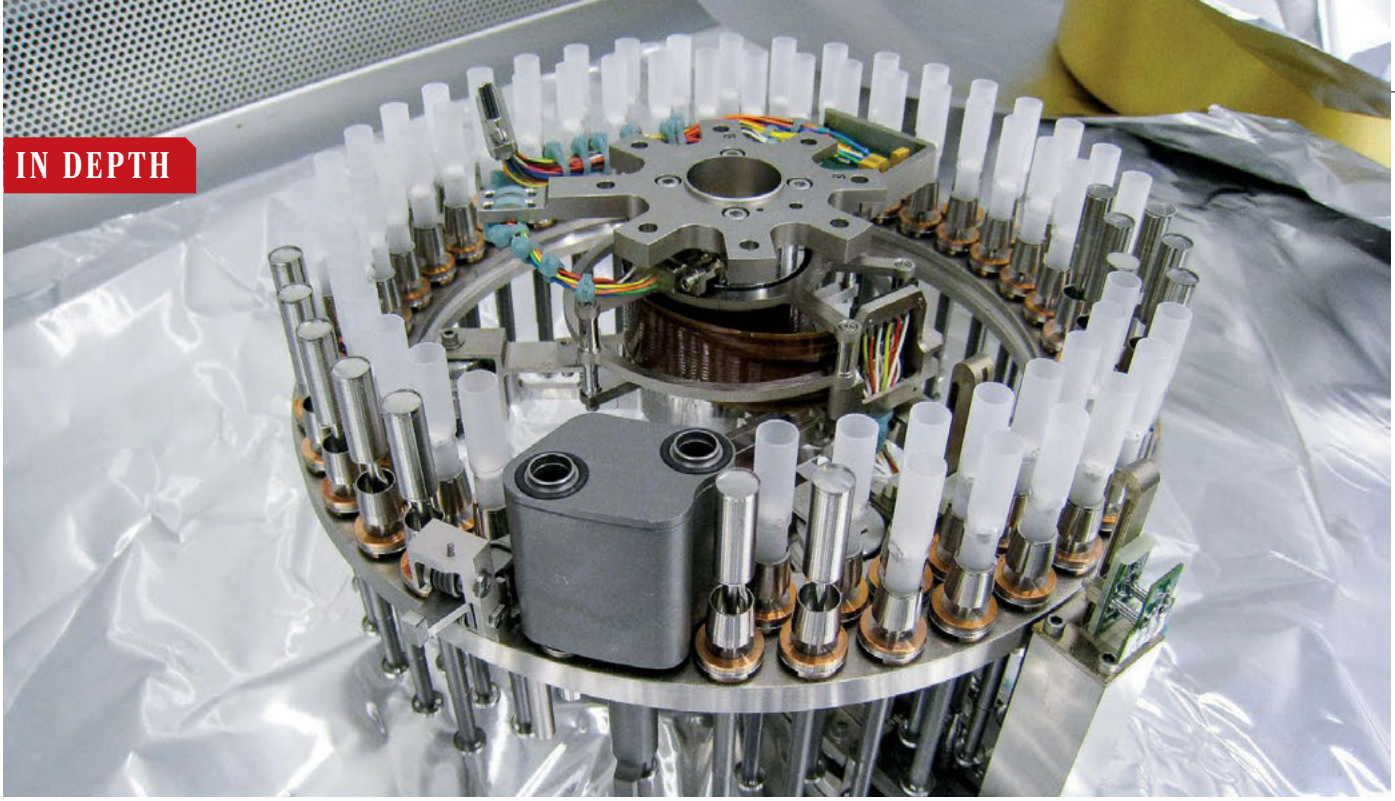

PHOTO: NASA GODDARD SPACE FLIGHT CENTER

Curiosity's lab carries quartz sample cups (white) and "wet lab" cups with solvent (silver).

PLANETARY SCIENCE

Mars rover finds long-chain organic compounds

Complex carbon molecules show that clues to past life—if any—could survive harsh martian conditions

By **Eric Hand**, *in The Woodlands, Texas*

For almost 40 years—ever since NASA's Viking missions—landers and rovers have searched the desiccated soil of Mars for the carbon-bearing organic compounds that would be essential for any Earth-like life. Last week here at the Lunar and Planetary Science Conference, scientists working with NASA's Curiosity rover announced a major milestone in that search. They reported the most definitive detections of organic molecules yet, along with hints of heavier, longer-chain molecules resembling those in cell walls.

The detected molecules do not necessarily indicate past or present life on Mars. They could also have come from asteroid impacts or rocks that burbled up from Mars's mantle. But they at least show that fragile organic materials can survive in the inhospitable environment—which bodes well for searches for clearer indicators of past life.

"We are all excited about it," says Paul Mahaffy, a scientist at the Goddard Space Flight Center in Greenbelt, Maryland, and principal investigator for the Sample Analysis at Mars (SAM) instrument on Curiosity, which made the detections. "The fact that there are any organic compounds in the near surface at all is very promising." It suggests, he says, that "biosignatures," if any exist, might survive billions of years to be detected today in spite of the harsh surface conditions.

Mars's soil is known to be filled with harsh oxidizers like perchlorate, which break down organic molecules. Ultraviolet (UV) light at the surface can also destroy organics, as can cosmic rays. The Viking landers may have detected organic molecules in the form of chloromethanes, but in such tiny quantities—about 15 parts per billion—that the team was never confident about making a claim.

The Curiosity team is now making a claim with gusto, having detected chlorobenzene—a six-carbon molecule in an aromatic ring structure—at levels of up to 300 parts per billion. They have also detected smaller two-, three-, and four-carbon chains in the alkane family at lesser abundances. The results were posted online on 4 March in advance of publication in the *Journal of Geophysical Research: Planets*.

The organics come from a sample that Curiosity collected nearly 2 years ago by drilling 6.5 centimeters into a mudstone—hardened sediment from an ancient lake—at a site called Cumberland. The SAM team took so long to announce their finding in part because they wanted to be sure they had not been fooled by contamination from leakage in their "wet labs," which hold thimblefuls of a solvent called MTBSTFA, used in isolating organic molecules. The SAM team has now controlled for this background contamination, and they have not seen the chlorobenzene at subsequent sampling sites—evidence that the Cumberland detection was real.

Curiosity scientists suspect that the chlorobenzene arose when organic molecules reacted with perchlorate in the soil as the sample was baked in SAM's ovens. To pin down the precursor molecules, the SAM team decided not to use any of their precious thimbles; instead they took advantage of the leaked MTBSTFA. They baked a sample from Cumberland to drive off any perchlorate and then exposed it to ambient MTBSTFA inside the onboard lab for 2 days. The solvent makes organic molecules much more volatile and thus more likely to be detected by SAM's mass spectrometer before they react with anything else (like perchlorate). "It gives them 'wings' so they can fly through the instrument unimpeded," Mahaffy says. After the exposure, the team slowly started heating the sample again. "That's when this beautiful set of rich organics showed up."

At the meeting, Danny Glavin, a SAM sci-

entist at Goddard, reported compounds that, in a preliminary analysis, were consistent with an eight-carbon molecule akin to a benzoic acid, an 11-carbon alcohol-like molecule, and, most interesting of all, a 10-carbon molecule that could be a fatty acid–like carboxylic acid. Glavin is excited that long-chain organics can survive in spite of the oxidizing compounds and UV-rich sunlight. "The fact that we see something long means this could be a good location for preservation," he says.

Other scientists wonder if the compounds could signify something more than just good odds for preservation. In the case of the 10-carbon fatty acid–like compound, "You're talking about cellular-wall material," says Marc Fries, a curation scientist at NASA's Astromaterials Acquisition and Curation Office at Johnson Space Center in Houston, Texas. "That's a potential biogenic molecule." But it could also be a contaminant, he cautions. Fries notes that a 2014 study by scientists at the Jet Propulsion Laboratory in Pasadena, California, where the rover was assembled, warned that Curiosity could harbor traces of carboxylic acids, which are found in plant and animal oils as well as synthetic lubricants.

But Glavin points out that six batches of martian soil went through the SAM instrument before the Cumberland sample and ought to have scrubbed the instrument of residual contamination. And George Cody, a geochemist at the Carnegie Institution for Science in Washington, D.C., says that the compound is unlikely to have come from Earth. Fatty acids from biological sources, like technicians' fingerprints, Cody says, tend to have 14, 16, or 18 carbon atoms, not 10. Also, if the contamination were something like residual machine oil, smaller chain organic compounds would have been detected in the background—molecules that Curiosity does not see.

Drill hole from the Cumberland site, in rock that was an ancient lakebed.

The Curiosity team has yet to use any of the seven MTBSTFA thimbles, or two with another type of solvent. Glavin says the team is saving them for promising rock formations farther up the mountain that Curiosity is now climbing: clay mineral–bearing deposits that, like the Cumberland mudstone, probably formed in water and could be a good location for preserving organics. Mahaffy hopes to get a chance to test one of his thimbles soon—and hopes to find even more-tantalizing organic molecules. "There's a lot of interesting sites coming along," he says. ■

'Fixed' nitrogen found in martian soil

By **Eric Hand**

Organic compounds aren't the only molecules of life on Earth: Inorganic NO_3-bearing chemicals, known as nitrates, are also crucial for living organisms and make up a key component of fertilizers. Now, in a study published this week in the *Proceedings of the National Academy of Sciences*, the NASA Curiosity rover team reports detecting nitrates on Mars.

The chemicals turned up in scoops of windblown dust as well as samples drilled out of a mudstone thought to have been made from lakebed deposits billions of years old. The rover's onboard lab, Sample Analysis at Mars, heated the rock dust to release gases and ran them through a mass spectrometer, which spotted the molecular signature of nitrogen. Mars's atmosphere is now just 2% nitrogen (N_2), but scientists suspect that it abounded in nitrogen in the past—just as Earth's atmosphere does today.

On Earth, microbes—especially bacteria living in the nodules of legume plants—do the hard work of breaking N_2's triple bonds and turning it into nitrate that can be "fixed" in the soil. Rover scientists say things probably happened differently on Mars, where the energy of asteroid impacts could have done the fixing in a flash. Regardless, the discovery shows nitrate would have been available as a nutrient in Mars's ancient past. "In a way, it provides what fertilizer would provide," says Jennifer Stern, a planetary geochemist at Goddard Space Flight Center in Greenbelt, Maryland, and lead author of the study. "It's another support for habitability." ■

PHOTO: NASA/JPL-CALTECH/MSSS

CHEMICAL REGULATION

Reform of toxics law is contentious

Plan to rewrite 1976 law draws bipartisan support but harsh criticism

By **Puneet Kollipara**

Of the roughly 80,000 industrial chemicals in commerce in the United States, the Environmental Protection Agency (EPA) has substantially restricted the use of less than 10. That's just one reason observers on all sides agree that the country's long-standing chemical testing law is broken. Last week, a U.S. Senate committee set out to fix it, launching what is expected to be a long, contentious effort to rewrite the 1976 Toxic Substances Control Act (TSCA).

"There has never been a bipartisan effort with this much potential," said Senator Tom Udall (D–NM) at an 18 March hearing of the Senate environment committee on a bill (S. 697) that he and 19 other senators, Democratic and Republican, recently rolled out that would revamp the law. Groups that rarely agree share that goal: Environmentalists and regulators decry TSCA because it gives EPA so little clout, while some industry groups complain that TSCA's flaws have led states to enact a patchwork of laws that complicate compliance.

But coming up with a new law that can satisfy everyone won't be easy. The legislation, co-sponsored by Senator David Vitter (R–LA), has drawn support from industry and the Environmental Defense Fund. Yet other environmental and public health groups, as well as some state officials, complain that Udall's bill would sometimes prevent states from writing their own tough regulations, fail to adequately accelerate EPA's efforts to screen potentially dangerous chemicals, and give industry too much voice in agency decisions. The bill "is worse than the current law. We can't go there," said Senator Barbara Boxer (D–CA), the top Democrat on the environment panel, at a 17 March press conference. She has offered an alternative bill that she argues would give EPA and state governments stronger oversight power.

Nearly 40 years ago, lawmakers approved

TSCA with high hopes that it would enable EPA to identify and ban chemicals that pose an "unreasonable risk" to public health or the environment. But EPA complains that it often lacks the power to compel companies to submit health and safety data, making risks hard to assess, and lacks the resources it needs to complete timely studies of the most worrisome substances. And even when EPA judges chemicals too risky, it has trouble restricting them, in part because the agency is forced to consider the economic cost of any ban, not just safety gains.

The new bill aims to make the process easier for EPA. It would shift the burden, for example, by requiring companies to show that a chemical is likely to be safe, rather than forcing EPA to prove that it isn't. The agency would also get new power to require firms to submit timely data. And it would be required to step up reviews of existing chemicals, starting with about 1000 "high-priority" substances.

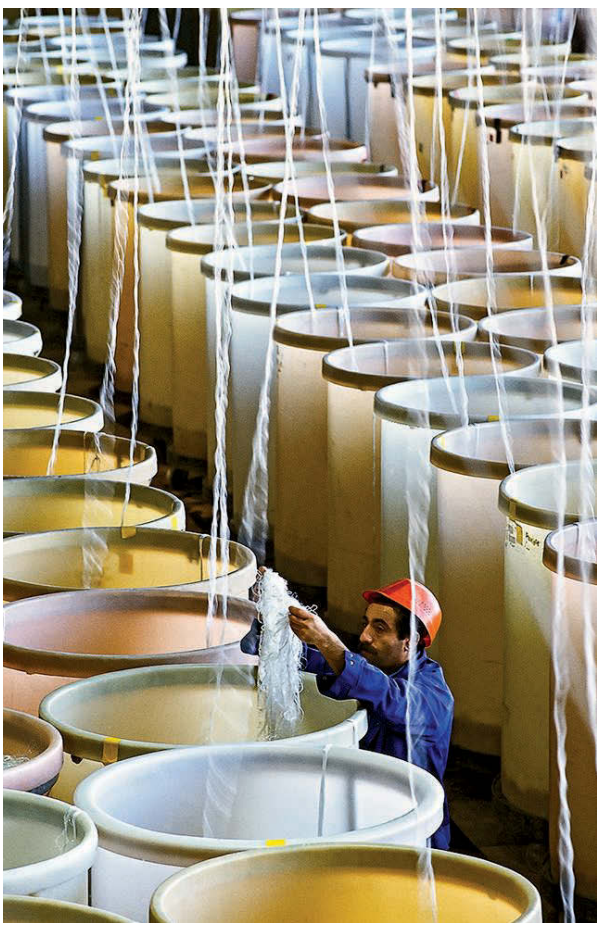

Nobody likes the nation's chemical-testing law, which regulates industrial chemicals, including those used to make textiles.

In a concession to industry, the bill would curb some state powers in order to create more uniform regulations nationally. Existing state regulations, such as a California program that annually lists chemicals that can cause cancer and birth defects, would stay on the books. But the bill would bar states from issuing new rules that are as strict or stricter than EPA's, and from targeting "high-priority" substances.

Other provisions aim to bring more, higher quality science into risk assessment. One would require EPA to use the "best available science" in regulations and establish a new panel of scientists, government officials, and others to provide technical advice. Another, backed by the American Chemical Society and other groups, creates a new multiagency panel to coordinate federal efforts to study and promote green chemistry. The bill would also encourage, but not require, EPA to develop and use animal-free testing methods.

That animal-testing provision is "kind of wishy-washy," but could encourage EPA to make greater use of alternative technologies, says Catherine Willett of the Humane Society of the United States in Boston. Computer modeling might predict whether a compound is harmful, for example, and robotic screening of cells that have been exposed to chemicals could quickly flag potential toxins.

The state preemption provisions, meanwhile, have drawn intense opposition. And the new advisory panels could give industry too much influence over scientific advice to EPA, worries the Union of Concerned Scientists (UCS), an advocacy group. "There are some serious issues that need to be resolved," says Andy Rosenberg, head of UCS's Center for Science and Democracy in Cambridge, Massachusetts.

Udall and Vitter say they are open to revisions, and even Boxer says she ultimately could support their bill if it moves closer to hers. Key lawmakers in the House of Representatives, meanwhile, say they are starting work on their own version, with a goal of voting on a bill by summer. Udall argues the clock is ticking. "Let's not wait another 40 years," he urged at a hearing on the bill, "to finally move forward." ■

Puneet Kollipara is a freelance writer in Washington, D.C.

GLACIOLOGY

Himalayan ice can fool climate studies

"Surging" glaciers in the Karakoram may actually be losing mass

By **Jane Qiu**, *in Kathmandu*

The glaciers of the Karakoram Range, at the geographic intersection of India, Pakistan, China, and Afghanistan, are prone to extremes. They hug some of the highest and steepest ground on Earth, over an exceptionally large elevation range: from 8610 meters above sea level at the storied summit of K2 down to as low as 2300 meters. Covering a total of nearly 18,000 square kilometers, they account for more than half of the total ice content in the Himalayas. And in a world of shrinking mountain glaciers, they are unruly exceptions.

After decades of retreat, in the 1980s, many Karakoram glaciers suddenly "changed their mind," says Kenneth Hewitt, a glaciologist at Wilfrid Laurier University, Waterloo, in Canada. "I began to see glacier thickening and advancing that I had not observed in the 35 years of field work before." Hewitt called it the "Karakoram anomaly," and climate-change skeptics made the most of it. "Many people use advancing Karakoram glaciers to deny climate change" or the overall ill health of Himalayan glaciers, says Graham Cogley, a remote-sensing expert at Trent University, Peterborough, in Canada. But new research suggests that the vigor of the Karakoram glaciers is more apparent than real.

"They may be advancing, but this does not necessarily mean they are gaining mass," says Frank Paul of the University of Zurich in Switzerland, who is also a remote-sensing expert. Some of the Karakoram's glaciers can surge over many years, giving an impression of steady growth, he says. Yet a video he presented at a meeting of the International Glaciological Society, held here early this month, showed that the growth is deceptive. A time-lapse view put together from 15 years of Landsat satellite images, it showed Karakoram glaciers "going wild," as he put it: collapsing at the top while gushing a massive amount of ice toward the terminus in tsunami-like

pulses. In the aftermath, the glaciers' surfaces were in tatters, with towers of ice protruding into the sky amid loops of moraine. The extra mass pushed the terminus forward but eventually dwindled.

Glacial surge can be spectacular from the ground: In 1953, Pakistan's Kutiah Glacier sent local inhabitants fleeing as the ice surged 12 kilometers over 3 months, swallowing villages, fields, and forests. Globally the behavior is rare, affecting less than 1% of all glaciers. But in the Karakoram, ground-based observers and satellites have documented it for hundreds of glaciers in recent decades. "Nowhere else on Earth could you find such a high concentration" of surge-type glaciers, says Christoph Mayer, a glaciologist at the Bavarian Academy of Sciences and Humanities in Munich, Germany.

A Karakoram glacier surge in 2005 deposited heaps of rubble and melting ice.

PHOTO: KENNETH HEWITT

Many of them "surge" in slow motion, Paul and his colleagues have now demonstrated, using satellite images captured since 1961 as well as maps and travel reports dating back to 1860. The 20 or so Karakoram glaciers they analyzed surged on a "surprisingly consistent" schedule, he says, at intervals ranging between 25 and 75 years. (Studies of other parts of the Karakoram reveal surge cycles as short as a few years or as long as over a century.)

Exactly what causes a glacier to surge is a mystery, but many glaciologists believe the surge cycle is internally regulated: After a surge, the lower part of the glacier thins while snow accumulates on the upper part until it reaches a critical threshold, triggering another surge. The Karakoram glaciers may be particularly prone to surging because of their steepness, vast elevation range—which means the conditions at the top and bottom are very different—and the heavy snowfalls they receive. "To surge or not to surge may have little to do with climate trends," Paul says.

The behavior not only makes changes in the length and area of these glaciers an unreliable indicator of climate change; it can also confuse satellite measurements of glacier mass change, says Tobias Bolch, a remote-sensing expert also at the University of Zurich. Satellites infer mass changes from changes in the elevation of the ice surface. But both optical and radar sensors are more prone to error at the top of the glacier, where they have trouble distinguishing ice from snow, than at the bottom, where the ice better contrasts with rocky surroundings. In a surging glacier, Bolch says, "we may be seeing the thickening near the terminus but only part of the thinning at the top"—and underestimating any loss of mass.

Because they are hard to monitor and seem to be responding to signals other than climate, Paul suggests that glaciers prone to surging should be omitted from studies of climate impacts. "We really need to see how 'normal' Karakoram glaciers are doing when surge-type glaciers are removed from the data set," he says. Given that so many large Karakoram glaciers are prone to surge, "the picture might be quite different."

Hewitt, however, thinks the surges may say something about climate. "The Karakoram anomaly is still partly, if not wholly, a response to climate change—one that is different from what is commonly understood," he says. Climate change at high altitudes—especially changes in temperature, wind, and the amount and timing of snowfall—could hasten or prolong surge cycles, Hewitt says.

Some wonder whether climate is already having an effect, pointing to a possible increase in glacier surges in the Karakoram in recent years. A 2011 study led by Luke Copland, a remote-sensing expert at the University of Ottawa, spotted 26 surges between 1990 and 2004, twice as many as in the previous 14 years. But Hewitt notes that it's unclear "whether this is an observation issue or a genuine trend."

Solving such puzzles is important not just to scientists. Glacier melt contributes some 30% of the total runoff of the Indus River and a staggering 50% in upstream basins, and glacial surges can unleash floods that threaten communities downstream. "There is an urgent need to understand what's happening with Karakoram glaciers," says David Molden, director general of the International Centre for Integrated Mountain Development here. "It's critical for planning policies and infrastructures and adapting to climate change." ■

Jane Qiu is a writer in Beijing. Her trip to Kathmandu was supported by a SciDev.Net fellowship.

The wild Karakoram

Mountain glaciers are dwindling across the Himalayas, but many Karakoram glaciers seem to be exceptions.

Henry Markram, the brain behind the Human Brain Project, has worn many hats for the initiative.

NEUROSCIENCE

A €1 billion brain reboot

Critics of Europe's Human Brain Project are vindicated

By **Martin Enserink**

Last summer, two neuroscientists staged a revolt. Their target: the Human Brain Project (HBP), a €1 billion, 10-year enterprise launched in 2013 and backed by the European Union. Alexandre Pouget of the University of Geneva in Switzerland wasn't involved in the project; Zachary Mainen of the Champalimaud Centre for the Unknown in Lisbon was a participant at high risk of losing his funding. Both were dismayed by the way HBP was run and by its stated ambition to create a computer model of the entire human brain by 2023—an aim Pouget calls "crazy." Together, they wrote an open letter asking the European Commission to step in. Hundreds of European colleagues signed on.

Now, the duo has scored an important victory. HBP's board of directors announced on 19 March that it will follow the advice of a mediation committee set up to find a way out of the crisis; the panel's recipe includes a management overhaul and a re-evaluation of the scientific goals that relegates modeling of the whole brain to the back burner.

"We're very pleased. It's a very positive step," Pouget says. But the critics say they will watch closely how the changes are implemented. And a broader question, they say, is why the European Commission was ready to spend so lavishly on a project in which both the mediation committee and a separate review panel set up by the commission found many flaws.

A project this size was bound to have some teething problems, says Philippe Gillet, HBP's board president. HBP is one of two flagship projects in the European Commission's Future and Emerging Technologies program, a funding scheme started in 2013 for visionary research with great potential for societal benefits. (The other flagship project focuses on graphene.) The European Union, through the commission, provides half of HBP's €1 billion budget for what is called the Core Project; countries, institutes, and companies are expected to foot the other half of the bill through HBP's Partnering Projects, although most of that funding has yet to materialize.

> ***"When all the dust has settled, there will be many interesting questions for historians of science to look at."***
>
> **Peter Dayan**, University College London

HBP is the brainchild of neuroscientist Henry Markram of the Swiss Federal Institute of Technology in Lausanne (EPFL), who also led a Swiss precursor called the Blue Brain Project. Markram is known for his charisma and media savvy, but his idea of simulating the brain "bottom-up"—all the way from individual genes, synapses, and circuits to the entire brain—has been assailed from the start as unrealistic and a waste of money (*Science*, 11 November 2011, p. 748). Many neuroscientists were also disgruntled over HBP's management. It boasts 113 partner institutes in more than 20 countries but is based at EPFL; power was concentrated in a three-member executive committee.

Pouget and Mainen published their open letter after HBP proposed moving a slice of the project on cognitive and systems neuroscience, in which Mainen participated, from the Core Project to the Partner Projects, alienating researchers who saw cognitive neuroscience as essential. "It was kind of the last straw," Pouget says. In response to the open letter, HBP asked Wolfgang Marquardt, an engineer and director of the Jülich Research Center in Germany, to form a mediation committee. The 30-member panel excluded Markram, Pouget, and Mainen; "I suppose it would have been very difficult to reach any sort of consensus with me and Henry in the room," Pouget says. But it did have other HBP representatives as well as outspoken critics.

In its report, released last week, the mediation panel vindicated Pouget and Mainen by stating that it "largely supports and emphasizes the critique voiced by parts of the scientific community regarding objectives, scientific approach, governance and management practices." It cited conflicts of interest, such as people benefiting from funding decisions made by panels they serve on. Markram played too many roles, it said: He serves on "all decision-making, executive and management bodies within the HBP, but also chairs them and supervises the administrative processes supporting these bodies," the report says. "Furthermore, he is a member of all the advisory boards and reports to them at the same time." It also said HBP lost scientific credibility by making "unrealistic" claims about whole-brain simulation and its potential to fight diseases such as Alzheimer's—"that was extremely troubling," says panel member Peter Dayan of University College London. What HBP needed, the panel said, was a "honest and more modest" communication strategy.

Among the recommendations is a major organizational overhaul that would put a new international entity in charge of the project,

PHOTO: AP PHOTO/KEYSTONE, JEAN-CHRISTOPHE BOTT

replacing EFPL. On the scientific side, the report says HBP's emphasis on whole-brain simulations was premature. "With regard to many aspects of brain function, knowledge is still much too limited to permit a credible bottom-up simulation," the panel concludes. Instead it recommends choosing a limited number of targets that are feasible within the budget and time frame, as the U.S. BRAIN Initiative did, with a focus on computational tools. Cognitive neuroscience is a vital part of the project and should stay within the Core Project, the panel said.

HBP's 22-member board unanimously adopted all the recommendations in a meeting on 18 March, and also those of an anonymous European Commission–appointed review panel that, too, was highly critical of the program, says HBP's Gillet, who is also EPFL's provost. The executive committee has already been abolished, and HBP has asked international institutions—such as CERN and the European Molecular Biology Laboratory—to advise it on a new structure. Gillet says Markram, who declined to comment for this article, had been pushing for the mediation and is "completely behind" the recommendations.

A critical question now is how the changes will be implemented, Pouget says. HBP has not commented on how it will handle a list of "observations" that the mediation panel did not reach an agreement on but that Pouget says contain the "meat in the report," especially about the scientific program. He worries that HBP's misguided dream of modeling the entire brain—talked up by Markram and Gillet in recent newspaper interviews—will refuse to die. "One of our goals has been to end the love fest between Markram and the media," Pouget says.

The European Commission in a statement said that it welcomes the mediation process and will discuss the findings with HBP. Critics, however, say the commission should reflect more on how it came to shower money on an effort riddled with shortcomings. The critical reports suggest that the selection process for the flagships—widely criticized as opaque at the time (*Science*, 1 February 2013, p. 497)—was flawed itself.

A commission representative dismissed that criticism in an e-mail to *Science*. HBP was selected "by a high-level evaluation panel including leading scientists, industrialists and specialists from a broad range of disciplines," in a process that lasted more than 2 years, the e-mail said. Dayan demurs. "A project of this scale that has so many problems leads to severe questions on how it came to be in the first place," he says. "When all the dust has settled, there will be many interesting questions for historians of science to look at." ■

INFECTIOUS DISEASES

A reassuring snapshot of Ebola

Virus sequences from Mali suggest pathogen has not changed enough to elude potential vaccines or treatments

By **Gretchen Vogel**

As Ebola has taken its horrific toll across West Africa, passing from person to person in its longest known chains of human infections, researchers worried the virus might mutate to become even more threatening. New viral genome data from Mali suggest a glimmer of good news: The Ebola virus that infected eight people there in October and November had not changed significantly from the one that infected people at the beginning of the known outbreak, back in March 2014.

Ebola virus (orange) isolated from a patient in Mali.

IMAGE: NIAID

Diagnostic tests, experimental antibody-based treatments, and potential vaccines for Ebola are all developed based on the virus's genetic sequence. If it were to change too much, cases could go unrecognized, and treatments and vaccines could become ineffective. Mutations might even lead to more dramatic symptoms or allow the virus to pass from person to person more easily. But when Heinz Feldmann, a virologist at the National Institute of Allergy and Infectious Diseases in Hamilton, Montana, and colleagues sequenced four recent Ebola virus samples, they found little sign that the virus has evolved.

Some earlier sequencing studies, which examine virus from the blood samples taken to diagnose patients, had been less reassuring. In August, for example, a research team published the first analysis of 99 Ebola virus genomes from infections in Sierra Leone. That snapshot found that a fairly large number of changes had appeared in the virus, when compared with past virus samples (*Science*, 29 August 2014, p. 989).

The Mali sequences, which Feldmann and colleagues describe in a paper published online this week in *Science* (http://scim.ag/THoenen), are from patients distant both in time and geographically and give a longer view of virus evolution. The new data confirm what many scientists had suspected—and hoped: that most viral mutations that pop up are weeded out before long, presumably because they are not beneficial to the virus.

Ebola virus spread to Mali twice last year from Guinea, where the epidemic hit hard. In October, an infected toddler traveled with family members from Guinea to the city of Kayes in western Mali, where she died without infecting anyone else. However, a few days later an infected man traveled from Guinea to Bamako, the capital, where he sparked an outbreak that sickened seven more people.

Feldmann and his colleagues sequenced virus samples from the toddler and from three patients in the second outbreak. They found only 15 nucleotide differences between the toddler's virus and virus from a patient in Guinea in March 2014, at the beginning of the West Africa outbreak. The viruses from the two Mali outbreaks were also quite similar, although there is no known connection between the cases.

The results are consistent with other publicly deposited sequences, notes Jim Kent of the University of California, Santa Cruz, who has set up an Ebola virus genome database (http://bit.ly/Ebolaportal). The new data "adds yet more confidence that a vaccine strategy should work," he says, because the virus appears fairly stable. "So, good news!"

Kristian Andersen of the Broad Institute in Cambridge, Massachusetts, who was a co-author on the earlier Sierra Leone sequences paper, warns, however, that introducing experimental treatments and vaccines will add new selective pressures. "It is essential that we keep monitoring" the virus's evolution, he says. ■

SOCIAL SCIENCES

Measuring child abuse's legacy

First large-scale, longitudinal study tracks abuse and neglect across generations

By **Emily Underwood**

The notion that victims of physical abuse as kids are more likely to abuse their own children, often described as the "cycle of violence," is widely held but sparsely documented. Now, the first large, longitudinal study to track how victims of child abuse treat their own children has found little evidence of a cycle of violence, but suggests that sexual abuse and neglect may indeed be passed down the generations.

Patricia Kohl, a social scientist at Washington University in St. Louis, calls the study, published on page 1480 of this issue, "seminal" for its size and the variety of data it drew on. But the study also makes a controversial claim: that heightened surveillance of families with a history of abuse may have biased some studies taken as evidence for the cycle of violence.

Without access to official records of abuse, researchers often rely on recollections made years later and are limited to short-term studies with small sample sizes, says psychologist Cathy Spatz Widom of the City University of New York. Those studies have come up with estimates of the proportion of abusive parents who themselves suffered child abuse ranging from as low as 7% to as high as 70%.

In 1986, Widom launched an ambitious effort to document the effects of child abuse in hundreds of people across many years. By combing through court records from a metropolitan area in the midwestern United States, she identified 908 reports of physical and sexual abuse and neglect in the years 1967 to 1971 and tracked down the victims, who ranged from infants to 11-year-olds at the time of the abuse. As Widom followed these individuals and compared them with a matched control group, she found that the abused children's risk of violence and delinquency as they grew up was far less than many had expected.

To test if the abused children would become abusive parents, Widom's team had to wait 30 years, until the original subjects averaged 47 years old. By then, roughly half had dropped out of the study, but the full original cohort had produced more than 700 of their own offspring, now about 22 years old on average. To examine what happened during those offspring's childhoods, the researchers delved into court records and documents from the U.S. Child Protective Services (CPS), a government agency that responds to reports of child abuse and neglect. They also hired surveyors to conduct more than 1400 wide-ranging interviews with both generations.

As the data rolled in, a complex story emerged. About one-fifth of parents who had experienced some form of abuse growing up had been reported to CPS for child maltreatment—roughly twice the rate of the control group. When the team broke the data down by forms of abuse, however, the results were surprising. According to the CPS data, children whose parents had been physically abused were no more at risk of physical abuse than those in the comparison group, a finding that directly contradicts the "cycle of violence."

New data challenge the cycle of violence, the idea that physically abused children, once they become parents, will similarly mistreat their kids.

The data on sexual abuse and neglect told a different story. The children of people who had suffered either sexual abuse or neglect were roughly twice as likely to experience such abuse: CPS reports of sexual abuse were filed for 3.4% in the control group and 7.7% in the abused group; the figures for neglect were 9.5% in the control group and 18% in the abused group. (The study didn't establish if the previously abused parent was responsible.) Similar trends emerged from the interviews, Kohl says: "Whether it's the child's, parent's, or a CPS report, you don't see transmission of physical abuse, but you do see intergenerational transmission of sexual abuse and neglect."

The study offers solace to victims of physical abuse, as well as guidance for judges and advisers involved in child custody cases, says Joan Kaufman, co-director of the Zigler Center Child Welfare Unit at Yale University's School of Medicine. Many people have been told that having a history of physical abuse makes them less qualified to be parents, but a cycle of abuse is "not inevitable," she says.

Yet Kenneth Dodge, a psychologist at Duke University in Durham, North Carolina, questions the data on physical abuse, because it can be so difficult to document. As a result, CPS workers may focus on filing claims of neglect rather than physical abuse when they fear for a child's safety, he says.

The study highlights a different kind of potential bias against parents with a formal record of being abused as children. Those who told surveyors they had abused their kids, or whose kids described being abused, were 2.5 times more likely to be reported to CPS than parents in the control group who admitted to abusing their children, or whose kids said they had been mistreated. This disparity suggests that parents previously known to the system as victims are far more likely to be flagged as abusers by social service programs, Widom says.

Dodge argues that it's "just as plausible" that the maltreatment previously abused parents visit upon their offspring is "more severe, chronic, and obvious, and therefore more likely to be detected" than those unfamiliar to CPS. But Kohl agrees with the study's conclusion of prejudice: "This does suggest that there is in fact some type of bias when families are previously known to the system."

If so, many cases of abuse in other families may be slipping by unnoticed, Widom says. To her, that is an important message of the study. "We really need to shift our focus to prevention, by promoting child well-being and strong families." ■

PHOTO: PRINCESSDLAF/ISTOCKPHOTO.COM

Doctors remove a tissue core from a cadaver for analysis.

PHOTO: QUIQUE BASSAT

CAUSE OF DEATH

No one knows why many people die in developing countries. A new technique, the minimally invasive autopsy, could change that—and transform global health

By **Sam Kean**, *in Maputo, Mozambique*

Neither half of the body looks abnormal by itself, but legs that skinny just don't belong on a chest that swollen. The 15-year-old boy, Antonio, died the previous day—he still has dirt between his toes—and several doctors have gathered in an autopsy room in the hospital here to determine why. But rather than slice his bloated torso open, pathologist Paola Castillo reaches for a clutch of needles.

At 9:08 a.m., she begins by sliding one needle into the soft spot between Antonio's skull and vertebra and collecting the cerebrospinal fluid that drips out. She then switches to a longer, 8-cm needle and tries to draw blood from above his right clavicle. It comes out thick and clotted, so she switches to the left side. But Antonio's head, stiff with rigor mortis, blocks the way, and an assistant named Bento Nhancale must wrestle it aside. This time, blood flows freely. But when Nhancale lets go, Antonio's head starts rotating back. Slowly at first, achingly slowly—and then it snaps into place, as if he's seen something.

It's an unsettling moment—one of several during the next hour. But wrenching Antonio's limbs aside and poking him with needles is still far less unnerving than the alternative: turning him inside-out for a full autopsy. In fact, that's partly why Castillo is performing this "minimally invasive autopsy" (MIA) on Antonio. MIAs are quicker, potentially cheaper, and cleaner than full autopsies—and advocates argue that they still provide the same

Published by AAAS

basic information about what kills people.

That's important, because—as startling as this sounds—health experts don't really know what kills many people worldwide. They're especially likely to be in the dark when the cause was some kind of infection and the victim was a child. And without this information, health officials don't know where to focus limited dollars, or how well current disease-reduction programs work.

Researchers are hoping that MIAs—which take fluids and bits of tissue from a half-dozen organs and examine them in the lab—can substitute for full autopsies and provide this critical mortality data. The general idea of MIAs actually dates back several decades, but they have become a hot idea as international health agencies seek crucial data on causes of death. That's why teams in several countries, including Mozambique, have spent the past few years testing both the scientific validity and cultural acceptability of MIAs—with an eye toward expanding them across the globe.

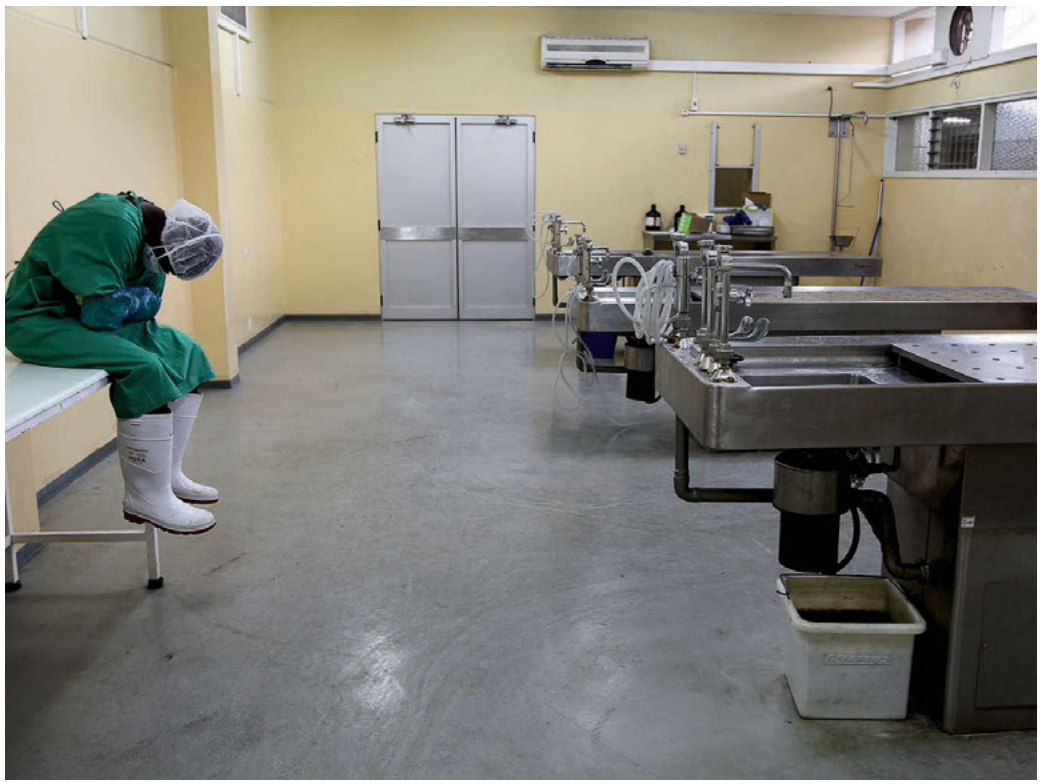

A technician gathers his thoughts before an autopsy in Maputo. Many countries in the developing world cannot afford widespread autopsies, and many people in those countries fear and mistrust full autopsies anyway.

Per the Mozambique team's protocol, Castillo takes a liver sample next. She palpates Antonio's chest, explaining that the liver often shifts upward in dead bodies. The liver needle works like a crossbow, cocking and then snapping forward. In doing so, it cuts out a centimeter-long worm of tissue.

Antonio twitches when the crossbow snaps. But when Castillo withdraws the needle, no purply worm of liver emerges. Pus shoots out instead—pale green and foaming. Castillo shifts and tries again. More pus. Liver tissue should be easy to collect, but after 20 chest punctures, there's nothing but pus.

It's a giant abscess, and Castillo suspects that it pushed Antonio's liver even higher. A student pathologist takes over and, several jabs later, finally finds solid tissue 10 cm above Antonio's nipple. But the worm that emerges is too white for liver. Is it lung? Shrugs all around—someone will have to examine it later under a microscope.

MOST PEOPLE in developing countries die at home, far from clinics, making it hard to know what killed them. But even within clinics, determining cause of death is tricky, because many patients (especially children) come down with multiple ailments at once. One 2005 study found that, compared with autopsies, physician-issued death certificates were wrong one-third of the time. A 2014 study from India uncovered "major errors" in half of all pediatric death certificates.

One figure—or really two figures—sums up the problem. A few years ago, the World Health Organization (WHO) and the Institute for Health Metrics and Evaluation (IHME) in Seattle, Washington, each tried to determine how many people died of malaria in 2010. WHO calculated 655,000 deaths, IHME 1.24 million. Two of the world's most respected health groups could barely agree within a factor of two, and similar problems exist with AIDS, tuberculosis, and other killers (see graph).

An uncertain toll

Two leading global health agencies sometimes come up with very different estimates of annual mortality from infectious diseases.

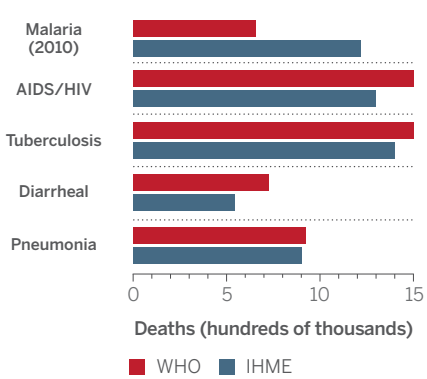

Most developing countries lack the funds and infrastructure for widespread autopsies, which could provide more certainty. (Several countries in Africa have zero pathologists.) What's more, many people in developing countries fear and mistrust the idea of cutting open a corpse. As a result, "the field has sort of given up on [full] autopsies," says Regina Rabinovich, a pediatrician with a background in tropical disease at Harvard University's School of Public Health in Boston, who formerly directed the infectious disease unit at the Bill & Melinda Gates Foundation in Seattle.

Many cause-of-death studies rely instead on "verbal autopsies," which involve asking family members of the deceased a list of questions. Unfortunately, verbal autopsies often take place months later, by which point people's memories are hazy. Family members often disagree about symptoms anyway, or give supernatural explanations—that someone died of a curse, for example. Worst, many infectious diseases produce ambiguous symptoms—fever, diarrhea, cough—that are nearly impossible to sort out with questions alone. Quique

CREDITS: (PHOTO) QUIQUE BASSAT; (DATA) WHO/IHME

Bassat, a pediatrician at the Barcelona Centre for International Health Research in Spain, sums up many doctors' feelings about verbal autopsies: "We think it's a crap method."

Many in the international health community hope that MIAs can reproduce the accuracy of full autopsies on the cheap. (Full autopsies now cost about $500. The full MIAs that Bassat's team is testing now cost about the same, but they plan to simplify the protocol eventually and cut the price to $200 to $400.) To this end, the Gates Foundation granted Bassat's team $2.3 million over 3 years to compare MIAs with full autopsies in 260 cases in Mozambique, divided into four cohorts—neonates, children, adults, and pregnant women. (A partner study in Brazil will analyze 60 additional cases.)

Bassat's MIAs collect and culture pathogens for study, something traditional autopsies don't do. And they are fast—an asset in places that lack refrigeration. After months of practice, Bassat says his team can now perform MIAs in just 30 minutes. At least in theory. As Antonio's case shows, MIAs in real life can get messy.

AFTER THE LIVER FIASCO, Castillo shifts to Antonio's lungs. The lung needle is long and fat, a trypanophobe's worst nightmare. Meanwhile, a student extracts bone marrow by grinding a T-shaped needle into Antonio's hip. It's the cleanest tissue core yet and earns a hooray from Castillo. To access Antonio's brain, they use the T to pierce the bone behind his nose.

As each tissue core emerges—the spleen and kidney are up next—Nhancale, the technician, snags it with forceps. Some cores get plopped into yellowish fluid, like worms into mezcal. (Airy lung tissue tends to float, dense brain to sink.) Flies circle the room, but there's almost no smell.

Nhancale, a slight and smiling Mozambican, began working for Bassat's team 9 years ago, at 19, before the MIA study began. As part of that earlier work, he had to jump right into full autopsies, and seeing naked dead bodies split open shook him. "It was so strange, so strange," he recalls. He had trouble sleeping for weeks and gave up eating liver for a while.

Many people in wealthier countries would have a similar reaction, of course. But they would generally acknowledge that doctors sometimes need to examine dead bodies for medical research. That tradition is lacking in much of the developing world, says Khátia Munguambe, a medical anthropologist on Bassat's team. Many people there see opening up the bodies as defiling them, and most don't see what good autopsies do anyway, considering the person has already died. Some also fear that doctors secretly sell people's organs—and even murder to get them.

MIAs, too, meet resistance, including from health workers. The pathologists in Mozambique working with Bassat's team say their colleagues are almost uniformly skeptical that mere specks of tissue can provide mortality data. Even Castillo, when she first heard of MIAs while working in Barcelona, doubted they would work. Many doctors and general health workers in Mozambique also fear that MIAs will be used to "check up" on them and prove that they misdiagnosed patients.

To determine how to make MIAs culturally acceptable, Bassat's team is running a second, anthropological study in Mozambique, Kenya, Gabon, Mali, and Pakistan. In particular, they're studying funeral practices to learn why people might reject MIAs. In Gabon, for instance, Munguambe learned that elders objected to doctors "penetrating," even with needles, adolescents who had not gone through sex-initiation rites.

Taboos against autopsies are especially strong in Muslim countries like Bangladesh, says Emily Gurley, an epidemiologist running a separate MIA project there through the International Centre for Diarrhoeal Disease Research, Bangladesh, in Dhaka. Muslims generally bury people before sundown the day they die, and autopsies can delay this. Muslims also wash the body after death, at which point doctors cannot touch it. Some sects also believe that the dead feel pain.

Despite these taboos, Gurley found that many Muslim leaders supported MIAs once they saw how little tissue she needed. Allowing family members of the deceased to observe MIAs also eased mistrust. And in Mozambique, Bassat's team has met with community leaders to hear their concerns. During one meeting in January, a 70-year-old grandmother in a pink T-shirt greeted the team with a complicated, multistep handshake. She then gathered everyone around her in plastic patio chairs and, amid clucking hens, explained her constituents' concerns. For example, many of them wanted to know why, if taking tissue cores is so useful, doctors don't use the procedure to diagnose living people and save them. She also emphasized their frustration over the lack of answers for why people die—a frustration the scientists share.

MIA advocates argue that this social-science research is every bit as crucial as the clinical work. "This is a supersensitive area," Bassat says. "If you skip one step you may jeopardize everything." That said, "if you get acceptance rates, the rest is just logistics."

ALTHOUGH PRELIMINARY, the results from Bassat's studies look promising. On the social-science side, interviews in all five countries revealed a high theoretical acceptance rate, around 80%. (For a non-theoretical comparison, five of 15 families in Bangladesh gave Gurley permission to actually perform MIAs.) And clinically, MIAs determined cause of death in 95% of cases, he says, a rate similar to full autopsies.

To save time and money, Bassat's team may streamline the procedure by paring down the number of tissue cores. (Liver, lung, and brain samples provide the most useful data.) They may also drop the pathogen cultures. Without microbiology, they can determine cause of death about 80% of the time.

That's still much better than verbal autopsies, but not all global health experts

Minimally invasive autopsy, point by point

This technique takes tissue and fluid samples from several different body parts, as shown below (in rough order of extraction). Scientists later examine them in the lab for signs of infection or other diseases.

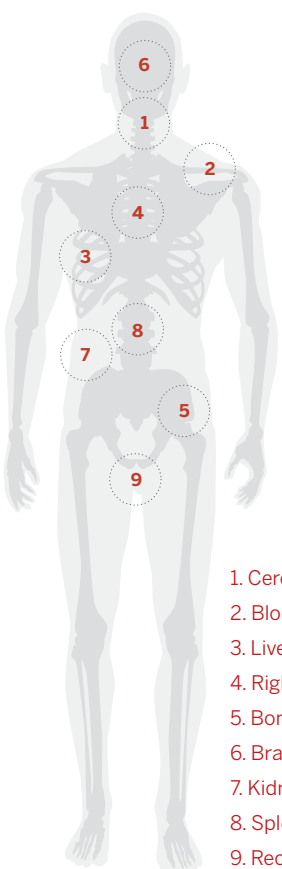

1. Cerebrospinal fluid
2. Blood
3. Liver
4. Right and left lung
5. Bone marrow
6. Brain
7. Kidney
8. Spleen
9. Rectal swab

ILLUSTRATION: WOEWCHIKYURY/ISTOCKPHOTO.COM

A woman in Mozambique answers questions during a "verbal autopsy" about the death of her infant son, the brother of the baby she is holding.

PHOTO: QUIQUE BASSAT

are sold on MIAs. "The concept of a minimally invasive autopsy certainly has some appeal," says Alan Lopez, an epidemiologist and expert in global health statistics at the University of Melbourne in Australia. "But I have yet to see any evidence to show how accurate it is, and for which diseases." He adds that, however promising MIAs prove for deaths in clinics, they may have "no relevance for the 60–70% [of people] in developing countries that die at home."

To reach some of those home deaths, Bassat wants to train nonphysicians like Nhancale as MIA technicians and push MIAs into rural areas. He is also considering deploying mobile MIA clinics: old converted ambulances with self-contained and self-cleaning units in back.

Ultimately, scientists and health officials want to spread MIAs across the globe. To that end, the Gates Foundation is launching a 20-year surveillance program called SEED (Sentinel Epidemiology and Etiology Data) in April. Gates will support the project with $75 million over its first 3 years, with $75 million more coming from other sources.

SEED will eventually open sites in roughly 25 places in Africa and Asia, some by 2018, and MIAs "will be the cornerstone for this surveillance," says Scott Dowell, a pediatrician who will head the effort. Overall, SEED aims to perform MIAs on roughly 20% of the deaths in each region, and although it will focus on children at first, Dowell says that it could easily expand to adults over time. If so, scientists may finally know, for the first time, why most people worldwide actually die.

FOR NOW, Bassat's team is still trying to nail down what killed Antonio.

His MIA wraps up late, clocking 70 minutes. The results will come after team members in Barcelona examine the tissue. But now a full autopsy must take place, to provide a point of comparison. The team retires to an operating theater next door to watch.

At this point the hospital "eviscerator" enters. This muscular youth slides a block beneath Antonio's nape, then flays his torso with a knife and fork. As he cuts, he encounters several liters of pus from the abscess, but he doesn't slow down or even seem to notice. He simply removes the dripping "organ block" from the abdomen and sets it between Antonio's legs.

The MIA team watches intently as a new pathologist enters and examines each organ. There are tumors in the lymph nodes, kidneys, and brain. Antonio also had meningitis—news that sends Castillo racing back into the autopsy room. The huge chest abscess gets special attention. It basically devoured Antonio's right lung. It also pushed Antonio's liver not up but down, which explains why Castillo couldn't find it. "You never see diseases get this far in the developed world," Bassat comments. "It's like case reports from the 1950s."

As the full autopsy wraps up, a debate begins about what killed Antonio. Bassat's team discusses AIDS, cancer, meningitis: Like the fall of the Roman Empire, there is no end of options. Bassat eventually zeroes in on the lymph node tumor. He suspects it swelled grotesquely and metastasized. Meanwhile, it also got infected (hence the abscess), and Antonio—already weak—finally died when the infection spread.

In some ways, the MIA justifies the suspicions that many pathologists entertain. Bassat's team couldn't even find the liver, for crying out loud, and their needle biopsies likely missed the kidney and brain tumors. But Bassat says that, when his colleagues look at the tissue, it will be obvious that the white "liver" core actually came from a lymph node tumor. They'll almost certainly find widespread signs of infection as well. Overall, he predicts that the MIA will catch the original problem and allow his team to determine cause of death.

> ***Many doctors feel verbal autopsies are "a crap method."***
>
> **Quique Bassat**, Barcelona Centre for International Health Research

A MIA would also have left Antonio's body in better shape for his family—pockmarked, but in one piece and recognizably human. Still, the eviscerator does what he can for decorum, sewing up the torso and scooping every organ—even the brain—into the abdomen. He slots the sternum into place, and tugs the final stitches taut.

The threads in his chest are pretty obvious—you can see why people object to autopsies. But Antonio's postmortem sacrifice did give scientists something valuable: a better understanding of why people like him die. And surprisingly, with all the pus drained out, that torso finally looks like it belongs to those legs. Antonio finally looks like a normal teenager. ■

Technologies to treat brain disorders *p. 1418*

Biography offers new insights on Pavlov *p. 1425*

PERSPECTIVES

INFECTIOUS DISEASE

How to bolster the antifungal pipeline

Few drugs are coming to market, but opportunities for drug development exist

By **David W. Denning**[1,2] *and* **Michael J. Bromley**[1,3]

About 1.2 billion people worldwide are estimated to suffer from a fungal disease (*1*, *2*). Most are infections of the skin or mucosa, which respond readily to therapy, but a substantial minority is invasive or chronic and difficult to diagnose and treat. An estimated 1.5 to 2 million people die of a fungal infection each year, surpassing those killed by either malaria or tuberculosis (*3*). Most of this mortality is caused by species belonging to four genera of fungi: *Aspergillus*, *Candida*, *Cryptococcus*, and *Pneumocystis*. Although great strides were made in the 1990s, drug development has largely stalled since then. Opportunities exist for accelerating development, particularly in fungal asthma, and to treat chronic and invasive aspergillosis.

INFECTIOUS DISEASE SERIES

Antifungal therapy has become progressively more effective since second-generation azoles, echinocandins, and lipid formulations of amphotericin B were introduced from the 1990s onward (*3*). These compounds act by inhibiting ergosterol and β-D-1,3 glucan synthesis and perturbing the cell membrane (see the figure). Voriconazole is now the agent of choice for invasive aspergillosis, allowing patients to survive leukemia and transplantation who would otherwise have died (*4*, *5*).

[1]*The University of Manchester, Manchester Academic Health Science Centre, Manchester, UK.* [2]*The National Aspergillosis Centre, University Hospital of South Manchester, Manchester, UK.* [3]*The Manchester Fungal Infection Group, The University of Manchester, Manchester, UK.*
E-mail: ddenning@manchester.ac.uk

Photomicrograph of *Aspergillus fumigatus*. This fungus causes life-threatening invasive and chronic aspergillosis as well as driving severe asthma. Although drug treatments exist, mortality remains high.

PHOTO: BSIP SA/ALAMY

Nevertheless, ~30 to 50% of invasive aspergillosis patients still die, for reasons that include late diagnosis, infection of sites such as the brain that are not effectively treated with drugs, and drug resistance. The mortality from candidemia, a fungal infection mainly treated with echinocandins and fluconazole, also remains high at ~50%. Since 2006, no new classes of antifungals have been approved. This is problematic because current agents are not sufficiently active, cannot be given orally, carry drug- or class-specific toxicities, or have major drug interactions.

VORICONAZOLE—A CASE STUDY. The development of voriconazole illustrates many of the challenges in developing novel antifungal treatments, particularly for invasive aspergillosis. Scientists at Pfizer synthesized over 1200 azole analogs before selecting voriconazole, which kills over 50% of *Aspergillus* strains. Both intravenous and oral formulations were developed (most antifungals are either intravenous or oral).

In phase 1 studies, blood levels of voriconazole varied widely among subjects. Increased abnormalities in liver function tests were seen at high blood levels. Furthermore, a peculiar visual adverse event of flickering lights or zigzag lines occurred in some subjects shortly after receiving higher doses. This last side effect had a silver lining: It showed that voriconazole entered the central nervous system. It thus correctly anticipated much-improved outcomes with voriconazole for cerebral aspergillosis, previously a uniformly fatal disease.

Phase 2 studies in Europe began in 1993 and laid the foundation for two phase 3 (parallel randomized controlled registration) studies (*6*). In the phase 3 studies, patients with low or undetectable voriconazole blood concentrations failed therapy, whereas those with very high levels experienced toxicity, mostly resulting in death. Thus, therapeutic drug monitoring is advised in every patient receiving this drug (*7*).

The phase 3 studies compared intravenous voriconazole with intravenous amphotericin B, followed by lipid amphotericin B or itraconazole (*8*). Over the course of 3 years from July 1997, 379 patients with invasive aspergillosis from 19 countries and 95 clinical referral centers were enrolled. In the study, voriconazole was shown to be superior to amphotericin B; several later case series confirmed it to lower mortality by 15 to 20% compared to non-azole drugs. Since voriconazole was licensed in 2002, it has been prescribed to millions of patients worldwide.

Despite voriconazole's undoubted benefits, it remains a challenging agent to use clinically, with major variations in exposure and metabolism, notable drug interactions, and appreciable toxicity in many patients. Thirty to 50% of patients with invasive aspergillosis still die despite treatment.

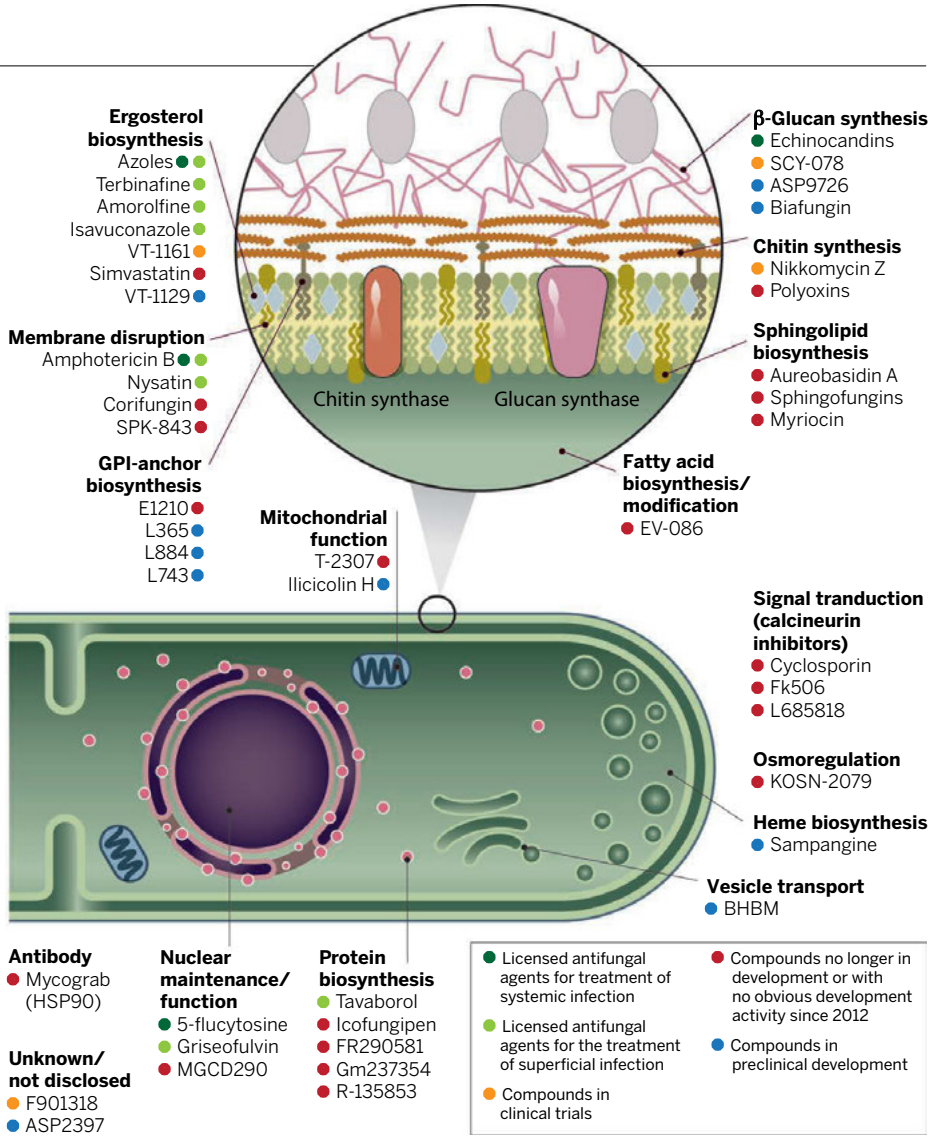

Antifungal drugs. With the exception of 5-flucytosine (the use of which is limited because of its narrow spectrum of activity and rapid development of resistance), all agents licensed for treating systemic fungal infection target cellular integrity. The pipeline of antifungal development is sparse, but it is promising that two compounds currently in clinical development are active against novel targets (nikkomycin Z, which targets chitin synthesis, and F901318, the novel target of which remains undisclosed) and that a number of preclinical agents target functions other than cellular integrity. GPI, glycosylphosphatidylinositol.

DRUG RESISTANCE IN FUNGI. Many fungi are intrinsically resistant to certain antifungals; notably, *Candida krusei* (to fluconazole), *Aspergillus terreus* (to amphotericin B), *Cryptococcus* spp. (to the echinocandins), and *Scedosporium* spp. (to all current antifungals). About 20 years ago, azole-sensitive *Candida albicans* dominated infections, with other *Candida* species rarely seen. After over two decades of systemic azole usage, this picture has changed. *C. glabrata* is particularly problematic: It is the second-most-commonly isolated *Candida* species in the European Union (EU) (>10%) and United States (>20%) and has high rates of resistance to fluconazole and voriconazole, as well as (more recently) to echinocandins. Intrinsically resistant mold infections are also being observed more frequently, such as zygomycetes and *Fusarium* spp. Azole- and echinocandin-resistant *C. glabrata* can only be treated with intravenous amphotericin B, which is often toxic and does not penetrate into urine, making some infections untreatable. Zygomycetes only respond to posaconazole and amphotericin B, and there are no drugs for *Scedosporium* (*9*).

The emergence of azole resistance is a growing problem, particularly in the Netherlands, where azole-resistant *Aspergillus fumigatus* is now commonplace. Unlike bacteria, fungi are not known to transfer resistance genes between them, nor is patient-to-patient transmission common. The

ILLUSTRATIONS: (TOP) C. SMITH/*SCIENCE* AND V. ALTOUNIAN/*SCIENCE*; (BOTTOM) C. SMITH/*SCIENCE*

prognosis for individuals infected with a resistant *Aspergilllus* strain is poor, with nearly 90% mortality against an expected mortality of ~50% for invasive aspergillosis.

Most resistant *A. fumigatus* strains that have been isolated have a specific mutation in the target of azole action, Cyp51A. Multiazole–resistant isolates carrying the same mutation have been found in Belgium, Denmark, Germany, the United Kingdom, China, India, Tanzania, Kuwait, and Iran. Agricultural and other commercial uses of azole fungicides are the likely, but not yet proven, culprit for the emergence of these resistant strains (*10*). Restriction of azole fungicide use has been proposed but is challenging for multiple reasons, notably, the lack of alternative fungicides for many key crops. Withdrawal of azole agricultural agents would reduce the annual wheat crop value by an estimated €4.6 billion by 2020 in the EU alone (*11*). Nonetheless, restriction of azole spraying to essential crops (i.e., not fence posts, plasterboard, cut flowers, etc.) may be a sensible first step to curb the problem. Once a novel human antifungal class is developed, fungicides of similar chemical structure should not be approvable, to minimize resistance development.

"In recent years there have been a number of failures in antifungal development..."

A SPARSE DISCOVERY PIPELINE. In recent years there have been a number of failures in antifungal development, notably the antibody against HSP90 (heat shock protein 90) Mycograb and the histone deacetylase inhibitor MGCD290, both of which were insufficiently active in patients. Searches of current literature, conference reports, and drug company pipeline reports suggest that only four compounds are in active clinical development for the treatment of systemic disease, with a further two agents expected to enter clinical development in 2015 (*12*). A few other compounds are in preclinical development, many with modes of action that differ from the currently marketed agents (see the figure); whether they will progress into clinical development remains uncertain.

Difficulties in identifying new broad-spectrum compounds and a chronic lack of investment in novel antifungal agents are both responsible for the limited drug development pipeline. Most major pharmaceutical companies are not investing in antifungals, preferring to focus on other, apparently more lucrative areas. EU (New Drugs 4 Bad Bugs) and U.S. (BARDA Broad Spectrum Antimicrobials) initiatives have stimulated investment in the development of antibiotics, but no similar initiatives exist for the development of antifungals. Attempts to address the lack of investment include the U.S. Food and Drug Administration's (FDA's) Generating Antibiotics Incentives Now (GAIN) Act, which allows a 5-year extension of market exclusivity for anti-infectives and specifically names *Aspergillus*, *Candida*, and *Cryptococcus* species as qualifying diseases.

In some ways, the challenges to the development of antifungals are more pronounced than those faced by antibacterial development. Because fungi, like mammals, are eukaryotes, many proteins that are potential targets for therapy are also found in humans, with substantial drug toxicity risk. However, there are some advantages to working in eukaryotes, particularly those with a diploid life stage. Chemically induced haploinsufficiency, a functional genomics technology, has been used in *C. albicans* and *Saccharomyces cerevisiae* to identify the mechanism of action of novel antifungal agents, yielding many new drug targets (*13*).

DEVELOPMENT OPPORTUNITIES. Awareness of the spectrum of fungal diseases continues to grow. For example, *Aspergillus* may have an important and treatable amplifier effect in cystic fibrosis (CF), asthma, and chronic obstructive pulmonary disease (COPD) (*14*). Severe asthma with fungal sensitization responds to oral antifungal therapy, and with 350,000 asthma deaths annually (*1*), approved and novel antifungals could play an important part in reducing deaths. Treatment of chronic pulmonary aspergillosis (including aspergilloma) probably reduces death rates, and certainly reduces morbidity (*15*). No drug development candidates exist yet for these indications, but alternatives to the azoles are urgently needed—partly because of inadequate response rates, partly because of adverse events, and definitively because of resistance.

Cryptococcal meningitis is another important development target. It responds poorly to fluconazole, with >60% mortality at 10 weeks in sub-Saharan Africa; the combination of amphotericin B and flucytosine is better, but not widely available and difficult to administer safely. A new potent agent for cryptococcal meningitis has the potential to save many lives.

OUTLOOK. Despite some effective drug treatments, mortality from fungal infections remains high, and new drugs are urgently needed. A major barrier to improved understanding of fungal diseases and the development of faster diagnostics and novel therapies is the general lack of capacity in fungal pathogen research (*16*). Greatly improved diagnostics mean that narrower-spectrum antifungals can now confidently be developed, making the early stages of drug development more straightforward. Alternative development pathways, relying heavily on pharmacodynamic modeling and focused clinical studies, have been proposed for antibacterial agents and should be applied to antifungals (*17*). Galactomannan Aspergillus antigen testing has been recognized as a surrogate marker for clinical studies (*18*), facilitating clinical development. The FDA has helped by granting new antifungals "orphan status," lowering clinical trial barriers. As understanding of key risk factors for fungal disease improves, stratification of patient groups will be possible, permitting more targeted clinical trials and ultimately leading to improved treatment regimens for patients. ■

REFERENCES AND NOTES

1. T. Vos *et al.*, *Lancet* **380**, 2163 (2012).
2. G. D. Brown *et al.*, *Sci. Transl. Med.* **4**, 165rv13 (2012).
3. www.gaffi.org
4. S. Perkhofer *et al.*, *Int. J. Antimicrob. Agents* **36**, 531 (2010).
5. J. M. Valdez *et al.*, *Clin. Infect. Dis.* **52**, 726 (2011).
6. D. W. Denning *et al.*, *Clin. Infect. Dis.* **34**, 563 (2002).
7. H. R. Ashbee *et al.*, *J. Antimicrob. Chemother.* **69**, 1162 (2014).
8. R. Herbrecht *et al.* Invasive Fungal Infections Group of the European Organisation for Research and Treatment of Cancer and the Global Aspergillus Study Group, *N. Engl. J. Med.* **347**, 408 (2002).
9. M. Slavin *et al.*, *Clin. Microbiol. Infect.* 10.1016/j.cmi.2014.12.021 (2015).
10. E. Snelders *et al.*, *PLOS ONE* **7**, e31801 (2012).
11. European Crop Protection Association, Assessment of the Economic Importance of Azoles in European Agriculture: Wheat Case Study; www.ecpa.eu/article/agriculture-today/assessment-economic-importance-azoles-european-agriculture-wheat-case-stud.
12. Investigational new drug (IND)–enabling studies: biafungin (Cidara), VT-1129 (Viament); phase I: F901318 (F2G Ltd.), nickkomycin Z (Valley Fever Solutions); phase II: SCY-078 (Scynexis); phase III: isavuconazole (Basilea Pharmaceutica Ltd.).
13. T. Roemer, C. Boone, *Nat. Chem. Biol.* **9**, 222 (2013).
14. D. W. Denning *et al.*, *Clin. Transl. Allergy* **4**, 14 (2014).
15. J. Cadranel *et al.*, *Eur. J. Clin. Microbiol. Infect. Dis.* **31**, 3231 (2012).
16. www.mrc.ac.uk/documents/pdf/fungal-disease-research-workshop-report
17. J. H. Rex *et al.*, *Lancet Infect. Dis.* **13**, 269 (2013).
18. www.fda.gov/downloads/drugs/guidancecomplianceregulatoryinformation/guidances/UCM420235.pdf

ACKNOWLEDGMENTS

D.W.D. holds founder shares in F2G Ltd, a University of Manchester spin-out antifungal discovery company, in Novocyt, which markets the Myconostica real-time molecular assays and has current grant support from the National Institute of Allergy and Infectious Diseases, National Institute of Health Research, NorthWest Lung Centre Charity, Medical Research Council, Astellas, and the Fungal Infection Trust. He acts as a consultant to Trinity Group, T2 Biosystems, GlaxoSmithKline, Sigma Tau, and Oxon Epidemiology. M.J.B. is a former employee of F2G Ltd. and founder of the diagnostic service laboratory Genon Laboratories Ltd. and currently receives grant support from F2G Ltd., Genon Laboratories Ltd., DuPont, and the EU's Seventh Framework Programme under Grant Agreement no. HEALTH-F3-2013-601963. He acts as a consultant for Synergy Health PLC .

10.1126/science.aaa6097

Exploiting weak interactions in DNA self-assembly

Weak stacking interactions allow dynamic assembly and disassembly of DNA origami shapes

By **William M. Shih**

Many dynamic biomolecular complexes, such as actin filaments or microtubules, are formed through the assembly of numerous subunits that can disassemble again after a modest input of energy. To achieve structural integrity, the interfaces between domains must be relatively large. At the same time, the overall adhesion energy of each interface must be sufficiently low so that it can be readily broken on command. On page 1446 of this issue, Gerling *et al.* (*1*) report a framework that satisfies these conditions for the programmable dynamic assembly and disassembly of rigid three-dimensional (3D) structures built from DNA origami. Such devices could prove useful for applications such as sensors and therapeutic delivery vehicles.

Structural DNA nanotechnology (*2*) exploits the robust sequence complementarity of DNA strands to program the assembly of complex shapes. One powerful variant, DNA origami (*3*–*7*), enables one-pot self-assembly of 2D or 3D custom shapes with up to 10,000 independently addressable base pairs. In this method, a long scaffold strand with a nonrepetitive sequence is combined with hundreds of shorter staple strands to fold together via base pairing into bundles of double helices in the desired configuration.

Hierarchical assembly between bundles has been explored using not just base-pairing interactions, but also blunt-end stacking interactions (*8*–*10*), which are weak adhesions between the ends of two double helices that each lack single-stranded overhangs. Specificity can be provided by "jigsaw" bundle ends, where the constituent double helices protrude to variable extents. Only bundle ends with shape-complementary sets of protusions can then dock in a manner to satisfy all blunt-end stacking interactions. In earlier studies, the origami pieces were linked along the helical axes of the 2D bundles. In contrast, Gerling *et al.* designed interfaces between bundles that face each other laterally. This has the advantage that, at low to moderate salt concentrations, electrostatic repulsion greatly exceeds generic attractive interactions. This net repulsion provides an energy barrier that only target interactions can overcome at moderate ionic strength, and no potential interactions can overcome at low ionic strength.

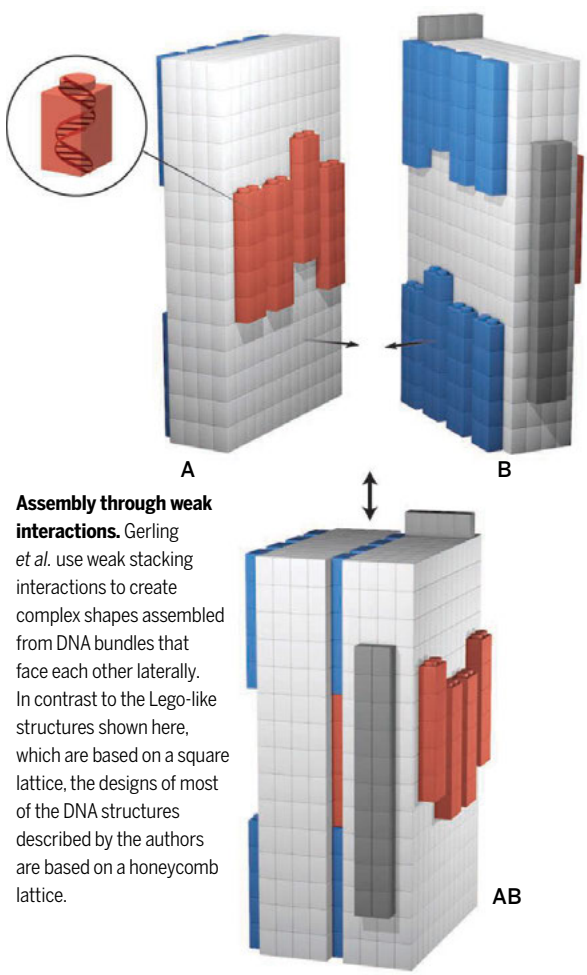

Assembly through weak interactions. Gerling *et al.* use weak stacking interactions to create complex shapes assembled from DNA bundles that face each other laterally. In contrast to the Lego-like structures shown here, which are based on a square lattice, the designs of most of the DNA structures described by the authors are based on a honeycomb lattice.

Department of Biological Chemistry and Molecular Pharmacology, Harvard Medical School, Boston, MA 02115, USA, and Department of Cancer Biology, Dana-Farber Cancer Institute, Boston, MA 02115, USA. E-mail: william.shih@wyss.harvard.edu

To engineer a specific attractive interaction, the authors designed a "plug" (a pair of double helices of defined length, terminating in pairs of blunt ends) on the side of one bundle and a corresponding "hole" (two flanking pairs of double helices that also terminate in pairs of blunt ends) on the side of the conjugate bundle. Together, a "plug" and a "hole" then form four blunt-end stacking interactions. An individual stacking interaction is only about half as strong as a base-pairing interaction (*11*); a single plug-hole interaction is therefore quite weak yet provides long-range registration, because the bonding is distributed between the two distant termini of the plug. The authors programmed shape-complementary distributions of plugs and holes that were designed to sterically exclude nontarget interactions.

Because the interaction energies of the interfaces are much lower than those holding together each bundle, external conditions can be used to modulate hierarchical assembly without compromising bundle integrity. The authors were able to cycle the assembly and disassembly of interfaces through altering cation concentrations or by shifting the temperature. In the latter case, they achieved more than 1000 cycles of opening and closing of a scissor motif over the course of 4 days with no detectable degradation. Closure upon cooling to 25°C took an average of 4 s, whereas opening after heating to 50°C was much more rapid.

The authors also demonstrate allosteric control via strand hybridization. Here, they engineered a single-stranded loop in the middle of a plug, such that when a complementary strand was added in trans, the plug was deformed, disrupting the interface. Subsequent removal of the complementary strand was achieved by toehold-mediated hybridization to a recovery strand added in trans. (A toehold is an additional 9-base single-stranded domain that gives strand displacement a thermodynamic advantage as well as a kinetic boost.) In the future, chemically powered autonomous cycling could be implemented with catalytic strand-displacement cascades (*12*).

Gerling *et al.* demonstrate the generality of their method through the assembly of example architectures, including a single-threaded filament of rectangular blocks, a 2D hexagonal array versus a dual-threaded filament of hexagonal blocks, a 2D array of scissor motifs, and sheets that fold up into hexagonal or rectangular blocks. One particularly delightful example involves a "nanorobot" that assembles from three separate components, reminiscent of the Voltron mecha cartoons from the 1980s.

One limitation of the current design is that the length of the plugs is restricted to

ILLUSTRATION: V. ALTOUNIAN/*SCIENCE*

integral numbers of double-helical turns. If future designs could modulate plug length to single-base-pair resolution, a much larger set of orthogonal interfaces could be constructed relative to a given bundle size. This would allow assembly of larger, more complex, and therefore more sophisticated devices.

The authors note some challenges for including base-pairing interactions, instead of only stacking interactions, to drive dynamic interfacial recognition. For example, the interaction energies may be too large when long sequences are used. Nonetheless, one can imagine interesting possibilities where base pairing is involved. For example, the use of short sticky ends (double-helix termini with single-stranded DNA overhangs available for base pairing) may be exploited to increase the combinatorial possibilities, although compensatory repulsive interactions may be required in conjunction to prevent the specific interfacial energy from becoming too large. Longer sequences could be used together with competitor displacement strands (*13*), where the specific interfacial energy can be tuned according to length, sequences, and concentrations of the latter strands. For example, Rogers and Manoharan (*14*) recently reported programming reentrant melting of DNA-functionalized colloids (which interact only within a specified temperature band) by exploiting competitive strand displacement schemes.

Given the great advances in static self-assembly of highly complex DNA shapes over the past decade, the time is ripe to explore how these architectures can be controlled dynamically. Through their pioneering forays into shape complementarity, weak interfacial energies, and remotely tunable repulsion energies, Gerling *et al.* point the way toward reconfigurable, rigid DNA nanodevices that may one day rival the functional sophistication of the biomolecular machines of the cell. ■

REFERENCES

1. T. Gerling, K. F. Wagenbauer, A. M. Neuner, H. Dietz, *Science* **347**, 1446 (2015).
2. N. C. Seeman, *Annu. Rev. Biochem.* **79**, 65 (2010).
3. P. W. Rothemund, *Nature* **440**, 297 (2006).
4. S. M. Douglas *et al.*, *Nature* **459**, 414 (2009).
5. H. Dietz, S. M. Douglas, W. M. Shih, *Science* **325**, 725 (2009).
6. Y. Ke *et al.*, *J. Am. Chem. Soc.* **131**, 15903 (2009).
7. D. Han *et al.*, *Science* **332**, 342 (2011).
8. M. Endo, T. Sugita, Y. Katsuda, K. Hidaka, H. Sugiyama, *Chemistry* **16**, 5362 (2010).
9. A. Rajendran *et al.*, *ACS Nano* **5**, 665 (2011).
10. S. Woo, P. W. Rothemund, *Nat. Chem.* **3**, 620 (2011).
11. P. Yakovchuk *et al.*, *Nucleic Acids Res.* **34**, 564 (2006).
12. S. J. Green *et al.*, *Phys. Rev. Lett.* **101**, 238101 (2008).
13. D. Y. Zhang *et al.*, *Nat. Chem.* **4**, 208 (2012).
14. W. B. Rogers, V. N. Manoharan, *Science* **347**, 639 (2015).

10.1126/science.aaa9483

NEUROSCIENCE

Treating brain disorders with neuromodulation

Nanoparticles, magnetic fields, and heat-sensitive ion channels are harnessed to manipulate brain activity

By **Yasin Temel** *and* **Ali Jahanshahi**

Altering the activity of specific brain structures to understand their function, but also to manage their dysfunction, has been a timeless mission for neuroscientists. Classical tools for studying brain structure and function are lesioning, electrical stimulation, and chemical modulation. Although effective at the level of the brain structure, these tools lack a high degree of selectivity and specificity. More advanced neuromodulation techniques are overcoming these limits, including optogenetic approaches and chemogenetic tools [such as designer receptors exclusively activated by designer drugs (DREADD)]. On page 1477 of this issue, Chen *et al.* (*1*) add magnetothermal neuromodulation to this list. The approach allows specific neurons to be activated by heat-emitting nanoparticles that respond to externally applied magnetic fields.

Chen *et al.* introduced the heat-sensitive calcium ion channel TRPV1 into neurons (via viral delivery of the encoding gene) located in the ventral tegmental area of the mouse brain. Four weeks later, magnetic nanoparticles were injected into the same region, where they were detected in the extracellular space (whether they are internalized by any cell in vivo remains to be shown). Mice were then exposed to an external alternating magnetic field that caused the nanoparticles to emit heat sufficient to activate the TRPV1 channels. The resulting influx of calcium was a proxy for neuronal membrane depolarization and excitation. This also triggered activity-dependent gene expression in the TRPV1 neurons. Moreover, neurons in the prefrontal cortex, which receive input from the ventral tegmental area, were activated.

As with optogenetics, which uses light to activate neurons that have been engineered to express light-sensitive ion channels, the approach of Chen *et al.* is clever, but has obvious limitations as far as clinical use. One issue is safety, related to heating, the presence of magnetic particles in the brain, and the use of viral tools. Another limit is specificity—do the nanoparticles respond to other magnetic fields that one confronts in daily life? The more immediate value for magnetothermal neuromodulation is in its use as a tool to excite specific subpopulations of neurons by remote control.

The development of new tools for intracranial neuromodulation (see the figure) evokes a concept hypothesized by Nobel Laureate António Egas Moniz in the first half of the 20th century—that a dysfunctional circuit of Papez (medial limbic circuit that connects the hypothalamus to the cortex) underlies major affective disorders. He and others intervened surgically with lesions of the frontal cortex by a transorbital route (lobotomy). The idea was to destroy connective nerve fibers or specific brain tissue, but the procedure only improved symptoms in some patients temporarily, and the risks included serious affective and cognitive side-effects such as apathy. Shortly after the introduction of the human stereotaxic apparatus in 1947 (*2*), which used a three-dimensional coordinate system to locate specific regions in the brain, surgeons approached deeply situated motor regions with more precise lesional surgery to treat patients with movement and psychiatric disorders.

> ***"...magnetohermal neuromodulation...could... enhance our knowledge of the brain's microcircuitry in normal and disease states."***

In the second half of the 20th century, electrodes placed temporarily in deeply situated areas of the brain became more popular. Limbic regions were thus stimulated to modulate affective behaviors of patients (*3*). A well-known animal study demonstrated that an attacking bull could be stopped instantly when an electrode, placed in its caudate area, was activated by a remote controller (*4*). Although these methods were hypothesis-driven, their main weakness was the lack of a robust scientific base, and they

Key neuromodulation approaches

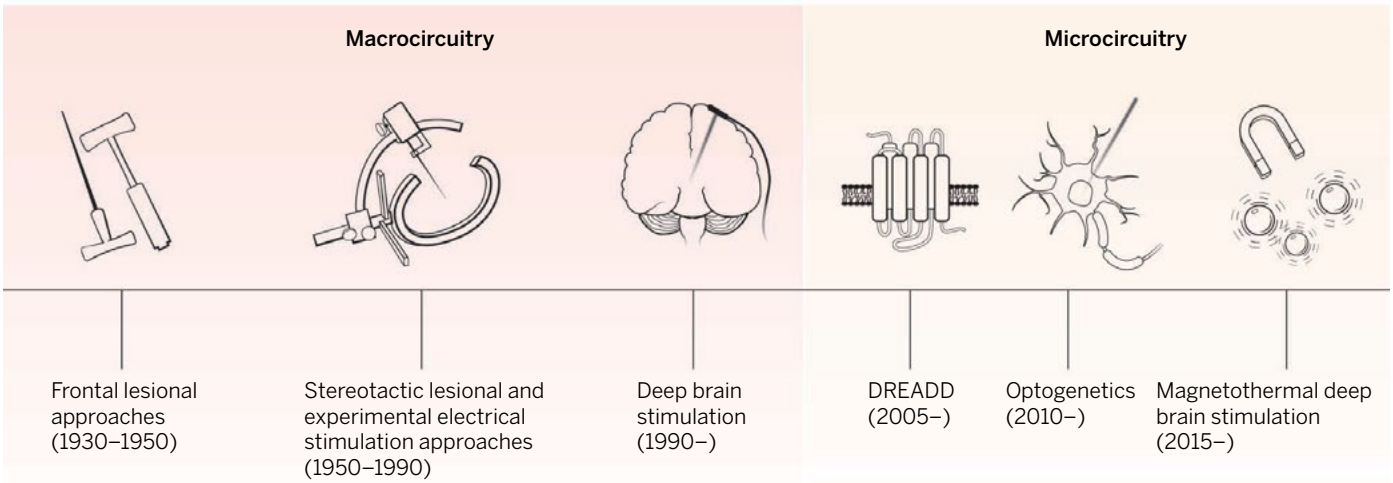

Trends in treatment. Techniques to alter neuron activity in the brain shifted from a macrocircuitry focus to one that now concentrates on modulating specific populations of neurons. The time periods indicate the global course of development.

fell into disuse with the rise of drugs targeting the central nervous system.

An increased understanding of the neuronal function was the determining factor for the successful application of deep brain stimulation of the subthalamic nucleus in patients with Parkinson's disease. In contrast to earlier techniques of electrical stimulation in which electrodes are placed temporarily in the brain and stimulated by external devices to simply drive neuronal activity, deep brain stimulation involves the chronic implantation of electrodes driven by an internal pacemaker to counteract abnormal neuronal activity. Studies on basal ganglia function in animal models of Parkinson's disease (*5*, *6*) paved the way for clinical application of deep brain stimulation of the subthalamic nucleus in 1993 (*7*). Since then, the technique has been applied in other neurological and psychiatric disorders, both in translational models and patients (*8*). In some patients, clear therapeutic effects have been seen, such as in dystonia, Tourette's syndrome, and obsessive-compulsive disorder. However, for other mental conditions such as intractable depressions (resistant to drugs, behavioral and electroconvulsive treatments) the approach has failed (*9*). Interestingly, the same methodology of deep brain stimulation for treating Parkinson's disease has been prescribed for patients with other neurological and psychiatric disorders, mainly because of limited progress in drug discovery for those disorders and the availability and safety of technology for deep brain stimulation. The risk here is that deep brain stimulation for these conditions, while hypothesis driven, lack a robust scientific base. Its application without understanding the fundamental neuronal underpinnings of the disorders could lead to negative outcomes, which could influence research in the field, as well as the interest of society.

Moreover, even with relevant knowledge, minimal invasiveness, safety, and disorder and symptom specificity, clinical success is not guaranteed. For example, clinical studies with intracranial adenovirus-based delivery of glutamic acid decarboxylase (*10*) or glia cell line–derived neurotrophic factor (*11*) had unfavorable outcomes despite promising results in translational models.

After a long period of technological downtime for treating brain disorders (*12*), a number of new approaches have been introduced. The DREADD approach, in which receptors are engineered to respond to synthetic small-molecule ligands, is gaining momentum as a neuromodulatory approach. For example, in an animal model of epilepsy, this approach attenuated focal neocortical seizures (*13*). In the field of deep brain stimulation, promising methods include adaptive/closed-loop deep brain stimulation (*14*) and current steering (*15*). In the former, stimulation is only activated when pathological neuronal activity starts. The latter approach involves the control of the direction of stimulation to avoid current spread to neighboring regions. For lesional surgery, ultrasound-based approaches are receiving interest. Speeding up these developments seems to be linked to the failure of systemic drug–based approaches to deliver breakthrough therapies for neurodegenerative and psychiatric diseases.

It is unclear whether or not hypothesis-driven molecular approaches that require viral delivery tools and genetic manipulations will enter the clinical arena. Meanwhile, technologies such as remote magnetothermal neuromodulation developed by Chen *et al.* could be used widely in translational models to enhance our knowledge of the brain's microcircuitry in normal and disease states. As with the development of deep brain stimulation for patients with Parkinson's disease, this new knowledge could spur the progress of future therapies—neuromodulation-based or not—for patients with brain disorders. ■

Department of Neurosurgery, Maastricht University Medical Center, P. Debyelaan 25, 6202 AZ, Maastricht, Netherlands. E-mail: y.temel@maastrichtuniversity.nl

REFERENCES

1. R. Chen *et al.*, *Science* **347**, 1477 (2015).
2. E. A. Spiegel, H. T. Wycis, M. Marks, A. J. Lee, *Science* **106**, 349 (1947).
3. R. G. Heath, *J. Nerv. Ment. Dis.* **165**, 300 (1977).
4. A. J. Osmundsen, "'Matador' with a radio stops wired bull modified behaviour in animals the subject of brain study," *New York Times*, 17 May 1965, pp. 1, 20.
5. H. Bergman, T. Wichmann, M. R. DeLong, *Science* **249**, 1436 (1990).
6. A. Benazzouz, C. Gross, J. Féger, T. Boraud, B. Bioulac, *Eur. J. Neurosci.* **5**, 382 (1993).
7. P. Pollak *et al.*, *Rev. Neurol.* **149**, 175 (1993).
8. C. Hamani, Y. Temel, *Sci. Transl. Med.* **4**, 142rv8 (2012).
9. T. Morishita, S. M. Fayad, M. A. Higuchi, K. A. Nestor, K. D. Foote, *Neurotherapeutics* **11**, 475 (2014).
10. P. A. LeWitt *et al.*, *Lancet Neurol.* **10**, 309 (2011).
11. A. E. Lang *et al.*, *Ann. Neurol.* **59**, 459 (2006).
12. C. Ineichen, W. Glannon, Y. Temel, C. R. Baumann, O. Sürücü, *Front. Hum. Neurosci.* **8**, 730 (2014).
13. D. Kätzel, E. Nicholson, S. Schorge, M. C. Walker, D. M. Kullmann, *Nat. Commun.* **5**, 3847 (2014).
14. B. Rosin *et al.*, *Neuron* **72**, 370 (2011).
15. M. F. Contarino *et al.*, *Neurology* **83**, 1163 (2014).

10.1126/science.aaa9610

ENVIRONMENTAL ECONOMICS

Do biofuel policies seek to cut emissions by cutting food?

Major models should make trade-offs more transparent

By T. Searchinger[1]*, R. Edwards[2]*, D. Mulligan[2], R. Heimlich[3], R. Plevin[4]

Debates about biofuels tend to focus separately on estimates of adverse effects on food security, poverty, and greenhouse gas (GHG) emissions driven by land-use change (LUC) (*1*–*4*). These estimates often rely on global agriculture and land-use models. Because models differ substantially in their estimates of each of these adverse effects (*2*, *3*, *5*), some argue that each individual effect is too uncertain to influence policy (*6*, *7*). Yet these arguments fail to recognize the trade-offs; much of the uncertainty is only about which adverse effects predominate, not whether adverse effects occur at all. Our analysis of the three major models used to set government policies in the United States and Europe suggests that ethanol policies in effect are relying on decreases in food consumption to generate GHG savings (*1*).

When biofuels divert crops from food and feed, three basic responses are possible. First, farms may replace crops by expanding cropland into forests and grasslands. This LUC releases carbon. Second, farms may replace crops by increasing yields on existing cropland more than they otherwise would. This "yield response" is the most desirable, but it can lead to greater use of fertilizer or water and increased emissions and may leave fewer options to boost yields to meet rising food demands. Third, some of the food may not be replaced, meaning that someone will eat less or less well. Although effects on different groups of the world's poor will differ, any reduction in global food consumption is likely to disproportionately affect some groups of the poor because they can less afford higher prices (*2*, *8*–*10*). In general, models predict at least some of each basic response. To the extent that a model predicts larger reductions in food consumption, it will predict less LUC, and vice versa.

POLICY

The role of food reductions depends on the percentage of crops diverted to biofuels that are not replaced. Modelers generally do not report this percentage—although they sometimes report food effects in less informative ways (*1*)—so we calculated the percentage from model outputs. We considered the consumption and supply effects on all crops, not just the biofuel feedstock, and accounted for the return to the food supply of biofuel feed by-products.

> *"...25 to 50% of net calories... diverted to ethanol are not replaced..."*

We analyzed results of the 2009 and 2014 versions of the Purdue Global Trade Analysis Project (PURDUE-GTAP) model (*11*, *12*) directly incorporated by the California Air Resources Board (CARB) into regulations, and of the Food and Agricultural Policy Research Institute Center for Agricultural and Rural Development (FAPRI-CARD) model similarly used by the U.S. Environmental Protection Agency (EPA) (*13*). We also analyzed the International Food Policy Research Institute Modeling International Relationships in Applied General Equilibrium (IFPRI-MIRAGE) model, used by the European Commission (EC) (*14*), to estimate LUC in proposed European legislation.

These models estimate changes in land use, crop production, and consumption, but agencies use separate models to flesh out remaining parts of life-cycle emissions estimates. Our intent is not to endorse any model but to illuminate trade-offs in what models predict.

CUTTING CALORIES AND QUALITY. These models estimate that roughly 25 to 50% of the net calories in corn or wheat diverted to ethanol are not replaced but instead come out of food and feed consumption (see table S3 in the supplementary materials). [Net calories account for return to the food and feed supply of ethanol by-products (see table S2).] Replacing fewer crops leads to lower GHG emissions from LUC. It also reduces direct emissions of carbon dioxide (CO_2) by people and livestock.

The table presents model estimates of major GHG sources and sinks attributed to the use of ethanol and compares them to relevant estimates of total gasoline emissions. The first column shows CARB, EPA, and the EC's Joint Research Centre (JRC) estimates of fossil carbon and trace gas emissions from growing crops and refining them into ethanol using methods separate from the land-use models (column A). One-third of net crop carbon is released during fermentation into ethanol (column B), and two-thirds during combustion of the ethanol (column C). Adding up all emission sources (A + B + C), before any credits for biogenic (plant-based) carbon offsets, GHG emissions vary from 67 to 100% higher than those of gasoline.

Most biofuel GHG analyses assume that carbon absorbed by growth of crops diverted to ethanol automatically offsets the carbon released by fermenting and burning them (columns B and C). But carbon absorbed by crops that would grow anyway cannot provide a valid offset because, by definition, it is not caused by biofuels and is not additional (*15*, *16*) (fig. S4). Thus, a valid crop growth offset comes only from growth of additional crops to replace those diverted to ethanol, whether from new cropland or from boosting yields on existing cropland (column D). However, conversion of forests or grassland to produce some more crops also releases carbon from LUC (column F), reducing or negating the net offset from producing more crops.

Significantly, crops that are not replaced provide an offset in another way. If those crops were not diverted to ethanol production, people or livestock would consume them and emit their carbon through respiration and waste. Reducing crop consumption therefore means that people or livestock emit less carbon. This offset ranges from 23 to 53 g CO_2/MJ for corn or wheat ethanol, equivalent to roughly 20 to 50% of the carbon in the diverted food (column E).

Including the offset for reduced food consumption, all but CARB's original GTAP-based results show modestly lower total emissions for ethanol than for gasoline (column G). However, without crediting reduced food consumption, none of these models would project lower GHGs for ethanol than for gasoline (column H). In that sense, the lower GHGs for ethanol depend on reductions in food consumption.

Although the table shows the flow of carbon that the models predict, the role of crop carbon emissions and offsets is normally

[1]Woodrow Wilson School of Public and International Affairs, Princeton University, Princeton, NJ 08544, USA. [2]Joint Research Centre, European Commission, Ispra 21027, Italy. [3]Agricultural Conservation Economics, Laurel, MD 20723, USA. [4]Institute of Transportation Studies, University of California at Davis, Davis, CA 95616, USA.
*E-mail: tsearchi@princeton.edu, robert.edwards@jrc.it

obscured because modelers present results following a convention of ignoring crop carbon altogether (columns B to E). That works mathematically because, by definition, the net carbon in crops devoted to ethanol and emitted (B + C) must equal and be canceled out by the carbon in crops that are either replaced or not replaced (D + E). However, this practice hides the role played by reduced food consumption. It also conceals that if all diverted crops were replaced, LUC emissions would be larger.

The MIRAGE model also projects reductions in the quality of food consumed (*1*, *14*). Much of the additional land used for corn or wheat for ethanol previously produced higher-value crops, such as oils and vegetables, which is not reflected by the loss of their calories. Without food quantity and quality reductions—if farmers replaced both the quantity and types of crops used for food—farms would require ~5 times as much LUC, resulting in 46% higher emissions for wheat ethanol than for gasoline and 68% higher emissions for corn ethanol.

MIRAGE results are informative because the model optimistically projects little LUC due to biofuels, in part because higher yields in response to higher prices replace three times as much crop area as does area expansion. Although the economic literature is sparse and debated, it generally finds a much larger area response than yield response (*1*, *17*). The fact that global yields more than doubled from 1961 to 2005, even as prices declined, also casts doubt on such a large yield response to price (*1*). Yet, even with little LUC for this reason, lower ethanol emissions than gasoline still rely on food reductions.

MAKE TRADE-OFFS TRANSPARENT. Although we illuminate model outputs, whether any of these models accurately project food or GHG consequences of increasing ethanol use is an important but separate subject. Many model parameters and functions are uncertain, debatable, or assumed for mathematical ease. We generally consider likely yield responses overstated and LUC understated. Models also may not depict consequences of increasing biofuels, for example, because one MJ of ethanol may not fully avoid one MJ of gasoline (*18*).

Yet, simpler economic methods also suggest that a substantial fraction of crops diverted to biofuels results in food reductions. That fraction depends only on the ratio of the demand response (reduced consumption) to the supply response (increased production). Typical estimates of supply-and-demand elasticities for individual crops (*19*, *20*) alone suggest that reduced consumption is substantial. One direct estimate of global supply-and-demand elasticities for aggregate calories from major staple crops implies that roughly one-fifth

Role of reduced food consumption in life-cycle greenhouse gas emissions

	DIRECT PRODUCTION AND USE EMISSIONS (CO_2EQ/MJ)			NET OFFSETS (CO_2EQ/MJ)			TOTALS AND % CHANGE FROM GASOLINE (CO_2EQ/MJ)	
		EMISSIONS AND OFFSETS OF CROP CARBON						
SOURCE OF FUEL	**A** Production and refining emissions from fossil fuels and trace gases	**B** Fermentation of grain	**C** Vehicle exhaust	**D** Additional crop production from both yield gains and new cropland (offset)	**E** Reduced respiration and waste due to reduced crop consumption (offset)	**F** LUC (emission from new cropland)	**G** Total including reduced food consumption (A+B+C+D+E+F)	**H** Total excluding reduced food consumption (A+B+C+D+F)
CALIFORNIA AIR RESOURCES BOARD								**GASOLINE = 99**
GTAP US CORN (2009)	69	36	71	–54	–53	42	111 (12%)	164 (65%)
GTAP NEW US CORN (HIGHER YIELD ELASTICITY	69	36	71	–75	–32	13	82 (-17%)	114 (15%)
GTAP NEW US CORN (LOWER YIELD ELASTICITY	69	36	71	–63	–44	25	94 (–5%)	138 (40%)
GTAP EU WHEAT (ORIGINAL)	67	36	71	–63	–44	155	223 (125%)	267 (169%)
U.S. ENVIRONMENTAL PROTECTION AGENCY								**GASOLINE = 93**
FAPRI US CORN (2022 ESTIMATE)	49	36	71	–86	–25	34	79 (–15%)	104 (12%)
EUROPEAN UNION								**GASOLINE = 87**
IFPRI-MIRAGE WHEAT	67	36	71	–73	–34	17	84 (–4%)	118 (36%)
IFPRI-MIRAGE EC CORN	69	36	71	–84	–23	11	80 (–8%)	103 (19%)

Benefits of biofuels relative to gasoline depend on reductions in food consumption. Ethanol emits fossil carbon and trace gases through production (**A**) and biogenic carbon from the crops during fermentation (**B**) and ethanol combustion (**C**). Additional crop production can offset these emissions (**D**), but the net effect of producing more crops must account for carbon released by LUC (**F**) (amortized 20 years for IFPRI and 30 years for EPA and CARB). An offset also occurs to the extent that crops are not replaced because people or livestock eat fewer crops and therefore respire and waste less carbon (**E**). Total including reduced food production can show lower emissions for ethanol (**G**) but excluding that offset shows higher emissions (**H**). MIRAGE results use updated JRC growing and refining emissions, rather than those in EU legislation, because of greater similarity with CARB and EPA methods. EPA LUC estimate is based on FAPRI only (*1*).

of calories diverted to biofuels are not replaced (*21*).

Regardless of model merits, biofuel policies are relying on estimates of reduction in food consumption to claim GHG benefits. Food reductions result not from a tailored tax on overconsumption or high-carbon foods but from broad global increases in crop prices (*8*, *9*). If models overstate the food reductions, then they understate the GHGs. Policy-makers who do not wish to mitigate climate change in this way could exclude the GHG credit for these reductions from their GHG calculations. Modelers need to make the trade-offs transparent so that policymakers can consider whether to seek climate mitigation through less food. ■

SUPPLEMENTARY MATERIALS

www.sciencemag.org/content/347/6229/1420/suppl/DC1

REFERENCES AND NOTES

1. See supplementary materials for details.
2. High Level Panel on Food Security, Biofuels and food security (Food and Agricultural Organization, Rome, 2013).
3. National Research Council, *Renewable Fuel Standard: Potential Economic and Environmental Effects of U.S. Biofuel Policy* (National Academies Press, Washington, DC, 2011).
4. U.K. Renewable Fuels Agency, *The Gallagher Review of the Indirect Effects of Biofuels Production* (Renewable Fuels Agency, London, 2008).
5. S. A. Decara *et al.*, *Land-Use Change and Environmental Consequences of Biofuels: A Quantitative Review of the Literature* (Institut National de la Recherche Agronomique, Paris, 2012).
6. M. Finkbeiner, *Biomass Bioenergy* **62**, 218 (2014).
7. D. Zilberman, G. Hochman, D. Rajagopal, *AgBiol. Forum* **13**, 11 (2010).
8. High Level Panel on Food Security, Price volatility and food security (Food and Agricultural Organization, Rome, 2011)
9. A. Dorward, *Food Security* **4**, 633 (2012).
10. M. Filipski, K. Covarrubia, in *Agricultural Policies for Poverty Reduction*, J. Brooks *et al.*, Eds. (OECD, Paris, 2010).
11. CARB, Proposed regulation to implement the low carbon fuel standard, Volume I, Staff Report: Initial Statement of Reasons (California Air Resources Board, Sacramento, CA 2009).
12. R. Edwards, D. Mulligan, L. Marelli, *Indirect land use change from increased biofuel demand: Comparison of models and results for marginal biofuels production from different feedstocks* (European Commission Joint Research Centre, Ispra, Italy 2010).
13. U.S. EPA, Renewable Fuel Standard Program (RFS2) Regulatory Impact Analysis, (U.S. Environmental Protection Agency, Washington, DC, 2010).
14. D. Laborde, *Assessing the Land Use Change Consequences of European Biofuel Policies* (International Food Policy Research Institute, Washington, DC, 2011)
15. T. D. Searchinger *et al.*, *Science* **326**, 527 (2009).
16. T. D. Searchinger, *Environ. Res. Lttrs.* **5**, 024007 (2010).
17. S. Berry, *Biofuel Policy and Empirical Inputs to GTAP Models, Report to the California Air Resources Board* (CARB, Sacramento 2011).
18. R. Plevin, M. Delucchi, F. Creutzig, *J. Ind. Ecol.* **18**, 73 (2014).
19. G. Hochman, D. Rajagopal, G. Timilsina, D. Zilberman, *Biomass Bioenergy* **68**, 106 (2014).
20. Food and Agricultural Policy Research Institute, Elasticity Database (accessed August 12, 2014); www.fapri.iastate.edu/tools/elasticity.aspx
21. M. Roberts, W. Schlenker, *Am. Econ. Rev.* **103**, 2265 (2013).

ACKNOWLEDGMENTS

The authors thank the David and Lucile Packard Foundation for financial support.

10.1126/science.1261221

GENETICS

For complex disease genetics, collaboration drives progress

Exome sequencing identifies a gene that causes amyotrophic lateral sclerosis

By **Andrew B. Singleton** *and* **Bryan J. Traynor**

A principal tool in the development of etiology-based therapies is the identification of the genetic determinants of disease. The logic of this approach rests on the expectation that knowledge of the genetic variants underlying disease will enhance our understanding of the molecular pathogenesis of disease and reveal viable points for therapeutic intervention. Because of the general adoption of this paradigm, genetics has been a dominant force in disease investigation over the past 25 years. Success in this area has come in waves, each driven by new methods and technology. Linkage (identifying segments of the genome that are associated with given traits), positional sequencing (sequencing specific candidate genes based on their location), genome-wide association (examining genetic variants in a genome-wide manner across individuals for association with a trait), and family-based next-generation sequencing have each produced startling new phases of genetic discovery. The study by Cirulli *et al.* (*1*), reported on page 1436 of this issue, marks an early success in another phase of gene discovery: the application of exome sequencing in large case-control cohorts to identify genetic factors involved in complex disease. This is one of the first successes in this area and provides insights into amyotrophic lateral sclerosis (ALS), as well as broader lessons for disease gene discovery.

The design of Cirulli *et al.*'s effort to identify new genes that associate with ALS was essentially that of a two-phase exome-wide association study. Several approaches were used in the initial stage, each centering on the identification of rare variants within the protein-coding regions of the genome

ALS genetics

Genetic discoveries in ALS, showing the percentage of cases each gene is involved in and the type of genetic analysis by which the gene was discovered [adapted from (*7*)].

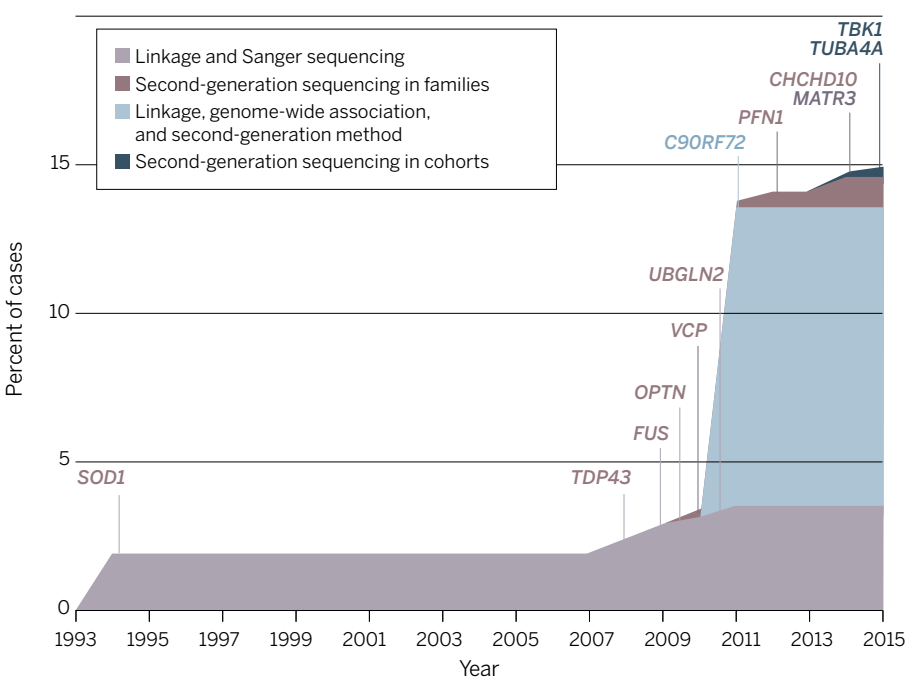

CREDIT: ADAPTED FROM (*7*)

of calories diverted to biofuels are not replaced (*21*).

Regardless of model merits, biofuel policies are relying on estimates of reduction in food consumption to claim GHG benefits. Food reductions result not from a tailored tax on overconsumption or high-carbon foods but from broad global increases in crop prices (*8*, *9*). If models overstate the food reductions, then they understate the GHGs. Policy-makers who do not wish to mitigate climate change in this way could exclude the GHG credit for these reductions from their GHG calculations. Modelers need to make the trade-offs transparent so that policymakers can consider whether to seek climate mitigation through less food. ■

SUPPLEMENTARY MATERIALS

www.sciencemag.org/content/347/6229/1420/suppl/DC1

REFERENCES AND NOTES

1. See supplementary materials for details.
2. High Level Panel on Food Security, Biofuels and food security (Food and Agricultural Organization, Rome, 2013).
3. National Research Council, *Renewable Fuel Standard: Potential Economic and Environmental Effects of U.S. Biofuel Policy* (National Academies Press, Washington, DC, 2011).
4. U.K. Renewable Fuels Agency, *The Gallagher Review of the Indirect Effects of Biofuels Production* (Renewable Fuels Agency, London, 2008).
5. S. A. Decara *et al.*, *Land-Use Change and Environmental Consequences of Biofuels: A Quantitative Review of the Literature* (Institut National de la Recherche Agronomique, Paris, 2012).
6. M. Finkbeiner, *Biomass Bioenergy* **62**, 218 (2014).
7. D. Zilberman, G. Hochman, D. Rajagopal, *AgBiol. Forum* **13**, 11 (2010).
8. High Level Panel on Food Security, Price volatility and food security (Food and Agricultural Organization, Rome, 2011)
9. A. Dorward, *Food Security* **4**, 633 (2012).
10. M. Filipski, K. Covarrubia, in *Agricultural Policies for Poverty Reduction*, J. Brooks *et al.*, Eds. (OECD, Paris, 2010).
11. CARB, Proposed regulation to implement the low carbon fuel standard, Volume I, Staff Report: Initial Statement of Reasons (California Air Resources Board, Sacramento, CA 2009).
12. R. Edwards, D. Mulligan, L. Marelli, *Indirect land use change from increased biofuel demand: Comparison of models and results for marginal biofuels production from different feedstocks* (European Commission Joint Research Centre, Ispra, Italy 2010).
13. U.S. EPA, Renewable Fuel Standard Program (RFS2) Regulatory Impact Analysis, (U.S. Environmental Protection Agency, Washington, DC, 2010).
14. D. Laborde, *Assessing the Land Use Change Consequences of European Biofuel Policies* (International Food Policy Research Institute, Washington, DC, 2011)
15. T. D. Searchinger *et al.*, *Science* **326**, 527 (2009).
16. T. D. Searchinger, *Environ. Res. Lttrs.* **5**, 024007 (2010).
17. S. Berry, *Biofuel Policy and Empirical Inputs to GTAP Models, Report to the California Air Resources Board* (CARB, Sacramento 2011).
18. R. Plevin, M. Delucchi, F. Creutzig, *J. Ind. Ecol.* **18**, 73 (2014).
19. G. Hochman, D. Rajagopal, G. Timilsina, D. Zilberman, *Biomass Bioenergy* **68**, 106 (2014).
20. Food and Agricultural Policy Research Institute, Elasticity Database (accessed August 12, 2014); www.fapri.iastate.edu/tools/elasticity.aspx
21. M. Roberts, W. Schlenker, *Am. Econ. Rev.* **103**, 2265 (2013).

ACKNOWLEDGMENTS

The authors thank the David and Lucile Packard Foundation for financial support.

10.1126/science.1261221

GENETICS

For complex disease genetics, collaboration drives progress

Exome sequencing identifies a gene that causes amyotrophic lateral sclerosis

By **Andrew B. Singleton** *and* **Bryan J. Traynor**

A principal tool in the development of etiology-based therapies is the identification of the genetic determinants of disease. The logic of this approach rests on the expectation that knowledge of the genetic variants underlying disease will enhance our understanding of the molecular pathogenesis of disease and reveal viable points for therapeutic intervention. Because of the general adoption of this paradigm, genetics has been a dominant force in disease investigation over the past 25 years. Success in this area has come in waves, each driven by new methods and technology. Linkage (identifying segments of the genome that are associated with given traits), positional sequencing (sequencing specific candidate genes based on their location), genome-wide association (examining genetic variants in a genome-wide manner across individuals for association with a trait), and family-based next-generation sequencing have each produced startling new phases of genetic discovery. The study by Cirulli *et al.* (*1*), reported on page 1436 of this issue, marks an early success in another phase of gene discovery: the application of exome sequencing in large case-control cohorts to identify genetic factors involved in complex disease. This is one of the first successes in this area and provides insights into amyotrophic lateral sclerosis (ALS), as well as broader lessons for disease gene discovery.

The design of Cirulli *et al.*'s effort to identify new genes that associate with ALS was essentially that of a two-phase exome-wide association study. Several approaches were used in the initial stage, each centering on the identification of rare variants within the protein-coding regions of the genome

ALS genetics

Genetic discoveries in ALS, showing the percentage of cases each gene is involved in and the type of genetic analysis by which the gene was discovered [adapted from (*7*)].

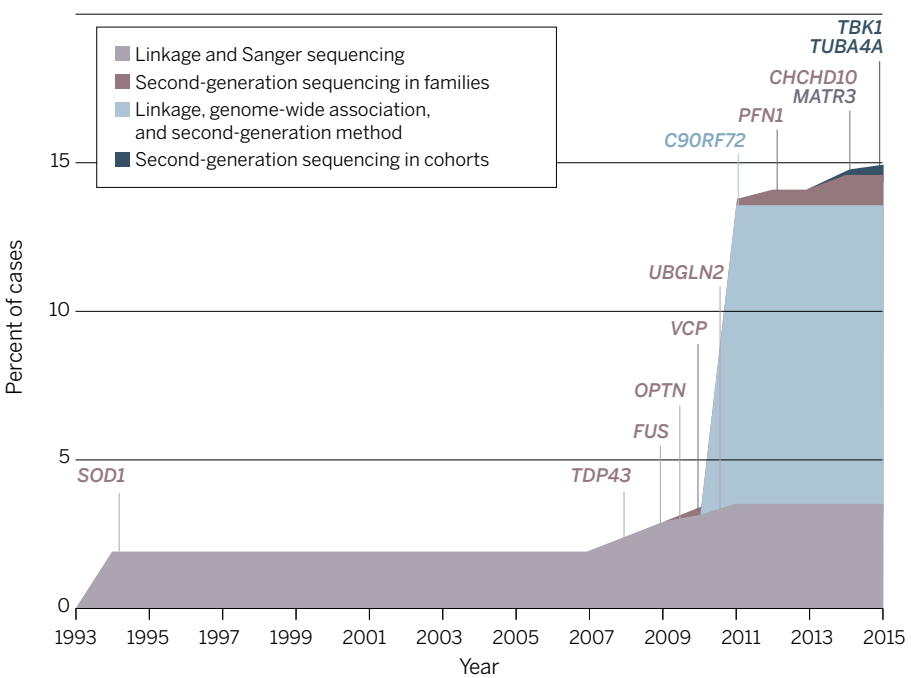

CREDIT: ADAPTED FROM (*7*)

(exomes) and a burden analysis aimed at prioritizing genes with an excess of variants in cases over controls. The authors focused on three different models for selecting rare variants from the discovery set of 2843 ALS cases and 4310 controls: investigating all nonsynonymous coding variants (when a nucleotide is substituted, thereby producing a different amino acid) and canonical splice variants; looking at nonsynonymous variants that are predicted to be damaging variants; and assessing loss-of-function variants. On the basis of these analyses, 51 genes were taken forward to a replication effort in an additional set of 1318 ALS cases and 2371 controls.

Although an attempt was made to exclude ALS cases with known mutations, it is notable that the top hit in the discovery effort was *SOD1*, a gene encoding superoxide dismutase 1, which is known to contain mutations that cause ALS. Other genes previously associated with ALS were also associated with disease in the analysis, including *TAR DNA BINDING PROTEIN* (*TARDBP*), *OPTINEURIN* (*OPTN*), *VALOSIN CONTAINING PROTEIN* (*VCP*), and *SPASTIC PARAPLEGIA* (*SPG11*).

Cirulli *et al.* performed a large number of analyses and identified a number of interesting genes potentially involved in risk for ALS. However, the most immediately important and compelling finding is the identification of a new association between ALS and variants in *TBK1*, which encodes a noncanonical IκB kinase family member, TANK-binding kinase 1. The authors report an overall excess of rare *TBK1* variants in cases under the "dominant not benign" model (dominant inherited variants that are predicted to be damaging to protein function), with a 0.19% allele frequency in controls versus 1.1% in cases (combined discovery and replication P value = 3.63×10^{-11}). Although these data intuitively suggest that *TBK1* variants play a role in ~0.9% of the ALS cases examined in the study, it is important to recognize that this does not suggest that *TBK1* mutation is sufficient to cause disease, nor does it explain the cause of 0.9% of ALS cases. A great deal of additional work is required to establish whether disease-linked variants in this gene are risk variants, or causal mutations, or both (*2*).

From a functional perspective, the linkage of *TBK1* to ALS is interesting, as it highlights the importance of autophagy and degradation of ubiquitinated proteins in motor neuron degeneration. *TBK1* phosphorylates the proteins encoded by genes previously linked to ALS, *OPTN* and *SEQUESTOSOME 1* (*SQSTM1*). Phosphorylation by Tbk1 enhances the ability of these proteins to shepherd ubiquitinated proteins to autophagosomes for destruction. Vcp and ubiquilin 2 (Ubqln2), also encoded by ALS-linked genes, are involved in later stages of the same cellular pathway, reinforcing the long-held view that ubiquitin-proteasome and autophagy pathways are central to ALS pathogenesis.

The genetics field has changed perhaps more than any other scientific discipline over the past two decades. This transformation has been focused not only on methodology, but also on a more fundamental shift in the way gene hunting is executed. Traditionally a highly competitive field, gene hunting has evolved into a collaborative endeavor in which consortia and open data sharing are central tenets. The type of collaboration typified by Cirulli *et al.* has become a requirement for success. Other examples include large collaborative efforts in Parkinson's disease and Alzheimer's disease (*3*, *4*). Another key to the success of Cirulli *et al.* was their access to publicly available data. Reference data from the Exome Aggregation Consortium (*5*) and the 1000 Genomes Project (*6*) were key steps in their filtering approach. The availability of such control and population sequence data is an essential resource for progress in disease research, and one that promotes efficiency and collaboration.

"The study...marks an early success in...the application of exome sequencing... to identify genetic factors involved in complex disease."

As Cirulli *et al.* rightly point out, much remains to be done to more fully understand the genetics of ALS (see the figure). Their work opens at least one new avenue into the investigation of molecular pathogenesis of disease, linking the protein product of *TBK1* with known ALS proteins. It is likely that their genetic data will also serve as the foundation for further gene discovery in ALS. Given this, it is particularly laudable that the authors have made individual-level exome sequence data rapidly available to the broader scientific community. ■

Laboratory of Neurogenetics, National Institute on Aging, Bethesda, MD 20892, USA. E-mail: singleta@mail.nih.gov

REFERENCES

1. E. T. Cirulli *et al.*, *Science* **347**, 1436 (2015).
2. A. Singleton, J. Hardy, *Hum. Mol. Genet.* **20**, R158 (2011).
3. M. A. Nalls *et al.*, *Nat. Genet.* **46**, 989 (2014).
4. J. C. Lambert *et al.*, *Nat. Genet.* **45**, 1452 (2013).
5. exac.broadinstitute.org
6. www.1000genomes.org
7. A. E. Renton, A. Chiò, B. J. Traynor, *Nat. Neurosci.* **17**, 17 (2014).

10.1126/science.aaa9838

APPLIED OPTICS

Sorting out light

Controlled interference can separate overlapping light beams for device functionality

By **David A. B. Miller**

When light beams become mixed up, can we sort them out again? Some cases are easy. The light from two flashlights on the other side of a room overlaps when it reaches us, but the lens in our eye separates them again as it constructs an image. By turning the flashlights on and off, we could also communicate two independent, spatial channels of information to different detectors at the back of our eyes.

But light is readily scrambled by anything more complicated than clear air. Trying to image through a strong scatterer, such as biological tissue, rapidly becomes impossible with increasing sample thickness. Even in the near-perfect glass fibers of optical communications, the slightest bend in the fiber can mix the light beams.

Mathematically, interference of light waves just involves adding and subtracting numbers (which is a linear process), so we can exploit the matrices of linear algebra. With effort, we can measure the optical system's matrix (*1*) and then calculate the inverse matrix that would mathematically undo the mixing. At least, we can do so in principle. However, we did not know how to implement such a (inverse) matrix as a lossless optical component. We did not even know if we could make an arbitrary linear optical device. Now, however, different mathematical approaches (*2*–*6*), together with modern microfabrication, may offer a solution. The optics may even solve the problem itself, thereby avoiding the need for any calculations (*5*, *6*).

Historically, optical components were simple objects, like lenses and mirrors. Now, the lithography developed for electronics offers more sophisticated possibilities. Silicon photonics (*7*) and other integrated approaches enable highly functional, complex (*8*) waveguide circuits near the top of a plane surface. Subwavelength patterning enables novel, nanophotonic structures, including photonic crystals,

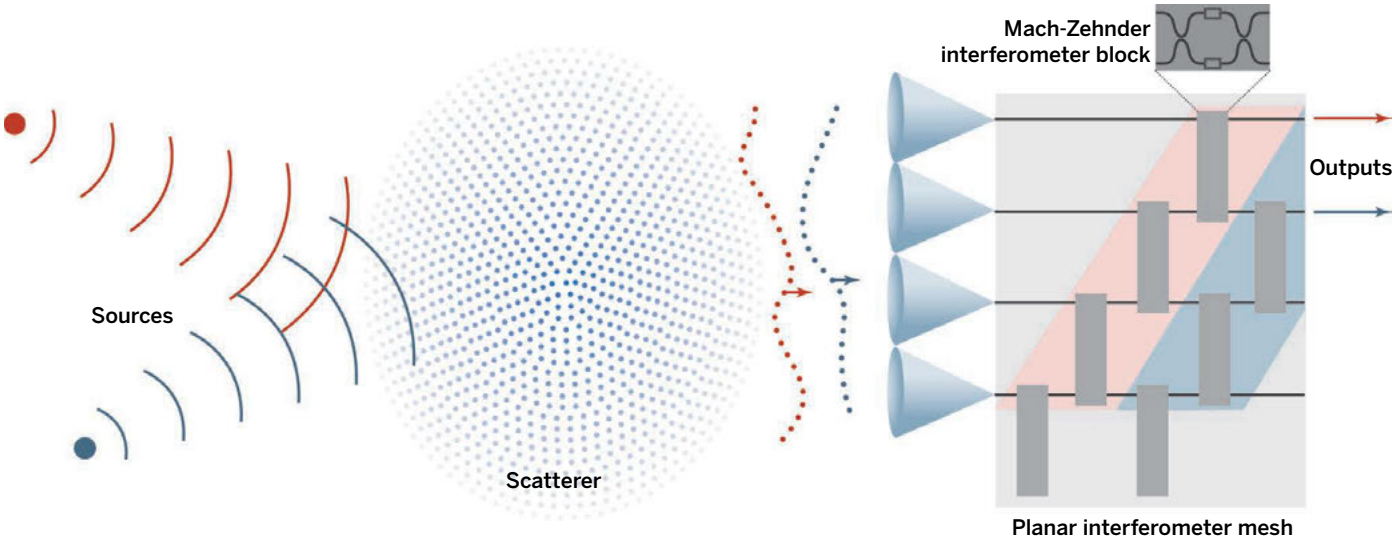

Disentangling light beams. Light from two sources is mixed and distorted by the scatterer but sorted out by the mesh. The scattered light is focused into waveguides in the interferometer mesh. Progressively adjusting the interferometers in the "red" row to maximize the "red" output separates the "red" power to the upper output. A similar algorithm on the "blue" row then separates the "blue" power to the lower output. Although shown as "red" and "blue," the sources can be the same color or wavelength.

waveguides, and resonators. Expanding beyond regular structures offers an even wider variety (*2*–*5*).

We already use lithography to make diffractive optical elements; in such elements, light travels through a thin sheet from one side to the other (or possibly reflects off it). Metasurfaces are extending these possibilities (*9*). By itself, such an approach cannot implement arbitrary linear optics. A fully arbitrary device (*5*) requires that every distinct element or pixel in the output light can be formed from an arbitrary combination of every distinct input pixel, not just by transmission or reflection from the same input pixel.

If the light travels inside the sheet, in waveguides or other complex structures, then light from every input element can possibly interfere to form each output. This multiple scattering makes device design hard, both mathematically speaking and from a fabrication point of view. Modern robust optimization algorithms allow efficient blind global optimization, however. Various compact nanophotonic devices have now been designed (*2*–*4*), for example, efficiently converting one set of input beams (or "modes") to another set of output beams (*2*, *3*).

Another planar approach uses meshes of interfering waveguides (*5*, *10*) (see the figure). The optical properties of the mesh can be programmed through fine adjustments of the lengths or phase shifts of waveguide links. The mesh settings have been known for one class of matrices (unitary transformations) for some time. Now, we know that an extended form of mesh can implement any matrix, finally proving that any linear optical component is possible in principle (*5*).

A key to this proof is that we can always perform a singular value decomposition (SVD) of such a matrix (*5*). The SVD has a simple physical interpretation: For any linear optical device or scatterer, there is a specific set of input beams or modes that couple, one by one, to a specific set of output beams or modes. These input/output pairs or communications modes (*5*) completely describe the device and give independent optical channels through it. The proof is also the design method, mapping the form of the SVD directly into the optics. This SVD approach has another benefit; it allows a progressive, even self-configuring, algorithm (*5*). We can then progressively train an extended version of the simple device shown in the figure, using the communications modes themselves, with no calculations.

There are still many challenges. We are only at the beginning in being able to fabricate actual optical structures and devices based on the optimization or self-configuring algorithms. The complexity of optical systems we can tackle this way will be limited. Imaging even a moderate number of pixels through a strong scatterer will remain very challenging. Not all the problems of using multiple mode fibers for communications can easily be solved in the optical domain; time delays between channels in long fibers may necessitate electronic information storage and calculations (*11*).

Beyond telecommunications or imaging, there are many other potential applications for bespoke linear optical elements. We need sophisticated optical networks for quantum information processing (*10*) and for sensor and signal processing generally. Linear optical processors could avoid the power dissipation of electronics. Complex optics could secure signals against decoding (*12*). Real-time self-configuration could allow automatic beam coupling, optical power combining, tracking of moving sources, and alignment or stabilization of complex optical systems (*5*). Extensions of these approaches could find the best channels through an optical system (*6*). The combination of micro- and nanofabrication, planar optical technologies, advanced robust optimization algorithms, and new self-configuring networks may both generate the new optical results we want and eliminate the ones we would rather avoid. ■

Ginzton Laboratory, Stanford University, 348 Via Pueblo Mall, Stanford, CA 94305-4088, USA. E-mail: dabm@ee.stanford.edu

REFERENCES AND NOTES

1. A. P. Mosk, A. Lagendijk, G. Lerosey, M. Fink, *Nat. Photonics* **6**, 283 (2012).
2. V. Liu, D. A. B. Miller, S. H. Fan, *Proc. IEEE* **101**, 484 (2013).
3. J. Lu, J. Vučković, *Opt. Express* **21**, 13351 (2013).
4. C. M. Lalau-Keraly, S. Bhargava, O. D. Miller, E. Yablonovitch, *Opt. Express* **21**, 21693 (2013).
5. D. A. B. Miller, *Photonics Res.* **1**, 1 (2013).
6. D. A. B. Miller, *J. Lightwave Technol.* **31**, 3987 (2013).
7. W. Bogaerts, M. Fiers, P. Dumon, *IEEE J. Sel. Top. Quantum Electron.* **20**, 1 (2014).
8. J. Sun, E. Timurdogan, A. Yaacobi, E. S. Hosseini, M. R. Watts, *Nature* **493**, 195 (2013).
9. N. Yu, F. Capasso, *Nat. Mater.* **13**, 139 (2014).
10. P. J. Shadbolt *et al.*, *Nat. Photonics* **6**, 45 (2012).
11. R. Ryf *et al.*, *J. Lightwave Technol.* **30**, 521 (2012).
12. S. A. Goorden, M. Horstmann, A. P. Mosk, B. Škorić, P. W. H. Pinkse, *Optica* **1**, 421 (2014).

ACKNOWLEDGMENTS

This work was supported by a Multidisciplinary University Research Initiative grant (Air Force Office of Scientific Research, FA9550-10-1-0264)

10.1126/science.aaa6801

ILLUSTRATION: C. SMITH/*SCIENCE*

SCIENCE LIVES

Ivan Pavlov, revealed

The life and times of Russia's famous physiologist

By **Stephen T. Casper**

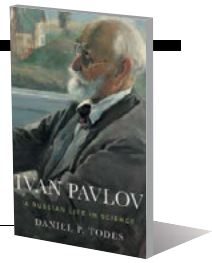

Ivan Pavlov
A Russian Life in Science
Daniel P. Todes
Oxford University Press, 2014. 891 pp.

With *Ivan Pavlov: A Russian Life in Science*, Daniel P. Todes achieves a level of mastery that transforms biography into history. The technical accomplishment of this volume, especially the originality of its multilingual sources and serious treatment of scientific research, marks it as an exemplary work of scholarship that reveals much about the history of 19th- and 20th-century Russia. In eminently readable and beautifully arranged chronological chapters, Todes captures both the *sluchainost'* (chance and randomness) and *pravil'nost'* (regularity and lawfulness) of Pavlov's life. And as those words—which appear frequently in Pavlov's writing—suggest, he, like his times, was characterized by many contradictions.

Born in 1849, Pavlov matured into the decadent, aristocratic, and yet impoverished feudal world of Tsarist Russia. He died in 1936, having witnessed a history filled with the assassinations, executions, and revolutions that led to the birth of the Soviet state, the repressions of Bolshevism, and the depravities and crimes of "Stalin Times." Trained for the priesthood, yet inspired to pursue a career in science by Ivan Sechenov's materialist *Reflexes of the Brain*, the self-proclaimed atheist and harsh critic of communism nonetheless believed that religious freedom was a basic human right and sometimes acknowledged unity in the missions of Jesus and the Communists. He would submit privately in his later years that religion served individual needs and fulfilled positive cultural roles in a healthy society.

Pavlov elevated skepticism in science to the status of virtue. Yet he could be dogmatic, petty, and unforgiving of those who dared entertain even minor differences of interpretation with him. He thought of himself as inclined to laziness but adopted the essayist Samuel Smiles's moral doctrine of industriousness (*1*) as his mantra and life's practice. Nine months of each year, he devoted himself obsessively to scientific work in St. Petersburg, and then for three summer months he enjoyed gardening, art, music, philosophy, and literature in his family's summer residence, with science seemingly forgotten. Clearly devoted to his wife and children, Pavlov nevertheless pursued an adulterous relationship in his last three decades. He furthermore could be a tyrannical and indifferent father.

The vigor with which Pavlov fought for deterministic interpretations in physiology and sought to establish *pravil'nost'* in his laboratories appears counterpoised to the *sluchainost'* of his external world. Providence could play a cruel role at times in Pavlov's personal life, not least by suddenly claiming the life of a son in 1883. Similarly, if ironically, professional failures and setbacks opened better (albeit later) professional opportunities. Randomness was a way of life for Pavlov and his compatriots. Even the name of his chosen city of residence—which, in his lifetime, began as St. Petersburg, was changed to Petrograd, and finally became Leningrad—was a reminder of impermanence and indeterminacy.

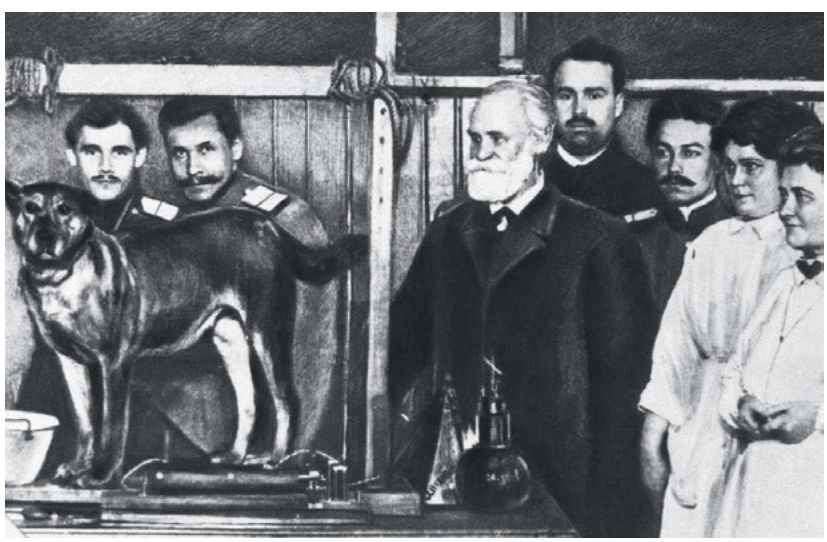

During the years of greatest deprivation in Russia, Pavlov and his co-workers would sometimes sacrifice their own food and fuel to keep the dogs that served as their research subjects alive.

Pavlov's career in physiology, defined by struggle and poverty until his fourth decade, was, beginning in his fifth, marked by illustrious achievements and ideas for new research programs. His Nobel Prize–winning research on the digestive glands gave way to an even more ambitious program that sought to explain the mysteries of the human psyche. In this later project, he posited that the conditional reflex characterized in his earlier work was the physiological correlate of psychological association. However, he was never able to satisfyingly demonstrate his overarching theory of the origins and formation of habits and temperaments. Despite this, his research program engaged with and contributed to a range of topics across the fields of clinical neurology, neurosurgery, psychoanalysis, psychiatry, human genetics, and Gestalt psychology.

Like Charles Darwin and Sigmund Freud, Pavlov possessed and set high intellectual aspirations for himself. But unlike Darwin and Freud, Pavlov published in Russian, and, perhaps for this reason, he never elicited the same adulation as those other "great men" (this is the first major biographical study that engages with the voluminous multilingual archival and literary sources from his life). The subtleties of his life and labor thus disappeared after his death. The discipline of physiology diminished over time, too. It was replaced by a myriad of other scientific disciplines and specialties. Many of these new disciplines, Todes notes, have lost interest in whole-organ function and bodily integration and ultimately even faith in the unification of science with medicine.

The reviewer is at the Department of Humanities and Social Sciences, Clarkson University, Potsdam, NY 13699, USA. E-mail: scasper@clarkson.edu

REFERENCES

1. S. Smiles, *Self Help; with Illustrations of Character and Conduct* (Ticknor and Fields, Boston, 1859).

10.1126/science.aaa5822

COMPLEXITY

Seeing the forest for the trees

Using approximation as a tool for improving understanding

By **Sybil Derrible**

We now live in a world obsessed with data, in which paper and pencil have been traded for code and algorithms. As a result, we often spend less time getting a feel for problems we are tackling than we would have 35 years ago. It was therefore very refreshing to read a book that encourages the reader to do just that.

The Art of Insight in Science and Engineering acts as a step-by-step guide that enables the reader to tackle fundamental scientific problems through simple back-of-the-envelope calculations. The main objective of the book is not to promote a thorough understanding of an underlying theory or to allow us to come to an exact solution but rather to encourage us to use our instincts and knowledge of the fundamental concepts to come to an approximate and reasonable solution. "Approximate first, and worry later," says the book's author, Sanjoy Mahajan. "Otherwise you never start, and you can never learn that the approximations would have been accurate enough—if only you had gathered the courage to make them."

> ***"Approximate first, and worry later," says the book's author, Sanjoy Mahajan.***

To gain insight into a variety of problems, Mahajan has devised a series of reasoning tools. He uses real-life examples to illustrate each tool's utility, showing the reader how to calculate everything from the energy needed for a plane to take off to the time needed to cook a fish to perfection (which is about 10 minutes, for those interested). Each is also cleverly illustrated by practical exercises that reinforce our understanding of the concepts.

The tools in the first section of the book enable us to make a problem more manageable. The divide-and-conquer strategy, for instance, tells us to divide a problem into subparts that can be solved or approximated easily and then aggregated back to the main answer (e.g., mass = density × volume).

In the second section, the reader is encouraged to simplify a problem by combining some of its elements. One way this can be done is by looking at a problem's symmetry. Here, Mahajan recalls the story of the German mathematician Carl Friedrich Gauss, who managed to calculate the sum 1 + 2 + ... + 100 quickly when he was only 3 years old by using symmetry.

The final section has tools to help us discard some elements of complexity and purposefully omit information to reach a conclusion, using techniques including probabilistic analysis and what Mahajan refers to as "lumping." As an example, instead of integrating complex velocity and acceleration profiles to estimate the airborne time of a falling object, Mahajan suggests lumping the profiles into rectangles and computing their areas to generate rough approximations.

Naturally, the book is not perfect. Mahajan clearly comes from a physics background, and he relies mostly on physics problems. The traditional electrical and spring models are used extensively, and so are the fundamentals of fluid mechanics. Moreover, toward the end of the book, Mahajan tackles much more complex problems, looking at sound, light, and gravitational radiation, for instance, which may be difficult for nonphysicists to appreciate. Nevertheless, these more advanced examples show that the overall approach is also applicable and even pertinent to more complex problems.

Senior undergraduate and graduate students will likely enjoy the book because it encourages them to think beyond the equation, and it may help build mental connections between many concepts learned in classes. Researchers and other professionals stand to benefit from it as well, because it may encourage them to think about their own problems in a slightly different way. Teachers will undoubtedly enjoy the book because it should equip them with a battery of techniques to improve their classes. Whichever applies to you, this book is definitely worth adding to your reading list.

10.1126/science.aaa5153

The reviewer is at the Complex and Sustainable Urban Networks (CSUN) Laboratory, University of Illinois at Chicago, Chicago, IL 60607, USA. E-mail: derrible@uic.edu

The Art of Insight in Science and Engineering
Mastering Complexity
Sanjoy Mahajan
MIT Press, 2014. 408 pp.

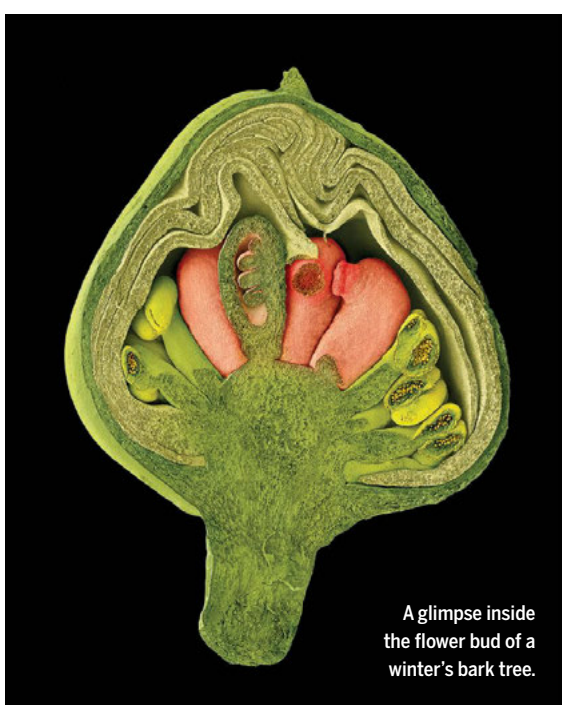

A glimpse inside the flower bud of a winter's bark tree.

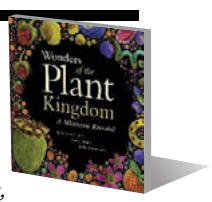

IN BRIEF

Wonders of the Plant Kingdom A Microcosm Revealed
By Wolfgang Stuppy, Rob Kesseler, and Madeline Harley
University of Chicago Press, 2015. 156 pp.

The pseudocolored electron micrographs that grace the pages of this striking book reveal the dazzling array of adaptations in the plant kingdom. Featuring a wide range of seeds, spores, fruits, and pollen, the accompanying text offers a straightforward primer on plant reproduction as well as a discussion of the Royal Botanic Gardens' efforts to protect plant biodiversity.

10.1126/science.aab0708

PHOTO: © WOLFGANG STUPPY, ROB KESSELER, AND MADELINE HARLEY/PAPADAKIS PUBLISHER

Edited by **Jennifer Sills**

Brazil's drought: Beware deforestation

BRAZIL, WHICH HAS the world's largest renewable water supplies, has recently experienced water shortages, and therefore energy crunches, caused by its worst drought since 1930 (*1*). The water crisis has spread across large areas of the country's breadbasket region—southeast Brazil—affecting crop production, industrial activities, and millions of people. After a lengthy delay, the São Paulo government has developed emergency measures to reduce the severity of the water crisis ("Drought triggers alarms in Brazil's biggest metropolis," In Depth, H. Escobar, 20 February, p. 812). Although pressing actions are needed to avoid water collapse in Brazil, an understanding of the importance of preserving large tracts of tropical forest, such as the Amazon rainforest, is essential to promote more effective climate change policies and lower the risk of future droughts.

Long-term research in the Amazon (*2*) suggests that the basin produces some 9.3 trillion liters of water vapor per year through the process of evapotranspiration from plants and the soil. A large portion of this water vapor—about 3.4 trillion liters per year—appears to be transported to South America's south (*2*). This means that, in a nondisturbed ecosystem, the forest and atmosphere are basically recycling the same water, as well as exporting a massive amount of water vapor to distant basins. To remove any of these elements impairs the whole natural system—a process that may not be easily repaired (*3*).

The unprecedented drought affecting Brazil may be a consequence of the depletion of water vapor from the Amazon basin that normally brings rain to Brazil's center and southeast regions. Indeed, precipitation levels in the last several months in the Amazon were just half that in 2014 to 2015 over the same period, according to Escobar's News story. Changes in rainfall patterns in the Amazon rainforest have been attributed to the ongoing human-induced activities such as forest conversion and habitat degradation (*4*). Brazilian Amazon deforestation rates over the past decade remain lower than historic patterns, but with rates rising sharply in recent years (*5*), the southeast and other Brazilian regions could well be receiving less rainfall.

Given growing concerns about global climate change, restoring lost forests and limiting deforestation and forest degradation are important strategies for solving climate change, and it should be a priority in the environmental agenda of developing nations such as Brazil. Otherwise, extreme hydrological events—such as the drought in São Paulo and the two severe droughts within the Amazon basin over the past decade (*6*)—could occur more frequently.

Alison G. Nazareno[1]* and William F. Laurance[2]

[1]University of São Paulo, São Paulo, São Paulo State, 05508-900, Brazil. [2]Centre for Tropical Environmental and Sustainability Science (TESS) and College of Marine and Environmental Sciences, James Cook University, Cairns, QLD, 4878, Australia.
*Corresponding author.
E-mail: alisongn@pg.ffclrp.usp.br

REFERENCES

1. A. P. A. Gutiérrez *et al.*, *Weather Clim. Extremes* **3**, 95 (2014).
2. P. M. Fearsinde, "Rios voadores e a água de São Paulo 2: A reciclagem da água" (http://amazoniareal.com.br/rios-voadores-e-a-agua-de-sao-paulo-2-a-reciclagem-da-agua/) [in Portuguese].
3. K. A. Brauman *et al.*, *Annu. Rev. Environ.* **32**, 67 (2007).
4. D. Laurance, K. Vandecar, *Nat. Clim. Change* **5**, 27 (2015).
5. R. Butler, "Deforestation climbing—along with fears—in the Amazon" (2015); http://news.mongabay.com/2015/0113-imazon-amazon-deforestation-2014.html.
6. S. L. Lewis *et al.*, *Science* **331**, 554 (2011).

Brazil's drought: Protect biodiversity

THE BRAZILIAN WATER crisis linked to climate change has led the government to take drastic measures ("Drought triggers alarms in Brazil's biggest metropolis," In Depth, H. Escobar, 20 February, p. 812),

ONLINE BUZZ: SCIENCE EDUCATION

Evolution in teaching

In his In Depth News story "Why many U.S. biology teachers are 'wishy-washy'" (6 March, p. 1054), J. Mervis describes a recent study showing that students training to become teachers do not understand or embrace the concept of evolution well enough to teach it. Readers shared their own experiences on the subject in the online comments section. Excerpts from their comments are below. Read the full comments, and add your own, at http://comments.sciencemag.org/content/10.1126/science.347.6226.1054.

A selection of your thoughts:

I am surprised that there is still this talk about the theory of evolution in Western countries. In India, when I first learned about the theory of evolution in 1966, I was absolutely fascinated, as this fits in very well with the Indian philosophy of the evolution of the spirit.... ***Vadakkuppattu Ramanathan***

...Decisions concerning curriculum and policy are often made by those who have little education in science, which is precisely the reason we must be sure we are adequately teaching the nature of science to all citizens.... Evolution is science, and educators must understand that what we teach must be what the evidence shows again and again, not what we simply want to be true. There is no refutation of religion in evolution, just as there is no denial of God in physics, or chemistry, or anatomy. Understanding the true nature of science can make this fact undeniably clear.... [We] absolutely need more educators at the primary and secondary level with strong content knowledge. This will not be done by attempting to educate those who want to be in the classroom, but by making the classroom appealing for those who excel in science.... ***Amy Connor***

...[B]iology teachers that are highly effective at developing in students an understanding of evolutionary biology [and] scientific investigation [depend on] real-life experiences with good mentors in the field. It should be a required part of any training for teaching.... ***R. Steven Gumbay***

...Evolutionary theory poorly taught ingrains misconceptions in students that can be difficult to counter later on, so I sympathize with teachers who hesitate to present the subject inexpertly. I didn't get a good foundation in evolutionary theory until graduate school and even after 20 years of teaching, I am acutely aware of how much more I have to learn about teaching it well. ***Mallory Pratt***

such as water diversion projects to transpose water between isolated river basins, without regard for biogeography or aquatic biodiversity. In São Paulo city, the largest metropolis of South America, authorities recently approved a project that will transfer water from the Paraíba do Sul catchment to the Cantareira system (*1*), watersheds that have distinct aquatic biota (*2*). This water diversion will lead to the substantial exchange of organisms between separate ecoregions (*2*), resulting in a massive introduction of distinct biodiversity, bioinvasions, and biotic homogenization (*3*). In turn, we expect that biodiversity and ecosystem services, including the sustainable provision of the water quality, will suffer.

Projects like this are not isolated actions; in semiarid zones (*1*), plans are under way to transpose the São Francisco River Basin to different naturally seasonal basins in northeastern Brazil (i.e., the Caatinga Biome). Authorities have clearly neglected or are unaware of the risks associated with biological invasions (*4*) and biotic homogenization (*5*, *6*). They blame climate change for the current water crisis, but acknowledge neither the role humans have played in surpassing

A severe drought has pushed river levels in Brazil's Amazon region to record lows.

PHOTO: STRINGER BRAZIL/REUTERS

operational limits of the planet nor the negative consequences of biodiversity loss on humanity (*7*).

Rather than implementing water diversion programs, local, state, and federal authorities must work together to raise public awareness to prevent water waste, conserve aquatic sources and aquatic diversity, and restore essential ecosystem services in urban centers and agricultural areas, according to The CBD 2020 Targets (*8*). Only by meeting these goals can we ensure a safe and constant water supply in a transparent and sustainable manner.

Jean Ricardo Simões Vitule,[1]*

Valter M. Azevedo-Santos,[2] Vanessa Salete Daga,[1] Dilermando Pereira Lima-Junior,[3] André Lincoln Barroso de Magalhães,[4] Mario Luís Orsi,[5] Fernando Mayer Pelicice,[6] Ângelo Antônio Agostinho[7]

[1]Laboratório de Ecologia e Conservação (LEC), Universidade Federal do Paraná, Curitiba, PR, 81531-970, Brazil. [2]Laboratório de Ictiologia, Departamento de Zoologia, Universidade Estadual Paulista "Júlio de Mesquita Filho," Campus de Botucatu, SP, 18618-970, Brazil. [3]Departamento de Ciências Biológicas e da Saúde, Universidade Federal do Mato Grosso, Campus Médio Araguaia, Pontal do Araguaia, MT, 78698-000, Brazil. [4]Universidade Federal de São João Del Rei, Programa de Pós-Graduação em Tecnologias para o Desenvolvimento Sustentável, Ouro Branco, MG, 36420-000, Brazil. [5]Museu de Zoologia, Departamento de Biologia Animal e Vegetal, Universidade Estadual de Londrina, Londrina, PR, 86051-990, Brazil. [6]Núcleo de Estudos Ambientais, Universidade Federal de Tocantins, Porto Nacional, TO, 77500-000, Brazil. [7]Núcleo de Pesquisas em Limnologia, Ictiologia e Aquicultura (NUPELIA)/DBI, UEM, Maringá, PR, 87020-900, Brazil.

*Corresponding author. E-mail: biovitule@gmail.com

REFERENCES

1. Ministério do Planejamento (www.planejamento.gov.br) [in Portuguese].
2. R. Abell *et al.*, *BioScience* **58**, 403 (2008).
3. F. J. Rahel, *Freshw. Biol.* **52**, 696 (2007).
4. D. Simberloff, J. R. S. Vitule, *Oikos* **123**, 408 (2014).
5. J. D. Olden *et al.*, *Trends Ecol. Evol.* **19**, 18 (2004).
6. B. Galil *et al.*, *Biol. Invas.* **17**, 972 (2015).
7. J. Rockström *et al.*, *Nature* **461**, 472 (2009).
8. C. Perrings *et al.*, *Science* **330**, 323 (2010).

Rush D. Holt, Ph.D., took the helm at AAAS in February 2015.

PHOTO: ATLANTIC PHOTOGRAPHY BOSTON

Rush Holt wants everyone to think like a scientist

We live in a science-centric nation, even if not everyone appreciates it, says AAAS's new CEO

By **Kathy Wren**

Rush Holt is, by all accounts, an unfailingly nice guy. He is so considerate of others that during an interview at a restaurant he will interrupt himself to wonder how one of the servers can carry his huge load of dishes. But, Holt also likes to argue and doesn't mind debating about climate change, as he told AAAS staff after becoming the Association's chief executive officer and the executive publisher of the *Science* family of journals.

Science lies at the heart of the paradox between Holt's kindly demeanor and the feistiness required in Congress, where he represented New Jersey's 12th district for 16 years. That's because arguing, Rush Holt–style, is not so much quarreling as it is marshaling the evidence. In fact, the principles of doing science—making evidence-based decisions, keeping an open mind, and inviting others to check your work—are also essential to making sound public policy and good decisions in general, according to Holt.

The physicist, educator, policy-maker, and leader of AAAS speaks often about how thinking like a scientist can help all people become better problem-solvers. Scientific thinkers can separate ideology from evidence, and they are more aware of the mental blind spots that we are prone to, such as a tendency to prioritize short-term benefits, when evaluating possible courses of action.

"I think it's great to study science even if you don't become a scientist," Holt said,

Embracing scientific thinking and encouraging more people to do so will remain a top priority for AAAS, according to Holt. "If you study the American way of thinking over the centuries, we've been a scientific nation even among the people not doing science professionally" and have long celebrated people such as Benjamin Franklin for their scientific and technological accomplishments, Holt said. AAAS must continue to cultivate the public's appreciation and support for science, which is largely "unhealthy" today, he said.

As a congressman, Holt took strong stances on many science- and technology-related issues, including climate change, civil liberties, environmental protection, and support for R&D and science education.

Rep. Bill Foster (D-IL), who is the lone physicist now serving in Congress, said that he and Holt shared a belief in the importance of "a quantitative approach to policy decisions." Foster praised Holt's work on national security and digital privacy issues and said that when parts of the Patriot Act come up for reauthorization in June, "his counsel and voice will be missed by many members of Congress, myself included."

Holt has shifted between academia and politics several times in his career: As a professor at Swarthmore College, he also completed a AAAS Science and Technology Policy Fellowship in the office of U.S. Representative Bob Edgar. He left Swarthmore to lead the Nuclear and Scientific Division of the Office of Strategic Forces at the U.S. Department of State for 2 years and then became the assistant director of the Princeton Plasma Physics Laboratory, where he served for 9 years before becoming a congressman.

This comfort with navigating both worlds developed early in Holt's life. "In the 7th grade, I had my own subscriptions to *Scientific American, Science News,* and the *Washington Post,*" he said. "Even then I saw no incompatibility between science and politics."

Holt's parents also blazed their own trail to Washington. Rush Holt Sr. served as a U.S. senator from West Virginia and was the youngest person to be popularly elected to the Senate.

"I would run into complete strangers who would tell me how much my father meant to them, how much he had helped them," Holt said. "That's one of the things that made it easy for me to go into politics."

Holt Jr. was 6 years old when his father passed away while serving in the West Virginia House of Delegates. Holt's mother, then a college biology teacher, filled Holt Sr.'s seat for the rest of his term and then became secretary of state and the first woman to hold statewide office in West Virginia. Later, Helen Holt was appointed by President Eisenhower to head a program to improve the country's nursing homes, and she worked for the Federal Housing Administration, later the Department of Housing and Urban Development, until the 1980s. She was reappointed by six U.S. presidents and is active today at age 101.

When his mother, who had a masters degree in zoology, was teaching at a local women's college, Holt would play in the laboratory stockroom after school. With a laugh, he recalled "taking some phosphorous out of the bottle, taking out some mercury and chasing the droplets around the floor, and any number of other things I shouldn't have been doing."

Holt continued, more soberly: "She was also raising three kids as a single mother," after her husband died. "She was more remarkable than I appreciated at the time."

Perhaps an early sign of Holt's willingness to try new things in front of a wide audience was when, as a graduate student at New York University, he tried out for the game show *Jeopardy!* and won five televised contests. Three decades later, while in Congress, Holt accepted an invitation to compete in a *Jeopardy!* match against IBM's computer Watson, in order to highlight the importance of R&D.

With a knack for remembering facts, including that "hippophobia" is a fear of horses, Holt was the only congressional contestant to outscore Watson in his round.

"I really wanted to draw attention to the kind of innovation that was contained in the Watson system," Holt said. "I thought we should be talking about R&D in corporations, and about the possibilities that come through research."

At AAAS, Holt has a new platform for encouraging all people to appreciate and engage with science. "We should be looking at the health of science in America in all its aspects, in some cases because nobody else is," he said.

PHOTO: ATLANTIC PHOTOGRAPHY BOSTON

AAAS Annual Meeting celebrates new ways to visualize science

By **Becky Ham**

With a light-activated protein and an optical fiber, Stanford bioengineer Karl Deisseroth can temporarily turn a fearful rat into a bold one. He and his colleagues can then trace the neural circuitry of this transformation with a technique that renders brain tissue as clear as glass. These imaging techniques have provided an unprecedented glimpse of the biology behind addiction, anxiety, and social behavior.

It's a cliché to say that new discoveries shed light on a scientific question, but the methods pioneered by Deisseroth and others are helping researchers actually see the brain in new ways. At the 181st AAAS Annual Meeting, researchers demonstrated the powerful potential of some of these visualization techniques in fields from psychology to astronomy. Some scientists at the meeting showed how 3D imaging can be used to guide facial reconstructive surgery. Other researchers demonstrated the potential of remote sensing technology to monitor Earth's atmosphere and oceans, and the use of adaptive optics to discover new planets with ground-based telescopes. In education-themed symposia, attendees learned about integrating mapping and graphical literacy into science classrooms. And, in public policy sessions, presenters discussed how neuroimaging could affect the use of memories in legal proceedings.

Researchers can now use these advances to work across fields and to engage nonscientists in their work. In his plenary address at the meeting, for instance, University of Washington biochemist David Baker discussed how his research on predicting 3D protein structures has led to citizen science offshoots that ask the public to solve protein-folding puzzles or to donate computing power to identify new structures for medicines and new materials.

University of Chicago paleontologist and plenary speaker Neil Shubin also praised the potential of new imaging techniques to open up science to the broadest possible audience. His lab is preparing digital blueprints of *Tiktaalik*, his research team's famous "fins to limbs" fossil discovery, so that more people can print out a 3D copy. "We're entering an age where you don't have to rely on a gatekeeper to study that fossil, you can use the Internet to study that fossil yourself," he said.

The imaging revolution "lets us visualize a world we never knew existed," said MIT geneticist and outgoing AAAS President Gerald Fink in his plenary address. "That vision changes the basis of our science, and changes the textbooks, and changes our view of the universe."

More than 9800 scientists, journalists, educators, and students attended the 12 to 16 February meeting, held for the first time in San Jose, California. AAAS's Family Science Days, a free public event with hands-on activities and demonstrations aimed at K-12 children, drew more than 5000 people.

Karl Deisseroth's sons ask Neil Shubin questions about the *Tiktaalik* fossil.

RESEARCH

Magnetic nanoparticles can stimulate the brain

Chen et al., *p. 1477*

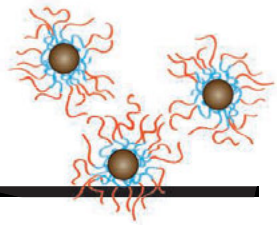

IN *SCIENCE* JOURNALS

Edited by **Stella Hurtley**

SUPERNOVAE

A place where stars are more predictable

Astrophysicists use reference objects of known brightness to determine distances. For example, type Ia supernova (SN Ia) always reach nearly the same peak brightness. This is because they explode when the progenitor white dwarf exceeds its supportable mass threshold. Kelly *et al.* find that a particular subset of SN Ia—those in environments with high ultraviolet surface brightness and star-formation density—can calibrate distances even more tightly. It seems that only one or two intrinsic parameters may drive the apparent relationship between luminosity, color, and fading with time. — MMM

Science, this issue p. 1459

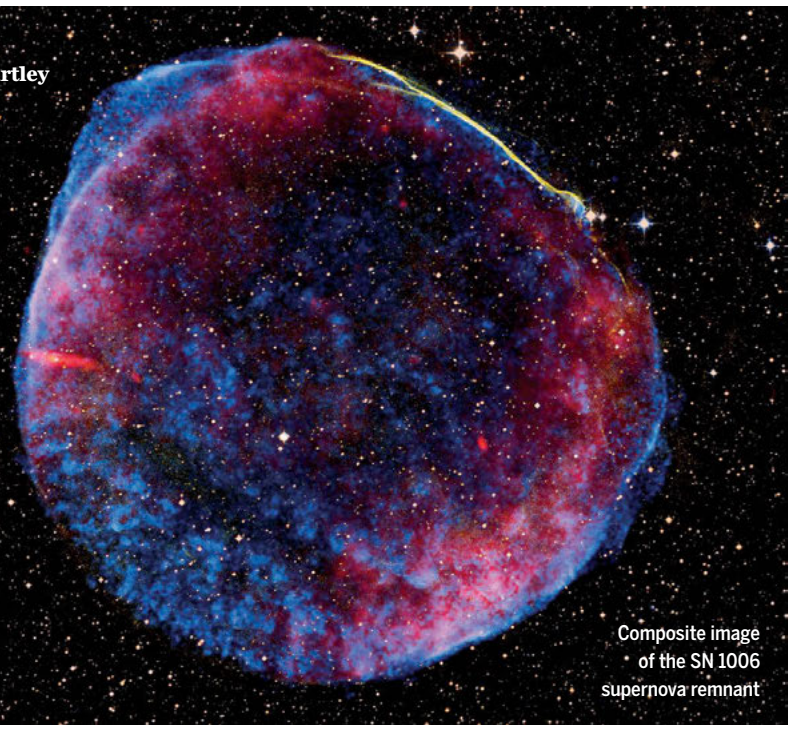

Composite image of the SN 1006 supernova remnant

SOCIAL SCIENCE

Abuse from generation to generation?

Parents who were abused as children are thought more likely to abuse their own children. Widom *et al.* compared reports from parents, from children, and from child protective service agency records gathered on the same families and on matched controls. They observed different findings depending on which information they used. Increases in sexual abuse and neglect relative to controls were reported by children of abuse victims. However, much of the believed transmission of abuse and neglect between generations could be ascribed to surveillance or detection bias targeted at parents with childhood histories of abuse or neglect. — BJ

Science, this issue p. 1480

PARASITOLOGY

Trypanosomes reveal tricky tricks in vivo

The sleeping sickness parasite, *Trypanosoma brucei*, is covered with variant surface glycoproteins (VSGs) recognized by the host's immune system. The parasite uses a repertoire of 2000 VSG genes to switch between different surface variants, continually evading the host's defensive responses. Classic experiments showed that one variant succeeded another, causing waves of infection; however, infection in animals shows different behavior. Mugnier *et al.* discovered that several VSGs are expressed simultaneously and that the repertoire for variation is amplified even more by recombination between the genes to make mosaic VSGs. — CA

Science, this issue p. 1470

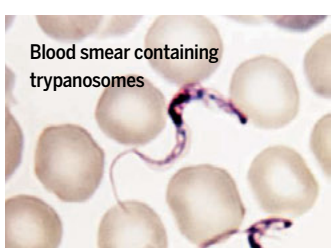

Blood smear containing trypanosomes

ALS GENES

New players in Lou Gehrig's disease

Amyotrophic lateral sclerosis (ALS), often referred to as "Lou Gehrig's disease," is a progressive neurodegenerative disease that affects nerve cells in the brain and the spinal cord. Cirulli *et al.* sequenced the expressed genes of nearly 3000 ALS patients and compared them with those of more than 6000 controls (see the Perspective by Singleton and Traynor). They identified several proteins that were linked to disease in patients. One such protein, TBK1, is implicated in innate immunity and autophagy and may represent a therapeutic target. — SMH

Science, this issue p. 1436; see also p. 1422

DNA ORIGAMI

Reconfigurable DNA structures

DNA origami—nanostructures created by programming the assembly of single-stranded DNA through base pairing—can create intricate structures. However, such structures lack the flexible and reversible interactions more typical of biomolecular recognition. Gerling *et al.* created three-dimensional DNA nanostructures that assemble though nucleotide base-stacking interactions (see the Perspective by Shih). These structures cycled

PHOTOS FROM TOP: X-RAY: NASA/CXC/RUTGERS/G.CASSAM-CHENAÏ, J.HUGHES *ET AL.*; RADIO: NRAO/AUI/NSF/GBT/VLA/DYER. MADDALENA & CORNWELL; OPTICAL: MIDDLEBURY COLLEGE/F.WINKLER. NOAO/AURA/NSF/CTIO SCHMIDT & DSS; BIOPHOTO A.

from open to closed states with changes in salt concentration or temperature. — PDS

Science, this issue p. 1446; see also p. 1417

NUCLEAR PHYSICS

Weighing the neutron against the proton

Elementary science textbooks often state that protons have the same mass as neutrons. This is not far from the truth—the neutron is about 0.14% heavier (and less stable) than the proton. The precise value is important, because if the mass difference were bigger or smaller, the world as we know it would likely not exist. Borsanyi *et al.* calculated the mass difference to high precision using a sophisticated approach that took into account the various forces that exist within a nucleon. The calculations reveal how finely tuned our universe needs to be. — JS

Science, this issue p. 1452

BONE BIOLOGY

Rebuilding bone in osteoporosis

The skeleton undergoes continuous turnover because osteoblast cells build bone and osteoclasts break it down. Too much turnover can cause osteoporosis. The receptor tyrosine kinase DDR2 tilts the balance in favor of bone formation. Zhang *et al.* found that DDR2 both enhanced the development of osteoblasts and prevented osteoclasts from fully developing and breaking down bone. Viral delivery of DDR2 increased bone density in a mouse model of osteoporosis. Thus, increasing DDR2 levels in both types of bone cells may benefit osteoporosis patients. — LKF

Sci. Signal. 8, ra31 (2015).

NEURODEVELOPMENT

Build the builders before the brain

Humans are much smarter than mice—key to this is the relative thickness of the human brain's neocortex. Florio *et al.* combed through genes expressed in the progenitor cells that build the neocortex and zeroed in on one gene found in humans but not in mice. The gene, which seems to differentiate humans from chimpanzees, drives proliferation of the key progenitor cells. Mice expressing this human gene during development built more elaborate brains. — PJH

Science, this issue p. 1465

SNARE PROTEINS

An explosive way to fuse membranes

The molecular machine that promotes membrane fusion during intracellular transport involves a number of so-called SNARE proteins. Ryu *et al.* describe the molecular mechanism by which two proteins —NSF and α-SNAP—disassemble SNARE complexes. A combination of single-molecule techniques resolved intermediate steps of the reaction. Surprisingly, unlike previously assumed, NSF did not unwind SNARE complexes processively. Instead, built-up tension was released in a single burst to "tear" the SNARE complex apart in a one-step global unfolding reaction. — SMH

Science, this issue p. 1485

1D NANOSTRUCTURES

Crafting organic-inorganic shish-kebabs

Functionalized inorganic nanocrystals can be assembled on polymeric chains like shish-kebabs. Xu *et al.* developed a clever and unconventional route for the synthesis of one-dimensional (1D) nanostructures. They capitalized on rationally designed amphiphilic wormlike precursors as nanoreactors. The approach opens the door for the design of intriguing hybrid materials with yet to be discovered properties. – ZHK

Science Advances 10.1126/sciadv.1500025 (2015).

IN OTHER JOURNALS

Edited by **Kristen Mueller** *and* **Jesse Smith**

Weaning enhances the regenerative potential of pancreatic beta cells

CELL REGENERATION

Weaning means more than no more milk

Nursing mothers provide much needed nutrition to offspring, but the full effects of weaning on offspring's physiology is unknown. Stolovich-Rain *et al.* now show that in mice, weaning affects the function of insulin-producing beta cells in the pancreas. The ability of beta cells to regenerate after injury or to modulate their insulin secretion decreases with age. However, beta cells also regenerated poorly in response to injury in very young mice and only gained this function upon weaning. These results suggest that at least for mouse beta cells, weaning jump-starts the cell cycle and modulates insulin production in response to glucose. — BAP

Curr. Biol. **24**, 2733 (2014).

CANCER BIOLOGY

A CRISPR view of tumor metastasis

Large tumors metastasize more often than small tumors. Is this simply because large tumors release a greater number of malignant cells into the circulation? Or is it because the genetic changes in tumor cells that drive them to proliferate rapidly are the same as those that promote their metastatic behavior? To explore this question, Chen *et al.* designed a screen based on a genome-editing technology called CRISPR-Cas9 to identify genes that, when inactivated, enhance tumor growth, lung metastasis, or both in mice. The small set of inactivated genes found in metastatic lesions largely overlapped with the set found in late-stage primary tumors, implying that functional loss of these genes drives both growth and metastasis. — PAK

Cell 10.1016/j.cell.2015.02.038 (2015).

CELL BIOLOGY

Fatty acid trafficking in starvation

Starving cells switch their metabolism from glucose-based to mitochondrial oxidation of fatty acids (FAs). This requires FAs to move from lipid droplets, their home during times of ample nutrition, to the mitochondria. Because free FAs in the cytoplasm are toxic to cells, cells stringently control their trafficking and metabolism. To better

PHOTO: TOM MCHUGH/SCIENCE SOURCE

ALSO IN *SCIENCE* JOURNALS

Edited by **Stella Hurtley**

POLLINATION

Conserving pollinator services for crops

If pollination fails, ecosystems are eroded and we will lose reliable sources of many critical foodstuffs. Focusing on the pollination services provided by bees, Goulson *et al.* review the stresses bees are experiencing from climate change, infectious diseases, and insecticides. We can mitigate some of the stress on bees by improving floral resources and adopting quarantine measures, and by surveillance of bee populations. Crucially, we need to resolve the controversy surrounding prophylactic use of pesticides. — CA

Science, this issue p. 1435

MOLECULAR MOTORS

Making a molecular motor fit for purpose

Dynactin is an essential cofactor of the microtubule motor, cytoplasmic dynein. Dynactin contains 23 subunits built around a short filament of an actin-related protein (Arp1). How dynactin is assembled, how it functions with dynein, and why it is built around an actin-like filament is unclear. Urnavicius *et al.* combined cryo–electron microscopy structural studies and a crystal structure to determine the three-dimensional architecture of dynactin and how it interacts with dynein. — SMH

Science, this issue p. 1441

INFECTIOUS DISEASE

Improving treatment options for fungal infections

Fungal diseases are common around the world. Many respond readily to treatment. However, infections such as invasive aspergillosis can be very difficult to treat, leading to high mortality. Drug resistance in fungal pathogens is also a growing problem. In a Perspective, Denning and Bromley explain the challenges encountered in developing new antifungal treatments. Although few antifungal drugs are currently coming to market, there are some reasons for hope: For example, some compounds in clinical or preclinical development are active against novel targets, and much improved diagnostics are making the early stages of drug development more straightforward. — JFU

Science, this issue p. 1414

GEOMICROBIOLOGY

Building a biogeochemical battery

Iron acts as both a source and sink of electrons for microorganisms in the environment. Some anaerobic bacteria use oxidized Fe(III) as an electron acceptor, whereas phototrophic bacteria can use reduced Fe(II) as an electron donor. Byrne *et al.* show that the iron-bearing mineral magnetite, which contains both Fe(II) and Fe(III), can serve as both an electron acceptor and donor. Cocultures of iron-reducing and iron-oxidizing bacteria exposed to simulated day/night cycles or changes in organic matter altered the ratio of Fe(II) to Fe(III) in magnetite particles. — NW

Science, this issue p. 1473

DARK MATTER

Uncloaking the influence of the invisible actor

The idea of dark matter enjoys popular support, but two major concerns persist: the so-called Standard Model excludes it, and it cannot be directly detected by any telescope. For now, astronomers can only observe dark matter's influence indirectly, such as when watching unseen creatures perturb the surface of a pond. Harvey *et al.* observed 72 galaxy collisions to compare the resulting centers of mass for the gas and stars (from direct observations) and for the dark matter (by inference). Based on these offsets, dark matter is clearly present. — MMM

Science, this issue p. 1462

NEUROTECHNIQUES

Exciting nerve cells deep inside the brain

Current techniques to stimulate regions inside the brain need a permanently implanted wire or an optical fiber. Working in mice, Chen *et al.* developed a method to overcome this problem (see the Perspective by Temel and Jahanshahi). They introduced heat-sensitive capsaicin receptors into nerve cells and then injected magnetic nanoparticles into specific brain regions. The nanoparticles could be heated by external alternating magnetic fields, which activated the ion channel–expressing neurons. Thus, cellular signaling deep inside the brain can be controlled remotely without permanent implants. — PRS

Science, this issue p. 1477; see also p. 1418

QUANTUM GASES

Atoms behaving in an orderly manner

In physics, interactions between components of a system can cause it to become more orderly in an attempt to minimize energy. Such ordered phases appear, for example, in magnetic systems. Schauss *et al.* simulated these phenomena using a collection of neutral atoms at low temperatures. By shining laser light on the atoms, the authors brought some of them into a high-energy state called the Rydberg state. By carefully varying the experimental parameters, they coaxed these Rydberg atoms into patterns reminiscent of crystal lattices in rod- and disk-shaped atomic samples. — JS

Science, this issue p. 1455

from open to closed states with changes in salt concentration or temperature. — PDS

Science, this issue p. 1446; see also p. 1417

NUCLEAR PHYSICS

Weighing the neutron against the proton

Elementary science textbooks often state that protons have the same mass as neutrons. This is not far from the truth—the neutron is about 0.14% heavier (and less stable) than the proton. The precise value is important, because if the mass difference were bigger or smaller, the world as we know it would likely not exist. Borsanyi *et al.* calculated the mass difference to high precision using a sophisticated approach that took into account the various forces that exist within a nucleon. The calculations reveal how finely tuned our universe needs to be. — JS

Science, this issue p. 1452

BONE BIOLOGY

Rebuilding bone in osteoporosis

The skeleton undergoes continuous turnover because osteoblast cells build bone and osteoclasts break it down. Too much turnover can cause osteoporosis. The receptor tyrosine kinase DDR2 tilts the balance in favor of bone formation. Zhang *et al.* found that DDR2 both enhanced the development of osteoblasts and prevented osteoclasts from fully developing and breaking down bone. Viral delivery of DDR2 increased bone density in a mouse model of osteoporosis. Thus, increasing DDR2 levels in both types of bone cells may benefit osteoporosis patients. — LKF

Sci. Signal. 8, ra31 (2015).

NEURODEVELOPMENT

Build the builders before the brain

Humans are much smarter than mice—key to this is the relative thickness of the human brain's neocortex. Florio *et al.* combed through genes expressed in the progenitor cells that build the neocortex and zeroed in on one gene found in humans but not in mice. The gene, which seems to differentiate humans from chimpanzees, drives proliferation of the key progenitor cells. Mice expressing this human gene during development built more elaborate brains. — PJH

Science, this issue p. 1465

SNARE PROTEINS

An explosive way to fuse membranes

The molecular machine that promotes membrane fusion during intracellular transport involves a number of so-called SNARE proteins. Ryu *et al.* describe the molecular mechanism by which two proteins —NSF and α-SNAP—disassemble SNARE complexes. A combination of single-molecule techniques resolved intermediate steps of the reaction. Surprisingly, unlike previously assumed, NSF did not unwind SNARE complexes processively. Instead, built-up tension was released in a single burst to "tear" the SNARE complex apart in a one-step global unfolding reaction. — SMH

Science, this issue p. 1485

1D NANOSTRUCTURES

Crafting organic-inorganic shish-kebabs

Functionalized inorganic nanocrystals can be assembled on polymeric chains like shish-kebabs. Xu *et al.* developed a clever and unconventional route for the synthesis of one-dimensional (1D) nanostructures. They capitalized on rationally designed amphiphilic wormlike precursors as nanoreactors. The approach opens the door for the design of intriguing hybrid materials with yet to be discovered properties. – ZHK

Science Advances 10.1126/sciadv.1500025 (2015).

IN OTHER JOURNALS

Edited by **Kristen Mueller** *and* **Jesse Smith**

Weaning enhances the regenerative potential of pancreatic beta cells

CELL REGENERATION

Weaning means more than no more milk

Nursing mothers provide much needed nutrition to offspring, but the full effects of weaning on offspring's physiology is unknown. Stolovich-Rain *et al.* now show that in mice, weaning affects the function of insulin-producing beta cells in the pancreas. The ability of beta cells to regenerate after injury or to modulate their insulin secretion decreases with age. However, beta cells also regenerated poorly in response to injury in very young mice and only gained this function upon weaning. These results suggest that at least for mouse beta cells, weaning jump-starts the cell cycle and modulates insulin production in response to glucose. — BAP

Curr. Biol. **24**, 2733 (2014).

CANCER BIOLOGY

A CRISPR view of tumor metastasis

Large tumors metastasize more often than small tumors. Is this simply because large tumors release a greater number of malignant cells into the circulation? Or is it because the genetic changes in tumor cells that drive them to proliferate rapidly are the same as those that promote their metastatic behavior? To explore this question, Chen *et al.* designed a screen based on a genome-editing technology called CRISPR-Cas9 to identify genes that, when inactivated, enhance tumor growth, lung metastasis, or both in mice. The small set of inactivated genes found in metastatic lesions largely overlapped with the set found in late-stage primary tumors, implying that functional loss of these genes drives both growth and metastasis. — PAK

Cell 10.1016/j.cell.2015.02.038 (2015).

CELL BIOLOGY

Fatty acid trafficking in starvation

Starving cells switch their metabolism from glucose-based to mitochondrial oxidation of fatty acids (FAs). This requires FAs to move from lipid droplets, their home during times of ample nutrition, to the mitochondria. Because free FAs in the cytoplasm are toxic to cells, cells stringently control their trafficking and metabolism. To better

PHOTO: TOM MCHUGH/SCIENCE SOURCE

CONSERVATION

The hazards of isolation

Climate change affects animals in many ways, including shrinking and shifting their range. On continents, shifts may facilitate adaptation, but many highly threatened species live in regions where geography limits how far their range can shift. One region facing this challenge is Madagascar, where most species are endemic. Brown and Yoder used a suite of spatial modeling approaches to predict how warming might affect Madagascar's iconic lemur species. They found that 60% of lemur species face range contractions due to climate change. They highlight regions of highest conservation concern and conclude that long-term persistence of lemurs will require maintaining dispersal corridors and reducing habitat loss. — SNV

Curr. Biol. **24**, 2733 (2014).

Climate change threatens lemurs in Madagascar.

understand how cells coordinate these processes during starvation, Rambold *et al.* tracked fluorescently labeled FAs in live mouse cells. Enzymes called lipases freed FAs from lipid droplets, allowing their transfer to highly fused mitochondria located nearby. Autophagy, an intracellular degradation process, replenished FAs to lipid droplets. Such careful coordination allows cells to generate substrates for mitochondrial energy production while preventing free FAs–related toxicity. — MSM

Dev. Cell 10.1016/j.devcel.2015.01.029 (2015).

ORGANIC CHEMISTRY

Ionic liquids can ring in carbon dioxide

The growing risks of atmospheric carbon dioxide (CO_2) emissions are prompting chemists to explore more productive uses for the gas. Hu *et al.* present a simple means of coaxing carbon dioxide into small, ring-shaped molecules called oxazolidinones, which are of interest in medicinal chemistry research. Specifically, they found that certain ionic liquids can act as both solvent and catalyst to couple CO_2 with propargylic amines. This environmentally benign approach avoids the need to add metals to accelerate the reaction. The solvent showed consistent performance over five cycles of recovery and reuse. — JSY

Angew. Chem. Int. Ed. 10.1002/anie.201411969 (2015).

MATERIALS SCIENCE

Something fishy about synthetic armor

Many fish are covered in rigid scales attached to a flexible dermis layer, an arrangement that is compliant, resistant to penetration, and lightweight—in other words, an efficient coat of armor. Fink *et al.* use this as inspiration for a synthetic protective material based on a stretchable mesh that supports a set of hard

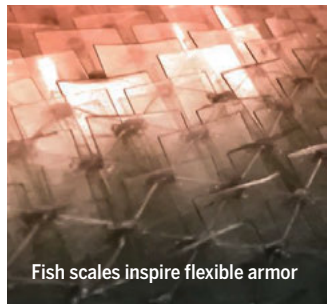

Fish scales inspire flexible armor

plastic tiles. The mesh, made from periodically repeating, sinusoidal polypropylene fibers, provides in-plane elasticity and holds the scales, made from cellulose acetate butyrate, in place as the material is deformed. It also provides a mechanism for scales to rotate and interact with adjacent scales. The mechanical response during in-plane deformation, flexure, and indentation showed many of the advantageous attributes of its biological counterpart. — MSL

ACS Appl. Mater. Interfaces 10.1021/acsami.5b00258 (2015).

EDUCATION

A CURE for promoting undergraduate research

In a perfect world, all undergraduate students would participate in a Course-based Undergraduate Research Experience (CURE). Students participating in CUREs report gains similar to those of students participating in research internships, promoting CUREs as a scalable alternative. What, exactly, do we know about the causal mechanisms underlying the efficacy of CUREs? Using a systems approach, Corwin *et al.* reviewed literature on CUREs and research internships, generated a comprehensive set of outcomes, and connected these outcomes to what students actually do while enrolled in a CURE. These individual outcome models were then combined into an overarching model depicting the relationships among student activities and outcomes. These models are presented with the hope that the CURE community will test and revise them. — MM

CBE Life Sci. Educ. 10.1187/cbe.14-10-0167 (2014).

PHOTOS FROM LEFT: FRANS LANTING/MINT IMAGES/SCIENCE SOURCE; ATASHA FUNK, MARK STOYKOVICH AND FRANCK J. VERNEREY

REVIEW SUMMARY

POLLINATION

Bee declines driven by combined stress from parasites, pesticides, and lack of flowers

Dave Goulson,* Elizabeth Nicholls, Cristina Botías, Ellen L. Rotheray

BACKGROUND: The species richness of wild bees and other pollinators has declined over the past 50 years, with some species undergoing major declines and a few going extinct. Evidence of the causes of these losses is patchy and incomplete, owing to inadequate monitoring systems. Managed honey bee stocks have also declined in North America and many European countries, although they have increased substantially in China. During this same period, the demand for insect pollination of crops has approximately tripled, and the importance of wild pollinators in providing such services has become increasingly apparent, leading to concern that we may be nearing a "pollination crisis" in which crop yields begin to fall. This has stimulated much-needed research into the causes of bee declines. Habitat loss, which has reduced the abundance and diversity of floral resources and nesting opportunities, has undoubtedly been a major long-term driver through the 20th century and still continues today. In addition, both wild and managed bees have been exposed to a succession of emerging parasites and pathogens that have been accidentally moved around the world by human action. The intensification of agriculture and increasing reliance on pesticides means that pollinators are also chronically exposed to cocktails of agrochemicals. Predicted changes in global climate are likely to further exacerbate such problems in the future.

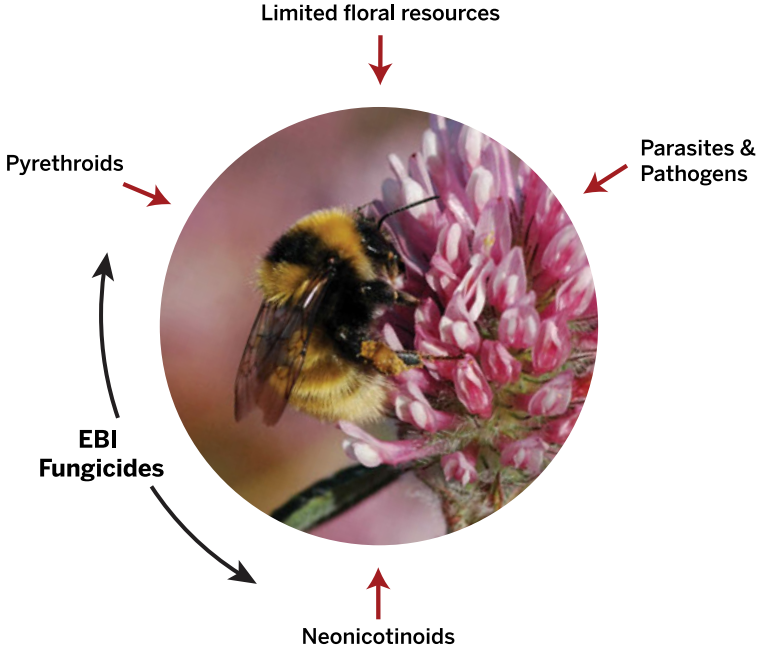

PHOTO CREDIT: DAVE GOULSON

Multiple interacting stressors drive bee declines. Both wild and managed bees are subject to a number of important and interacting stressors. For example, exposure to some fungicides can greatly increase the toxicity of insecticides, whereas exposure to insecticides reduces resistance to diseases. Dietary stresses are likely to reduce the ability of bees to cope with both toxins and pathogens.

ON OUR WEB SITE

Read the full article at http://dx.doi.org/10.1126/science.1255957

ADVANCES: It has lately become clear that stressors do not act in isolation and that their interactions may be difficult to predict; for example, some pesticides act synergistically rather than additively. Both pesticide exposure and food stress can impair immune responses, rendering bees more susceptible to parasites. It seems certain that chronic exposure to multiple interacting stressors is driving honey bee colony losses and declines of wild pollinators, but the precise combination apparently differs from place to place.

Although the causes of pollinator decline may be complex and subject to disagreement, solutions need not be; taking steps to reduce or remove any of these stresses is likely to benefit pollinator health. Several techniques are available that have been demonstrated to effectively increase floral availability in farmland. Similarly, encouraging gardeners to grow appropriate bee-friendly flowers and to improve management of amenity grasslands can also reduce dietary stress. Retaining or restoring areas of seminatural habitat within farmland will improve nest site availability. A return to the principles of integrated pest management and avoidance of prophylactic use of agrochemicals could greatly decrease exposure of bees to pesticides.

OUTLOOK: Interactions among agrochemicals and stressors are not addressed by current regulatory procedures, which typically expose well-fed, parasite-free bees to a single pesticide for a short period of time. Devising approaches to study these interactions and incorporating them into the regulatory process poses a major challenge. In the meantime, providing support and advice for farmers in more sustainable farming methods with reduced pesticide use is likely to have broad benefits for farmland biodiversity. Enforcing effective quarantine measures on bee movements to prevent further spread of bee parasites is also vital. Finally, effective monitoring of wild pollinator populations is urgently needed to inform management strategies. Without this, we have no early warning system to tell us how close we may be to a pollination crisis. With a growing human population and rapid growth in global demand for pollination services, we cannot afford to see crop yields begin to fall, and we would be well advised to take preemptive action to ensure that we have adequate pollination services into the future. ■

School of Life Sciences, University of Sussex, Falmer, Brighton BN1 9QG, UK.
*Corresponding author. E-mail: d.goulson@sussex.ac.uk
Cite this article as D. Goulson *et al.*, *Science* **347**, 1255957 (2015). DOI: 10.1126/science.1255957

REVIEW

POLLINATION

Bee declines driven by combined stress from parasites, pesticides, and lack of flowers

Dave Goulson,* Elizabeth Nicholls, Cristina Botías, Ellen L. Rotheray

Bees are subject to numerous pressures in the modern world. The abundance and diversity of flowers has declined; bees are chronically exposed to cocktails of agrochemicals, and they are simultaneously exposed to novel parasites accidentally spread by humans. Climate change is likely to exacerbate these problems in the future. Stressors do not act in isolation; for example, pesticide exposure can impair both detoxification mechanisms and immune responses, rendering bees more susceptible to parasites. It seems certain that chronic exposure to multiple interacting stressors is driving honey bee colony losses and declines of wild pollinators, but such interactions are not addressed by current regulatory procedures, and studying these interactions experimentally poses a major challenge. In the meantime, taking steps to reduce stress on bees would seem prudent; incorporating flower-rich habitat into farmland, reducing pesticide use through adopting more sustainable farming methods, and enforcing effective quarantine measures on bee movements are all practical measures that should be adopted. Effective monitoring of wild pollinator populations is urgently needed to inform management strategies into the future.

Insect pollination is vitally important to terrestrial ecosystems and to crop production. The oft-quoted statistics are that 75% of our crop species benefit from insect pollinators (*1*), which provide a global service worth $215 billion to food production (*2*). Hence, the chance that we may be facing a "pollination crisis" (*3*, *4*), in which crop yields begin to fall because of inadequate pollination, has generated understandable debate and concern and stimulated much research in recent decades. Nonetheless, knowledge gaps remain substantial with regard to both the extent and causes of pollinator declines. Indeed, for most regions of the globe and for most wild pollinator taxa, we have no data as to whether there have actually been declines. Our best estimates are for numbers of domesticated honey bee colonies, which can be obtained for many countries with varying reliability. These suggest that numbers of managed honey bee colonies have decreased in Europe [25% loss of colonies in central Europe between 1985 and 2005 (*5*)] and markedly in North America [59% loss of colonies between 1947 and 2005 (*6*, *7*)]. However, overall global stocks actually increased by ~45% between 1961 and 2008 because of a major increase in numbers of hives in countries such as China and Argentina (*8*). Conversely, there are widespread reports of unusually high rates of honey bee colony loss from many parts of the world, sometimes ascribed to a syndrome known as colony collapse disorder (CCD) (*9*). It seems that socio-economic factors such as increasing demand for pollination or honey (*10*) are at present sufficient to incentivize beekeepers to overcome problems with bee health when examined at a global scale, but not locally in North America and Europe.

If we turn to wild pollinators, the best data available are for bumblebees (*11*). In Europe, many species have undergone substantial range contractions and localized extinction, with four species going extinct throughout the continent (*11*, *12*) (Fig. 1A). In North America, some formerly abundant and widespread species such as *Bombus terricola* and *B. occidentalis* underwent severe declines from the late 1990s onward and now occupy only a small fraction of their former range (Fig. 1B) (*13*, *14*). *Bombus franklini*, a species formerly found in northern California and Oregon, has not been recorded since 2006 and is presumed extinct. In a study of the bumblebee fauna of Illinois over the past 100 years, Grixti *et al.* (*15*) described substantial declines in species diversity, particularly during the period 1940–1960, with the extirpation of four species during the 20th century. In South America, the recent invasion by the European species *B. terrestris* is causing precipitous declines in the native *B. dahlbomii* (*16*). There is some evidence of loss of species richness from lowland areas of Sichuan in China (*17*, *18*) and a few reports of declines in Japan from the mid-1990s onward (*19*, *20*), but elsewhere in the world, few data are available. For the remaining wild bees, data are exceedingly sparse, although they comprise the large majority of the world's approximately 22,000 bee species. Analysis of historic records suggests that diversity of both bumblebees and other wild bees declined in the United Kingdom, the Netherlands, and Belgium during the 20th century, but that these declines have decelerated since 1990 (*21*, *22*). In surveys in Illinois, 50% of wild bee species went extinct over a 120-year period to 2010 (*23*). Given that bee diversity has declined in both Europe and the Americas, it is probably reasonable to assume that declines are also occurring elsewhere across the globe.

The biggest knowledge gap concerns bee abundance; although we have maps of past and present distributions of bees for some well-studied countries such as the United Kingdom, we have almost no data on how populations have changed over time. Hence, we do not know whether common species such as *B. terrestris* in Europe or *B. impatiens* in North America are less abundant than formerly, or whether they are currently in decline. Most pollination is delivered by a small number of these abundant species, which tend to have large distributions. Declines in their abundance would not be detected in distribution maps until they become extinct in parts of their range, which is rather late to introduce conservation measures.

Another way to examine the likelihood or proximity of a pollination crisis is to examine delivery of pollination services. Although global honey bee stocks have increased by ~45%, demand has risen more than supply; the fraction of global crops that require animal pollination has tripled over the same time period (*8*), making food production more dependent on pollinators than before. It has also emerged that the majority of crop pollination at a global scale is delivered by wild pollinators rather than honey bees. Yields correlate better with wild pollinator abundance than with abundance of honey bees (*24*–*26*); hence, increasing honey bee numbers alone is unlikely to provide a complete solution to the increasing demand for pollination. Reliance on a single species is also a risky strategy (*27*). Whereas Aizen *et al.* (*28*) concluded from a global analysis of changing crop yields over time that there was not yet any clear evidence that a shortage of pollinators was reducing yield, a subsequent analysis of the same data set by Garibaldi *et al.* (*29*) showed that yields of pollinator-dependent crops are more variable, and have increased less, than crops that do not benefit from pollinators, to the extent that a shortage of pollinators is reducing the stability of agricultural food production. In a meta-analysis of 29 studies on diverse crops and contrasting biomes, Garibaldi *et al.* (*30*) found that wild pollinator visitation and yields generally drop with increasing distance from natural areas, which suggests that yields on some farms are already affected by inadequate pollination.

To summarize the changes during the past 50 years: Global honey bee stocks have increased while wild bees appear to have declined substantially, as evidenced by data for bumblebees and very scant data for other bee species. The demand for insect pollinators in farming has tripled during the same period. There is clearly no major pollination crisis yet, but there is evidence

School of Life Sciences, University of Sussex, Falmer, Brighton BN1 9QG, UK.
*Corresponding author. E-mail: d.goulson@sussex.ac.uk

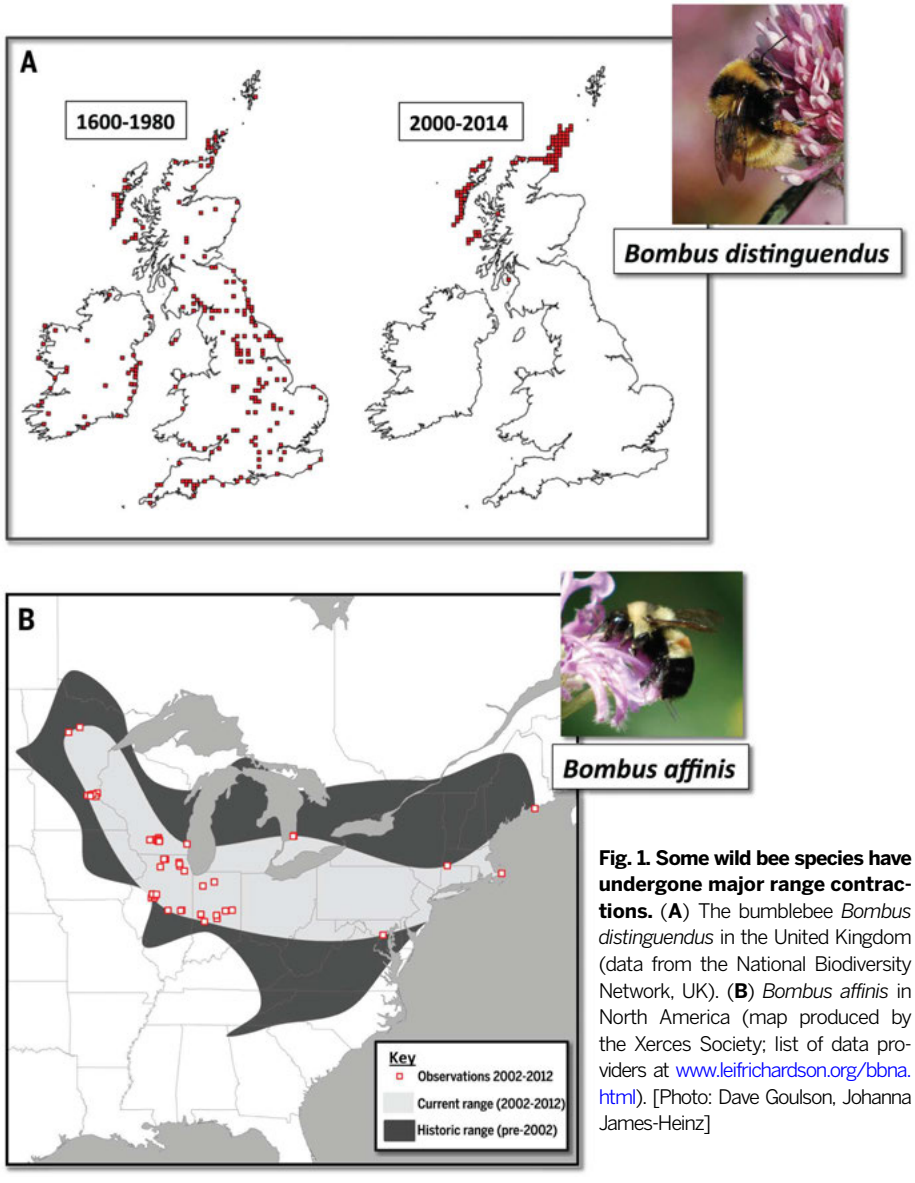

Fig. 1. Some wild bee species have undergone major range contractions. (**A**) The bumblebee *Bombus distinguendus* in the United Kingdom (data from the National Biodiversity Network, UK). (**B**) *Bombus affinis* in North America (map produced by the Xerces Society; list of data providers at www.leifrichardson.org/bbna.html). [Photo: Dave Goulson, Johanna James-Heinz]

for localized limitation of crop yield as a result of inadequate pollination.

Drivers of wild bee declines and honey bee colony losses

Habitat loss

Bee declines have been attributed to many factors, some more plausible than others; however, the clear consensus is that loss of habitat has been a long-term contributor to declines (*11*, *31*–*33*). Bees require appropriate floral resources during the adult flight season, which may be short for some solitary species or yearlong for social species in tropical environments. They also require undisturbed nest sites, with different species occupying diverse locations (e.g., cavities underground, hollow-stemmed twigs, burrows in the soil, even abandoned snail shells). The conversion of natural and seminatural flower-rich habitat to farmland has been a major driver of long-term declines in bees. For example, in the United Kingdom, approximately 97% of flower-rich grasslands were lost in the 20th century (*34*), and this has resulted in major range contractions of bee species associated with this habitat, particularly long-tongued bumblebees (*11*). Declines of similar magnitude have affected the grasslands of North America, although these began in the early 19th century (*35*).

Urbanization also contributes to loss of natural habitat, but the net effect on bees is less clear. Gardens can support high densities of wild bees, particularly bumblebees and some solitary bee species, but highly urbanized environments have few bees (*36*, *37*), and the building of roads and other infrastructure undoubtedly contributes to the ongoing fragmentation and degradation of habitats. Increased traffic can also cause direct mortality through collisions (*38*), although the number of bees killed in this way is not known. The planting of road verges and traffic islands with wildflowers is often promoted as a means of boosting urban pollinator populations, but it might increase mortality by vehicle collisions.

Parasites and disease

Bees naturally suffer from a broad range of parasites, parasitoids, and pathogens, the latter including protozoans, fungi, bacteria, and viruses. By far the majority of research has focused on those associated with honey bees and to a lesser extent with bumblebees; very little is known about the pathogens of other wild bee species. Some bee disease agents, such as deformed wing virus (DWV) and *Nosema ceranae*, have broad host ranges and are able to infect both honey bees and bumblebees; others, such as *Crithidia bombi* or *Paenibacillus larvae*, seem to be more host-specific (*39*–*41*). Although natural pathogens undoubtedly play an important but poorly understood role in influencing the population dynamics of their bee hosts, our focus here is on the impacts that non-native parasites and pathogens may have.

The spread of most honey bee parasites and pathogens has occurred inadvertently as a result of transporting honey bees long distances. Much of this happened in historic times, but it continues despite some improvements in quarantine procedures. The best-known example is the mite *Varroa destructor*, originally associated with the Asian honey bee *Apis cerana*. *Varroa* has since jumped hosts to the European honey bee *Apis mellifera*, which has little resistance to this pest. Since the 1960s, *Varroa* has spread from Asia to Europe, the Americas, and most recently to New Zealand. The mite acts as a vector for pathogens such as DWV, and the combined effect of the mite and the diseases it transmits is a major contributor to honey bee colony losses in North America and Europe (*42*, *43*). Fortunately, the mite appears unable to survive on bees outside the genus *Apis*.

A strikingly similar series of events has also seen the microsporidian *N. ceranae* jump from *A. cerana* to *A. mellifera*, and in the past 20 years it has spread to Europe and the Americas, where it is now prevalent at high frequency (Fig. 2) (*44*, *45*). It has also been detected in wild bumblebees in Europe, China, and South America (*41*, *46*, *47*) and in solitary bees in Europe (*48*). In the lab, *N. ceranae* appears to have higher virulence in bumblebees than it does in honey bees (*41*), although the impact it has had on wild populations is unknown. Asia is not the only source of non-native diseases; the African honey bee parasite *Aethina tumida* (small hive beetle) recently invaded North America, Egypt, Australia, and Europe, and causes considerable damage to *B. impatiens* colonies (*49*, *50*). It seems highly likely that it also attacks other wild bumblebee species that are not so readily cultured and are therefore less well studied.

Bee diseases are also being redistributed around the globe by the commercial trade in bumblebee colonies, which are mainly used for pollination of greenhouse crops such as tomatoes. This trade began in the 1980s in Europe, and now more

than 1 million nests of the European *B. terrestris* are reared each year and exported to various countries. In North America, the eastern American species *B. impatiens* is reared for this purpose. Unfortunately, it does not yet seem possible to rear colonies that are free of disease, not least because the bees are reared on honey bee–collected pollen, providing a route for exposure to many bee pathogens. Commercial colonies of *B. terrestris* are commonly infected with one or more parasites, including *Nosema bombi*, *N. ceranae*, *Apicystis bombi*, and DWV (*41*).

There is evidence that non-native pathogens or pathogen strains associated with these colonies are having devastating impacts on wild bumblebee populations. In North America, the accidental importation of a non-native strain of the parasite *N. bombi* via commercial bumblebees has been implicated in the marked decline of several bumblebee species, although convincing causal evidence remains elusive (*51*, *52*). The evidence from South America is clearer; here, *B. terrestris* were deliberately introduced by the Chilean government despite the presence of native *Bombus* species, with *terrestris* spreading rapidly to occupy a vast area of southern South America. The arrival of *B. terrestris* appears to have led to the rapid local extinction of the native *B. dahlbomii* at a speed plausibly explained only by pathogen spillover (*16*). Although the parasite responsible has yet to be ascertained with certainty, both *A. bombi* and *C. bombi* have been shown to be highly prevalent in the invasive species (*16*, *53*). There is a clear parallel with the devastating impact of European diseases on native Americans 500 years ago.

Even when commercial bees are free of disease upon arrival or are infected only with indigenous parasites, they can still affect native pollinators. High-density populations of managed bees may provide conditions for the rapid multiplication of parasites that then spill over into wild populations (*54*–*56*). A combination of field observations and modeling suggests that waves of *Crithidia bombi* infection travel outward from greenhouses containing commercial bumblebees. Prediction indicates that waves can spread at ~2 km per week, with up to 100% of wild bees within the spreading radius becoming infected, although this is not yet well supported by direct evidence (*55*).

In general, we know little about the natural geographic range, host range, prevalence, or virulence of most bee pathogens, and so it would seem wise to take very careful precautions to prevent further introductions of bee pathogens from outside their native range, in addition to minimizing any spillover from commercial pollination operations (*52*, *57*).

Pesticides

Pesticides are the most controversial and debated cause of bee declines. When appropriately used, pesticides provide a clear economic benefit, but they bring the welfare of bees into direct conflict with industrial agriculture. Herbicides are highly effective at minimizing weed problems in most cropping systems, enabling farmers to grow near-pure monocultures, but their use inevitably reduces the availability of flowers for pollinators and can contribute substantially to rendering farmland an inhospitable environment for bees (*11*, *58*, *59*). Understandably, most attention has been paid to the direct toxic effects of pesticides on bees, particularly the impacts of insecticides. Of the 161 different pesticides that have been detected in honey bee colonies (*60*, *61*), Sanchez-Bayo and Goka (*61*) predicted that three neonicotinoids (thiamethoxam, imidacloprid, and clothianidin) and two organophosphates (phosmet and chlorpyrifos) pose the biggest risk to honey bees at a global scale, as determined

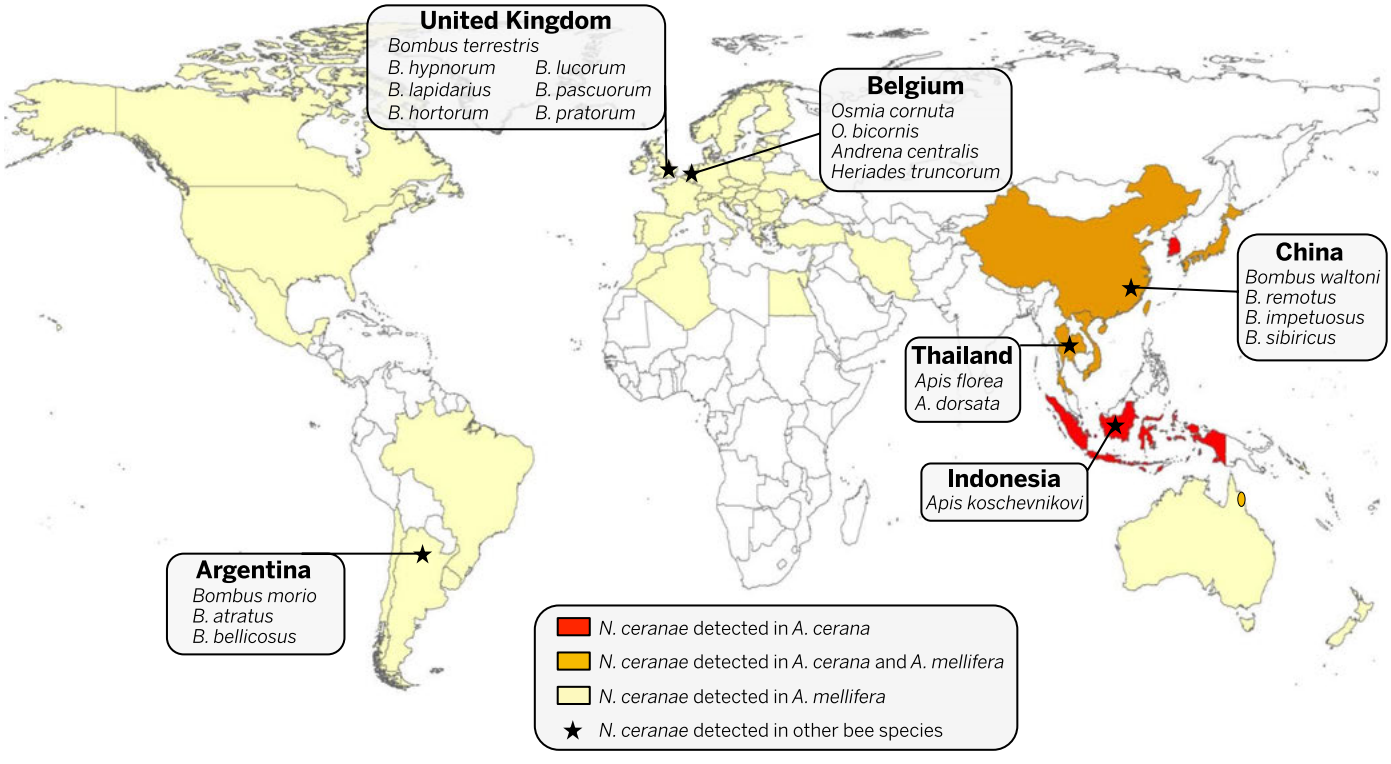

Fig. 2. World distribution of the microsporidian pathogen *Nosema ceranae* in different bee hosts. This parasite was first isolated from the Eastern honeybee (*A. cerana*) collected in China in 1996 (*163*) and was subsequently found infecting Western honey bees (*A. mellifera*) in Europe in 2005 (*164*). Soon after, *N. ceranae* was detected in *A. mellifera* in many regions of the world, including Africa, Asia, the Americas, and Oceania (*44*, *45*, *165*–*168*), and more recently in other bee species including several Asian *Apis* species (*169*, *170*) and wild bumblebee species from Europe, China, and South America (*41*, *46*, *47*). *N. ceranae* has also now been detected in solitary bees from Europe (*48*), confirming a very wide range of hosts and high dispersal rate. Although the origins and primary host of *N. ceranae* are yet to be accurately established, the apparent late and gradual invasions of *N. ceranae* into different *A. mellifera* populations have led some authors to suggest that *A. cerana* may be the primary host of *N. ceranae* and that it may have only recently emerged as a parasite of Western bees (*170*). The mechanism by which *N. ceranae* broadened its host range from an Asian bee species to other bee species across the world is unknown, but there has been human-mediated contact between Asian and Western bees for at least a century. Note that regions in the figure where *Nosema* appears to be absent (white) may be due to a lack of sampling in these areas.

from data on toxicity, frequency in hives, and concentrations detected. It is clear that bees are often chronically exposed to cocktails of pesticides throughout their development and adult life (61–64), but the effects of this are poorly understood and are not examined by current regulatory procedures for risk assessment (65).

Neonicotinoids are the newest of the main insecticide classes and are the group most strongly implicated in bee declines (65, 66). They are neurotoxins that target the insect central nervous system, binding to postsynaptic nicotinic acetylcholine receptors and causing overstimulation, paralysis, and death (67). These insecticides are commonly applied as seed treatments and are systemic within plants, spreading through plant tissues and into the pollen and nectar of flowering crops such as canola. They are also water-soluble but highly persistent in soil and soil water, and as a result have been found at biologically relevant concentrations in the pollen and nectar of wildflowers near crops (63). Thus, there is a clear route for ingestion by bees. Oral toxicity is high, with the short-term LD_{50} for the most commonly used neonicotinoids in the range of 4 to 5 ng per honey bee (68) (LD_{50} = lethal dose 50%, the dose that kills 50% of test organisms). Long-term chronic exposure results in mortality in overwintering honey bees when feeding on food contaminated with concentrations as low as 0.25 ppb (69). Sublethal effects of neonicotinoid exposure have also been observed in both honey bees and bumblebees, including reductions in learning, foraging ability, and homing ability, all of which are essential to bee survival (70–74). Yang *et al.* (75) recently showed that even low exposure during the larval stage (0.04 ng per larva, equating to less than 1% of the LC_{50} for adult bees) can have a lasting impact on learning in adult honey bees (LC_{50} = lethal concentration 50%, the concentration that kills 50% of test organisms).

It seems very likely that bees living in most arable farmland are routinely exposed to sufficient neonicotinoids to suffer both lethal and sublethal effects. However, whether this translates into a detrimental effect at the colony level remains disputed. In bumblebees, exposure of colonies to field-realistic concentrations of imidacloprid greatly impaired colony growth and reduced queen production by 85% (76). In contrast, field studies with honey bee colonies have proved more challenging to perform convincingly (77, 78), not least because of the huge areas over which honey bees forage, the lack of a clear endpoint to colony development, and their long-term storage of food reserves. This lack of clear evidence of harm in the field is often misinterpreted as evidence that toxicological studies on individual bees do not translate into colony losses in the field, rather than as the absence of evidence.

Monotonous diets

Intensively farmed areas provide few wildflowers but do provide spatially and temporally isolated gluts of flowers, in the form of mass-flowering crops such as sunflowers and canola. If a human were to consume nothing but sardines one month, chocolate the next, turnips the month after, and so on, one could reasonably expect that person to fall ill. This may seem a frivolous example, but it is a reasonable parallel to the experience of some honey bee colonies, particularly those in North America that are transported back and forth across the continent each year to provide pollination for major crops such as almonds in California, blueberries in Maine, and citrus in Florida. Where the nectar or pollen of crop flowers contain toxins, such as the glycoside amygdalin found in almonds (79), bees might potentially consume harmful concentrations of such substances.

More generally, it seems certain that bees inhabiting intensive farmland have a more monotonous diet than they would have experienced in their evolutionary past, but how this might affect their fitness remains unclear. The pollen of different plant species varies greatly in protein content, amino acid composition, lipid, starch, and vitamin and mineral content. Nectar commonly contains varying and low concentrations of a range of nutrients and other compounds of largely unknown importance (80–84). Thus, we might expect the type and range of flowers available to affect individual bee health and colony fitness in multiple ways; for example, in honey bees, both pollen quality and diversity influence longevity, physiology, and resistance or tolerance to disease (85–88). However, this topic has been little investigated, particularly for wild bees. The perception that honey bees may be receiving an inadequate diet has led to the development of protein supplements, but once again, there has been little research on the long-term effectiveness of such supplements on colony health (89, 90).

Interpreting the effects of availability of mass-flowering crops on bees and their colonies is further complicated because visiting such crops often exposes bees to pesticide residues, so that positive effects of increased food availability may be offset by negative effects of the pesticide. Some studies have found positive effects of proximity to canola on bumblebee colony growth and abundance (91, 92) and on numbers of nesting red mason bees *Osmia bicornis* (93, 94); others have found no relationship for bumblebees (58, 95) nor for solitary bees (96). Interestingly, none of these studies considered what role pesticides might have played in mediating the effect of the crop, or even reported which pesticides were applied to crops in the study area—an omission that now seems naïve, given the recent focus on impacts of neonicotinoid insecticides on bees.

Shipping fever

It seems reasonable to hypothesize that the long-distance transport of bees, as routinely occurs for honey bees in North America and for commercial bumblebee colonies, places stress on the colonies. For several days, they may be confined and subject to vibration, high temperatures, high levels of carbon dioxide, and irregular disturbance. It has long been known that such stress can activate bacterial and viral infections in vertebrate livestock (97), but this has not been investigated in bees, although Bakonyi *et al.* (98) suggested that shipping stress may have contributed to honey bee colony losses in Hungary. This is clearly an area where further research is needed.

Competition

The role of competition in determining the relative abundance of species is notoriously difficult to ascertain in mobile organisms such as bees, but it seems likely that competition for floral resources and perhaps also for nest sites does occur in natural communities, and that it can be exacerbated by the introduction of non-native species, particularly when the latter are present at high densities (57). For example, there is evidence that high concentrations of domestic honey bee hives can displace wild bumblebees from their preferred foodplants and from whole areas if hive densities are sufficiently high (99, 100). This can result in a reduction in the size of bumblebee workers (101) and reduced reproductive success of bumblebee colonies (102). Although in general, the interests of honey bee keepers and wild bee conservationists are aligned (all would agree on the benefits of increasing floral resources, reducing exposure to pesticides, and preventing invasions of alien pathogens), there may occasionally be conflict where beekeepers wish to place hives in areas with important populations of rare wild bees (57).

Climate change

Climate change is widely accepted to pose one of the largest threats to biodiversity worldwide, but likely impacts on pollinators and pollination are not well understood. One danger is that the phenology of pollinators may diverge from that of the plants they pollinate, with potentially disastrous consequences for both, but there is little evidence that this has happened so far (103). Advances in flowering and bee emergence are often broadly similar, and in any case few plants are dependent on a single pollinator, so that any mismatch with one pollinator is likely to be compensated by increased availability of another (103, 104).

Another potential effect of climate change is as a driver of range shifts, leading to a spatial mismatch between plants and pollinators. Range shifts in response to climate have been demonstrated in butterflies (105) and are to be expected in bees (13); for example, there is already evidence that the lower altitudinal limit of some montane bumblebees has shifted uphill in Spain (106). We would predict declines in bumblebees at the southern edge of their range because they tend to be poorly adapted to high temperatures.

Of course, climate change is not solely associated with warming; extreme weather events such as storms, floods, and droughts are predicted to increase, and we would expect these to have major impacts on local bee communities. For example, flooding is likely to be harmful to the many bee species that nest or hibernate underground.

Overall, although there is little strong evidence that climate change has yet had any great effect on bees, it is likely to provide a growing

source of stress in the future that would exacerbate the impact of other factors such as habitat loss.

Interactions between stressors

Unfortunately, the public debate on bee health has often become polarized, with claims that, for example, *Varroa* or neonicotinoid insecticides are the sole or primary cause of bee declines or honey bee colony losses. If a middle-aged man who is overweight, does little exercise, and smokes and drinks heavily were to die of a heart attack, we would not be surprised and we might not spend too long arguing over which single risk factor was most important in bringing about his untimely demise. Similarly, wild bee declines and honey bee colony losses are clearly due to multiple, interacting, and sometimes synergistic factors, and the combination of factors involved no doubt varies in time and space.

In general, the combined effect of multiple stressors is likely to be more harmful than one stressor alone (*107*–*109*) (Fig. 3). In the worst-case scenario, sublethal stressors that do not incur harmful effects in isolation could, in combination, result in lethal effects. As we have already seen, bees are often exposed chronically to mixtures of pesticides and other chemicals. Some, such as ergosterol biosynthesis inhibitor (EBI) fungicides, have very low toxicity in themselves but may increase the toxicity of some neonicotinoids and pyrethroids by as much as a factor of 1000 (*110*–*112*). Piperonyl butoxide is often added to pesticide formulations and also acts synergistically with some neonicotinoids, increasing toxicity by a factor of up to 244 (*111*). Intriguingly, while imidacloprid alone has been shown to impair olfactory learning (*113*), combined exposure to imidacloprid and coumaphos has been shown to result in a slight increase in learning in honey bees (*114*). So although regulatory processes examine the effects on bees of exposure to a single pesticide at a time, in reality bees are simultaneously exposed to many pesticides, some of which have combined effects that cannot be predicted from studies of their effects when used in isolation.

Several recent studies indicate that interactive effects between pesticides and pathogens could be especially harmful for bees (*115*–*121*). For instance, developmental exposure to neonicotinoid insecticides renders honey bees more susceptible to the impact of the invasive pathogen *N. ceranae* (*122*). Imidacloprid can act synergistically with *Nosema* spp. by increasing the prevalence of *Nosema* infections in hives (*116*) and increasing *Nosema*-induced mortality (*115*). Similarly, Aufauvre *et al.* (*118*) showed that mortality of honey bees was greater when bees were exposed to the insecticide fipronil and infected by *N. ceranae* than when only a single stress factor was present. There is evidence that exposure to pesticides may impair the immune function of insects, which would explain these effects (*43*, *123*–*125*). For example, Di Prisco *et al.* (*126*) recently showed that exposure to neonicotinoids (clothianidin or imidacloprid) leads to immunosuppression in honey bees, which in turn promotes the replication of DWV in insects with covert infections. This effect was found at very low concentrations, well below those that bees are likely to encounter in the field.

Interactions between stressors are not confined to pesticides and pathogens. The ability of bees to survive parasite infections is compromised by nutritional stress. For example, *Crithidia bombi* causes little mortality in well-fed bumblebees but becomes virulent in bumblebees with a restricted diet (*127*). Activating the immune response has a metabolic cost; bumblebees increase their food consumption when immune responses are up-regulated (*128*), and artificially stimulating the immune response by injecting latex beads caused mortality in starving bumblebees but not in those that were well fed (*129*). Increased food consumption in infected bees could also increase exposure to pesticides. Activating immunity has been shown to impair learning in both honey bees (*130*) and bumblebees (*131*, *132*), and impaired learning will reduce the bees' ability to locate floral resources and extract rewards, thus exacerbating nutritional stresses.

Although to our knowledge this has not yet been examined, it seems highly likely that nutritional stress may also modulate the ability of bees to cope with pesticides, and this may explain in part why the observed LD_{50} of toxins in bees is highly variable across studies (*65*).

In summary, stressors do not act in isolation. Bees of all species are likely to encounter multiple stressors during their lives, and each is likely to reduce the ability of bees to cope with the others. A bee or bee colony that appears to have succumbed to a pathogen may not have died if it had not also been exposed to a sublethal dose of a pesticide and/or been subject to food stress (which might in turn be due to drought or heavy rain induced by climate change, or competition from a high density of honey bee hives placed nearby). Unfortunately, conducting well-replicated studies of the effects of multiple interacting stressors on bee colonies is exceedingly difficult. The number of stressor combinations rapidly becomes large, and exposure to stressors is hard or impossible to control with free-flying bees. Nonetheless, a strong argument can be made that it is the interaction among parasites, pesticides, and diet that lies at the heart of current bee health problems.

Sustainable pollination into the future

There is universal agreement that we must ensure adequate pollinator populations into the future if we wish to continue to grow a diversity of insect-pollinated crops and also ensure the integrity of natural ecosystems. It is also clear that moving toward heavy reliance on only a few species of managed pollinators, such as honey bees or one or two species of bumblebee, runs the risk of supply failure; for example, should honey bee stocks in North America fall much further, the viability of almond production in California would be threatened (*133*). Wild pollinators provide a

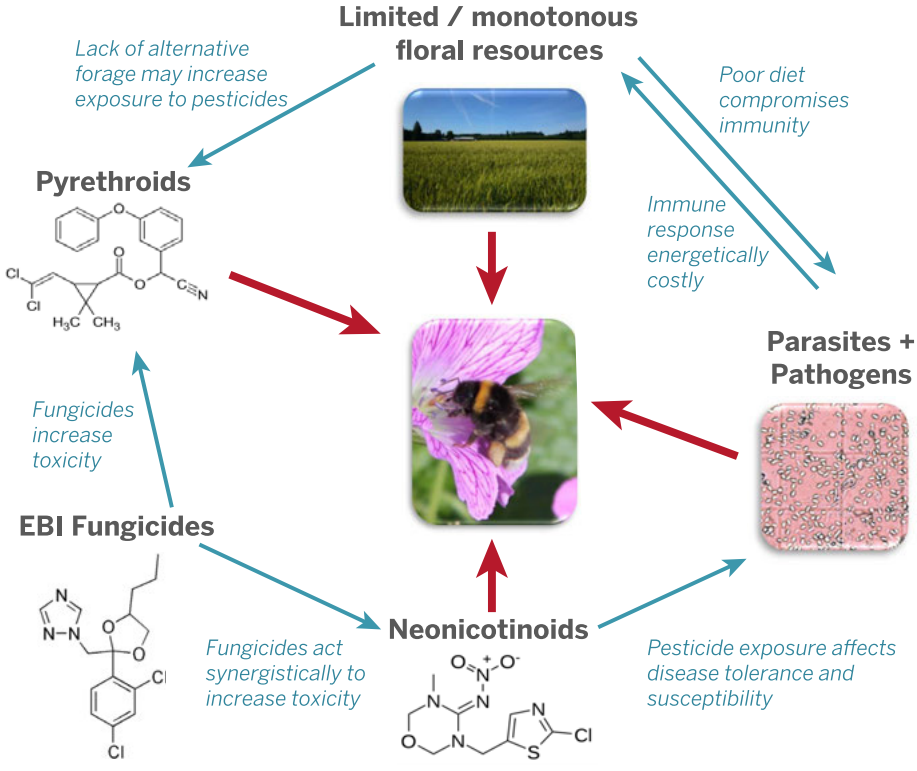

Fig. 3. Both wild and managed bees are subject to a number of significant and interacting stressors. For example, exposure to some fungicides can greatly increase toxicity of insecticides (*110*–*112*), whereas exposure to insecticides reduces resistance to diseases (*115*–*123*, *125*, *126*). Dietary stresses are likely to reduce the ability of bees to cope with both toxins and pathogens (*127*–*129*). [Photo: Beth Nicholls; Flickr Commons, *AJC1*]

service that is largely free and globally already contributes to the majority of crop pollination (*24*, *25*, *134*, *135*). Maintaining a diversity of pollinator species improves crop success via functional complementarity; different species visit different parts of the crop or crop plant, at different times of the day or year, and respond differently to environmental perturbations (*1*, *136*–*141*). A diversity of pollinators can buffer impacts of climate change that might otherwise result in a mismatch in phenology of pollinators with the flowering of crops (*104*). It is thus essential that we take steps to conserve a broad community of pollinators in farmland.

Fortunately, although the causes of pollinator ill health may be complex and varied, conserving pollinators need not be difficult or expensive. If we accept that declines are due to interacting stressors, then it follows logically that removing or reducing any of the stressors we have described is likely to benefit bee populations. Measures can be taken that are likely to simultaneously benefit a broad suite of species, both domesticated and wild.

Increasing abundance, diversity, and continuity of floral resources

Schemes such as the sowing of flower-rich field margins or hedgerows, or retaining patches of seminatural habitat among or near farmland, provide clear benefits to bee diversity and abundance (*30*, *141*–*148*) (Fig. 4A). This in turn increases pollination to nearby crops and provides an economic incentive to farmers growing insect-pollinated crops (*149*). Many countries also offer financial incentives to farmers for taking measures to boost biodiversity that help to offset implementation and opportunity costs. However, take-up of schemes to boost pollinators remains low in most countries, perhaps reflecting a lack of understanding of the economic and environmental benefits or a lack of familiarity with implementation of such measures. Education and outreach in this area could pay great dividends for pollinator conservation.

Planting of appropriate flowers in gardens and amenity areas can also contribute to pollinator conservation (*150*, *151*) (Fig. 4B). There is evidence that urban areas can support higher populations of some pollinators than farmland [e.g., (*36*)] and can boost bee numbers in adjacent farmland (*58*). Many lists of bee- or wildlife-friendly flowers are available on the Internet, but they tend to be based on anecdote rather than evidence, and there is a need to develop regionally appropriate, evidence-based advice as to the best plants to grow (*152*).

Providing nest sites

Wild bees use a diversity of habitats for nesting, including burrowing into bare soil and using existing cavities underground, holes in wood, or hollow plant stems. Seminatural habitats, hedgerows, and permanently uncropped field margins allow for many of these; hence, schemes to boost floral diversity are also likely to boost nesting opportunities (*141*). Additional nest sites can also be provided by providing bundles of hollow reeds or canes, or patches of bare soil (*153*).

Reducing exposure to pesticides

Bees are currently chronically exposed to a cocktail of pesticides, some of which act synergistically. Since the late 1990s, the cost of pesticides has fallen markedly relative to labor and fuel costs and the value of the crops (*154*). As a result, current levels of pesticide use are generally high and are not always justified by evidence that they are necessary to maintain yield (*66*, *155*). The widespread prophylactic use of systemic insecticides (such as neonicotinoids) as seed dressings exposes bees and other nontarget wildlife, results in accumulation of pesticides in the environment, and places strong selection pressure on pests to evolve resistance. A return to the principles of integrated pest management (IPM) (*156*), which depends on preventive methods such as crop rotation and views the use of pesticides as a last resort in the battle against insect pests, could greatly reduce exposure of bees, benefit the environment, and improve farming profitability. Some European countries have independently developed national pesticide reduction programs (*156*), and the European Union Sustainable Use of Pesticides Directive 2009/128/EC required member states to implement national action plans to minimize pesticide use by January 2014. In most EU member states, this directive appears to have had little or no impact on farming practices.

Current risk assessment procedures, which examine the short-term impact of a single pesticide in isolation, are clearly not adequate to encapsulate the true scenario faced by bees living in farmland. Improvements are needed to make them more realistic while keeping the cost of regulatory tests affordable, posing a considerable challenge to the ingenuity of scientists and regulators.

The EU moratorium on the use of three neonicotinoids (which started in December 2013) is an attempt to use policy change to reduce exposure of bees to stressors, following a review by the European Food Standards Agency (*157*–*159*) that declared neonicotinoids an "unacceptable risk" to bees. However, if this simply leads farmers to replace neonicotinoids with other pesticides, this may not be of great benefit to bees or the environment. Funding for research and for the provision of clear, independent advice for farmers with regard to how to reduce pesticide use generally by adopting IPM practices might provide a better and more sustainable long-term solution.

Preventing further introductions of non-native bees, parasites, and pathogens

The careless disregard with which we ship bees from country to country has resulted in the irreversible spread of many serious parasites and pathogens. Strict quarantine controls should be implemented on the movement of all commercial bees, and there is an urgent need to develop means of rearing commercial bumblebees that are free from disease. Deliberate introductions of non-native bee species (such as the recent introduction of the European *B. terrestris* to South

Fig. 4. Increasing floral abundance in the landscape is very likely to benefit pollinator populations. (**A**) Schemes to boost flower abundance in farmland, such as this wildflower strip along a field margin, have been demonstrated to provide clear benefits for wild bee populations [e.g., (*140*–*145*)]. (**B**) Urban areas can support high populations of pollinators, which may spill over into neighboring farmland. Conversion of amenity grasslands in urban areas to wildflower patches has been shown to greatly boost numbers of wild pollinators (*151*).

America) should of course be prevented. The companies that rear commercial bees should bear some responsibility here and should refuse to sell bees to regions where they are not native. There is clear hypocrisy in the policies of countries that prevent importation of non-native species but allow exportation of species to places where they do not naturally occur.

Develop monitoring programs

We have good distribution maps for pollinators in some countries, particularly for bumblebees, and citizen science schemes such as Bumble Bee Watch in North America and Beewatch in the United Kingdom can help to track changes in these distributions. However, the lack of long-term data on pollinator abundance is a glaring knowledge gap that urgently needs to be filled. It will probably never be possible to monitor all pollinator species at a global scale, but it would be practical to systematically collect data on the abundance of a subset of the more abundant and economically important pollinators. Citizen science surveys can provide a cost-effective means for large-scale population monitoring; for example, the UK butterfly monitoring scheme uses volunteers to walk regular transects using a standard methodology to count the butterflies seen, and has generated a large and long-term data set that has provided powerful insights into insect population change (*160*, *161*). Beewalks, a similar scheme to count bumblebees, has been launched by the Bumblebee Conservation Trust to obtain population data for bumblebees in the United Kingdom, although it is still in its infancy. In the United States, the Great Sunflower Project asks volunteers to count pollinators in flower patches in their local area. However, such schemes are limited by the taxonomic skills of volunteers, particularly for the many pollinator taxa that are hard or impossible to identify in the field. LeBuhn *et al.* (*162*) argue that a pan-trapping network, which could use citizen scientists to place out the traps but experts to identify the catch, would be the most cost-effective means for monitoring a large cross section of pollinator species on a large geographic scale. Indeed, for a relatively modest sum, it would be possible to set up an international pan-trapping network to monitor pollinators, following a standard methodology. Until good population data become available, we cannot identify species or regions under most threat and hence we cannot prioritize management.

In the absence of pollinator monitoring, we have no early warning system to tell us how close we may be to a pollination crisis. With a growing human population and rapid growth in global demand for pollination services, we cannot afford to see crop yields begin to fall, and we would be well advised to take preemptive action to ensure that we have adequate pollination services into the future.

REFERENCES AND NOTES

1. A.-M. Klein, I. Steffan-Dewenter, T. Tscharntke, Fruit set of highland coffee increases with the diversity of pollinating bees. *Proc. R. Soc. B* **270**, 955–961 (2003). doi: 10.1098/rspb.2002.2306; pmid: 12803911
2. N. Gallai, J.-M. Salles, J. Settele, B. E. Vaissière, Economic valuation of the vulnerability of world agriculture confronted with pollinator decline. *Ecol. Econ.* **68**, 810–821 (2009). doi: 10.1016/j.ecolecon.2008.06.014
3. C. Holden, Report warns of looming pollination crisis in North America. *Science* **314**, 397 (2006). doi: 10.1126/science.314.5798.397; pmid: 17053115
4. M. Gross, Bee gloom deepens. *Curr. Biol.* **18**, 1073 (2008). doi: 10.1016/j.cub.2008.11.013
5. S. G. Potts *et al.*, Declines of managed honey bees and beekeepers in Europe. *J. Apic. Res.* **49**, 15–22 (2010). doi: 10.3896/IBRA.1.49.1.02
6. National Resource Council, *Status of Pollinators in North America* (National Academies Press, Washington, DC, 2007).
7. D. van Engelsdorp, J. Hayes Jr., R. M. Underwood, J. Pettis, A survey of honey bee colony losses in the U.S., fall 2007 to spring 2008. *PLOS ONE* **3**, e4071 (2008). pmid: 19115015
8. M. A. Aizen, L. D. Harder, The global stock of domesticated honey bees is growing slower than agricultural demand for pollination. *Curr. Biol.* **19**, 915–918 (2009). doi: 10.1016/j.cub.2009.03.071; pmid: 19427214
9. D. Van Engelsdorp *et al.*, Colony collapse disorder: A descriptive study. *PLOS ONE* **4**, e6481 (2009). doi: 10.1371/journal.pone.0006481; pmid: 19649264
10. K. M. Smith *et al.*, Pathogens, pests, and economics: Drivers of honey bee colony declines and losses. *EcoHealth* **10**, 434–445 (2013). doi: 10.1007/s10393-013-0870-2 pmid: 24496582
11. D. Goulson, G. C. Lye, B. Darvill, Decline and conservation of bumble bees. *Annu. Rev. Entomol.* **53**, 191–208 (2008). doi: 10.1146/annurev.ento.53.103106.093454; pmid: 17803456
12. A. Kosior *et al.*, The decline of the bumble bees and cuckoo bees (Hymenoptera: Apidae: Bombini) of Western and Central Europe. *Oryx* **41**, 79–88 (2007). doi: 10.1017/S0030605307001597
13. P. H. Williams, J. L. Osborne, Bumblebee vulnerability and conservation world-wide. *Apidologie* **40**, 367–387 (2009). doi: 10.1051/apido/2009025
14. P. H. Williams, R. W. Thorp, L. L. Richardson, S. R. Colla, *Bumble Bees of North America: An Identification Guide* (Princeton Univ. Press, Princeton, NJ, 2014).
15. J. C. Grixti, L. T. Wong, S. A. Cameron, C. Favret, Decline of bumble bees (*Bombus*) in the North American Midwest. *Biol. Conserv.* **142**, 75–84 (2009). doi: 10.1016/j.biocon.2008.09.027
16. R. Schmid-Hempel *et al.*, The invasion of southern South America by imported bumblebees and associated parasites. *J. Anim. Ecol.* **83**, 823–837 (2013). doi: 10.1111/1365-2656.12185; pmid: 24256429
17. Z. Xie, P. H. Williams, Y. Tang, The effect of grazing on bumblebees in the high rangelands of the eastern Tibetan Plateau of Sichuan. *J. Insect Conserv.* **12**, 695–703 (2008). doi: 10.1007/s10841-008-9180-3
18. P. Williams, Y. Tang, J. Yao, S. Cameron, The bumblebees of Sichuan (Hymenoptera: Apidae, Bombini). *Syst. Biodivers.* **7**, 101–189 (2009). doi: 10.1017/S1477200008002843
19. C. Matsumura, J. Yokoyama, I. Washitani, Invasion status and potential ecological impacts of an invasive alien bumblebee, *Bombus terrestris* L. (Hymenoptera: Apidae) naturalized in Southern Hokkaido, Japan. *Glob. Environ. Res.* **8**, 51–66 (2004).
20. M. N. Inoue, J. Yokoyama, I. Washitani, Displacement of Japanese native bumblebees by the recently introduced *Bombus terrestris* (L.) (Hymenoptera: Apidae). *J. Insect Conserv.* **12**, 135–146 (2008). doi: 10.1007/s10841-007-9071-z
21. L. G. Carvalheiro *et al.*, Species richness declines and biotic homogenisation have slowed down for NW-European pollinators and plants. *Ecol. Lett.* **16**, 870–878 (2013). doi: 10.1111/ele.12121; pmid: 23692632
22. J. C. Biesmeijer *et al.*, Parallel declines in pollinators and insect-pollinated plants in Britain and the Netherlands. *Science* **313**, 351–354 (2006). doi: 10.1126/science.1127863; pmid: 16857940
23. L. A. Burkle, J. C. Marlin, T. M. Knight, Plant-pollinator interactions over 120 years: Loss of species, co-occurrence, and function. *Science* **339**, 1611–1615 (2013). pmid: 23449999
24. T. D. Breeze, P. Bailey, K. G. Balcombe, S. G. Potts, Pollination services in the UK: How important are honeybees? *Agric. Ecosyst. Environ.* **142**, 137–143 (2011). doi: 10.1016/j.agee.2011.03.020
25. L. A. Garibaldi *et al.*, Wild pollinators enhance fruit set of crops regardless of honey bee abundance. *Science* **339**, 1608–1611 (2013). doi: 10.1126/science.1230200; pmid: 23449997
26. R. E. Mallinger, C. Gratton, Species richness of wild bees, but not the use of managed honeybees, increases fruit set of a pollinator-dependent crop. *J. Appl. Ecol.* 10.1111/1365-2664.12377 (2014). doi: 10.1111/1365-2664.12377
27. C. A. Kearns, D. W. Inouye, N. M. Waser, Endangered mutalisms: The conservation of plant-pollinator interactions. *Annu. Rev. Ecol. Syst.* **29**, 83–112 (1998). doi: 10.1146/annurev.ecolsys.29.1.83
28. M. A. Aizen, L. A. Garibaldi, S. A. Cunningham, A. M. Klein, Long-term global trends in crop yield and production reveal no current pollination shortage but increasing pollinator dependency. *Curr. Biol.* **18**, 1572–1575 (2008). doi: 10.1016/j.cub.2008.08.066; pmid: 18926704
29. L. A. Garibaldi, M. A. Aizen, A. M. Klein, S. A. Cunningham, L. D. Harder, Global growth and stability of agricultural yield decrease with pollinator dependence. *Proc. Natl. Acad. Sci. U.S.A.* **108**, 5909–5914 (2011). doi: 10.1073/pnas.1012431108; pmid: 21422295
30. L. A. Garibaldi *et al.*, Stability of pollination services decreases with isolation from natural areas despite honey bee visits. *Ecol. Lett.* **14**, 1062–1072 (2011). doi: 10.1111/j.1461-0248.2011.01669.x; pmid: 21806746
31. M. J. F. Brown, R. J. Paxton, The conservation of bees: A global perspective. *Apidologie* **40**, 410–416 (2009). doi: 10.1051/apido/2009019
32. S. G. Potts *et al.*, Global pollinator declines: Trends, impacts and drivers. *Trends Ecol. Evol.* **25**, 345–353 (2010). doi: 10.1016/j.tree.2010.01.007; pmid: 20188434
33. A. J. Vanbergen, I. P. Initiative, Threats to an ecosystem service: Pressures on pollinators. *Front. Ecol. Environ* **11**, 251–259 (2013). doi: 10.1890/120126
34. D. C. Howard, J. W. Watkins, R. T. Clarke, C. L. Barnett, G. J. Stark, Estimating the extent and change in broad habitats in Great Britain. *J. Environ. Manage.* **67**, 219–227 (2003). doi: 10.1016/S0301-4797(02)00175-5; pmid: 12667472
35. F. Samson, F. Knopf, Prairie conservation in North America. *Bioscience* **44**, 418–421 (1994). doi: 10.2307/1312365
36. J. L. Osborne *et al.*, Quantifying and comparing bumblebee nest densities in gardens and countryside habitats. *J. Appl. Ecol.* **45**, 784–792 (2008). doi: 10.1111/j.1365-2664.2007.01359.x
37. A. J. Bates *et al.*, Changing bee and hoverfly pollinator assemblages along an urban-rural gradient. *PLOS ONE* **6**, e23459 (2011). doi: 10.1371/journal.pone.0023459; pmid: 21858128
38. P. Skórka, M. Lenda, D. Moroń, K. Kalarus, P. Tryjanowski, Factors affecting road mortality and the suitability of road verges for butterflies. *Biol. Conserv.* **159**, 148–157 (2013). doi: 10.1016/j.biocon.2012.12.028
39. E. Genersch, American foulbrood in honeybees and its causative agent, *Paenibacillus* larvae. *J. Invertebr. Pathol.* **103** (suppl. 1), S10–S19 (2010). doi: 10.1016/j.jip.2009.06.015
40. E. Genersch, C. Yue, I. Fries, J. R. de Miranda, Detection of deformed wing virus, a honey bee viral pathogen, in bumble bees (*Bombus terrestris* and *Bombus pascuorum*) with wing deformities. *J. Invertebr. Pathol.* **91**, 61–63 (2006). doi: 10.1016/j.jip.2005.10.002; pmid: 16300785
41. P. Graystock, K. Yates, B. Darvill, D. Goulson, W. O. H. Hughes, Emerging dangers: Deadly effects of an emergent parasite in a new pollinator host. *J. Invertebr. Pathol.* **114**, 114–119 (2013). doi: 10.1016/j.jip.2013.06.005; pmid: 23816821
42. P. Rosenkranz, P. Aumeier, B. Ziegelmann, Biology and control of *Varroa destructor*. *J. Invertebr. Pathol.* **103** (suppl. 1), S96–S119 (2010). doi: 10.1016/j.jip.2009.07.016
43. F. Nazzi *et al.*, Synergistic parasite-pathogen interactions mediated by host immunity can drive the collapse of honeybee colonies. *PLOS Pathog.* **8**, e1002735 (2012). doi: 10.1371/journal.ppat.1002735; pmid: 22719246
44. J. Klee *et al.*, Widespread dispersal of the microsporidian *Nosema ceranae*, an emergent pathogen of the western honey bee, *Apis mellifera*. *J. Invertebr. Pathol.* **96**, 1–10 (2007). doi: 10.1016/j.jip.2007.02.014; pmid: 17428493
45. Y. Chen, J. D. Evans, I. B. Smith, J. S. Pettis, *Nosema ceranae* is a long-present and wide-spread microsporidian infection of the European honey bee (*Apis mellifera*) in the United States. *J. Invertebr. Pathol.* **97**, 186–188 (2008). doi: 10.1016/j.jip.2007.07.010; pmid: 17880997
46. J. Li *et al.*, Diversity of *Nosema* associated with bumblebees (*Bombus* spp.) from China. *Int. J. Parasitol.* **42**, 49–61 (2012). doi: 10.1016/j.ijpara.2011.10.005; pmid: 22138016

47. S. Plischuk *et al*., South American native bumblebees (Hymenoptera: Apidae) infected by *Nosema ceranae* (Microsporidia), an emerging pathogen of honeybees (*Apis mellifera*). *Environ. Microbiol. Rep.* **1**, 131–135 (2009). doi: 10.1111/j.1758-2229.2009.00018.x; pmid: 23765744
48. J. Ravoet *et al*., Widespread occurrence of honey bee pathogens in solitary bees. *J. Invertebr. Pathol.* **122**, 55–58 (2014). doi: 10.1016/j.jip.2014.08.007; pmid: 25196470
49. S. Spiewok, P. Neumann, Infestation of commercial bumblebee (*Bombus impatiens*) field colonies by small hive beetles (*Aethina tumida*). *Ecol. Entomol.* **31**, 623–628 (2006). doi: 10.1111/j.1365-2311.2006.00827.x
50. D. Hoffmann, J. S. Pettis, P. Neumann, Potential host shift of the small hive beetle (*Aethina tumida*) to bumblebee colonies (*Bombus impatiens*). *Insectes Soc.* **55**, 153–162 (2008). doi: 10.1007/s00040-008-0982-9
51. S. A. Cameron *et al*., Patterns of widespread decline in North American bumble bees. *Proc. Natl. Acad. Sci. U.S.A.* **108**, 662–667 (2011). doi: 10.1073/pnas.1014743108; pmid: 21199943
52. I. Meeus, M. J. F. Brown, D. C. De Graaf, G. Smagghe, Effects of invasive parasites on bumble bee declines. *Conserv. Biol.* **25**, 662–671 (2011). doi: 10.1111/j.1523-1739.2011.01707.x; pmid: 21771075
53. M. P. Arbetman, I. Meeus, C. L. Morales, M. A. Aizen, G. Smagghe, Alien parasite hitchhikes to Patagonia on invasive bumblebee. *Biol. Invasions* **15**, 489–494 (2013). doi: 10.1007/s10530-012-0311-0
54. S. R. Colla, M. C. Otterstatter, R. J. Gegear, J. D. Thomson, Plight of the bumble bee: Pathogen spillover from commercial to wild populations. *Biol. Conserv.* **129**, 461–467 (2006). doi: 10.1016/j.biocon.2005.11.013
55. M. C. Otterstatter, J. D. Thomson, Does pathogen spillover from commercially reared bumble bees threaten wild pollinators? *PLOS ONE* **3**, e2771 (2008). doi: 10.1371/journal.pone.0002771
56. M. Yoneda, H. Furuta, K. Tsuchida, K. Okabe, K. Goka, Commercial colonies of *Bombus terrestris* (Hymenopter: Apidae) are reservoirs of the tracheal mite *Locustacarus buchneri* (Acari: Podapolipidae). *Appl. Entomol. Zool.* **43**, 73–76 (2008). doi: 10.1303/aez.2008.73
57. D. Goulson, Effects of introduced bees on native ecosystems. *Annu. Rev. Ecol. Evol. Syst.* **34**, 1–26 (2003). doi: 10.1146/annurev.ecolsys.34.011802.132355
58. D. Goulson *et al*., Effects of land use at a landscape scale on bumblebee nest density and survival. *J. Appl. Ecol.* **47**, 1207–1215 (2010). doi: 10.1111/j.1365-2664.2010.01872.x
59. L. A. Morandin, M. L. Winston, Wild bee abundance and seed production in conventional, organic, and genetically modified canola. *Ecol. Appl.* **15**, 871–881 (2005). doi: 10.1890/03-5271
60. M. P. Chauzat *et al*., A survey of pesticide residues in pollen loads collected by honey bees in France. *J. Econ. Entomol.* **99**, 253–262 (2006). doi: 10.1093/jee/99.2.253; pmid: 16686121
61. F. Sanchez-Bayo, K. Goka, Pesticide residues and bees—a risk assessment. *PLOS ONE* **9**, e94482 (2014). doi: 10.1371/journal.pone.0094482; pmid: 24718419
62. C. A. Mullin *et al*., High levels of miticides and agrochemicals in North American apiaries: Implications for honey bee health. *PLOS ONE* **5**, e9754 (2010). doi: 10.1371/journal.pone.0009754; pmid: 20333298
63. C. H. Krupke, G. J. Hunt, B. D. Eitzer, G. Andino, K. Given, Multiple routes of pesticide exposure for honey bees living near agricultural fields. *PLOS ONE* **7**, e29268 (2012). doi: 10.1371/journal.pone.0029268; pmid: 22235278
64. D. Paradis, G. Bérail, J. M. Bonmatin, L. P. Belzunces, Sensitive analytical methods for 22 relevant insecticides of 3 chemical families in honey by GC-MS/MS and LC-MS/MS. *Anal. Bioanal. Chem.* **406**, 621–633 (2014). doi: 10.1007/s00216-013-7483-z; pmid: 24253411
65. L. W. Pisa *et al*., Effects of neonicotinoids and fipronil on non-target invertebrates. *Environ. Sci. Pollut. Res. Int.* **22**, 68–102 (2015). pmid: 25223353
66. D. Goulson, An overview of the environmental risks posed by neonicotinoid insecticides. *J. Appl. Ecol.* **50**, 977–987 (2013). doi: 10.1111/1365-2664.12111
67. M. Tomizawa, J. E. Casida, Neonicotinoid insecticide toxicology: Mechanisms of selective action. *Annu. Rev. Pharmacol. Toxicol.* **45**, 247–268 (2005). doi: 10.1146/annurev.pharmtox.45.120403.095930; pmid: 15822177
68. S. Suchail, D. Guez, L. P. Belzunces, Characteristics of imidacloprid toxicity in two *Apis mellifera* subspecies. *Environ. Toxicol. Chem.* **19**, 1901–1905 (2000). doi: 10.1897/1551-5028(2000)019<1901:COITIT>2.3.CO;2
69. G. Rondeau *et al*., Delayed and time-cumulative toxicity of imidacloprid in bees, ants and termites. *Sci. Rep.* **4**, 5566 (2014). doi: 10.1038/srep05566; pmid: 24993452
70. E. C. Yang, Y. C. Chuang, Y. L. Chen, L. H. Chang, Abnormal foraging behavior induced by sublethal dosage of imidacloprid in the honey bee (Hymenoptera: Apidae). *J. Econ. Entomol.* **101**, 1743–1748 (2008). doi: 10.1603/0022-0493-101.6.1743; pmid: 19133451
71. V. Mommaerts *et al*., Risk assessment for side-effects of neonicotinoids against bumblebees with and without impairing foraging behavior. *Ecotoxicology* **19**, 207–215 (2010). doi: 10.1007/s10646-009-0406-2; pmid: 19757031
72. M. Henry *et al*., A common pesticide decreases foraging success and survival in honey bees. *Science* **336**, 348–350 (2012). doi: 10.1126/science.1215039; pmid: 22461498
73. H. Feltham, K. Park, D. Goulson, Field realistic doses of pesticide imidacloprid reduce bumblebee pollen foraging efficiency. *Ecotoxicology* **23**, 317–323 (2014). doi: 10.1007/s10646-014-1189-7; pmid: 24448674
74. P. Han, C. Y. Niu, C. L. Lei, J. J. Cui, N. Desneux, Quantification of toxins in a Cry1Ac + CpTI cotton cultivar and its potential effects on the honey bee *Apis mellifera* L. *Ecotoxicology* **19**, 1452–1459 (2010). doi: 10.1007/s10646-010-0530-z; pmid: 20700762
75. E. C. Yang, H. C. Chang, W. Y. Wu, Y. W. Chen, Impaired olfactory associative behavior of honeybee workers due to contamination of imidacloprid in the larval stage. *PLOS ONE* **7**, e49472 (2012). doi: 10.1371/journal.pone.0049472; pmid: 23166680
76. P. R. Whitehorn, S. O'Connor, F. L. Wackers, D. Goulson, Neonicotinoid pesticide reduces bumble bee colony growth and queen production. *Science* **336**, 351–352 (2012). doi: 10.1126/science.1215025; pmid: 22461500
77. G. C. Cutler, C. D. Scott-Dupree, Exposure to clothianidin seed-treated canola has no long-term impact on honey bees. *J. Econ. Entomol.* **100**, 765–772 (2007). doi: 10.1603/0022-0493(2007)100[765:ETCSCH]2.0.CO;2; pmid: 17598537
78. E. Pilling, P. Campbell, M. Coulson, N. Ruddle, I. Tornier, A four-year field program investigating long-term effects of repeated exposure of honey bee colonies to flowering crops treated with thiamethoxam. *PLOS ONE* **8**, e77193 (2013). doi: 10.1371/journal.pone.0077193; pmid: 24194871
79. I. London-Shafir, S. Shafir, D. Eisikowitch, Amygdalin in almond nectar and pollen-facts and possible roles. *Plant Syst. Evol.* **238**, 87–95 (2003).
80. R. G. Stanley, H. F. Linskens, *Pollen: Biology, Biochemistry, Management* (Springer-Verlag, Berlin, 1974).
81. T. H. Roulston, S. L. Buchmann, A phylogenetic reconsideration of the pollen starch-pollination correlation. *Evol. Ecol. Res.* **2**, 627–643 (2000).
82. M. E. Hanley, M. Franco, S. Pichon, B. Darvill, D. Goulson, Breeding system, pollinator choice and variation in pollen quality in British herbaceous plants. *Funct. Ecol.* **22**, 592–598 (2008). doi: 10.1111/j.1365-2435.2008.01415.x
83. G. A. Wright *et al*., Caffeine in floral nectar enhances a pollinator's memory of reward. *Science* **339**, 1202–1204 (2013). doi: 10.1126/science.1228806; pmid: 23471406
84. W. Mao, M. A. Schuler, M. R. Berenbaum, Honey constituents up-regulate detoxification and immunity genes in the western honey bee *Apis mellifera*. *Proc. Natl. Acad. Sci. U.S.A.* **110**, 8842–8846 (2013). doi: 10.1073/pnas.1303884110; pmid: 23630255
85. A. Maurizio, The influence of pollen feeding and brood rearing on the length of life and physiological condition of the honeybee. *Bee World* **31**, 9–12 (1950).
86. L. N. Standifer, A comparison of the protein quality of pollens for growth-stimulation of the hypopharyngeal glands and longevity of honey bees, *Apis mellifera* L. (Hymenoptera: Apidae). *Insectes Soc.* **14**, 415–425 (1967). doi: 10.1007/BF02223687
87. L. S. Schmidt, J. O. Schmidt, H. Rao, W. Wang, L. Xu, Feeding preference and survival of young worker honeybees (Hymenoptera: Apidae) fed rape, sesame, and sunflower pollen. *J. Econ. Entomol.* **88**, 1591–1595 (1995). doi: 10.1093/jee/88.6.1591
88. G. Di Pasquale *et al*., Influence of pollen nutrition on honey bee health: Do pollen quality and diversity matter? *PLOS ONE* **8**, e72016 (2013). doi: 10.1371/journal.pone.0072016; pmid: 23940803
89. M. M. Morais *et al*., Evaluation of inexpensive pollen substitute diets through quantification of haemolymph proteins. *J. Apic. Res.* **52**, 119–121 (2013). doi: 10.3896/IBRA.1.52.3.01
90. R. Kumar, R. C. Mishra, O. P. Agrawal, Effect of feeding artificial diets to honey bees during dearth period under Panchkula (Haryana) conditions. *J. Entomol. Res.* **37**, 41–46 (2013).
91. M. E. Knight *et al*., Bumblebee nest density and the scale of available forage in arable landscapes. *Insect Conserv. Divers.* **2**, 116–124 (2009). doi: 10.1111/j.1752-4598.2009.00049.x
92. C. Westphal, I. Steffan-Dewenter, T. Tscharntke, Mass flowering oilseed rape improves early colony growth but not sexual reproduction of bumblebees. *J. Appl. Ecol.* **46**, 187–193 (2009). doi: 10.1111/j.1365-2664.2008.01580.x
93. F. Jauker, F. Peter, V. Wolters, T. Diekötter, Early reproductive benefits of mass-flowering crops to the solitary bee *Osmia rufa* outbalance post-flowering disadvantages. *Basic Appl. Ecol.* **13**, 268–276 (2012). doi: 10.1016/j.baae.2012.03.010
94. A. Holzschuh, C. F. Dormann, T. Tscharntke, I. Steffan-Dewenter, Mass-flowering crops enhance wild bee abundance. *Oecologia* **172**, 477–484 (2013). doi: 10.1007/s00442-012-2515-5; pmid: 23114428
95. F. Herrmann, C. Westphal, R. F. A. Moritz, I. Steffan-Dewenter, Genetic diversity and mass resources promote colony size and forager densities of a social bee (*Bombus pascuorum*) in agricultural landscapes. *Mol. Ecol.* **16**, 1167–1178 (2007). doi: 10.1111/j.1365-294X.2007.03226.x; pmid: 17391404
96. A. Kovács-Hostyánszki *et al*., Contrasting effects of mass-flowering crops on bee pollination of hedge plants at different spatial and temporal scales. *Ecol. Appl.* **23**, 1938–1946 (2013). doi: 10.1890/12-2012.1; pmid: 24555319
97. W. D. Yates, A review of infectious bovine rhinotracheitis, shipping fever pneumonia and viral-bacterial synergism in respiratory disease of cattle. *Can. J. Comp. Med.* **46**, 225–263 (1982). pmid: 6290011
98. T. Bakonyi, R. Farkas, A. Szendrői, M. Dobos-Kovács, M. Rusvai, Detection of acute bee paralysis virus by RT-PCR in honey bee and *Varroa destructor* field samples: Rapid screening of representative Hungarian apiaries. *Apidologie* **33**, 63–74 (2002). doi: 10.1051/apido:2001004
99. M. L. Forup, J. Memmott, The relationship between the abundance of bumblebees and honeybees in a native habitat. *Ecol. Entomol.* **30**, 47–57 (2005). doi: 10.1111/j.0307-6946.2005.00660.x
100. K. Walther-Hellwig *et al*., Increased density of honeybee colonies affects foraging bumblebees. *Apidologie* **37**, 517–532 (2006). doi: 10.1051/apido:2006035
101. D. Goulson, K. R. Sparrow, Evidence for competition between honeybees and bumblebees; effects on bumblebee worker size. *J. Insect Conserv.* **13**, 177–181 (2008). doi: 10.1007/s10841-008-9140-y
102. D. M. Thomson, Detecting the effects of introduced species: A case study of competition between *Apis* and *Bombus*. *Oikos* **114**, 407–418 (2006). doi: 10.1111/j.2006.0030-1299.14604.x
103. P. Willmer, Pollinator-plant synchrony tested by climate change. *Curr. Biol.* **22**, R131–R132 (2012). doi: 10.1016/j.cub.2012.01.009; pmid: 22361150
104. I. Bartomeus *et al*., Biodiversity ensures plant-pollinator phenological synchrony against climate change. *Ecol. Lett.* **16**, 1331–1338 (2013). doi: 10.1111/ele.12170; pmid: 23968538
105. M. L. Forister *et al*., Compounded effects of climate change and habitat alteration shift patterns of butterfly diversity. *Proc. Natl. Acad. Sci. U.S.A.* **107**, 2088–2092 (2010). doi: 10.1073/pnas.0909686107; pmid: 20133854
106. E. F. Ploquin, J. M. Herrera, J. R. Obeso, Bumblebee community homogenization after uphill shifts in montane areas of northern Spain. *Oecologia* **173**, 1649–1660 (2013). doi: 10.1007/s00442-013-2731-7; pmid: 23852029
107. A. Sih, A. M. Bell, J. L. Kerby, Two stressors are far deadlier than one. *Trends Ecol. Evol.* **19**, 274–276 (2004). doi: 10.1016/j.tree.2004.02.010; pmid: 16701268
108. A. Coors, L. De Meester, Synergistic, antagonistic and additive effects of multiple stressors: Predation threat, parasitism and pesticide exposure in *Daphnia magna*. *J. Appl. Ecol.* **45**, 1820–1828 (2008). doi: 10.1111/j.1365-2664.2008.01566.x
109. R. J. Gill, O. Ramos-Rodriguez, N. E. Raine, Combined pesticide exposure severely affects individual- and colony-level traits in bees. *Nature* **491**, 105–108 (2012). doi: 10.1038/nature11585; pmid: 23086150
110. R. Schmuck, T. Stadler, H. W. Schmidt, Field relevance of a synergistic effect observed in the laboratory between an EBI fungicide and a chloronicotinyl insecticide in the honeybee (*Apis mellifera* L, Hymenoptera). *Pest Manag.*

Sci. **59**, 279–286 (2003). doi: 10.1002/ps.626; pmid: 12639044
111. T. Iwasa, N. Motoyama, J. T. Ambrose, R. M. M. Roe, Mechanism for the differential toxicity of neonicotinoid insecticides in the honey bee, *Apis mellifera*. *Crop Prot.* **23**, 371–378 (2004). doi: 10.1016/j.cropro.2003.08.018
112. E. D. Pilling, P. C. Jepson, Synergism between EBI fungicides and a pyrethroid insecticide in the honeybee (*Apis mellifera*). *Pestic. Sci.* **39**, 293–297 (1993). doi: 10.1002/ps.2780390407
113. A. Decourtye *et al*., Imidacloprid impairs memory and brain metabolism in the honeybee (*Apis mellifera* L.). *Pestic. Biochem. Physiol.* **78**, 83–92 (2004). doi: 10.1016/j.pestbp.2003.10.001
114. S. M. Williamson, G. A. Wright, Exposure to multiple cholinergic pesticides impairs olfactory learning and memory in honeybees. *J. Exp. Biol.* **216**, 1799–1807 (2013). doi: 10.1242/jeb.083931; pmid: 23393272
115. C. Alaux *et al*., Interactions between *Nosema* microspores and a neonicotinoid weaken honeybees (*Apis mellifera*). *Environ. Microbiol.* **12**, 774–782 (2010). doi: 10.1111/j.1462-2920.2009.02123.x; pmid: 20050872
116. J. S. Pettis, D. vanEngelsdorp, J. Johnson, G. Dively, Pesticide exposure in honey bees results in increased levels of the gut pathogen *Nosema*. *Naturwissenschaften* **99**, 153–158 (2012). doi: 10.1007/s00114-011-0881-1; pmid: 22246149
117. C. Vidau *et al*., Exposure to sublethal doses of fipronil and thiacloprid highly increases mortality of honeybees previously infected by *Nosema ceranae*. *PLOS ONE* **6**, e21550 (2011). doi: 10.1371/journal.pone.0021550; pmid: 21738706
118. J. Aufauvre *et al*., Parasite-insecticide interactions: A case study of Nosema ceranae and fipronil synergy on honeybee. *Sci. Rep.* **2**, 326 (2012). doi: 10.1038/srep00326; pmid: 22442753
119. G. L. Baron, N. E. Raine, M. J. F. Brown, Impact of chronic exposure to a pyrethroid pesticide on bumblebees and interactions with a trypanosome parasite. *J. Appl. Ecol.* **51**, 460–469 (2014). doi: 10.1111/1365-2664.12205
120. A. Fauser-Misslin, B. M. Sadd, P. Neumann, C. Sandrock, Influence of combined pesticide and parasite exposure on bumblebee colony traits in the laboratory. *J. Appl. Ecol.* **51**, 450–459 (2014). doi: 10.1111/1365-2664.12188
121. V. Doublet, M. Labarussias, J. R. de Miranda, R. F. A. Moritz, R. J. Paxton, Bees under stress: Sublethal doses of a neonicotinoid pesticide and pathogens interact to elevate honey bee mortality across the life cycle. *Environ. Microbiol.* 10.1111/1462-2920.12426 (2014). doi: 10.1111/1462-2920.12426; pmid: 25611325
122. J. Y. Wu, M. D. Smart, C. M. Anelli, W. S. Sheppard, Honey bees (*Apis mellifera*) reared in brood combs containing high levels of pesticide residues exhibit increased susceptibility to *Nosema* (Microsporidia) infection. *J. Invertebr. Pathol.* **109**, 326–329 (2012). doi: 10.1016/j.jip.2012.01.005; pmid: 22285445
123. R. R. James, J. Xu, Mechanisms by which pesticides affect insect immunity. *J. Invertebr. Pathol.* **109**, 175–182 (2012). doi: 10.1016/j.jip.2011.12.005; pmid: 22206912
124. F. S. Brunner, P. Schmid-Hempel, S. M. Barribeau, Immune gene expression in *Bombus terrestris*: Signatures of infection despite strong variation among populations, colonies, and sister workers. *PLOS ONE* **8**, e68181 (2013). doi: 10.1371/journal.pone.0068181; pmid: 23869212
125. H. Boncristiani *et al*., Direct effect of acaricides on pathogen loads and gene expression levels in honey bees *Apis mellifera*. *J. Insect Physiol.* **58**, 613–620 (2012). doi: 10.1016/j.jinsphys.2011.12.011; pmid: 22212860
126. G. Di Prisco *et al*., Neonicotinoid clothianidin adversely affects insect immunity and promotes replication of a viral pathogen in honey bees. *Proc. Natl. Acad. Sci. U.S.A.* **110**, 18466–18471 (2013). doi: 10.1073/pnas.1314923110 pmid: 24145453
127. M. J. F. Brown, R. Loosli, P. Schmid-Hempel, Condition-dependent expression of virulence in a trypanosome infecting bumblebees. *Oikos* **91**, 421–427 (2000). doi: 10.1034/j.1600-0706.2000.910302.x
128. E. R. Tyler, S. Adams, E. B. Mallon, An immune response in the bumblebee, *Bombus terrestris* leads to increased food consumption. *BMC Physiol.* **6**, 6 (2006). doi: 10.1186/1472-6793-6-6; pmid: 16846495
129. Y. Moret, P. Schmid-Hempel, Survival for immunity: The price of immune system activation for bumblebee workers. *Science* **290**, 1166–1168 (2000). doi: 10.1126/science.290.5494.1166; pmid: 11073456
130. E. B. Mallon, A. Brockmann, P. Schmid-Hempel, Immune response inhibits associative learning in insects. *Proc. R. Soc. B* **270**, 2471–2473 (2003). doi: 10.1098/rspb.2003.2456; pmid: 14667337
131. C. E. Riddell, E. B. Mallon, Insect psychoneuroimmunology: Immune response reduces learning in protein starved bumblebees (*Bombus terrestris*). *Brain Behav. Immun.* **20**, 135–138 (2006). doi: 10.1016/j.bbi.2005.06.008; pmid: 16084688
132. A. Alghamdi, L. Dalton, A. Phillis, E. Rosato, E. B. Mallon, Immune response impairs learning in free-flying bumblebees. *Biol. Lett.* **4**, 479–481 (2008). doi: 10.1098/rsbl.2008.0331; pmid: 18628116
133. D. Van Engelsdorp, M. D. Meixner, A historical review of managed honey bee populations in Europe and the United States and the factors that may affect them. *J. Invertebr. Pathol.* **103** (suppl. 1), S80–S95 (2010). doi: 10.1016/j.jip.2009.06.011; pmid: 19909973
134. R. Winfree, C. Kremen, Are ecosystem services stabilized by differences among species? A test using crop pollination. *Proc. R. Soc. B* **276**, 229–237 (2009). doi: 10.1098/rspb.2008.0709; pmid: 18796401
135. R. Rader, B. G. Howlett, S. A. Cunningham, D. A. Westcott, W. Edwards, Spatial and temporal variation in pollinator effectiveness: Do unmanaged insects provide consistent pollination services to mass flowering crops? *J. Appl. Ecol.* **49**, 126–134 (2012). doi: 10.1111/j.1365-2664.2011.02066.x
136. P. Hoehn, T. Tscharntke, J. M. Tylianakis, I. Steffan-Dewenter, Functional group diversity of bee pollinators increases crop yield. *Proc. R. Soc. B* **275**, 2283–2291 (2008). pmid: 18595841
137. J. K. Tuell, R. Isaacs, Community and species-specific responses of wild bees to insect pest control programs applied to a pollinator-dependent crop. *J. Econ. Entomol.* **103**, 668–675 (2010). doi: 10.1603/EC09314; pmid: 20568612
138. N. Blüthgen, A. M. Klein, Functional complementarity and specialisation: The role of biodiversity in plant-pollinator interactions. *Basic Appl. Ecol.* **12**, 282–291 (2011). doi: 10.1016/j.baae.2010.11.001
139. C. Brittain, N. Williams, C. Kremen, A. Klein, Synergistic effects of non-*Apis* bees and honey bees for pollination services. *Proc. R. Soc. B* **280**, 20122767 (2013). doi: 10.1098/rspb.2012.2767
140. I. Steffan-Dewenter, U. Münzenberg, C. Bürger, C. Thies, T. Tscharntke, Scale-dependent effects of landscape context on three pollinator guilds. *Ecology* **83**, 1421–1432 (2002). doi: 10.1890/0012-9658(2002)083[1421:SDEOLC]2.0.CO;2
141. L. A. Garibaldi *et al*., From research to action: Enhancing crop yield through wild pollinators. *Front. Ecol. Environ.* **12**, 439–447 (2014). doi: 10.1890/130330
142. R. F. Pywell *et al*., Effectiveness of new agri-environment schemes in providing foraging resources for bumblebees in intensively farmed landscapes. *Biol. Conserv.* **129**, 192–206 (2006). doi: 10.1016/j.biocon.2005.10.034
143. R. F. Pywell *et al*., Providing foraging resources for bumblebees in intensively farmed landscapes. *Biol. Conserv.* **121**, 479–494 (2005). doi: 10.1016/j.biocon.2004.05.020
144. C. Carvell, W. R. Meek, R. F. Pywell, D. Goulson, M. Nowakowski, Comparing the efficacy of agri-environment schemes to enhance bumble bee abundance and diversity on arable field margins. *J. Appl. Ecol.* **44**, 29–40 (2006). doi: 10.1111/j.1365-2664.2006.01249.x
145. M. Rundlöf, H. Nilsson, H. G. Smith, Interacting effects of farming practice and landscape context on bumble bees. *Biol. Conserv.* **141**, 417–426 (2008). doi: 10.1016/j.biocon.2007.10.011
146. C. M. Kennedy *et al*., A global quantitative synthesis of local and landscape effects on wild bee pollinators in agroecosystems. *Ecol. Lett.* **16**, 584–599 (2013). doi: 10.1111/ele.12082; pmid: 23489285
147. S. D. Wratten, M. Gillespie, A. Decourtye, E. Mader, N. Desneux, Pollinator habitat enhancement: Benefits to other ecosystem services. *Agric. Ecosyst. Environ.* **159**, 112–122 (2012). doi: 10.1016/j.agee.2012.06.020
148. L. A. Morandin, M. L. Winston, V. A. Abbott, M. T. Franklin, Can pastureland increase wild bee abundance in agriculturally intense areas? *Basic Appl. Ecol.* **8**, 117–124 (2007). doi: 10.1016/j.baae.2006.06.003
149. B. R. Blaauw, R. Isaacs, Flower plantings increase wild bee abundance and the pollination services provided to a pollination-dependent crop. *J. Appl. Ecol.* **51**, 890–898 (2014). doi: 10.1111/1365-2664.12257
150. D. Goulson, *Bumblebees: Behaviour, Ecology, and Conservation* (Oxford Univ. Press, Oxford, 2010).
151. L. M. Blackmore, D. Goulson, Evaluating the effectiveness of wildflower seed mixes for boosting floral diversity and bumblebee and hoverfly abundance in urban areas. *Insect Conserv. Divers.* **7**, 480–484 (2014). doi: 10.1111/icad.12071
152. M. Garbuzov, F. L. W. Ratnieks, Quantifying variation among garden plants in attractiveness to bees and other flower-visiting insects. *Funct. Ecol.* **28**, 364–374 (2014). doi: 10.1111/1365-2435.12178
153. I. Steffan-Dewenter, S. Schiele, Do resources or natural enemies drive bee population dynamics in fragmented habitats? *Ecology* **89**, 1375–1387 (2008). doi: 10.1890/06-1323.1; pmid: 18543630
154. C. D. Osteen, J. Fernandez-Cornejo, Economic and policy issues of U.S. agricultural pesticide use trends. *Pest Manag. Sci.* **69**, 1001–1025 (2013). doi: 10.1002/ps.3529; pmid: 23483682
155. S. Stevens, P. Jenkins, "Heavy costs: Weighing the value of neonicotinoid insecticides in agriculture" (Center for Food Safety, Washington, DC, 2014).
156. B. Freier, E. F. Boller, Integrated pest management in Europe—history, policy, achievements and implementation. In *Integrated Pest Management: Dissemination and Impact*, R. Peshin, A. K. Dhawan, Eds. (Springer, New York, 2009), pp. 435–454.
157. EFSA, Conclusion on the peer review of the pesticide risk assessment for bees for the active substance thiamethoxam. *EFSA J.* **11**, 3067 (2013); www.efsa.europa.eu/en/efsajournal/pub/3067.htm.
158. EFSA, Conclusion on the peer review of the pesticide risk assessment for bees for the active substance clothianidin. *EFSA J.* **11**, 3066 (2013); www.efsa.europa.eu/en/efsajournal/pub/3066.htm.
159. EFSA, Conclusion on the peer review of the pesticide risk assessment for bees for the active substance imidacloprid. *EFSA J.* **11**, 3068 (2013); www.efsa.europa.eu/en/efsajournal/pub/3068.htm.
160. M. S. Warren *et al*., Rapid responses of British butterflies to opposing forces of climate and habitat change. *Nature* **414**, 65–69 (2001). doi: 10.1038/35102054; pmid: 11689943
161. R. M. Pateman, J. K. Hill, D. B. Roy, R. Fox, C. D. Thomas, Temperature-dependent alterations in host use drive rapid range expansion in a butterfly. *Science* **336**, 1028–1030 (2012). doi: 10.1126/science.1216980; pmid: 22628653
162. G. Lebuhn *et al*., Detecting insect pollinator declines on regional and global scales. *Conserv. Biol.* **27**, 113–120 (2013). doi: 10.1111/j.1523-1739.2012.01962.x; pmid: 23240651
163. I. Fries, F. Feng, A. da Silva, S. B. Slemenda, N. J. Pieniazek, *Nosema ceranae* n. sp. (Microspora, Nosematidae), morphological and molecular characterization of a microsporidian parasite of the Asian honey bee *Apis cerana* (Hymenoptera, Apidae). *Eur. J. Protistol.* **32**, 356–365 (1996). doi: 10.1016/S0932-4739(96)80059-9
164. M. Higes, R. Martín, A. Meana, *Nosema ceranae*, a new microsporidian parasite in honeybees in Europe. *J. Invertebr. Pathol.* **92**, 93–95 (2006). doi: 10.1016/j.jip.2006.02.005; pmid: 16574143
165. C. M. Aurori, D. S. Dezmirean, L. A. Mărghitaş, R. F. A. Moritz, *Nosema apis* and *N. ceranae* in western honeybee (*Apis mellifera*)—geographical distribution and current methods of diagnosis. *Bull. UASVM Anim. Sci. Biotechnol.* **68**, 63–70 (2011).
166. J. Roberts, D. Anderson, Establishing the disease status of the Asian honeybee in the Cairns region (Rural Industries Research and Development Corporation, RIRDC Publ. No. 13/082, RIRDC Proj. No. PRJ-008433, Australian Government, 2013).
167. J. Martínez, G. Leal, P. Conget, *Nosema ceranae* an emergent pathogen of *Apis mellifera* in Chile. *Parasitol. Res.* **111**, 601–607 (2012). doi: 10.1007/s00436-012-2875-0; pmid: 22453498
168. Y. Chen *et al*., Asymmetrical coexistence of *Nosema ceranae* and *Nosema apis* in honey bees. *J. Invertebr. Pathol.* **101**, 204–209 (2009). doi: 10.1016/j.jip.2009.05.012; pmid: 19467238
169. V. Chaimanee, N. Warrit, P. Chantawannakul, Infections of *Nosema ceranae* in four different honeybee species. *J. Invertebr. Pathol.* **105**, 207–210 (2010). doi: 10.1016/j.jip.2010.06.005; pmid: 20600087
170. C. Botías *et al*., Further evidence of an oriental origin for *Nosema ceranae* (Microsporidia: Nosematidae). *J. Invertebr. Pathol.* **110**, 108–113 (2012). doi: 10.1016/j.jip.2012.02.014; pmid: 22425522

ACKNOWLEDGMENTS

We thank R. Hatfield and S. Jepsen for their help with Fig. 1B.

10.1126/science.1255957

RESEARCH ARTICLES

ALS GENES

Exome sequencing in amyotrophic lateral sclerosis identifies risk genes and pathways

Elizabeth T. Cirulli,[1*] Brittany N. Lasseigne,[2*] Slavé Petrovski,[3] Peter C. Sapp,[4] Patrick A. Dion,[5] Claire S. Leblond,[5] Julien Couthouis,[6] Yi-Fan Lu,[3] Quanli Wang,[3] Brian J. Krueger,[3] Zhong Ren,[3] Jonathan Keebler,[7] Yujun Han,[7] Shawn E. Levy,[2] Braden E. Boone,[2] Jack R. Wimbish,[2] Lindsay L. Waite,[2] Angela L. Jones,[2] John P. Carulli,[8] Aaron G. Day-Williams,[8] John F. Staropoli,[8] Winnie W. Xin,[9] Alessandra Chesi,[6] Alya R. Raphael,[6] Diane McKenna-Yasek,[4] Janet Cady,[10] J. M. B. Vianney de Jong,[11] Kevin P. Kenna,[12] Bradley N. Smith,[13] Simon Topp,[13] Jack Miller,[13] Athina Gkazi,[13] FALS Sequencing Consortium,† Ammar Al-Chalabi,[13] Leonard H. van den Berg,[14] Jan Veldink,[14] Vincenzo Silani,[15] Nicola Ticozzi,[15] Christopher E. Shaw,[13] Robert H. Baloh,[16] Stanley Appel,[17] Ericka Simpson,[17] Clotilde Lagier-Tourenne,[18] Stefan M. Pulst,[19] Summer Gibson,[19] John Q. Trojanowski,[20] Lauren Elman,[21] Leo McCluskey,[21] Murray Grossman,[22] Neil A. Shneider,[23] Wendy K. Chung,[24] John M. Ravits,[25] Jonathan D. Glass,[26] Katherine B. Sims,[9] Vivianna M. Van Deerlin,[20] Tom Maniatis,[27] Sebastian D. Hayes,[8,28] Alban Ordureau,[28] Sharan Swarup,[28] John Landers,[4] Frank Baas,[11] Andrew S. Allen,[29] Richard S. Bedlack,[30] J. Wade Harper,[28] Aaron D. Gitler,[6] Guy A. Rouleau,[5] Robert Brown,[4] Matthew B. Harms,[10] Gregory M. Cooper,[2] Tim Harris,[8]‡ Richard M. Myers,[2]§ David B. Goldstein[3]§

Amyotrophic lateral sclerosis (ALS) is a devastating neurological disease with no effective treatment. We report the results of a moderate-scale sequencing study aimed at increasing the number of genes known to contribute to predisposition for ALS. We performed whole-exome sequencing of 2869 ALS patients and 6405 controls. Several known ALS genes were found to be associated, and *TBK1* (the gene encoding TANK-binding kinase 1) was identified as an ALS gene. TBK1 is known to bind to and phosphorylate a number of proteins involved in innate immunity and autophagy, including optineurin (OPTN) and p62 (SQSTM1/sequestosome), both of which have also been implicated in ALS. These observations reveal a key role of the autophagic pathway in ALS and suggest specific targets for therapeutic intervention.

Amyotrophic lateral sclerosis (ALS) is a fatal, progressive neurodegenerative disease characterized by loss of motor neuron function for which there is no effective treatment or definitive diagnostic test (most cases are diagnosed clinically) (*1*). Approximately 10% of ALS cases are familial and inherited in an autosomal dominant, autosomal recessive, or X-linked mode; the remaining cases are apparently sporadic (*2*, *3*). Approximately 20 genes collectively explain a majority of familial cases, but these genes can explain only a minority (about 10%) of sporadic cases (*2*, *3*) (Table 1).

Protein and protein-RNA aggregates are a common feature of ALS pathology. These aggregates often include proteins encoded by genes that cause ALS when mutated, including those encoding SOD1, TARDBP (TDP-43), and FUS (*4*). Multiple genes (e.g., *C9orf72*, *GRN*, *VCP*, *UBQLN2*, *OPTN*, *NIPA1*, *SQSTM1*) in addition to *TARDBP* harbor variants pathogenic for TARDBP proteinopathy manifesting as ALS. This pathological TARDBP is part of a common pathway linked to neurodegeneration caused by diverse genetic abnormalities (*5*). Although murine models of ALS are limited, silencing certain ALS genes can cause regression of the disease phenotypes and clearance of the protein aggregates (*6*).

Identifying ALS genes

To identify genetic variants associated with ALS, we sequenced the exomes of 2869 patients with ALS and 6405 controls. We ran a standard collapsing analysis in which the gene was the unit of analysis, and we coded individuals according to the presence or absence of "qualifying" variants in each sequenced gene, where qualifying was defined according to one of six different genetic models: dominant coding, recessive coding, dominant not benign, recessive not benign, dominant loss of function (LoF), and recessive LoF (*7*). A total of 17,249 genes had more than one case or control sample with a genetic variant meeting the inclusion criteria for at least one of the genetic models tested (Fig. 1 and figs. S1 and S2). After correcting for multiple tests, the known ALS gene *SOD1* ($P = 7.05 \times 10^{-8}$; dominant coding model) was found to have a study-wide significant enrichment of rare variants in ALS cases relative to controls, with qualifying variants in 0.871% of cases and 0.078% of controls. The genes *HLA-B*, *ZNF729*, *SIRPA*, and *TP53* were found to have a significant enrichment of variants in controls; however, these associations appear to be due to sequencing differences and to subsets of the controls having been ascertained on the basis of relevant phenotypes.

On the basis of their associations with ALS in a preliminary discovery-phase analysis that used 2843 cases and 4310 controls, we chose 51 genes (table S4) for analysis in an additional 1318 cases

[1]Center for Applied Genomics and Precision Medicine, Duke University School of Medicine, Durham, NC 27708, USA. [2]HudsonAlpha Institute for Biotechnology, Huntsville, AL 35806, USA. [3]Institute for Genomic Medicine, Columbia University, New York, NY 10032, USA. [4]Department of Neurology, University of Massachusetts Medical School, Worcester, MA 01655, USA. [5]Montreal Neurological Institute, Department of Neurology and Neurosurgery, McGill University, Montreal, Quebec H3A 2B4, Canada. [6]Department of Genetics, Stanford University School of Medicine, Stanford, CA 94305, USA. [7]Duke University School of Medicine, Durham, NC 27708, USA. [8]Biogen Idec, Cambridge, MA 02142, USA. [9]Neurogenetics DNA Diagnostic Laboratory, Center for Human Genetics Research, Department of Neurology, Massachusetts General Hospital, Boston, MA 02114, USA. [10]Neurology, Washington University School of Medicine, St. Louis, MO 63110, USA. [11]Department of Genome Analysis, Academic Medical Center, Meibergdreef 9, 1105AZ Amsterdam, Netherlands. [12]Academic Unit of Neurology, Trinity Biomedical Sciences Institute, Trinity College Dublin, Dublin, Republic of Ireland. [13]Department of Basic and Clinical Neuroscience, King's College London, Institute of Psychiatry, Psychology and Neuroscience, London SE5 8AF, UK. [14]Department of Neurology, Brain Center Rudolf Magnus, University Medical Centre Utrecht, 3508 GA Utrecht, Netherlands. [15]Department of Neurology and Laboratory of Neuroscience, IRCCS Istituto Auxologico Italiano, Milan 20149, Italy, and Department of Pathophysiology and Transplantation, Dino Ferrari Center, Università degli Studi di Milano, Milan 20122, Italy. [16]Cedars Sinai Medical Center, Los Angeles, CA 90048, USA. [17]Houston Methodist Hospital, Houston, TX 77030, USA, and Weill Cornell Medical College of Cornell University, New York, NY 10065, USA. [18]Ludwig Institute for Cancer Research and Department of Neurosciences, University of California, San Diego, La Jolla, CA 92093, USA. [19]Department of Neurology, University of Utah School of Medicine, Salt Lake City, UT 84112, USA. [20]Department of Pathology and Laboratory Medicine, Perelman School of Medicine, University of Pennsylvania, Philadelphia, PA 19104, USA. [21]Department of Neurology, Penn ALS Center, Perelman School of Medicine, University of Pennsylvania, Philadelphia, PA 19104, USA. [22]Department of Neurology, Penn Frontotemporal Degeneration Center, Perelman School of Medicine at the University of Pennsylvania, Philadelphia, PA 19104, USA. [23]Department of Neurology, Center for Motor Neuron Biology and Disease, Columbia University, New York, NY 10032, USA. [24]Department of Pediatrics and Medicine, Columbia University, New York, NY 10032, USA. [25]Department of Neurosciences, University of California, San Diego, La Jolla, CA 92093, USA. [26]Department of Neurology, Emory University, Atlanta, GA 30322, USA. [27]Department of Biochemistry & Molecular Biophysics, Columbia University, New York, NY 10027, USA. [28]Department of Cell Biology, Harvard Medical School, Boston, MA 02115, USA. [29]Department of Biostatistics and Bioinformatics, Duke University School of Medicine, Durham, NC 27708, USA. [30]Duke ALS Clinic and Durham VA Medical Center, Durham, NC 27708, USA.

*These authors contributed equally to this work. †The full author list is included at the end of the manuscript. **‡Corresponding author. E-mail: tim.harris@biogenidec.com** §These authors contributed equally to this work.

Table 1. Variants in previously described and currently reported ALS genes. Entries for reported inheritance model, reported FALS explained, and reported SALS explained are adapted from (*3*, *4*, *51*) with additional information from (*17*–*21*, *52*–*54*). AD, autosomal dominant; AR, autosomal recessive; XD, X-linked. Best-model data are based on discovery data set for genes not included in the replication data set, and otherwise D = discovery, R = replication, and C = combined. Potential ALS cases explained are calculated as [(cases with variant in best model) − (controls with variant in best model)]; as case variants are risk factors for disease and may not be causal, this represents the potential percentage of cases for which this gene plays a role in disease.

Gene	Reported inheritance model	Reported FALS explained	Reported SALS explained	Best model with case enrichment in present study (*P* value)	Cases with variant in best model	Controls with variant in best model	Potential ALS cases explained
TBK1	N/A	N/A	N/A	Dom not benign (D = 1.12×10^{-5}; R = 5.78×10^{-7}; C = 3.60×10^{-11})	D = 23 (0.802%); R = 23 (1.745%); C = 46 (1.099%)	D = 12 (0.187%); R = 5 (0.211%); C = 17 (0.194%)	0.905%
NEK1	N/A	N/A	N/A	Dom LoF (D = 1.06×10^{-6}; R = 0.001; C = 3.15×10^{-9})	D = 25 (0.871%); R = 10 (0.759%); C = 35 (0.836%)	D = 6 (0.094%); R = 2 (0.084%); C = 8 (0.091%)	0.745%
SOD1	AR/AD	12%	1.50%	Dom coding (7.05×10^{-8})	25 (0.871%)	5 (0.078%)	0.793%
TARDBP	AD	4%	1%	Dom coding (2.93×10^{-6})	19 (0.662%)	6 (0.094%)	0.569%
OPTN	AR/AD	<1%	<1%	Dom not benign (D = 0.023; R = 0.002; C = 0.002)	D = 18 (0.627%); R = 8 (0.607%); C = 26 (0.621%)	D = 16 (0.25%); R = 4 (0.169%); C = 20 (0.228%)	0.393%
SPG11	AR	<1%	<1%	Dom LoF (D = 0.022; R = 0.183; C = 0.023)	D = 20 (0.697%); R = 5 (0.379%); C = 25 (0.597%)	D = 20 (0.312%); R = 7 (0.295%); C = 27 (0.308%)	0.289%
VCP	AD	1%	1%	Dom coding (0.022)	8 (0.279%)	4 (0.062%)	0.216%
HNRNPA1	AD	<1%	<1%	Dom coding (0.103)	6 (0.209%)	5 (0.078%)	0.131%
*ATXN2**	AD	<1%	<1%	Rec coding (0.205)	4 (0.139%)	2 (0.031%)	0.108%
ANG	AD	<1%	<1%	Dom LoF (0.217)	2 (0.070%)	1 (0.016%)	0.054%
CHCHD10	AD	<1%	<1%	Dom coding (0.225)	2 (0.070%)	0 (0%)	0.070%
SIGMAR1	AR	<1%	<1%	Dom LoF (0.226)	1 (0.035%)	0 (0%)	0.035%
FIG4	AR/AD	<1%	<1%	Dom LoF (0.232)	9 (0.314%)	12 (0.187%)	0.126%
SS18L1	AD	<1%	<1%	Dom LoF (0.241)	1 (0.035%)	0 (0%)	0.035%
GRN	AD	<1%	<1%	Dom not benign (0.357)	14 (0.488%)	24 (0.375%)	0.113%
SETX	AD	<1%	<1%	Rec not benign (0.379)	3 (0.105%)	4 (0.062%)	0.042%
HNRNPA2B1	AD	<1%	<1%	Dom not benign (0.423)	3 (0.105%)	4 (0.062%)	0.042%
SQSTM1	AD	1%	<1%	Dom LoF (0.546)	1 (0.035%)	2 (0.031%)	0.004%
TAF15	AR/AD	<1%	<1%	Rec not benign (0.555)	2 (0.070%)	1 (0.016%)	0.054%
FUS	AR/AD	4%	1%	Dom LoF (0.612)	2 (0.070%)	3 (0.047%)	0.023%
ALS2	AR	<1%	<1%	Rec coding (0.655)	2 (0.070%)	4 (0.062%)	0.007%
VAPB	AD	<1%	<1%	Dom not benign (0.688)	3 (0.105%)	5 (0.078%)	0.027%
NEFH	AD	<1%	<1%	Dom coding (0.673)	22 (0.767%)	37 (0.578%)	0.189%
*C9orf72**	AD	40%	7%	Dom not benign (1.000)	4 (0.139%)	7 (0.109%)	0.030%
CHMP2B	AD	<1%	<1%	Rec coding (1.000)	1 (0.035%)	1 (0.016%)	0.019%
MATR3	AD	<1%	<1%	Dom coding (1.000)	19 (0.662%)	35 (0.546%)	0.116%
PFN1	AD	<1%	<1%	Rec coding (1.000)	9 (0.314%)	15 (0.234%)	0.080%
PRPH	AD	<1%	<1%	Dom LoF (1.000)	1 (0.035%)	2 (0.031%)	0.004%
SPAST	AD	<1%	<1%	Dom coding (1.000)	6 (0.209%)	12 (0.187%)	0.022%
TUBA4A	AD	1%	<1%	Dom not benign (1.000)	2 (0.070%)	3 (0.047%)	0.023%
ELP3†	Allelic	<1%	<1%	Rec coding (1.000)	0 (0%)	0 (0%)	0%
DAO†	AD	<1%	<1%	Rec coding (1.000)	0 (0%)	0 (0%)	0%
DCTN1†	AD	<1%	<1%	Dom coding (0.668)	32 (1.115%)	76 (1.187%)	0%
EWSR1†	AD	<1%	<1%	Dom coding (0.375)	10 (0.349%)	28 (0.437%)	0%
GLE1†	AD	<1%	<1%	Rec LoF (1.000)	0 (0%)	0 (0%)	0%
UBQLN2†	XD	<1%	<1%	Dom LoF (1.000)	0 (0%)	0 (0%)	0%

*Because the known causal variants are repeat expansions that are not generally captured by next-generation sequencing, no case enrichment is expected. †No model showed case enrichment.

and 2371 controls (sequenced using either whole exome or custom capture) (*7*). This analysis definitively identified TANK-binding kinase 1 (*TBK1*) as an ALS gene, with a discovery association $P = 1.12 \times 10^{-5}$, a replication $P = 5.78 \times 10^{-7}$, and a combined $P = 3.60 \times 10^{-11}$ (dominant not benign model). In the combined data set, dominant not benign variants in this gene were found in 1.099% of cases and 0.194% of controls, with LoF variants occurring in 0.382% of cases and 0.034% of controls.

Analysis of clinical features

We also performed gene-based collapsing analyses to identify genes associated with patients' age of onset, site of onset, and survival time. No genes showed genome-wide significant association with any of these features. When applying multiple-test correction to only known ALS predisposition genes and *TBK1*, we found that D-amino acid oxidase (*DAO*) significantly correlated with survival times, with variant carriers showing shorter survival times ($P = 5.5 \times 10^{-7}$, dominant coding model). In mice, DAO is required for the clearance of D-serine. Indeed, D-serine levels are increased in SOD1 mutant mice and in spinal cords from people with familial ALS (FALS) or sporadic ALS (SALS) (*8*, *9*). Known FALS mutations seem to reduce DAO activity, leading to neurotoxicity (*10*).

ALS patients with mutations in more than one known ALS gene are reported to have a younger age of onset (*11*). We did not replicate this finding in our data set. Without sequence data for known *C9orf72* carriers (by far the most common ALS variant) and without information about *ATXN2* expansions, we cannot adequately assess such an association.

Associations with other ALS genes

Although *SOD1* was the only previously known ALS gene to attain a genome-wide significant association in our data, many other known ALS genes showed strong associations. For example, rare coding variants in *TARDBP* occurred in 0.662% of the ALS cases and 0.094% of controls in our study, ranking this gene second to *SOD1* genome-wide under the dominant coding model (discovery data set, $P = 2.93 \times 10^{-6}$; Fig. 1). Consistent with previous reports and the ALS pathogenic *TARDBP* "DM" variants in the Human Genome Mutation Database (HGMD) (*3*, *12*), we observed that the implicated nonsynonymous variants were generally predicted to have a benign effect on protein structure and function by PolyPhen-2 (*13*) and were clearly concentrated in the 3′ protein-coding portion of the gene in the ALS cases relative to controls (Fig. 2).

In the case of *OPTN*, we observed rare damaging variants in 0.621% of ALS cases and 0.228% of controls (combined dominant not benign model, $P = 0.002$). The greatest enrichment was for LoF variants, which occur in 0.334% of cases and 0.114% of controls (combined dominant LoF model, $P = 0.013$). Whereas the initial studies of *OPTN* in ALS found a role in only a few families with a recessive genetic model, subsequent studies identified dominant mutations (*14*, *15*). Here, dominant variants appeared to make a substantial contribution to sporadic disease.

Finally, we also observed a modest excess of qualifying variants in *VCP* (discovery dominant coding model, $P = 0.022$) and of LoF variants in *SPG11* (combined dominant LoF model, $P = 0.023$). The former was driven by variants near the cell division protein 48 domain 2 region, where variants were found in 71% of case variants as compared to 25% of control variants (Fig. 2). Similar to *OPTN*, *SPG11* has previously been reported as a cause of recessive juvenile ALS, but our data indicate that it could play a broader role because these cases did not have early onset (*16*).

We did not identify even a nominal association with other previously reported ALS genes in our data set, including the recently reported *TUBA4A*, *MATR3*, *GLE1*, *SS18L1*, and *CHCHD10* (Table 1) (*17*–*21*). A fraction of our samples were genetically screened for some of the known genes and positive cases had been removed before sequencing, which may partially explain the lack of signal (*7*). Additionally, a comparison with genes implicated in a recent assessment of the role of 169 previously reported and candidate ALS genes in 242 sporadic ALS cases and 129 controls showed no overlap beyond signals for *SOD1* and *SPG11* (*22*). Some of these previously studied genes are mutated so rarely that even the sample size presented here is not sufficient to detect causal variant enrichment, while others simply show comparable proportions of rare variants among cases and controls. Finally, certain genes did not show associations owing to the nature of the causal variation: Most known pathogenic variants in *ATXN2* and *C9orf72* are repeats that cannot be identified in our sequence data.

TBK1, autophagy, and neuroinflammation

Previous studies have implicated both *OPTN* (optineurin) (*23*) and *SQSTM1* (p62) (*24*) in ALS. The current study implicates *TBK1* and suggests that *OPTN* is a more important disease gene than previously recognized. These genes play important and interconnected roles in both autophagy and inflammation, emerging areas of interest in ALS research (Fig. 3) (*25*–*27*). Mutations in *SOD1*, *TARDBP*, and *FUS* result in the formation of protein aggregates that stain with antibodies to SQSTM1 and OPTN (*28*). These aggregates are thought to lead to a cargo-specific subtype of autophagy involved in the degradation of ubiquitinated proteins through the lysosome (*29*). The SQSTM1 and OPTN proteins function as cargo receptors, recruiting ubiquitinated proteins to the autophagosome via their LC3 interaction region (LIR) motifs. TBK1 binds and phosphorylates both OPTN and SQSTM1 (*30*–*32*) and enhances the binding of OPTN to the essential autophagosome

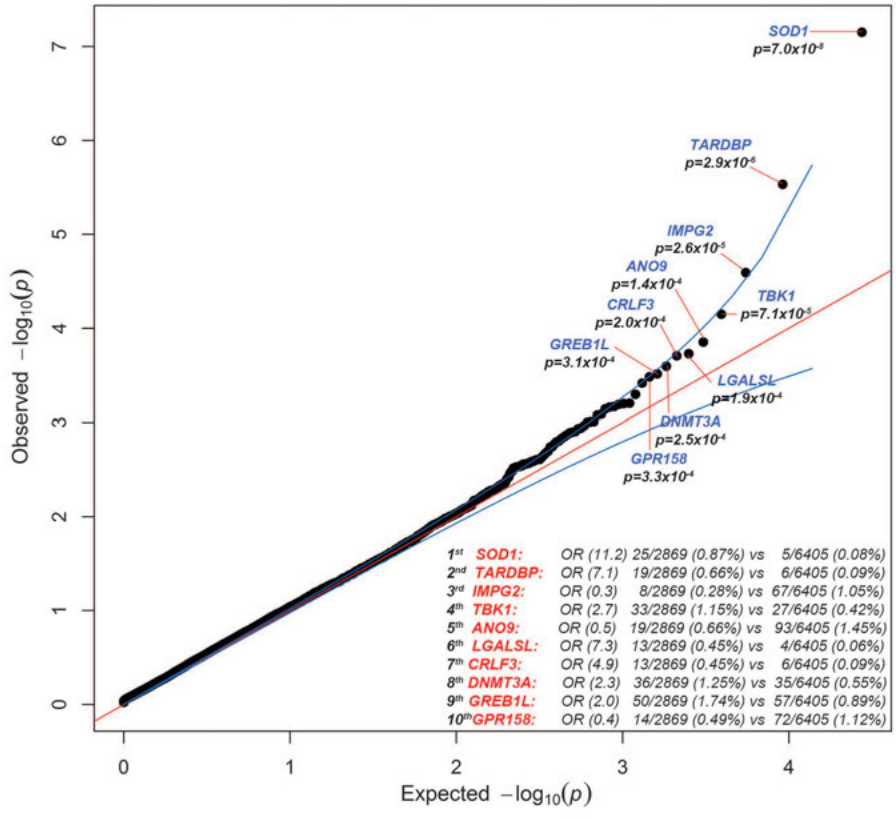

Fig. 1. Quantile-quantile plot of discovery results for dominant coding model. Results for the analysis of 2869 case and 6405 control exomes are shown; 16,491 covered genes passed quality control with more than one case or control carrier for this test. The genes with the top 10 associations are labeled. The genomic inflation factor λ is 1.060. The association with *SOD1* passed correction for multiple tests.

protein LC3, thereby facilitating the autophagic turnover of infectious bacteria coated with ubiquitinated proteins, a specific cargo of the OPTN adaptor (*33*). Considering that TBK1 colocalizes with OPTN and SQSTM1 in autophagosomes, it is possible that all three proteins associate with protein aggregates in ALS (*33*). Indeed, TBK1 appears to play a role in the degradation of protein aggregates by autophagy (*34*). Additionally, OPTN also functions in the autophagic turnover of damaged mitochondria via the Parkin ubiquitin ligase pathway (*35*). Finally, VCP, encoded by another gene with mutations that cause ALS, also binds to ubiquitinated protein aggregates. VCP and autophagy are required for the removal of stress granules (dense cytoplasmic protein-RNA aggregates), which are a common feature of ALS pathology (*36*). Thus, OPTN, SQSTM1, VCP, and TBK1 may be critical components of the aggresome pathway required for the removal of pathological ribonucleoprotein inclusions (*37*). It appears that defects in this pathway can be selective for motor neuron death, in some cases apparently sparing other neuronal cell types.

In addition to their roles in autophagy, OPTN, SQSTM1, and TBK1 all function in the NF-κB pathway (Fig. 3) (*27*, *38*). For example, IκB kinases (IKKα and IKKβ) phosphorylate the IKK-related kinase TBK1, which in turn phosphorylates the IκB kinases, suppressing their activity in a negative autoregulatory feedback loop (*39*). TBK1 also phosphorylates and activates the transcription factor IRF3 (*40*–*42*) and the critical innate immunity signaling components MAVS and STING (*43*). The coordinate activation of NF-κB and IRF3 turns on the transcription of many inflammatory genes, including interferon-β (*44*). The innate immune pathway and neuroinflammation in general are thought to be important aspects of neurodegenerative disease progression (*45*). Thus, pathogenic variants in *OPTN*, *SQSTM1*, or *TBK1* would be expected to lead to defects in autophagy and in key innate immunity signaling

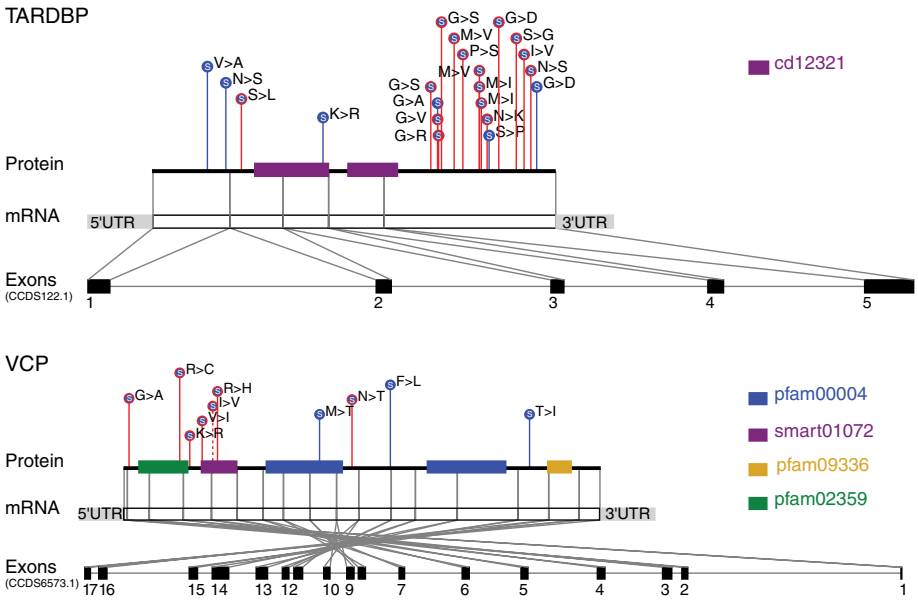

Fig. 2. Variants in *TARDBP* and *VCP*. Dominant coding variants are shown in *TARDBP* and *VCP* (discovery data set). Case variants are enriched at the 3′ end of the gene in TARDBP and near the cell division protein 48 domain 2 region in *VCP*. LoF variants are filled in red, and nonsynonymous variants are filled in blue. Case variants are shown with red lines, control variants are shown with blue lines, and variants found in both cases and controls are shown with dashed lines.

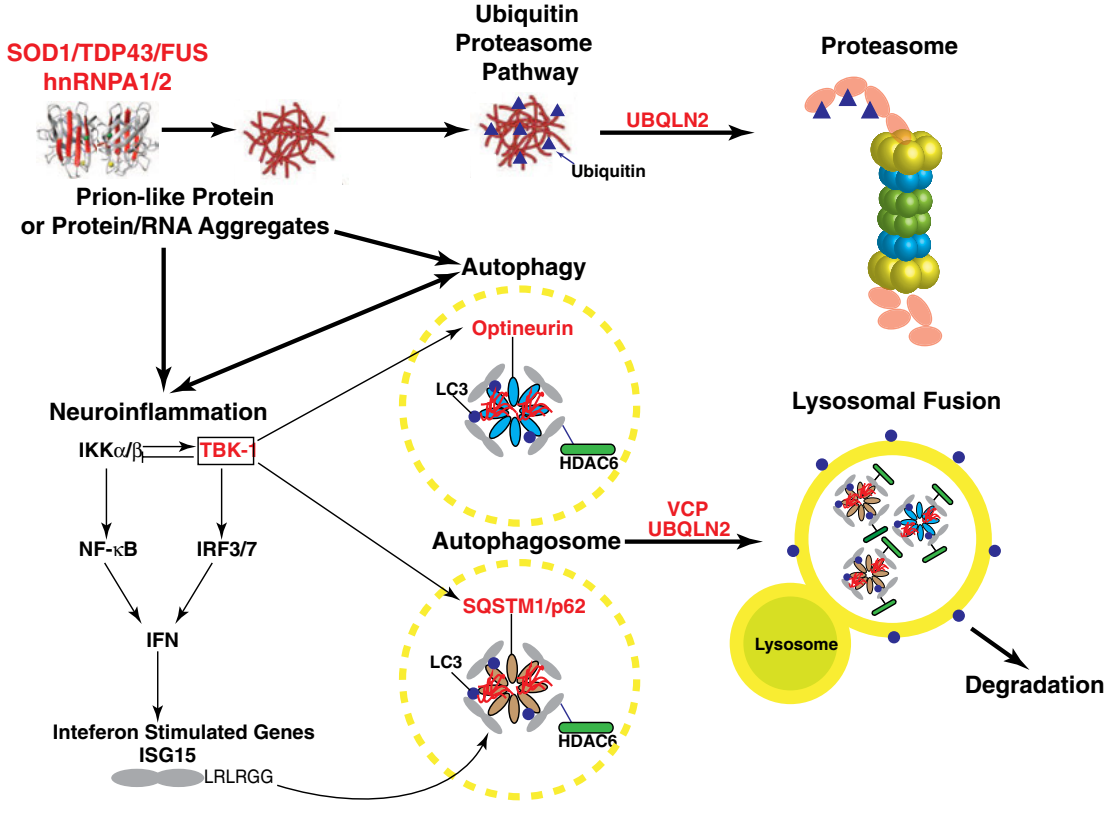

Fig. 3. Genes and pathways implicated in ALS disease progression. Genes known to have sequence variants that cause or are associated with ALS are indicated in red. These mutations can lead to the formation of protein or protein-RNA aggregates that appear as inclusion bodies in post mortem samples from both familial and sporadic ALS patients. Some of the mutant proteins adopt "prion-like" structures (see text for more detail). The misfolded proteins activate the ubiquitin-proteasome autophagy pathways to remove the misfolded proteins. Ubiquilin2 (UBQLN2) functions in both the ubiquitin-proteasome and autophagy pathways. TBK-1 (boxed) lies at the interface between autophagy and inflammation and associates with and phosphorylates both optineurin and p62, which can in turn enhance inflammation. ISG15 is induced by type I interferons (α and β) and interacts with p62 and HDAC6 in the autophagosome.

pathways. Mutations in these genes might therefore interfere with the normal function of these pathways in maintaining normal cellular riboproteostasis (*37*).

The simple observation of enrichment of qualifying variants in patients shows that some of the variants we have identified influence risk of disease. We cannot determine, however, the extent to which they may interact with any other variants or other risk factors in determining risk. We therefore focus on estimating the proportion of patients in which variants in the relevant genes either cause or contribute to disease by subtracting the proportion of controls with qualifying variants in a gene from the proportion of cases with such variants. Although we saw no enrichment of case variants in *SQSTM1*, variants in *OPTN* and *TBK1* were estimated to explain or contribute to 1.30% of cases in our data set when taken together (combined data set), suggesting an important subgroup of patients that may have a common biological etiology. No individual ALS cases had qualifying variants in more than one of these three genes.

The case variants found in *OPTN* and *TBK1* were largely heterozygous and LoF, which suggests that a reduction in trafficking of cargo through the autophagosomal pathway or disruption of autophagosomal maturation may promote disease. Although the most obvious enrichment of case variants in *TBK1* was seen for LoF, there was also a signal for nonsynonymous variants, which were found in 1.027% of cases and 0.365% of controls (combined data set). If any of these nonsynonymous variants are selective LoF for specific TBK1 functions as opposed to complete LoF variants, they may help elucidate which TBK1 function is most relevant to disease. We did not observe any clear concentration of qualifying variants in any part of the *TBK1* gene (Fig. 4).

NEK1 associates with ALS2 and VAPB

Although no additional genes showed sufficiently strong evidence to be definitively declared disease genes at this point, some of the strongly associated genes identified here may be securely implicated as sample sizes increase. One gene of particular interest is *NEK1* (NIMA-related kinase 1). This gene just reached experiment-wide significance in the combined discovery and replication data sets (discovery $P = 1.06 \times 10^{-6}$, replication $P = 0.001$, combined $P = 3.15 \times 10^{-9}$; dominant LoF model). In the combined data set, dominant LoF variants in this gene were found in 0.836% of cases and 0.091% of controls (fig. S3). Additional studies are needed to confirm this suggestive association. Even if LoF variants in this gene do predispose to ALS, their relatively high prevalence in our controls and in public databases indicates that such variants have quite low penetrance, given that the lifetime prevalence of ALS is approximately 0.2%.

NEK1 is a widely expressed multifunctional kinase linked to multiple cellular processes, but it has not been linked to ALS. In an unbiased proteomic search for NEK1-interacting proteins in human embryonic kidney (HEK) 293T cells, we discovered an interaction between NEK1 and two widely expressed proteins previously found to be mutated in familial ALS: (i) the RAB guanine nucleotide exchange factor ALS2 (also called Alsin) involved in endosomal trafficking, and (ii) the endoplasmic reticulum protein VAPB involved in lipid trafficking to the plasma membrane (fig. S4, A and B, and table S5) (*46*). ALS2 reciprocally associated with NEK1 in HEK293T cells, and both ALS2 and VAPB associated with NEK1 reciprocally in mouse neuronal cell line NSC-34 (fig. S4, C to E).

Other top genes showing interesting association patterns but not obtaining genome-wide significance included *ENAH*, with variants in 0.263% of cases and 0.011% of controls (combined data set) (discovery $P = 1.82 \times 10^{-5}$, replication $P = 0.133$, combined $P = 9.58 \times 10^{-6}$; recessive not benign model); *CRLF3*, with variants in 0.453% of cases and 0.094% of controls (discovery $P = 0.0002$; dominant coding model); *DNMT3A*, with variants in 1.003% of cases and 0.456% of controls (combined data set) (discovery $P = 0.0002$, replication $P = 0.261$, combined $P = 0.0002$; dominant not benign model); and *LGALSL*, with variants in 0.382% of cases and 0.068% of controls (combined data set) (discovery $P = 0.0002$, replication $P = 0.356$, combined $P = 0.0002$; dominant coding model).

Conclusions

Our results implicate *TBK1* as an ALS gene, thereby providing insight into disease biology and suggesting possible directions for drug screening programs. We have also provided evidence that *OPTN* plays a broader role in ALS than previously recognized. Both TBK1 and OPTN are involved in autophagy, with TBK1 possibly playing a crucial role in autophagosome maturation as well as the clearance of pathological aggregates (*31*, *34*). These observations highlight a critical role of autophagy and/or inflammation in disease predisposition. It is also noteworthy that many drugs have been developed that act on TBK1-mediated pathways owing to their role in tumor cell survival (*47*) and can therefore be used to investigate the effects of drug-dependent loss of function of the kinase.

We also provide a large genetic data set for ALS, which suggests other possible ALS genes and provides a substantial collection of pathogenic variants across ALS genes (for genotype counts for all genes for all cases from this study, see alsdb.org). After removing the number of variants expected to be seen on the basis of frequencies of rare variants in controls, we identify more than 70 distinct pathogenic mutations across *SOD1*, *OPTN*, *TARDBP*, *VCP*, *SPG11*, and *TBK1* that can be used in future efforts to functionally characterize the role of these ALS genes. The identification of *TBK1* and the expanded role for *OPTN* as ALS genes reinforce the growing recognition of the central role of autophagy and neuroinflammation in the pathophysiology of ALS (Fig. 3). These pathways appear to be activated in response to the formation of various types of cellular inclusions, the most prominent of which appear to be ribonucleoprotein complexes; this has led to the proposal that the control of protein misfolding (proteostasis) or ribonucleoprotein/RNA misfolding ("ribostasis") plays a key role in neurodegenerative diseases (*37*). Cellular ribonucleoprotein inclusions can be caused by mutations in low-complexity sequence domains or "prion" domains of RNA binding proteins (*37*, *48*) and can be exacerbated by

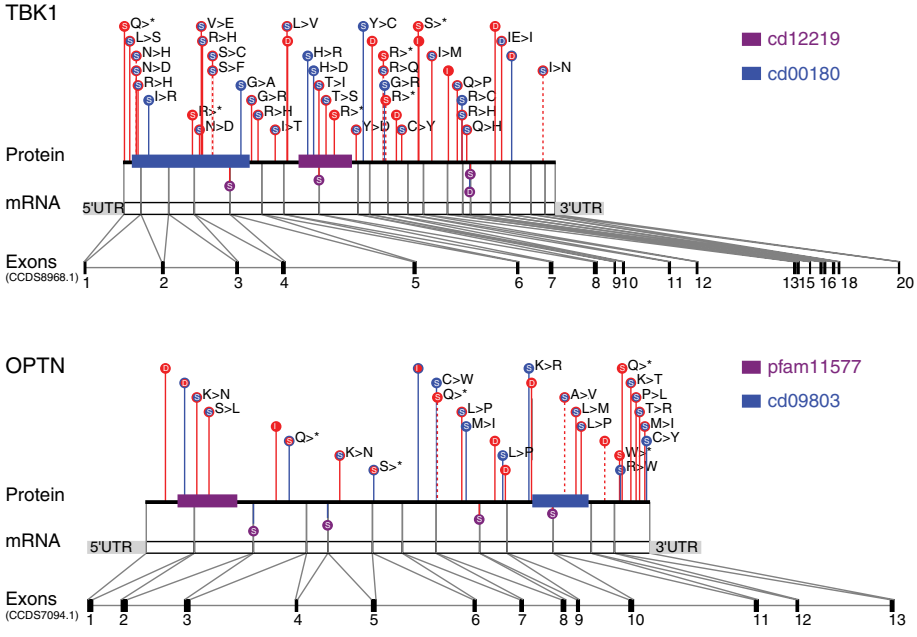

Fig. 4. Variants in *TBK1* and *OPTN*. Dominant not benign variants are shown in *TBK1* and *OPTN* (combined data sets). LoF variants are filled in red, nonsynonymous variants are filled in blue, and splice variants are filled in purple and shown below the protein line. Case variants are shown with red lines, control variants are shown with blue lines, and variants found in both cases and controls are shown with dashed lines.

mutations that diminish the autophagy pathway. Remarkably, a hallmark of motor neuron pathology in >95% of sporadic and familial ALS patients is the formation of TARDBP inclusions, which suggests that defects in ribostasis are a common feature of the disease (*5*, *49*). The prominence of this disease mechanism in ALS has been proposed to be the consequence of the normal function of low-complexity domains in RNA binding proteins in the assembly of functional "RNA granules" such as P-bodies and stress granules [see (*37*) for detailed discussion].

Our exome sequencing study has identified variants that definitively predispose humans to a sporadic, complex human disease. Larger exome sequencing studies may reveal identifiable roles for genes that have not yet achieved significant associations. There is reason for optimism that such studies will begin to fill in an increasingly complete picture of the key genes implicated in ALS, providing multiple entry points for therapeutic intervention (Fig. 3). It is also likely that whole-genome sequencing (especially with longer reads) will prove of particular value in ALS, given that there are many causal variants refractory to identification by contemporary exome sequencing. Finally, we note that effective studies will depend critically on the control samples available. For example, we used the recently released ExAC data set of >60,000 samples to focus on extremely rare variants in our samples (*50*). Well-characterized, publicly available control sample sets will be of great importance for further discovery of variants associated with complex traits, in particular for whole-genome sequencing studies.

REFERENCES AND NOTES

1. L. Poppe, L. Rué, W. Robberecht, L. Van Den Bosch, *Exp. Neurol.* **262**, 138–151 (2014).
2. S. Chen, P. Sayana, X. Zhang, W. Le, *Mol. Neurodegener.* **8**, 28 (2013).
3. A. E. Renton, A. Chiò, B. J. Traynor, *Nat. Neurosci.* **17**, 17–23 (2014).
4. A. Al-Chalabi *et al.*, *Acta Neuropathol.* **124**, 339–352 (2012).
5. M. Neumann, *Rev. Neurol.* **169**, 793–798 (2013).
6. R. A. Smith *et al.*, *J. Clin. Invest.* **116**, 2290–2296 (2006).
7. See supplementary materials on *Science* Online.
8. J. Sasabe *et al.*, *EMBO J.* **26**, 4149–4159 (2007).
9. M. Thompson *et al.*, *J. Neurochem.* **120**, 598–610 (2012).
10. P. Paul, J. de Belleroche, *Amino Acids* **43**, 1823–1831 (2012).
11. J. Cady *et al.*, *Ann. Neurol.* **77**, 100–113 (2015).
12. P. D. Stenson *et al.*, *Hum. Mutat.* **21**, 577–581 (2003).
13. I. A. Adzhubei *et al.*, *Nat. Methods* **7**, 248–249 (2010).
14. A. Iida *et al.*, *Neurobiol. Aging* **33**, 1843.e19–1843.e24 (2012).
15. M. van Blitterswijk *et al.*, *Neurobiol. Aging* **33**, 1016.e1–1016.e7 (2012).
16. H. Daoud *et al.*, *Neurobiol. Aging* **33**, 839.e5–839.e9 (2012).
17. B. N. Smith *et al.*, *Neuron* **84**, 324–331 (2014).
18. J. O. Johnson *et al.*, *Nat. Neurosci.* **17**, 664–666 (2014).
19. H. M. Kaneb *et al.*, *Hum. Mol. Genet.* **24**, 1363–1373 (2015).
20. A. Chaussenot *et al.*, *Neurobiol. Aging* **35**, 2884.e1–2884.e4 (2014).
21. S. Bannwarth *et al.*, *Brain* **137**, 2329–2345 (2014).
22. J. Couthouis, A. R. Raphael, R. Daneshjou, A. D. Gitler, *PLOS Genet.* **10**, e1004704 (2014).
23. H. Maruyama *et al.*, *Nature* **465**, 223–226 (2010).
24. S. L. Rea, V. Majcher, M. S. Searle, R. Layfield, *Exp. Cell Res.* **325**, 27–37 (2014).
25. H. Maruyama, H. Kawakami, *Geriatr. Gerontol. Int.* **13**, 528–532 (2013).
26. M. Thomas, J. Alegre-Abarrategui, R. Wade-Martins, *Brain* **136**, 1345–1360 (2013).
27. D. Kachaner, P. Génin, E. Laplantine, R. Weil, *Cell Cycle* **11**, 2808–2818 (2012).
28. B. A. Keller *et al.*, *Acta Neuropathol.* **124**, 733–747 (2012).
29. E. L. Scotter *et al.*, *J. Cell Sci.* **127**, 1263–1278 (2014).
30. S. Morton, L. Hesson, M. Peggie, P. Cohen, *FEBS Lett.* **582**, 997–1002 (2008).
31. M. Pilli *et al.*, *Immunity* **37**, 223–234 (2012).
32. C. E. Gleason, A. Ordureau, R. Gourlay, J. S. Arthur, P. Cohen, *J. Biol. Chem.* **286**, 35663–35674 (2011).
33. P. Wild *et al.*, *Science* **333**, 228–233 (2011).
34. J. Korac *et al.*, *J. Cell Sci.* **126**, 580–592 (2013).
35. Y. C. Wong, E. L. Holzbaur, *Proc. Natl. Acad. Sci. U.S.A.* **111**, E4439–E4448 (2014).
36. J. R. Buchan, R. M. Kolaitis, J. P. Taylor, R. Parker, *Cell* **153**, 1461–1474 (2013).
37. M. Ramaswami, J. P. Taylor, R. Parker, *Cell* **154**, 727–736 (2013).
38. M. Komatsu, S. Kageyama, Y. Ichimura, *Pharmacol. Res.* **66**, 457–462 (2012).
39. K. Clark *et al.*, *Biochem. J.* **434**, 93–104 (2011).
40. S. Sharma *et al.*, *Science* **300**, 1148–1151 (2003).
41. K. A. Fitzgerald *et al.*, *Nat. Immunol.* **4**, 491–496 (2003).
42. H. Hemmi *et al.*, *J. Exp. Med.* **199**, 1641–1650 (2004).
43. S. Liu *et al.*, *Science* 10.1126/science.aaa2630 (2015).
44. M. G. Wathelet *et al.*, *Mol. Cell* **1**, 507–518 (1998).
45. C. K. Glass, K. Saijo, B. Winner, M. C. Marchetto, F. H. Gage, *Cell* **140**, 918–934 (2010).
46. Y. Yang *et al.*, *Nat. Genet.* **29**, 160–165 (2001).
47. J. Li *et al.*, *Int. J. Cancer* **134**, 1972–1980 (2014).
48. M. Kato *et al.*, *Cell* **149**, 753–767 (2012).
49. E. B. Lee, V. M. Lee, J. Q. Trojanowski, *Nat. Rev. Neurosci.* **13**, 38–50 (2012).
50. Exome Aggregation Consortium (ExAC); http://exac.broadinstitute.org.
51. P. Van Damme, W. Robberecht, *Curr. Opin. Neurol.* **26**, 466–472 (2013).
52. C. Münch, A. Rolfs, T. Meyer, *Amyotroph. Lateral Scler.* **9**, 251–253 (2008).
53. T. Meyer *et al.*, *Neurology* **65**, 141–143 (2005).
54. A. Chesi *et al.*, *Nat. Neurosci.* **16**, 851–855 (2013).

ACKNOWLEDGMENTS

J.W.H. is a consultant for Biogen Idec and Millennium: the Takeda Oncology Company. R.B. is a consultant for Biogen Idec and a cofounder of AviTx. F.B. is a founder of Regenesance. D.B.G. and R.M.M. are consultants for Biogen Idec. Some of the human samples were provided under a material transfer agreement from Washington University. The results presented in this study can be found in table S6. The case genotype counts for all variants in all genes can be found at alsdb.org. See the supplementary materials for full acknowledgments including funding sources.

FALS Sequencing Consortium members:
Peter C. Sapp,[1] Claire S. Leblond,[2] Diane McKenna-Yasek,[1] Kevin P. Kenna,[3] Bradley N. Smith,[4] Simon Topp,[4] Jack Miller,[4] Athina Gkazi,[4] Ammar Al-Chalabi,[4] Leonard H. van den Berg,[5] Jan Veldink,[5] Vincenzo Silani,[6] Nicola Ticozzi,[6] John Landers,[1] Frank Baas,[7] Christopher E. Shaw,[4] Jonathan D. Glass,[8] Guy A. Rouleau,[9] Robert Brown[1]; other consortium members can be found in the supplementary materials.

[1]Department of Neurology, University of Massachusetts Medical School, Worcester, MA 01655, USA. [2]Montreal Neurological Institute, Department of Neurology and Neurosurgery, McGill University, Montreal, Quebec H3A 2B4, Canada. [3]Academic Unit of Neurology, Trinity Biomedical Sciences Institute, Trinity College Dublin, Dublin, Republic of Ireland. [4]Department of Basic and Clinical Neuroscience, King's College London, Institute of Psychiatry, Psychology and Neuroscience, London SE5 8AF, UK. [5]Department of Neurology, Brain Center Rudolf Magnus, University Medical Centre Utrecht, 3508 GA Utrecht, Netherlands. [6]Department of Neurology and Laboratory of Neuroscience, IRCCS Istituto Auxologico Italiano, Milan 20149, Italy, and Department of Pathophysiology and Transplantation, Dino Ferrari Center, Università degli Studi di Milano, Milan 20122, Italy. [7]Department of Genome Analysis, Academic Medical Center. Meibergdreef 9, 1105AZ Amsterdam, Netherlands. [8]Department of Neurology, Emory University, Atlanta, GA 30322, USA. [9]Montreal Neurological Institute, Department of Neurology and Neurosurgery, McGill University, Montreal, Quebec H3A 2B4, Canada.

SUPPLEMENTARY MATERIALS

www.sciencemag.org/content/347/6229/1436/suppl/DC1
Materials and Methods
Supplementary Text
Figs. S1 to S4
Tables S1 to S6
References (*55*–*65*)

11 October 2014; accepted 11 February 2015
Published online 19 February 2015;
10.1126/science.aaa3650

MOLECULAR MOTORS

The structure of the dynactin complex and its interaction with dynein

Linas Urnavicius,[1]* Kai Zhang,[1]* Aristides G. Diamant,[1]* Carina Motz,[1] Max A. Schlager,[1] Minmin Yu,[1] Nisha A. Patel,[2] Carol V. Robinson,[2] Andrew P. Carter[1]†

Dynactin is an essential cofactor for the microtubule motor cytoplasmic dynein-1. We report the structure of the 23-subunit dynactin complex by cryo-electron microscopy to 4.0 angstroms. Our reconstruction reveals how dynactin is built around a filament containing eight copies of the actin-related protein Arp1 and one of β-actin. The filament is capped at each end by distinct protein complexes, and its length is defined by elongated peptides that emerge from the α-helical shoulder domain. A further 8.2 angstrom structure of the complex between dynein, dynactin, and the motility-inducing cargo adaptor Bicaudal-D2 shows how the translational symmetry of the dynein tail matches that of the dynactin filament. The Bicaudal-D2 coiled coil runs between dynein and dynactin to stabilize the mutually dependent interactions between all three components.

Dynactin works with the cytoplasmic dynein-1 motor (dynein) to transport cargos along the microtubule cytoskeleton (*1*–*3*). Together, these protein complexes maintain the cell's spatial organization, return components from the cell's periphery, and assist with cellular division (*4*). Mutations in either complex cause neurodegeneration (*5*), and both can be co-opted by viruses that travel to the nucleus (*6*). Dynein and dynactin are similar in size and

complexity. Dynein contains two copies of six different proteins and has a mass of 1.4 MD. Dynactin, at ~1.0 MD, contains more than 20 subunits, corresponding to 11 different proteins. Dynactin is built around a filament of actin-related protein 1 (Arp1). In analogy to actin, the filament has a barbed end and a pointed end, each capped by a different protein complex. On top sits the shoulder domain (*7*) from which emerges a long projection, corresponding to dynactin's largest subunit, p150^{Glued} (DCTN1) (*8*).

Despite the presence of a dynein binding site in p150^{Glued} (*9*–*11*), purified dynein and dynactin form a stable complex only in the presence of the cargo adaptor Bicaudal-D2 (BICD2) (*12*–*14*), a coiled-coil protein associated with transport of vesicles, mRNAs, and nuclei (*15*). This interaction activates dynein and converts it into a highly processive motor (*13*, *14*).

Current models for dynactin's architecture (*7*, *16*, *17*) and its interaction with dynein (*13*, *14*) come from low-resolution negative-stain and platinum-shadowing electron microscopy (EM). A number of questions remain. What makes the filament in dynactin short and defined, when purified Arp1 filaments vary in length (*18*)? How does dynein bind to dynactin, and why does the interaction require BICD2 (*12*–*14*)? Why does dynactin, the cofactor for a microtubule motor, contain an actin-related filament? To address these questions, we took advantage of recent advances in cryo-electron microscopy (cryo-EM) (*19*) to improve our structural understanding of dynactin.

[1]Medical Research Council Laboratory of Molecular Biology, Division of Structural Studies, Francis Crick Avenue, Cambridge CB2 0QH, UK. [2]Department of Chemistry, Physical and Theoretical Chemistry Laboratory, University of Oxford, Oxford OX1 3QZ, UK.
*These authors contributed equally to this work. †Corresponding author. E-mail: cartera@mrc-lmb.cam.ac.uk

Dynactin structure determination

Dynactin is a challenging target for cryo-EM (*17*). This complex's extreme preferred orientation on EM grids makes it hard to obtain the broad distribution of views required for a three-dimensional (3D) reconstruction. Furthermore, dynactin's thin elongated shape limits its contrast, making it difficult to assign views accurately. We overcame these hurdles (*20*) to determine cryo-EM maps of native dynactin purified from pig brain (fig. S1), initially at 6.3 Å (Dynactin-1 in table S1) and subsequently at 4.0 Å overall and 3.5 Å in the dynactin filament (Dynactin-2, -3, and -4 in table S1; Fig. 1, A and B; fig. S2; and movies S1 and S2). We used both maps to build a model of dynactin (Fig. 1C and table S2). The filament and pointed-end–capping protein Arp11 were built de novo and refined (table S3). Homology models of the barbed-end–capping protein CapZαβ (*21*) and the pointed-end proteins p25 (DCTN5) and p27 (DCTN6) (*22*) were fitted into density. The pointed-end protein p62 and the shoulder—which contains p150^{Glued} (DCTN1), p50 (dynamitin or DCTN2), and p24 (DCTN3)—were built as backbone models (Fig. 1D).

The dynactin filament contains eight Arp-1 subunits and one β-actin

The dynactin filament is nine subunits long and consists of two protofilaments that wrap around each other (Fig. 1, A and C): five subunits (A, C, E, G, and I) in the top protofilament and four (B, D, F, and H) in the bottom. The presence of β-actin in the filament is controversial (*7*, *23*). Our cryo-EM map was of sufficient quality (fig. S3A) to show that subunit H is β-actin (β-actin–H), whereas the others are Arp1 (Arp1-A to Arp1-I). We confirmed the presence of Arp1 and β-actin at an 8:1 ratio by mass spectrometry (MS)–based label-free quantitative proteomic analysis (table S4).

Capping the dynactin filament

The dynactin filament is similar to that of actin (*24*), consistent with the high (53%) sequence identity between β-actin and Arp1 (fig. S3B). Both consist of four subdomains surrounding a nucleotide binding site (fig. S4). A key contact within the filament is the subdomain-2 loop binding the groove between subdomains 1 and 3 on the neighboring subunit. Blocking this interaction provides a mechanism to cap both actin and dynactin filaments.

At the barbed end of dynactin, a CapZαβ heterodimer binds across both protofilaments. The C-terminal helices (tentacles) of CapZα and CapZβ fit into the groove between subdomains 1 and 3 on Arp1-B and Arp1-A (Fig. 2A, fig. S5, and movie S3) and prevent further subunit binding. CapZαβ interacts with dynactin in the same way as proposed for the actin filament (*25*). However, there is a loop (called the "plug") (*24*) that contains four negatively charged residues in Arp1 but only one in actin (Fig. 2B). This loop is close to a cluster of four positively charged residues on CapZα, suggesting that CapZαβ binds Arp1 with a higher affinity than actin. This explains why a pool of CapZαβ remains bound to dynactin but not to actin, when most CapZαβ is depleted by small interfering RNA (*26*). The tight binding of CapZαβ reflects its role in stabilizing dynactin's structure.

At the pointed end, the bottom protofilament ends in β-actin, whereas the top ends in Arp1

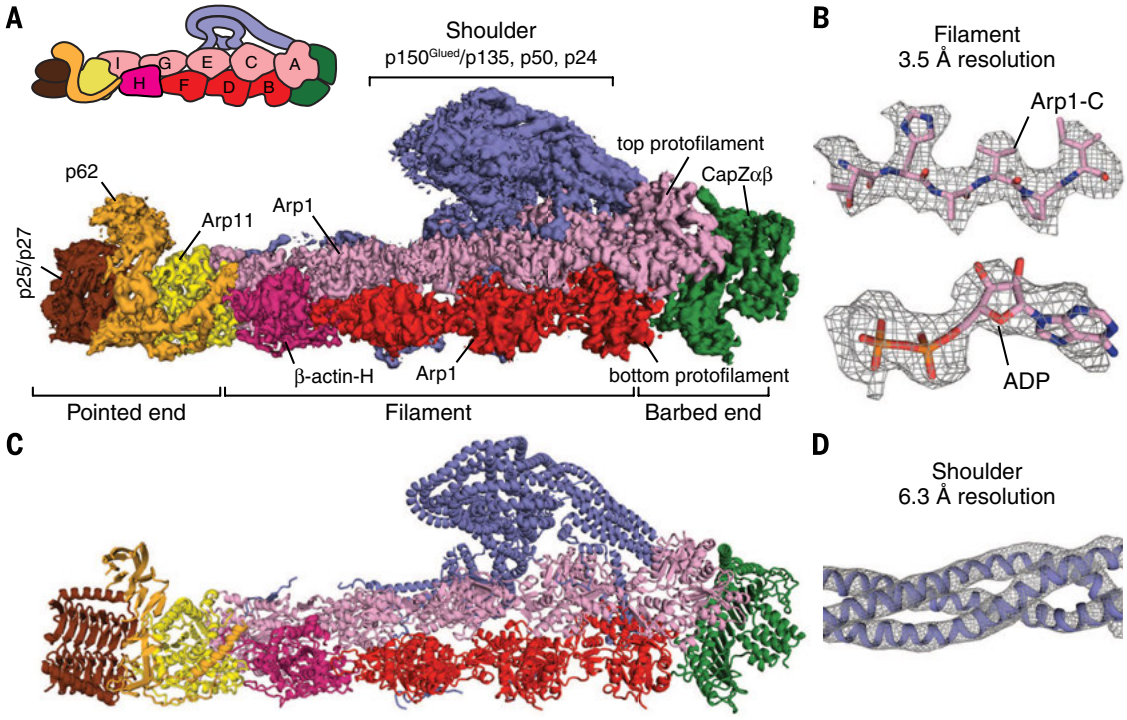

Fig. 1. Cryo-EM structure of dynactin. (**A**) A 4.0 Å cryo-EM map of dynactin segmented and colored according to its components. (**B**) A density map of a β strand and an adenosine diphosphate (ADP) molecule in Arp1-C. (**C**) A molecular model of dynactin. (**D**) A 6.3 Å cryo-EM map showing helices in the dynactin shoulder.

(Fig. 1A). This creates a distinctive binding site for Arp11, the most evolutionarily distant of all the actin-related proteins (*27*). Our structural data reveal how a single Arp11 subunit can cap both protofilaments. The bottom protofilament directly binds Arp11, preventing further subunit addition because its subdomain-2 loop is too short (*27*) (Fig. 2C). Subunit addition to the Arp1-I subunit on the top protofilament is blocked sterically by subdomain 4 of Arp11 (asterisk in Fig. 2D) and also because the Arp1-I subdomain-2 loop is sequestered by Arp11 (Fig. 2D).

Arp11 binds p25, p27, and p62 to form the pointed-end complex (Fig. 2E). The p25 and p27 subunits consist of a triangular β-sheet structure (*22*) followed by an α helix (fig. S6). They pack side to edge (fig. S6A) and bind end-on to Arp11 (Fig. 2F). The interaction is reinforced by p62, which wraps around the Arp11:p25-p27 contact site (Fig. 2E). Only Arp11 directly caps the pointed end, suggesting that the other components have a different role, such as cargo attachment (*28*), and explaining why some fungal species contain Arp11 but lack p25, p27, and p62 (*29*).

The p150^{Glued} projection extends more than 50 nm from the shoulder

Previous antibody labeling showed that p150^{Glued} forms dynactin's shoulder projection (*7*). Existing models suggest that it is 24 nm long and contains the p150^{Glued} N-terminal Cap-Gly domain and the CC1A coiled coil (Fig. 3A) (*7*, *8*). Owing to its flexibility, the projection is not visible in our high-resolution EM maps. However, we determined an 8.6 Å structure from a subset of particles (Fig. 3B, table S1, and fig. S7) in which it is visible because it docks against the side of dynactin (fig. S8, A and B). The projection is more than 50 nm long and contains three coiled coils, which we assigned to those in p150^{Glued} on the basis of their length (fig. S8C). An ~18-nm coiled coil (CC2) emerges from the shoulder and joins a globular domain consisting of a dimer (fig. S8D) of two ~40-kD subunits [intercoiled domain (ICD)]. Another ~24-nm coiled coil (CC1B) extends from the ICD before doubling back for ~18 nm (CC1A). Our model predicts that the Cap-Gly domain at the N terminus of CC1A is located close to the ICD. This is not visible in our structure, owing to its flexibility and because the majority of our dynactin contains the shorter isoform of p150^{Glued} (p135), which lacks a Cap-Gly domain (Fig. 3A). Our 50-nm projection is similar in appearance to structures observed in the images of dynactin viewed by rotary shadowing (*7*). Furthermore, the interaction made by CC1A folding back onto CC1B agrees with recent biochemical data (*30*).

The shoulder's symmetry is broken by binding the dynactin filament

Previous models suggest that the shoulder consists mainly of p150^{Glued} (*8*). Our finding that most of p150^{Glued} is in the projection implies that the shoulder contains predominantly p24 and p50. We confirmed that dynactin contains four copies of p50 and two copies of p24 (*27*), because the mass of dynactin calculated from this stoichiometry matches (table S5) that measured by MS (1,066,889 daltons) (Fig. 3C). We verified this composition by tandem MS (Fig. 3D) and by measuring the resulting subcomplexes (table S5).

The shoulder's flexibility results in a lower-resolution cryo-EM map and makes it challenging to assign individual α helices to specific proteins. Instead, the structures reveal an intrinsic twofold symmetry of the shoulder that was not obvious in previous images of dynactin (*17*). The shoulder contains two identical arms (Fig. 3, E and F) made of bundles of three α helices (Fig. 1D) that meet at a dimerization domain (fig. S9A). The end of each arm meets another short bundle of helices at an acute angle (hook domain) and a variably positioned paddle domain (Fig. 3E and fig. S9B). The symmetry between the two arms is broken as they twist to contact the dynactin filament.

The stoichiometry of p24 and p50 and their predicted helical and coiled-coil structures (*8*, *31*) suggest that each arm contains one helix from p24 and two from p50. The length of p24 (186 residues) is similar to the length of one arm, whereas that of p50 (401 residues) is longer, suggesting that p50 contributes to other structures such as the hook or paddle domain. The two p150^{Glued} copies enter the shoulder between the two arms (Fig. 3F) and then split and run

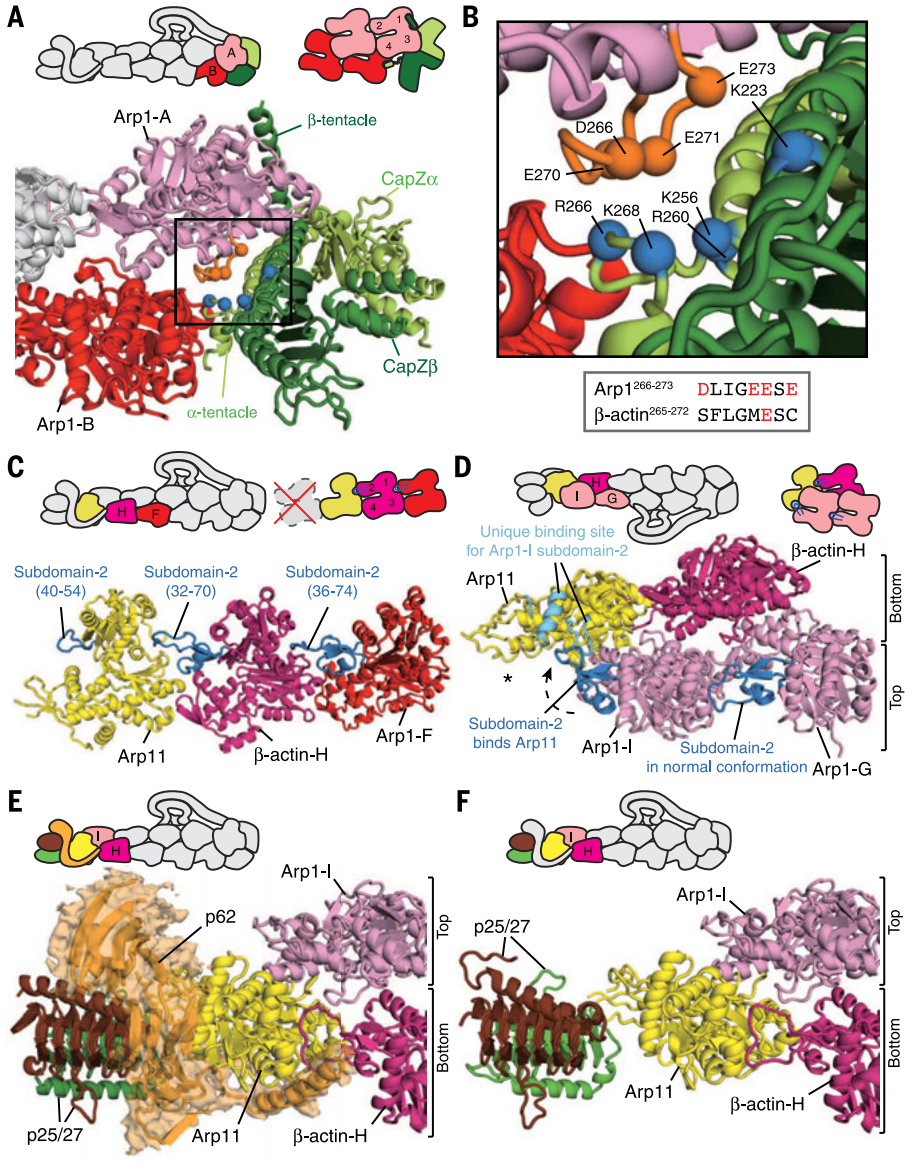

Fig. 2. Capping the dynactin filament. (**A**) The barbed end is capped by CapZαβ. (**B**) CapZαβ contains five positive residues (blue) that interact with four negative residues (orange) on Arp1. The equivalent loop in actin contains only one negative residue. C, Cys; D, Asp; E, Glu; F, Phe; G, Gly; I, Ile; K, Lys; L, Leu; M, Met; R, Arg; S, Ser. (**C**) The short Arp11 subdomain-2 loop prevents further subunit addition to the bottom protofilament. (**D**) Arp11 caps the top protofilament by binding the subdomain-2 loop of Arp1-I and sterically blocking (asterisk) subsequent subunit binding. (**E**) The pointed-end complex: p62 extends over Arp11 to touch β-actin–H. (**F**) p25 and p27 pack end-on to Arp11 as a continuation of the bottom protofilament.

along each arm before joining the hook domains. Thus, the role of the p150^{Glued} C terminus is to stick the two p50-p24 arms together.

Extended peptides from the shoulder span the length of the dynactin filament

The invariant size of the dynactin filament implies that some mechanism specifies its length (*7*, *17*, *32*). The shoulder is the best candidate for dynactin's molecular ruler. Its main body contacts four Arp1 subunits close to the barbed end (fig. S10). In addition, four extended regions (ERs) emerge from the shoulder and coat the rest of the filament (Fig. 4). The ends of all four are structurally identical (fig. S11, A to D), which suggests that they correspond to p50, the only tetramer in dynactin (*8*). The ERs are most likely the N termini of p50, which are predicted to be unstructured, contain a sequence that fits the clearest parts of the ER density (fig. S11E), and are able to displace the shoulder from the dynactin filament (*26*). Two pairs of ERs emerge from each shoulder paddle (Fig. 4, A and B). One of each pair contacts the top protofilament: ER-1 runs from Arp1-C to Arp1-E and ER-2 from Arp1-G to Arp1-I (Fig. 4C). The other reaches down to contact the bottom protofilament: ER-3 runs from Arp1-B to Arp1-D, and ER-4 contacts Arp1-F (Fig. 4D). The ends of all four ERs occupy a positively charged groove on the dynactin filament that is equivalent to the tropomyosin binding groove on actin (*33*) (fig. S12, A and B). Although it is structurally different from tropomyosin (*24*), the N terminus of p50 is similarly rich in negatively charged residues (fig. S12C), which explains why both bind an equivalent site.

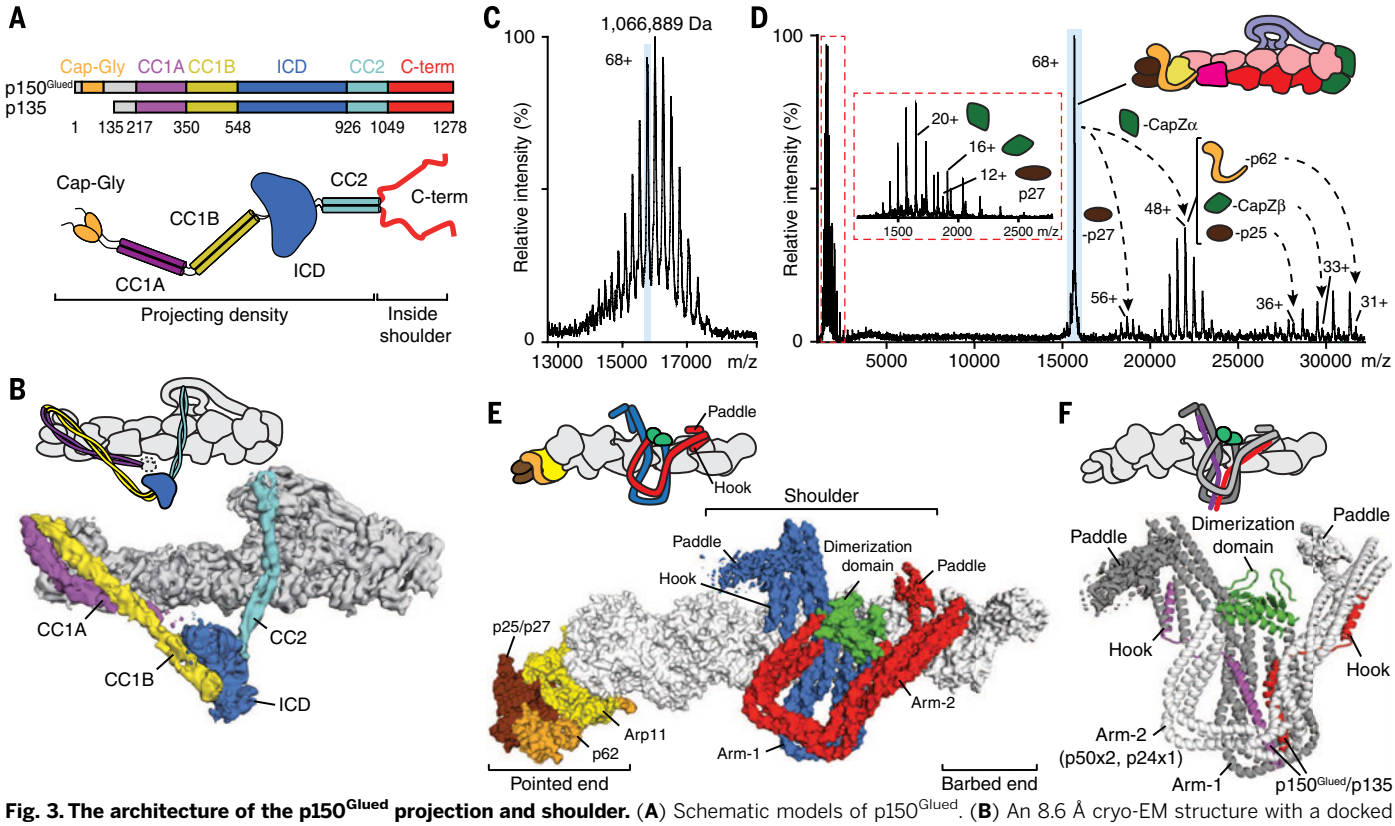

Fig. 3. The architecture of the p150^{Glued} projection and shoulder. (**A**) Schematic models of p150^{Glued}. (**B**) An 8.6 Å cryo-EM structure with a docked p150^{Glued} projection, colored according to (A). (**C**) Native MS of dynactin reveals the mass of the intact complex. m/z, mass/charge ratio. (**D**) Tandem MS confirms the subunit composition of the complex. (**E**) The shoulder contains two arms (red and blue) that emerge from a dimerization center (green) and end in hook and paddle domains. (**F**) The C terminus of the p150^{Glued} dimer enters the shoulder and splits into separate helices.

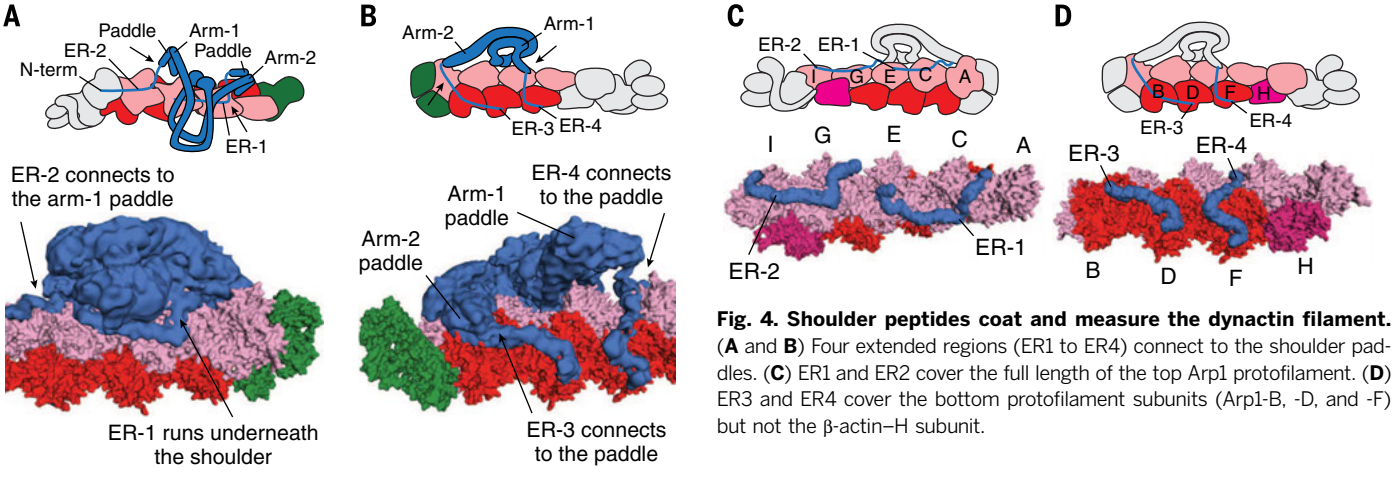

Fig. 4. Shoulder peptides coat and measure the dynactin filament. (**A** and **B**) Four extended regions (ER1 to ER4) connect to the shoulder paddles. (**C**) ER1 and ER2 cover the full length of the top Arp1 protofilament. (**D**) ER3 and ER4 cover the bottom protofilament subunits (Arp1-B, -D, and -F) but not the β-actin–H subunit.

The shoulder and its ERs contact every filament subunit except for β-actin–H (fig. S12, D and E), suggesting the following model for dynactin assembly. The shoulder and ERs recruit eight Arp1s and stabilize their polymerization into a structure with five subunits on the top protofilament and three on the bottom. The gap in position H is filled by β-actin, perhaps owing to actin's high abundance in the cell. The interface formed by Arp1-I and β-actin–H specifically recruits Arp11. Together with CapZαβ binding to the barbed end, this results in a highly stable complex of an exactly defined length.

Dynein and BICD2 bind the dynactin filament

Dynein, dynactin, and the N terminus of BICD2 (BICD2N) form a stable complex only when all three components are present (*12*–*14*). In this dynein-dynactin-BICD2N (DDB) complex, dynein binds dynactin via its tail, whereas its motor domains remain flexible (*13*). Currently there are no 3D structures of either the dynein tail or its interaction with dynactin. We therefore formed a stable tail-dynactin-BICD2N (TDB) complex (fig. S13) and determined its structure by cryo-EM to 8.2 Å (fig. S14 and movie S4).

The dynein tail binds directly to the Arp1 filament (Fig. 5, A and B), stretching from β-actin–H to the barbed end. The interaction is stabilized by a ~270-residue coiled coil of BICD2N that runs the length of the filament. Projections of the TDB complex are very similar to negative-stain images of the DDB complex (fig. S15) (*13*), suggesting that the flexible, C-terminal motor domains of dynein lie close to the barbed end of dynactin (fig. S15). To determine the orientation of BICD2N, we removed the N-terminal green fluorescent protein tag (table S1 and fig. S16) and showed that the globular density at one end disappeared (fig. S16). Therefore, the BICD2N N terminus lies close to the barbed end, and its C terminus emerges from the pointed end. The C terminus of BICD2 and the pointed-end complex of dynactin, which are implicated in cargo binding (*28*, *34*), are thus diametrically opposed to the dynein motor domains (Fig. 5A).

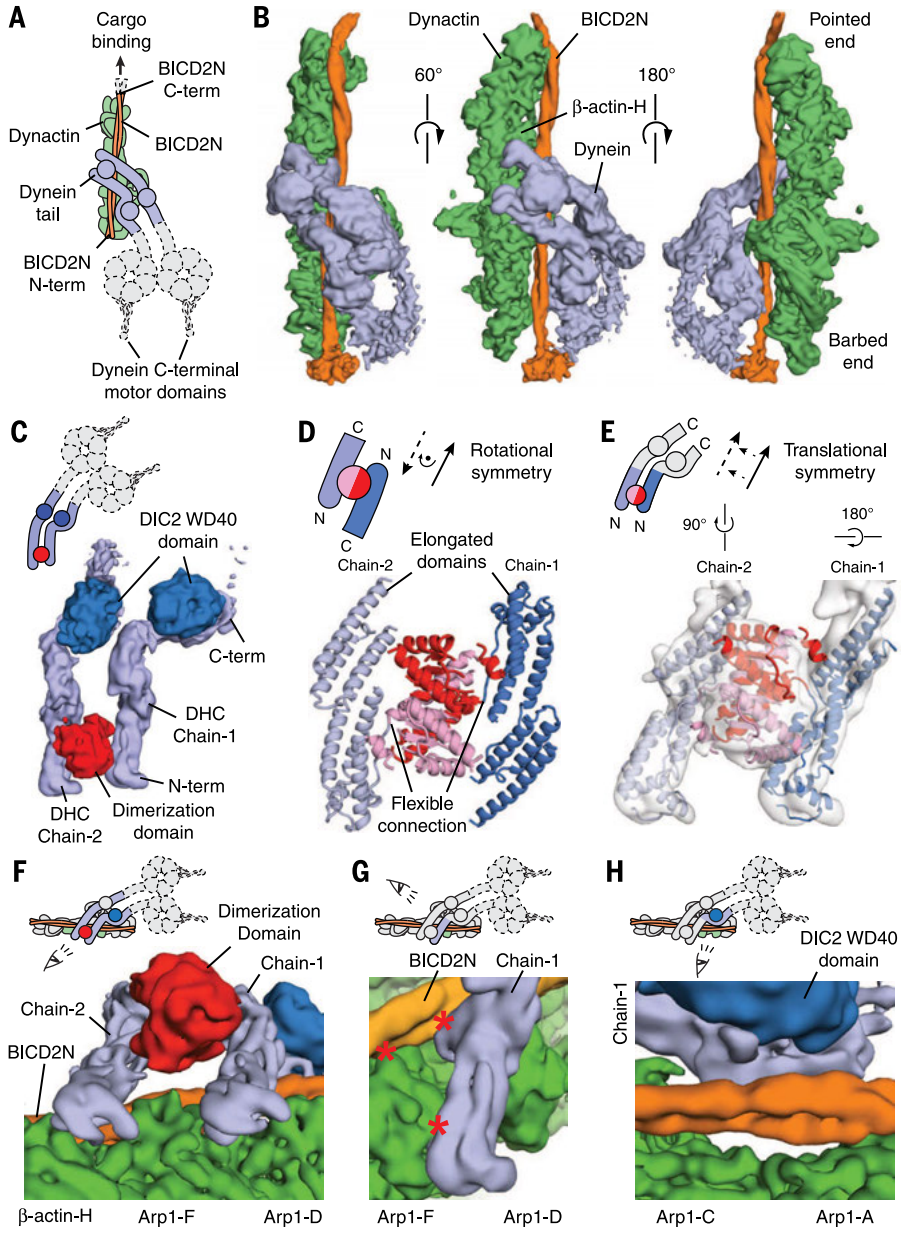

Fig. 5. The dynein tail and its interaction with dynactin and BICD2N. (**A**) Cartoon model of the dynein tail–dynactin–BICD2N complex (TDB). (**B**) An 8.2 Å cryo-EM structure of TDB. (**C**) An N-terminal domain dimerizes the dynein heavy chain (DHC) elongated domains, which wrap around the dynein intermediate chain (DIC2). (**D**) Crystal structure of the *S. cerevisiae* DHC N terminus (Dyn1$^{1\text{-}557}$). (**E**) The Dyn1$^{1\text{-}557}$ structure fits well into the cryo-EM map. (**F**) The translational symmetry of DHC chains 1 and 2 matches the dynactin filament. (**G**) Interaction of chain 1 with BICD2N and dynactin (asterisks). (**H**) The second interaction site of chain 1 with dynactin is solely mediated by BICD2N.

The dynein heavy chain contains an N-terminal dimerization domain

The dynein tail consists of two copies of the dynein heavy chain (DHC), intermediate chain (DIC2), light intermediate chain (DLIC1), and light chains (Roadblock, Tctex, and LC8). The tail, within the TDB complex, contains two elongated S-shaped domains corresponding to the DHCs: chain 1 and chain 2 (Fig. 5C). The DHC C termini, which contain the binding site for DLIC1 (*35*), are mainly disordered (Fig. 5B). The middle of each DHC wraps around a circular density corresponding in size, shape, and position (*35*) to the WD40 β propeller of DIC2 (Fig. 5C and fig. S17). Toward their N termini, the two DHC chains are joined by a small (~40 kDa) globular domain (Fig. 5C). We hypothesized that this domain represents a previously unknown dimerization domain of the DHC itself. To verify this, we determined a crystal structure of the N-terminal 557 amino acids of the *Saccharomyces cerevisiae* DHC (Dyn1$^{1\text{-}557}$) to 5 Å resolution (Fig. 5D, fig. S18, and table S6). This shows two elongated domains, made up of bundles of α helices, that fit well with the helices observed by cryo-EM (fig. S18, C and D). Furthermore, it reveals that the elongated domains are joined by an N-terminal dimerization domain (Fig. 5D).

In the crystal structure, the elongated domains are related by rotational symmetry, with their C termini pointing in opposite directions (Fig. 5D). In the TDB structure, each elongated domain has rotated about the flexible connection to the dimerization domain (movie S5) so that they lie parallel to each other (Fig. 5E). This is probably caused by the light-chain–mediated dimerization of DIC2 (*36*, *37*), which serves to hold the DHCs together toward their C termini.

The symmetry in the dynein tail matches the dynactin filament

The N termini of the elongated domains have translational symmetry (a sideways movement relates

one onto the other) (Fig. 5E), which matches that of their binding sites on the filament (Fig. 5F). They bind adjacent clefts between Arp1-D and -F (chain 1) and Arp1-F and β-actin–H (chain 2) (Fig. 5, F and G). These sites are equivalent to the myosin motor binding site on actin (fig. S19 and movie S6). The translational symmetry between DHC chains is lost toward their C termini as chain 2 twists relative to chain 1 (Fig. 5C). Chain 2 makes no further contacts with the dynactin filament, whereas chain 1 binds it again at Arp1-A and -C (Fig. 5H).

BICD2N is involved in all interactions between the dynein tail and the dynactin filament (Fig. 5, F, G, and H; and movie S7). In the clefts between Arp1-D and -F and between Arp1-F and β-actin–H, BICD2N stabilizes the interaction of the DHC chains with the filament (Fig. 5G). At the Arp1-A and -C site, BICD2N sits between chain 1 and dynactin. The network of contacts from BICD2N to dynein, BICD2N to dynactin, and dynein to dynactin explains why all three components must be present to form a stable complex (*12*–*14*). The long BICD2N coiled coil may be suited as a cargo adaptor because it spans the length of the dynactin filament. Many other dynein adaptors—including TRAK1 and -2 (*38*); RILP (*39*); and Rab11-Fip3, Hook3, and Spindly (*14*)—contain coiled coils and may recruit dynein and dynactin in a similar way. The requirement to form a three-way complex would reduce the chance of stochastic binding of dynein to its cargos.

The shoulder coats three sides of the filament (fig. S12, D and E), leaving the front face free for interaction with BICD2N and the dynein tail. We do not observe a direct interaction between the shoulder and dynein in our structure. However, the well-reported interaction between the p150^{Glued} CC1 region of dynactin and the N terminus of DIC2 (*11*) is too flexible to be visualized directly. The p150^{Glued} projection binds to the same face of the dynactin filament as BICD2N (Figs. 3B and 5, A and B), and both occupy the same cleft on the pointed-end complex (fig. S8B and Fig. 5B). Thus, BICD2N binding could free p150^{Glued} CC1 to make contact with DIC2 and so add an additional contact that stabilizes the TDB complex.

How does recruitment of dynactin by a cargo adaptor (*13*, *14*) activate dynein? Both the microtubule binding Cap-Gly (*14*) and DIC2 binding CC1B (*30*) regions of p150^{Glued} have been implicated. Our structure raises a third, but not mutually exclusive, possibility. Studies with artificially dimerized dynein motor domains suggest that they self-associate in an auto-inhibited conformation unless they are sufficiently separated (*40*). We suggest that dynactin activates the motor domains by reorienting the two DHCs. Both DHC N termini are anchored parallel to each other, but the C termini are forced to twist apart because only one chain binds the second site on dynactin. This hypothesis explains why dynactin is built around an actin-like filament. The translational symmetry of the filament matches that of the DHC N termini, whereas the filament length provides additional binding sites that force dynein to adopt its active conformation.

REFERENCES AND NOTES

1. S. R. Gill *et al.*, *J. Cell Biol.* **115**, 1639–1650 (1991).
2. M. McGrail *et al.*, *J. Cell Biol.* **131**, 411–425 (1995).
3. M. Plamann, P. F. Minke, J. H. Tinsley, K. S. Bruno, *J. Cell Biol.* **127**, 139–149 (1994).
4. V. J. Allan, *Biochem. Soc. Trans.* **39**, 1169–1178 (2011).
5. G. Schiavo, L. Greensmith, M. Hafezparast, E. M. C. Fisher, *Trends Neurosci.* **36**, 641–651 (2013).
6. M. P. Dodding, M. Way, *EMBO J.* **30**, 3527–3539 (2011).
7. D. A. Schafer, S. R. Gill, J. A. Cooper, J. E. Heuser, T. A. Schroer, *J. Cell Biol.* **126**, 403–412 (1994).
8. T. A. Schroer, *Annu. Rev. Cell Dev. Biol.* **20**, 759–779 (2004).
9. A. E. Siglin *et al.*, *PLOS ONE* **8**, e59453 (2013).
10. C. Duellberg *et al.*, *Nat. Cell Biol.* **16**, 804–811 (2014).
11. S. J. King, C. L. Brown, K. C. Maier, N. J. Quintyne, T. A. Schroer, *Mol. Biol. Cell* **14**, 5089–5097 (2003).
12. D. Splinter *et al.*, *Mol. Biol. Cell* **23**, 4226–4241 (2012).
13. M. A. Schlager, H. T. Hoang, L. Urnavicius, S. L. Bullock, A. P. Carter, *EMBO J.* **33**, 1855–1868 (2014).
14. R. J. McKenney, W. Huynh, M. E. Tanenbaum, G. Bhabha, R. D. Vale, *Science* **345**, 337–341 (2014).
15. M. Dienstbier, X. Li, *Biochem. Soc. Trans.* **37**, 1066–1071 (2009).
16. J. L. Hodgkinson, C. Peters, S. A. Kuznetsov, W. Steffen, *Proc. Natl. Acad. Sci. U.S.A.* **102**, 3667–3672 (2005).
17. H. Imai, A. Narita, Y. Maéda, T. A. Schroer, *J. Mol. Biol.* **426**, 3262–3271 (2014).
18. J. B. Bingham, T. A. Schroer, *Curr. Biol.* **9**, 223–226 (1999).
19. X.-C. Bai, G. McMullan, S. H. W. Scheres, *Trends Biochem. Sci.* **40**, 49–57 (2015).
20. Materials and methods are available as supplementary materials on *Science* Online.
21. A. Yamashita, K. Maeda, Y. Maéda, *EMBO J.* **22**, 1529–1538 (2003).
22. T. Y. Yeh *et al.*, *EMBO J.* **32**, 1023–1035 (2013).
23. E. A. Holleran, M. K. Tokito, S. Karki, E. L. Holzbaur, *J. Cell Biol.* **135**, 1815–1829 (1996).
24. J. von der Ecken *et al.*, *Nature* 10.1038/nature14033 (2014).
25. A. Narita, S. Takeda, A. Yamashita, Y. Maéda, *EMBO J.* **25**, 5626–5633 (2006).
26. F. K. Y. Cheong, L. Feng, A. Sarkeshik, J. R. Yates III, T. A. Schroer, *Mol. Biol. Cell* **25**, 2171–2180 (2014).
27. D. M. Eckley *et al.*, *J. Cell Biol.* **147**, 307–320 (1999).
28. T. Y. Yeh, N. J. Quintyne, B. R. Scipioni, D. M. Eckley, T. A. Schroer, *Mol. Biol. Cell* **23**, 3827–3837 (2012).
29. B. Hammesfahr, M. Kollmar, *BMC Evol. Biol.* **12**, 95 (2012).
30. S. K. Tripathy *et al.*, *Nat. Cell Biol.* **16**, 1192–1201 (2014).
31. K. K. Pfister, S. E. Benashski, J. F. Dillman III, R. S. Patel-King, S. M. King, *Cell Motil. Cytoskeleton* **41**, 154–167 (1998).
32. J. P. Lees-Miller, D. M. Helfman, T. A. Schroer, *Nature* **359**, 244–246 (1992).
33. E. Behrmann *et al.*, *Cell* **150**, 327–338 (2012).
34. Y. Liu *et al.*, *Genes Dev.* **27**, 1233–1246 (2013).
35. S. H. Tynan, M. A. Gee, R. B. Vallee, *J. Biol. Chem.* **275**, 32769–32774 (2000).
36. J. C. Williams *et al.*, *Proc. Natl. Acad. Sci. U.S.A.* **104**, 10028–10033 (2007).
37. G. Benison, P. A. Karplus, E. Barbar, *J. Mol. Biol.* **371**, 457–468 (2007).
38. M. van Spronsen *et al.*, *Neuron* **77**, 485–502 (2013).
39. I. Jordens *et al.*, *Curr. Biol.* **11**, 1680–1685 (2001).
40. T. Torisawa *et al.*, *Nat. Cell Biol.* **16**, 1118–1124 (2014).

ACKNOWLEDGMENTS

We thank S. Scheres and X. Bai for cryo-EM advice; G. McMullan, C. Savva, J. Grimmett, and T. Darling for technical support; S. Leech for fresh pig brains; V. Beilsten-Edmands for assistance with proteomic analyses; S. Bullock, R. McKenney, and J. Pennell for comments on the manuscript; and Y. Toyoshima for sharing her unpublished negative-stain EM model of the p150^{Glued} projection, which helped us to interpret our observations. This work was funded by the Medical Research Council, UK (MC_UP_A025_1011), and a Wellcome Trust New Investigator Award (WT100387). Cryo-EM maps are deposited with the Electron Microscopy Data Bank (EMD-2854, EMD-2855, EMD-2856, EMD-2857, EMD-2860, EMD-2861, and EMD-2862), and coordinates are deposited with the Protein Data Bank (5AFT, 5AFU, and 5AFR). Author contributions: L.U. prepared dynactin and determined the TDB structure. K.Z. determined the structure of dynactin. A.G.D. and M.Y. determined the crystal structure of the DHC N terminus. C.M. and M.A.S. prepared the dynein tail complex. N.A.P. and C.V.R performed MS. A.P.C. initiated the project and designed the experiments.

SUPPLEMENTARY MATERIALS

www.sciencemag.org/content/347/6229/1441/suppl/DC1
Materials and Methods
Figs. S1 to S19
Tables S1 to S6
References (*41*–*65*)
Movies S1 to S7

2 December 2014; accepted 30 January 2015
Published online 12 February 2015;
10.1126/science.aaa4080

DNA ORIGAMI

Dynamic DNA devices and assemblies formed by shape-complementary, non–base pairing 3D components

Thomas Gerling, Klaus F. Wagenbauer, Andrea M. Neuner, Hendrik Dietz*

We demonstrate that discrete three-dimensional (3D) DNA components can specifically self-assemble in solution on the basis of shape-complementarity and without base pairing. Using this principle, we produced homo- and heteromultimeric objects, including micrometer-scale one- and two-stranded filaments and lattices, as well as reconfigurable devices, including an actuator, a switchable gear, an unfoldable nanobook, and a nanorobot. These multidomain assemblies were stabilized via short-ranged nucleobase stacking bonds that compete against electrostatic repulsion between the components' interfaces. Using imaging by electron microscopy, ensemble and single-molecule fluorescence resonance energy transfer spectroscopy, and electrophoretic mobility analysis, we show that the balance between attractive and repulsive interactions, and thus the conformation of the assemblies, may be finely controlled by global parameters such as cation concentration or temperature and by an allosteric mechanism based on strand-displacement reactions.

To form complexes with other molecules, proteins often interact via shape-complementary interfaces to select and constrain the position of binding partners (*1*, *2*). Proteins also tend to form only fragile contact interactions that enable turnover and allow for conformational dynamics. Proteins thus teach a versatile principle for self-assembling complex and dynamic macromolecular objects, which entails encoding building blocks in sequence space and

programming the structure and dynamics of higher-order complexes via weak interactions in shape space. More rarely, nucleic acid molecules can bind through weaker interactions than base pairing. Such recognition occurs between ribonuclease P (RNase P), an RNA-based enzyme, and its substrate, pre–transfer RNA (tRNA), which undergoes cleavage of its 5′ leader strand to yield mature tRNA (*3*). Here, we imitate the principle by which RNase P recognizes tRNA using programmable self-assembly with DNA (*4*–*12*) to produce discrete, shape-complementary three-dimensional (3D) components that interact via short-ranged, nucleobase stacking bonds. We present three means for actively influencing the conformation of objects once assembled: (i) changing cation concentration; (ii) changing solution temperature; and (iii) a site-directed allosteric mechanism based on toehold-mediated strand displacement reactions (*13*–*20*). With our method, a designer can encode a diversity of readily reconfigurable DNA devices and assemblies based on simple geometrical considerations and without having to program detailed strand sequences for connecting components.

Physik Department, Walter Schottky Institute, Technische Universität München Am Coulombwall 4a, 85748 Garching near Munich, Germany
*Corresponding author. E-mail: dietz@tum.de

In the system that inspired our assembly strategy, RNase P forms a particular tertiary fold that contains two structurally separated regions: one that scaffolds the active site and another that binds and orients the tRNA substrate (*21*) (Fig. 1A). Specifically, the acceptor stem and the T loop of tRNA appear to "click" precisely into a correspondingly shaped binding pocket in RNase P where they are held in place by a few nucleobase stacking interactions with the S domain of RNase P (Fig. 1A) (*21*). Together with the finding that edge-complementary single-layer DNA objects can interact specifically via DNA blunt-end stacking interactions on 2D substrates (*22*–*24*), we hypothesized that stacking interactions might suffice to stabilize 3D higher-order complexes made from multilayer DNA objects in solution.

Motif design

We thus abstracted and translated the type of shape recognition RNase P shows for tRNA to the

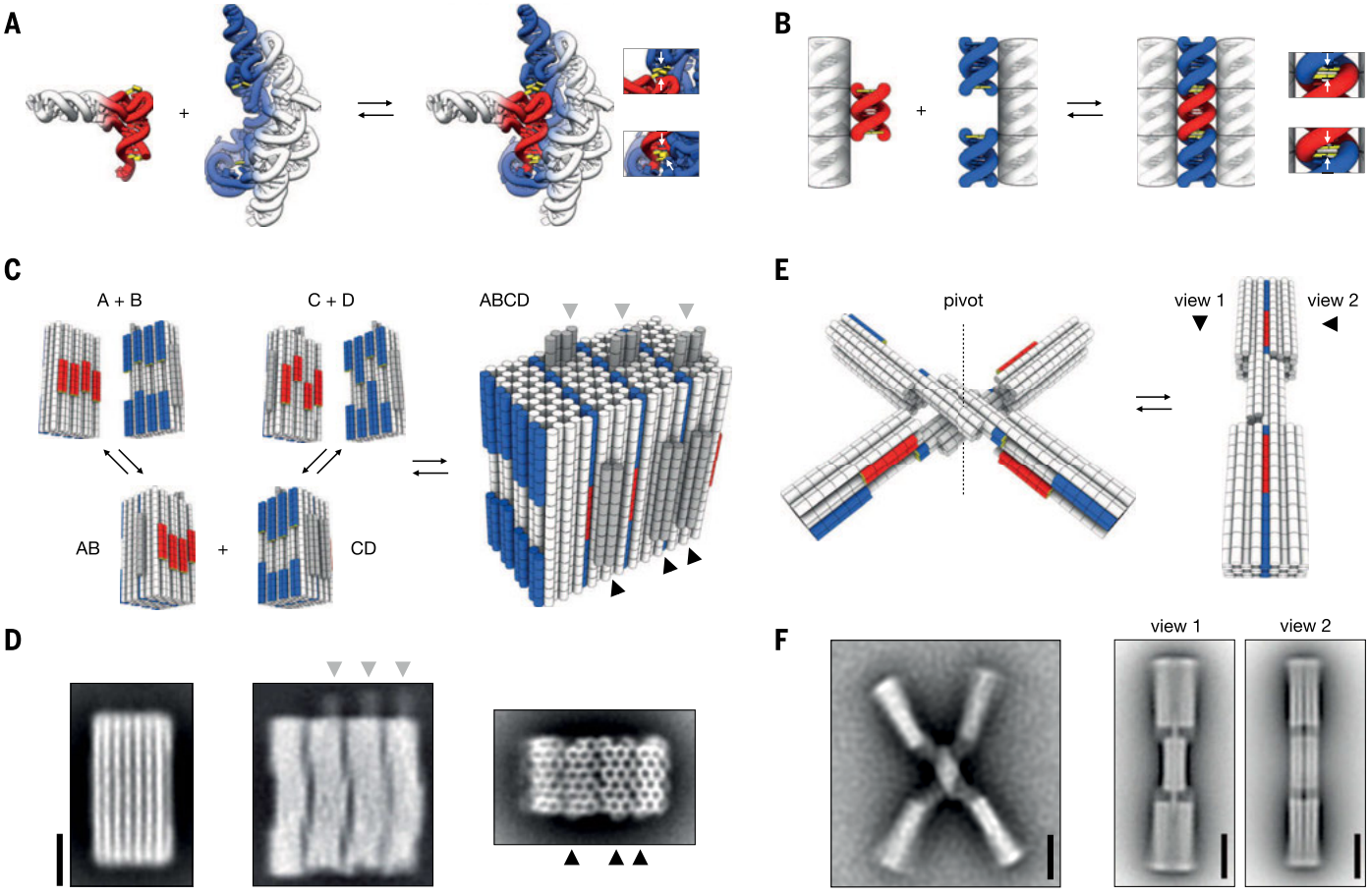

Fig. 1. Translating nonhybridization-based shape recognition principles from natural RNA to synthetic DNA objects. (**A**) Illustration of the mechanism by which RNase P (blue and gray) recognizes tRNA (red and gray). Red: T-loop and the acceptor stem of tRNA. Blue: the shape-complementary binding pocket in RNase P. Yellow: interfacial nucleobases that interact through stacking interactions when tRNA binds to RNase P. The images were prepared with UCSF Chimera (*28*) based on the atomic coordinates listed in 3Q1R.pdb (*29*). (**B**) Schematic representation of RNAse P–inspired shape recognition between complementary DNA components. Cylinder elements indicate double-helical DNA domains that are one helical turn long. (**C**) Schematic representation of four shape-complementary, orthogonal multilayer DNA origami bricks. Double-helical DNA domain protrusions are highlighted in red; recessions are shown in blue. Asymmetrical features are indicated in dark gray. Arrowheads indicate asymmetric features along the helical and along the honeycomb pattern, respectively. Models are tilted such that the shape-complementary patterns for forming dimers AB and CD, and tetramer ABCD, are visible. AB and CD dimers thus show the faces of bricks B and C, respectively, that are not visible in the monomer models above. (**D**) Average negative-stain TEM micrographs of the self-assembled DNA tetrameric object ABCD in the presence of 25 mM $MgCl_2$. Black and gray arrowheads highlight the density from the designed asymmetrical features, as indicated above in (C). Scale bar, 20 nm. (**E**) Schematics of a switch object with one rotational degree of freedom in the open and closed conformations. Shape-complementary DNA double-helical domain protrusions and recessions are highlighted in red and blue, respectively. (**F**) Average negative-stain TEM micrographs of switch particles. Left: open state as populated in the presence of 5 mM $MgCl_2$. Right: two orthogonal transmission projections of the closed state, which is adopted in the presence of 25 mM $MgCl_2$. Scale bars, 20 nm.

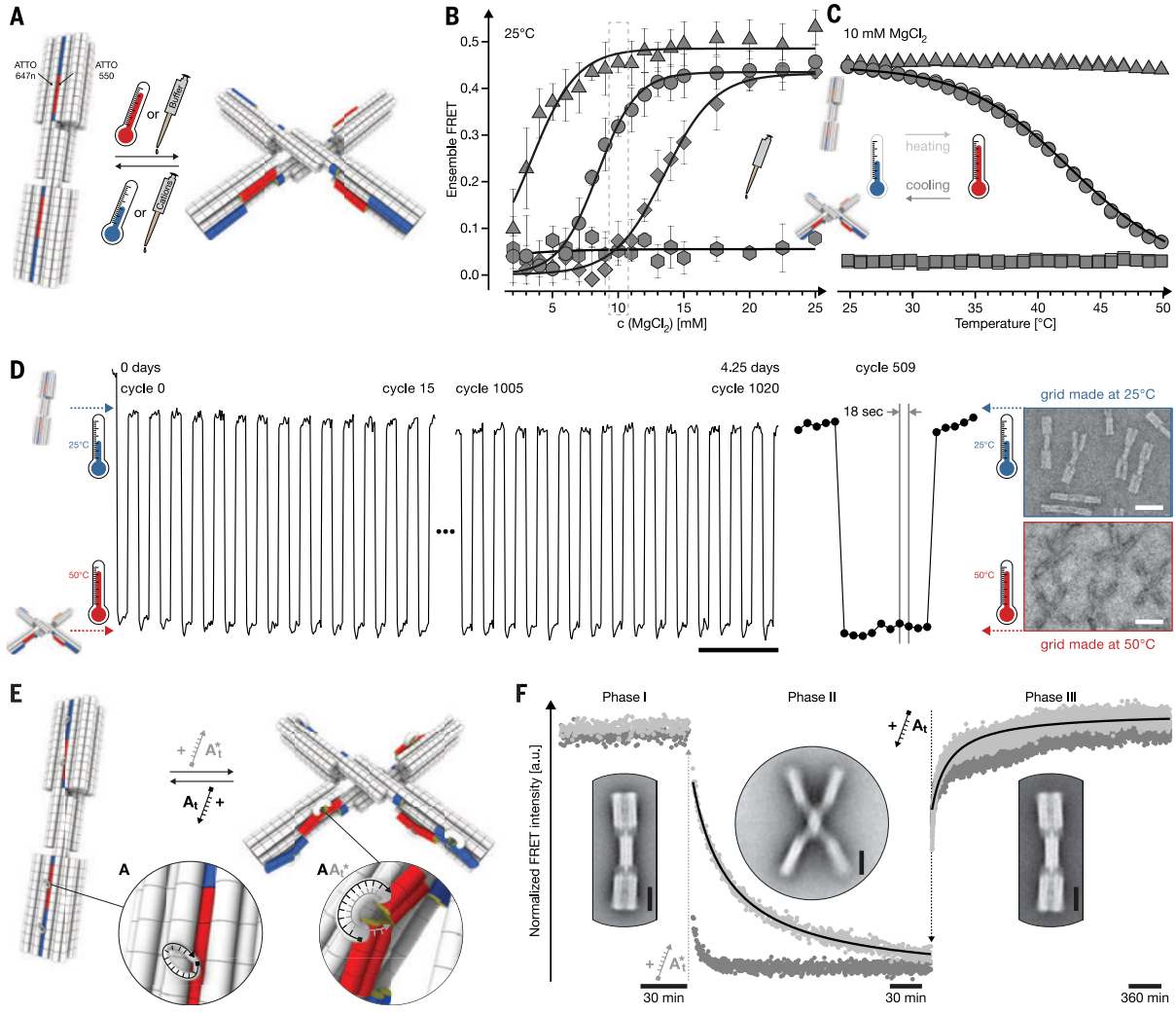

Fig. 2. Reversible reconfiguration of shape-complementary DNA objects by changes in cation concentration or temperature and with a site-specific allosteric control mechanism. (**A**) Schematics of the switch object in the open and closed conformations, as in Fig. 1E. Arrows indicate positions of the organic dyes Atto550 and Atto647n, respectively, that were installed to enable a FRET-based readout of the conformation of switch ensembles in solution. (**B**) Ensemble FRET measured via donor quenching when titrating the concentration of $MgCl_2$ in solutions containing switch variants. Triangles: a variant with three-base-long hybridization bonds instead of stacking bonds at 16 sites. Circles and diamonds: variants with 16 or 12 possible stacking bonds in the closed state, respectively. Hexagon: a variant that cannot form stacking bonds to stabilize the closed state. The titrations were performed each in triplicate; error bars are the SD from the mean value. Solid lines: fit using a two-state model with a free-energy term that depends linearly on the cation concentration. The free-energy difference between the closed and open states at 5 mM $MgCl_2$ is +2.8 and +1.6 kcal/mol for the versions with 12 and 16 designed stacking contacts, respectively. The free energy changes by −0.36 and −0.42 kcal/mol per 1 mM $MgCl_2$ added for the versions with 12 and 16 designed stacking contacts, respectively. See fig. S35 for data obtained when titrating NaCl. (**C**) Temperature-dependent ensemble FRET measurements in solution, acquired for three switch variants. Triangles indicate the variant with hybridization bonds as in (B); squares indicate a static switch variant that is locked in the open state (see fig. S34); circles denote a gel-purified dynamic switch version with 16 stacking interactions. Solid line: two-state model fit with parameters ΔH = 46.2 kcal/mol and ΔS = 0.146 kcal/(mol•K). (**D**) Absolute intensity (in units "counts") of the acceptor dye emission upon donor dye excitation (no normalization) as measured during 1020 cycles of temperature jumping with 3-min-long dwells at 25° and 50°C for the switch version with 16 stacking interactions [circles in (B)]. High-intensity levels at 25°C correspond to >90% of closed switches, and low-intensity levels at 50°C to <10% closed switches, as observed by TEM imaging. The experiment was performed in the presence of 11 mM $MgCl_2$ in solution. (Inset) Negative-stain TEM images acquired from samples fixated at 25°C and fixated at 50°C. See methods section. Scale bars, 50 nm. (**E**) Schematics of allosterically active switch objects. Insets highlight single-stranded DNA loops that were installed in the vicinity of the shape-complementary beam interfaces. A^*_t and A_t denote DNA single strands. A^*_t is complementary to the single-stranded loops on the switch and features an additional nine-bases-long toehold motif. A_t is fully complementary to A^*_t and can be used to displace A^*_t again from the switch. (**F**) Time-resolved ensemble FRET measurements with allosterically active switch objects. Absolute acceptor emission intensity upon donor excitation was normalized to the acceptor emission upon direct excitation to compensate dilution effects. Phase I: switch particles were equilibrated in 45 mM $MgCl_2$. The high FRET level corresponds to switch particles in the closed state, as corroborated by direct TEM imaging. Phase II: A^*_t was added to the solution. The FRET signal drops to levels consistent with switch opening. Phase III: A_t was added to the solution. The FRET signal increases again to the original high FRET levels. Light gray: experiment performed with A^*_t and A_t at 50 and 100 nM effective concentration, respectively. Dark gray: A^*_t and A_t at 0.4 and 0.8 μM effective concentration. Solid lines: fit according to a bimolecular reaction model with zero off-rate and equimolar reactant concentrations. Phase II: on-rate = 3.1×10^4 1/(M·s); phase III: on-rate = 0.7×10^4 1/(M·s). (Insets) Average TEM micrographs acquired from samples in the respective phases. Scale bars, 20 nm.

arena of DNA molecules. Blunt-ended double-helical DNA protrusions on one domain assume the role of the tRNA acceptor stem, and corresponding recessions on another domain mimic the RNase P binding pocket (Fig. 1B). Nucleobase stacking interactions engage at the double-helical interfaces of the shape-complementary protrusions and recessions when the two domains are brought into contact, but only upon correct fit of the helices and given correct helical orientation of the interfacial nucleobase pairs. We used these building blocks in a combinatorial fashion (Fig. 1C) to create libraries of shape-complementary motifs. Shape-complementary partners will be accepted and precisely oriented, but noncomplementary binding partners will be sterically rejected.

To illustrate the shape selectivity and the ability of our recognition scheme to constrain the

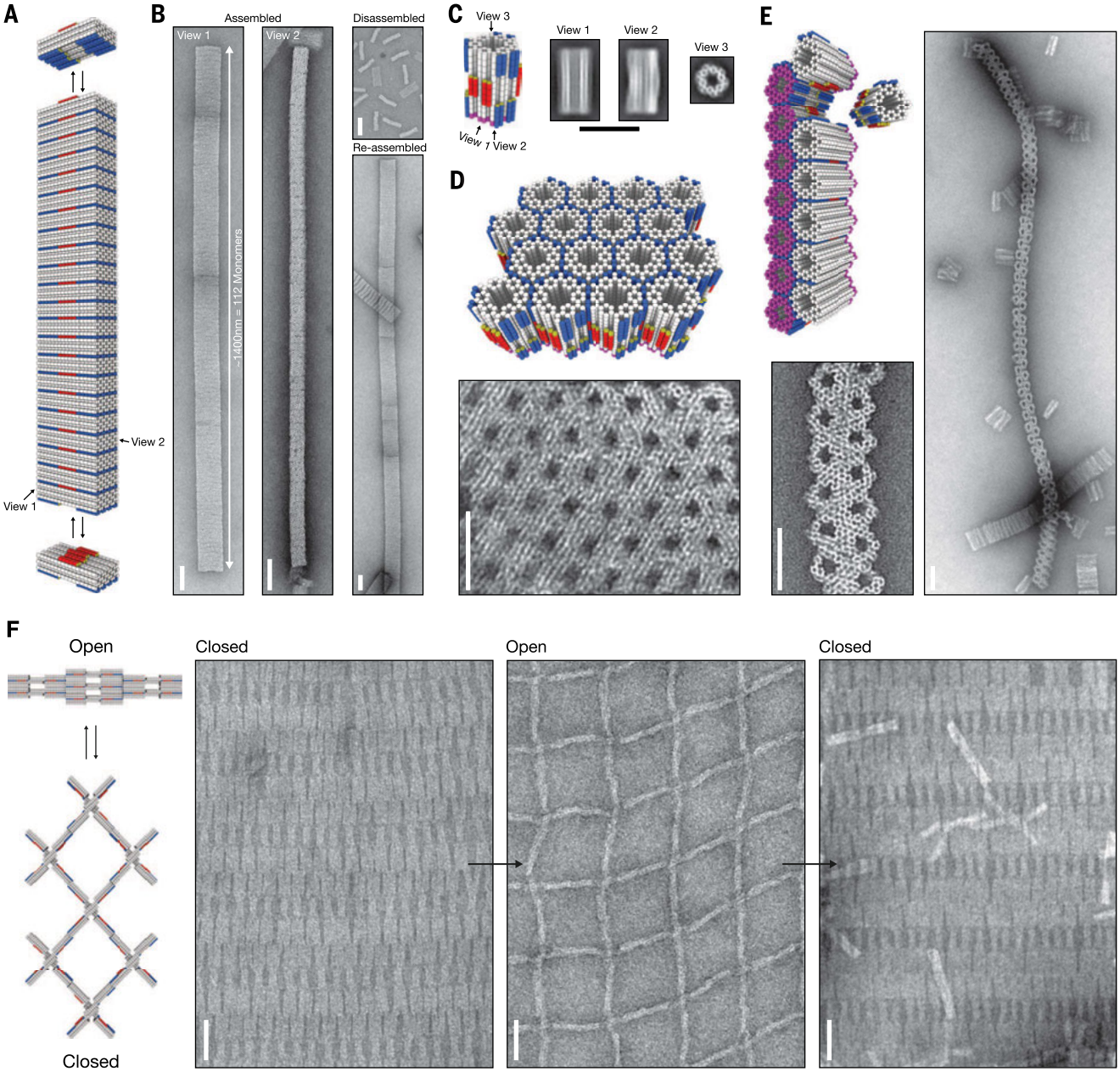

Fig. 3. Self-assembly of higher-order non–base pairing shape-complementary DNA objects, demonstrating long-range order, ability to template multimerization geometries by shape, and reconfigurability. (**A**) Schematic representation of filaments formed by cation-dependent reversible multimerization of a self-complementary multilayer DNA origami brick. (**B**) Negative-stain TEM micrographs showing typical filaments that grow in the presence of 25 mM $MgCl_2$. When the cation concentration is reduced to 5 mM $MgCl_2$, the filaments fall apart (top right). Increasing the cation concentration to 25 mM $MgCl_2$ gives filaments again (bottom right). Scale bar, 50 nm. (**C**) Schematic representation of a multilayer DNA origami hexagon with shape-complementary patterns of protrusions and recessions. Averaged single-particle negative-stain TEM micrographs of the hexagon in different views were acquired at 10 mM $MgCl_2$. Scale bar, 50 nm. (**D**) Schematic representation of a reconfigurable lattice formed by 2D polymerization of the hexagon and a typical negative-stain TEM micrograph acquired in the presence of 38 mM $MgCl_2$. Scale bar, 50 nm. (**E**) Schematic representation of a two-stranded filament that is formed from a modified hexagon (see fig. S82) and negative-stain TEM micrographs acquired at 35 mM $MgCl_2$. Scale bar, 50 nm. (**F**) Left: schematic representation of reconfigurable lattices formed by 2D polymerization of dynamic switch particles with 16 stacking interactions (see fig. S87). Negative-stain TEM micrographs of switch lattices taken at 25 mM $MgCl_2$ in the closed state (left; scale bar, 50 nm), at 5 mM $MgCl_2$ in the open state (middle; scale bar, 50 nm), and after raising the cation concentration again to 25 mM in the closed state (right image; scale bar, 50 nm) (see figs. S88 to S90 for lower-magnification images).

position and orientation of individual DNA objects within larger complexes, we designed four multilayer DNA origami bricks (Fig. 1C and figs. S1 to S7) that form the subunits of a tetrameric complex. The embossed surface of brick A fits precisely into the recessed surface of brick B and likewise for combinations of B with C and C with D. Bricks B, C, and D exhibit characteristic asymmetric features that helped identify their orientation when the bricks were imaged with transmission electron microscopy (TEM). Negative-stain TEM image data and an electrophoretic mobility analysis confirmed the successful assembly of the designed overall bricklike objects (fig. S7, A and B), as well as the self-assembly into all possible multimeric complexes as they are prescribed by the designed shape complementarity, including dimers, trimers, and a tetramer (Fig. 1D; fig. S7, B to F; and figs. S8 to S21).

To illustrate the ability of the click-in shape recognition scheme for precisely defining conformational states within a multidomain DNA object, we designed a switchlike DNA object consisting of two rigid beams connected by a pivot (Fig. 1E and fig. S22). The switch can dwell either in an ensemble of open states or in a closed state. The structure of the closed state is prescribed by shape-complementary patterns of double-helical DNA domains that can click into each other when the two beams draw together (Fig. 1E, right). Direct imaging by negative-stain TEM confirms that the switch adopts open and closed conformations, where the closed conformation is structurally well defined (Fig. 1F).

Structural switching

Our RNAse P–inspired shape recognition scheme creates a tiered hierarchy between intradomain stability and interdomain interaction because it is based on few nucleobase stacking interactions, rather than the many nucleobase pairing interactions that stabilize entire DNA objects. As in RNAse P (*25*, *26*), the conformational equilibrium of objects that utilize such shape-complementary interactions is sensitive to the concentration of counterions in solution because of repulsions between the negatively charged surfaces of the DNA binding partners. These two properties, the tiered interaction hierarchy and the repulsive interfaces, create rich opportunities for adjusting the conformational equilibrium, and changing it reversibly and rapidly, by global parameters such as cation concentration and solution temperature. We test these options in detail using ensemble and single-molecule fluorescence resonance energy transfer (FRET) experiments, as well as TEM imaging and electrophoretic mobility analysis performed as a function of cation concentration and temperature with the switch object and for a dimeric brick complex. For both the switch and the dimeric bricks, increasing the cation concentration shifted the conformational equilibrium from the open or monomeric states to the closed or dimeric states, respectively (Fig. 2, A and B, and figs. S12 to S14; S23, A to D; S24 to S29; and S30, A and B). This process occurred in the presence of both monovalent and divalent cations, but only when attractive stacking bonds or even stronger hybridization-based interactions were included (Fig. 2B, supplementary text S1, and figs. S23, B to C, and S31 to S40), thus pointing against unspecific counterion-induced condensation effects. The transitions were reversible upon cyclic changes in the concentration of cations (fig. S23E). The isotherms generated by cation titration agreed well with the predictions of a two-state model with a free-energy term that depends linearly on the concentration of cations (Fig. 2B and fig. S30B). Single switch particles sample the designed open and closed states on the time scale of fractions of seconds (supplementary text S2 and figs. S23, F to I, and S41 to S49). Increasing the concentration of cations shifts the equilibrium toward the closed state by predominantly reducing the average time that the switch dwells in the open state (fig. S23I).

The greater the strength of the designed interaction between the shape-complementary interfaces of the switch, the lower the cation concentration necessary for stabilizing the closed state (Fig. 2B and fig. S23, B and C). In the switch version with 16 stacking bonds, the transition occurred over a narrow concentration interval ranging from 6 to 12 mM $MgCl_2$. For stronger hybridization-based interactions at all complementary sites instead of the minimal stacking

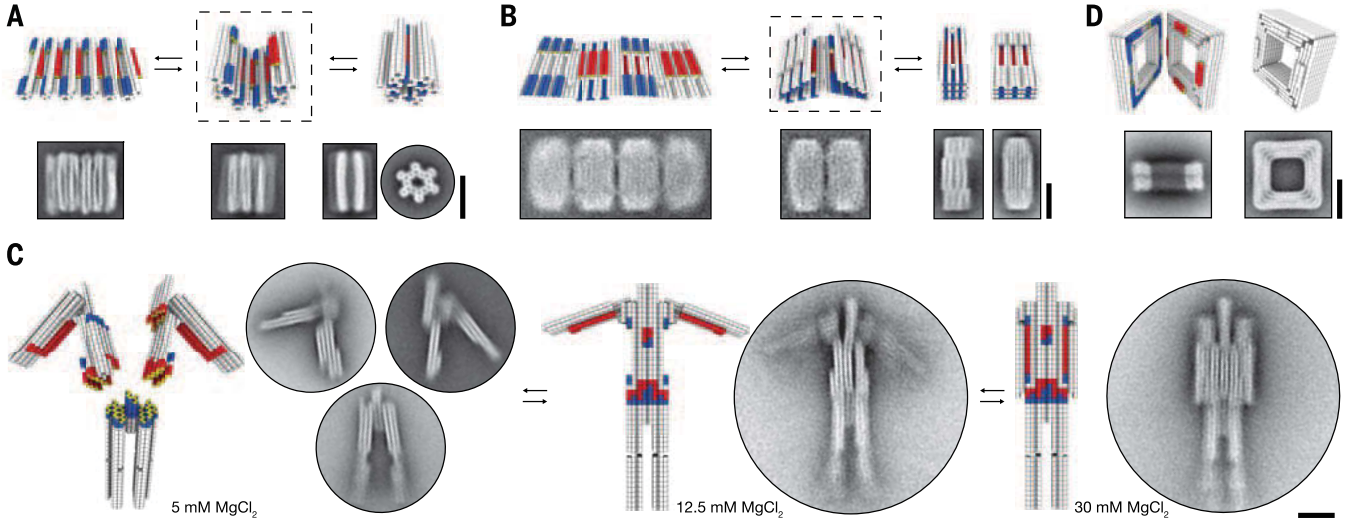

Fig. 4. Reversibly reconfigurable non–base pairing multistate DNA devices with arbitrary shapes. (**A**) Top row: schematic representations of a reconfigurable gear in a fully open state (left), in a partially compacted intermediate state (center), and in a fully closed state (right). The states can be cyclically prepared by adjusting, e.g., the cation concentration. Bottom row: average negative-stain TEM micrographs of the gear, acquired at 100 mM $MgCl_2$ (left) and at 20 mM $MgCl_2$ (center and right). The cation-dependent operation principle opening or closing is reversed with respect to, e.g., the switch (Figs. 1 and 2) due to additional cation-dependent attractive surface interactions with the TEM support grid that "pull" the gear open. (**B**) Top row: schematic representation of a nanobook in three states. Bottom row: averaged negative-stain TEM micrographs acquired at 5 mM (left) and at 50 mM (center and right) $MgCl_2$. (**C**) Schematic representation of a heterotrimeric reconfigurable nanorobot (15 MD) that can be reversibly reconfigured in three different conformational states: disassembled, and assembled with open or closed arms, respectively, by calibrating the concentration of cations in solutions. Average negative-stain TEM micrographs of the nanorobot were acquired in the presence of the indicated $MgCl_2$ concentrations. $MgCl_2$ concentration increase was achieved by adding $MgCl_2$ stock solution; concentration reduction was achieved by diluting with Mg-free buffer. (See figs. S99 and S100 for TEM images from a complete assembly, opening, closing, disassembly cycle.) (**D**) Top row: schematic representation of two shape-complementary multilayer DNA origami objects in square-lattice packing (all other objects in this work were honeycomb-lattice packing). Bottom row: average negative-stain TEM micrographs in two distinct views of the heterodimeric complex at 50 mM $MgCl_2$. Scale bars, 25 nm.

interactions, the transition shifted to the low cation concentrations where the open state could not be prepared without compromising the overall structural integrity of the switch (Fig. 2B and figs. S23, B and C, and S31 to S34). When we used hybridization-based interactions distributed over fewer sites across the beam interfaces, the possibility for shifting the equilibrium could be restored, but at the expense of a structurally less-well-defined closed state (figs. S50 to S58). Analogous observations were made for the brick system (figs. S59 to S67). Changing the temperature of solutions containing switch variants or the dimeric bricks could also reversibly shift the equilibrium from closed or dimeric states to open or monomeric states, respectively (Fig. 2C and figs. S23J, S30C, and S68). The ability to shift the equilibrium by temperature changes depended on the concentration of cations in solution (figs. S23K and S30C).

Temperature-jump experiments (Fig. 2D) highlighted the robust reversibility of our shape recognition scheme and the absence of structural or functional degradation. During the course of 4.25 days, a solution containing the dynamic switch with 16 stacking interactions was cycled 1020 times between 25°C (closed state) and 50°C (open state; Fig. 2D and figs. S69 and S70). Ensemble FRET signals were collected in 18-s intervals (total illumination time = 13 min). Upon heating and cooling, the FRET signals decreased and increased in a steplike fashion to levels corresponding to the open and closed states of the switch ensemble, respectively (Fig. 2D). These results imply rapid equilibration with a time constant of <4 s, which is consistent with the average lifetimes of the open and closed states determined at room temperature with single-particle FRET experiments (fig. S23I). The shape-complementary brick monomer-dimer equilibrium showed rapid dissociation upon temperature jumps to 50°C (figs. S30D and S71) but slower association upon jumping back to 25°C. The data were consistent with the equilibration dynamics of a dimerization reaction starting from monomeric states (fig. S30D, inset, and supplementary text S7).

Methods that rely on toehold-mediated DNA strand displacement can directly influence the conformation of DNA objects by creating or resolving double-helical DNA domains (*8*–*15*) that stabilize those conformations. Because our RNAse P–inspired recognition scheme relies on shape complementarity on the one hand, and because DNA origami objects are elastic macromolecular structures on the other hand, binding equilibria can now also be affected allosterically—that is, through deformations that follow from molecular binding events at distal sites. To show this possibility, we installed single-stranded DNA loops in the vicinity of the shape-complementary interfaces in the switch and in the dimeric brick objects (Fig. 2E and fig. S30E, left). The hybridization of loop-complementary DNA "signal" strands deforms the shape-complementary interfacial patterns (Fig. 2E and fig. S30E, right) and thus can inhibit the attractive interaction. By separating the "signal" strand from the loops via toehold-mediated strand displacement, the deformation was reversed, and the attractive interaction between the shape-complementary interfaces was restored. We demonstrate this mechanism using ensemble FRET experiments performed with the switch and the brick dimers (Fig. 2F and figs. S30F and S72 to S79). The transition kinetics that we observed is consistent with those found for toehold-mediated strand displacement reactions (*27*). Hence, our shape recognition scheme can also be coupled to the well-established strand displacement methods in DNA nanotechnology.

Applications

Several attractive opportunities are created by the possibility to self-assemble higher-order DNA objects using our shape recognition scheme. First, the position of binding partners may be constrained with sufficient rigidity to template long-range orientation, as seen in experiments with a self-complementary brick that self-assembled into homomultimeric filaments with apparently seamless integration of up to hundreds of monomers and absence of bending deformations up to the micrometer length scale (Fig. 3, A and B, left, and fig. S80).

Second, simply decreasing or increasing the cation concentration allows recovering of the constituent monomers or restoring the growth of filaments, respectively (Fig. 3B, right, and fig. S81). The ability to reversibly shrink and grow filaments is of interest for creating active materials and in polymerization-based propulsion applications.

Third, different higher-order objects may be created from a family of similar building blocks by using simple shape alterations and without having to design interfaces with specific DNA sequences. To show this possibility, we have designed a hexagonal multilayer DNA origami brick where the six faces feature recession and protrusion patterns such that opposing faces are pairwise complementary but noncomplementary to the other faces of the hexagon (Fig. 3C and figs. S82 and S83). The hexagon can be prepared as a monomer (Fig. 3C) and self-assembled into 2D hexagonal lattices by raising the cation concentration (Fig. 3D and fig. S84). We also altered the hexagon brick such that only four out of its six faces could participate in shape-complementary stacking interactions, where two opposing hexagon faces may interact with each other and also two neighboring faces may interact, but only when rotating one binding partner around its short axis by 180° (Fig. 3E and fig. S85). This design modification caused the hexagon bricks to self-assemble specifically into two-stranded filaments (Fig. 3E and fig. S86). Natural two-stranded filaments such as actin also self-assemble from a single monomer and offer interesting properties such as nucleated growth and a superior length-to-monomer concentration ratio as compared to single-stranded filaments.

Fourth, nanoscopic changes in the geometry of individual building blocks may also be amplified up to the micrometer scale, which is an important step in creating synthetic assemblies that could attain the high level of structural integration of active components seen in biology, such as in muscle tissue. We polymerized a variant of the dynamic switch from Figs. 1 and 2 into 2D lattices, using hybridization-based interactions. These lattices contained up to 1000 switch particles (Fig. 3F and figs. S87 to S90) arranged in a regular fashion. The lattices could be reversibly expanded and contracted simply by decreasing and increasing the concentration of cations in the solution, respectively.

Finally, we illustrate the opportunities for creating various reversibly reconfigurable DNA devices with arbitrary shapes when using our shape recognition scheme. We designed and self-assembled a reconfigurable gear that can be switched between a pinionrack-like shape and a gearlike shape (Fig. 4A and figs. S91 and S92). We also designed a reconfigurable nanobook that can reversibly fold and unfold (Fig. 4B and figs. S93 to S95). As for all other objects shown in this work, the conformational equilibrium of the reconfigurable gear and the nanobook can be adjusted by the cation concentration in solution. Both devices provide starting points for objects that can serve encapsulation purposes. In addition, we produced a heterotrimeric 15 MD complex comprising three asymmetric subunits that assemble specifically on the basis of shape recognition (Fig. 4C and figs. S96 to S100) to form a nanorobot. Two modules form the robot's torso, and one module forms its legs. The torso modules each feature an armlike domain hooked up to a shoulderlike protrusion via a pivot similar to the pivot in the switch. The arms can switch between open and closed states, where the closed states are stabilized by shape-complementary stacking bonds between the forearm and the hip of the robot. We used cation concentration as a control parameter; a designed hierarchy of strengths between the various stacking bonds within the robot allows it to be tasked to self-assemble, open its arms, close its arms, split up into its modules, and reassemble (Fig. 4C). We controlled the sequence of events by the temporal pattern of cation concentrations.

Taken together, the methods put forward herein provide ready access to a diversity of dynamic DNA-based devices and assemblies. By simply considering geometry in 3D space, as exemplified here with differently shaped multilayer DNA origami objects in honeycomb-lattice packing as well as square-lattice packing (Fig. 4D and figs. S101 to S103), and minimized nucleobase stacking interactions as a universal molecular glue, a designer can encode complex higher-order objects and also dynamic objects in DNA sequences (see movies S1 to S7).

Discussion

In computer science, high-level languages use an interpreter to enable the creation of complex software without having to deal with detailed machine code. By analogy, DNA sequences may be considered as the machine code used to create structural modules. Our shape recognition method expands the palette of potential interactions for

DNA-based nanotechnology and adds a layer of abstraction in which components may be treated conceptually as objects that interact in shape space, rather than in sequence space. This property enables the design on a higher structural level without having to program the detailed DNA strand sequences for connecting components. We anticipate that our findings will help in creating dynamic macromolecular devices and assemblies as scaffolds for various purposes. Specifically, we envision potential applications in advanced therapeutics, biosensing, active plasmonics, and responsive nanostructured materials.

REFERENCES AND NOTES

1. J. Janin, R. P. Bahadur, P. Chakrabarti, *Q. Rev. Biophys.* **41**, 133–180 (2008).
2. S. Jones, J. M. Thornton, *Proc. Natl. Acad. Sci. U.S.A.* **93**, 13–20 (1996).
3. C. Guerrier-Takada, K. Gardiner, T. Marsh, N. Pace, S. Altman, *Cell* **35**, 849–857 (1983).
4. P. W. Rothemund, *Nature* **440**, 297–302 (2006).
5. S. M. Douglas *et al.*, *Nature* **459**, 414–418 (2009).
6. Y. Ke *et al.*, *J. Am. Chem. Soc.* **131**, 15903–15908 (2009).
7. S. M. Douglas *et al.*, *Nucleic Acids Res.* **37**, 5001–5006 (2009).
8. H. Dietz, S. M. Douglas, W. M. Shih, *Science* **325**, 725–730 (2009).
9. E. S. Andersen *et al.*, *Nature* **459**, 73–76 (2009).
10. J. P. Sobczak, T. G. Martin, T. Gerling, H. Dietz, *Science* **338**, 1458–1461 (2012).
11. N. C. Seeman, *J. Theor. Biol.* **99**, 237–247 (1982).
12. T. J. Fu, N. C. Seeman, *Biochemistry* **32**, 3211–3220 (1993).
13. B. Yurke, A. J. Turberfield, A. P. Mills Jr., F. C. Simmel, J. L. Neumann, *Nature* **406**, 605–608 (2000).
14. D. Y. Zhang, A. J. Turberfield, B. Yurke, E. Winfree, *Science* **318**, 1121–1125 (2007).
15. K. Lund *et al.*, *Nature* **465**, 206–210 (2010).
16. L. Qian, E. Winfree, J. Bruck, *Nature* **475**, 368–372 (2011).
17. R. P. Goodman *et al.*, *Nat. Nanotechnol.* **3**, 93–96 (2008).
18. Y. Krishnan, F. C. Simmel, *Angew. Chem.* **50**, 3124–3156 (2011).
19. F. Wang, C. H. Lu, I. Willner, *Chem. Rev.* **114**, 2881–2941 (2014).
20. S. F. Wickham *et al.*, *Nat. Nanotechnol.* **7**, 169–173 (2012).
21. N. J. Reiter *et al.*, *Nature* **468**, 784–789 (2010).
22. S. Woo, P. W. Rothemund, *Nat. Chem.* **3**, 620–627 (2011).
23. M. Endo, T. Sugita, Y. Katsuda, K. Hidaka, H. Sugiyama, *Chemistry* **16**, 5362–5368 (2010).
24. R. Wang, A. Kuzuya, W. Liu, N. C. Seeman, *Chem. Commun. (Camb.)* **46**, 4905 (2010).
25. D. Smith, A. B. Burgin, E. S. Haas, N. R. Pace, *J. Biol. Chem.* **267**, 2429–2436 (1992).
26. J. Hsieh, C. A. Fierke, *RNA* **15**, 1565–1577 (2009).
27. N. Srinivas *et al.*, *Nucleic Acids Res.* **41**, 10641–10658 (2013).
28. E. F. Pettersen *et al.*, *J. Comput. Chem.* **25**, 1605–1612 (2004).
29. G. Tang *et al.*, *J. Struct. Biol.* **157**, 38–46 (2007).

ACKNOWLEDGMENTS

We thank E. Stahl, T. Martin, J. Funke, M. Schickinger, F. Kilchherr, C. Wachauf, L. Meregalli, and V. Hechtl for technical assistance. F. Praetorius is acknowledged for scaffold DNA preparations. This work was supported by a European Research Council Starting Grant to H.D. (GA no.256270) and the Deutsche Forschungsgemeinschaft through grants provided within the Excellence Clusters CIPSM (Center for Integrated Protein Science Munich), NIM (Nanosystems Initiative Munich), the Sonderforschungsbereich SFB863, the Technische Universität München (TUM) Institute for Advanced Study, and the TUM International Graduate School of Science and Engineering (IGSSE). K.F.W. and H.D. are grateful for additional support from the Hans L. Merkle Foundation. T.G., K.F.W., and A.N. performed research. H.D. designed research and wrote the manuscript. T.G., K.F.W., and H.D. prepared figures. T.G., K.F.W., and H.D. analyzed and discussed data and edited the manuscript. We confirm no competing financial interests. The data reported in this paper are tabulated in the supplementary materials.

SUPPLEMENTARY MATERIALS

www.sciencemag.org/content/347/6229/1446/suppl/DC1
Materials and Methods
Supplementary Text S1 to S7
Figs. S1 to S103
Movies S1 to S8
List of Oligonucleotides
Overview of Strand Diagrams
References (*30*–*32*)

19 December 2014; accepted 9 February 2015
10.1126/science.aaa5372

REPORTS

NUCLEAR PHYSICS

Ab initio calculation of the neutron-proton mass difference

Sz. Borsanyi,[1] S. Durr,[1,2] Z. Fodor,[1,2,3]* C. Hoelbling,[1] S. D. Katz,[3,4] S. Krieg,[1,2] L. Lellouch,[5] T. Lippert,[1,2] A. Portelli,[5,6] K. K. Szabo,[1,2] B. C. Toth[1]

The existence and stability of atoms rely on the fact that neutrons are more massive than protons. The measured mass difference is only 0.14% of the average of the two masses. A slightly smaller or larger value would have led to a dramatically different universe. Here, we show that this difference results from the competition between electromagnetic and mass isospin breaking effects. We performed lattice quantum-chromodynamics and quantum-electrodynamics computations with four nondegenerate Wilson fermion flavors and computed the neutron-proton mass-splitting with an accuracy of 300 kilo–electron volts, which is greater than 0 by 5 standard deviations. We also determine the splittings in the Σ, Ξ, *D*, and Ξ_{cc} isospin multiplets, exceeding in some cases the precision of experimental measurements.

The mass of the visible universe is a consequence of the strong interaction (*1*), which is the force that binds together quarks into protons and neutrons. To establish this with percent-level accuracy, very precise calculations based on the lattice formulation of quantum chromodynamics (QCD), the theory of the strong interaction, were needed. Going beyond such calculations to control much finer effects that are at the per mil (‰) level is necessary to, for instance, account for the relative neutron-proton mass difference, which was experimentally measured to be close to 0.14% (*2*). Precisely, this difference is needed to explain the physical world as we know it today (*3*). For example, a relative neutron-proton mass difference smaller than about one third of the observed 0.14% would cause hydrogen atoms to undergo inverse beta decay, leaving predominantly neutrons. A value somewhat larger than 0.05% would have resulted in the Big Bang Nucleosynthesis (BBN), producing much more helium-4 and far less hydrogen than it did in our universe. As a result, stars would not have ignited in the way they did. On the other hand, a value considerably larger than 0.14% would have resulted in a much faster beta decay for neutrons. This would have led to far fewer neutrons at the end of the BBN epoch and would have made the burning of hydrogen in stars and the synthesis of heavy elements more difficult. We show here that this tiny mass splitting is the result of a subtle cancellation between electromagnetic and quark mass difference effects.

The Standard Model of Particle Physics is a $SU(3) \times SU(2) \times U(1)$ gauge theory with massless fermions. During the expansion of the early universe, the Higgs mechanism broke this symmetry down to $SU(3) \times U(1)$, and elementary particles acquired masses proportional to their couplings to the Higgs field. As the universe continued to expand, a QCD transition took place, confining quarks and gluons into hadrons and giving those particles most of their mass. This same theory today is believed to be responsible for the tiny isospin splittings, which are the subject of this paper. At the level of precision that we aim for here, the effects of the weak interaction, of leptons, and of the two heaviest quarks can either be neglected or absorbed into the remaining parameters of the theory. The resulting theory is one of *u*, *d*, *s*, and *c* (up, down, strange, and charm, respectively) quarks, gluons, photons, and their interactions. The

[1]Department of Physics, University of Wuppertal, D-42119 Wuppertal, Germany. [2]Jülich Supercomputing Centre, Forschungszentrum Jülich, D-52428 Jülich, Germany. [3]Institute for Theoretical Physics, Eötvös University, H-1117 Budapest, Hungary. [4]Lendület Lattice Gauge Theory Research Group, Magyar Tudományos Akadémia–Eötvös Loránd University, H-1117 Budapest, Hungary. [5]CNRS, Aix-Marseille Université, Université de Toulon, CPT UMR 7332, F-13288, Marseille, France. [6]School of Physics and Astronomy, University of Southampton, Southampton SO17 1BJ, UK.
***Corresponding author. E-mail: fodor@bodri.elte.hu**

Euclidean Lagrangian for this theory is $\mathcal{L} = 1/(4e^2)F_{\mu v}F_{\mu v} + 1/(2g^2)\mathrm{Tr}G_{\mu v}G_{\mu v} + \sum_f \overline{\psi}_f[\gamma_\mu(\partial_\mu + iq_f A_\mu + iB_\mu) + m_f]\psi_f$, where γ_μ are the Dirac matrices, f runs over the four flavors of quarks, the m_f are their masses, and the q_f are their charges in units of the electron charge e. Moreover, $F_{\mu v} = \partial_\mu A_v - \partial_v A_\mu$, $G_{\mu v} = \partial_\mu B_v - \partial_v B_\mu + [B_\mu, B_v]$, and g is the QCD coupling constant. In electrodynamics, the gauge potential A_μ is the real valued photon field, whereas in QCD, B_μ is a Hermitian 3 by 3 matrix field. The ψ_f are Dirac-spinor fields representing the quarks and carry a "color" index, which runs from 1 to 3. In the present work, we consider all of the degrees of freedom of this Lagrangian; that is, we include quantum electrodynamics (QED) and QCD, as well as the four nondegenerate quark flavors, in a fully dynamical formulation.

The action S of QCD+QED is defined as the spacetime integral of $\mathcal{L}$. Particle propagators are averages of products of fields over all possible field configurations, weighted by the Boltzmann factor $\exp(-S)$. A notable feature of QCD is asymptotic freedom, which means that the interaction becomes weaker and weaker as the relative momentum of the interacting particles increases (*4*, *5*). Thus, at high energies the coupling constant is small, and a perturbative treatment is possible. However, at energies typical of quarks and gluons within hadrons, the coupling is large, and the interactions become highly nonlinear. The most systematic way to obtain predictions in this nonperturbative regime of QCD involves introducing a hypercubic spacetime lattice with lattice spacing a (*6*) on which the above Lagrangian is discretized, numerically evaluating the resulting propagators and extrapolating the results to the continuum ($a \to 0$). The discretization procedure puts fermionic variables on the lattice sites, whereas gauge fields are represented by unitary 3 by 3 matrices residing on the links between neighboring sites. The discretized theory can be viewed as a four-dimensional statistical physics system.

Calculating the mass differences between the neutral and charged hadron partners by using lattice techniques has involved different levels of approximation. In the pioneering work of (*7*), the quenched approximation was used both for QCD and QED. Recent studies (*8*–*10*) have typically performed dynamical QCD computations with quenched QED fields. Another quenched QED approach, in which the path integral is expanded to $O(\alpha)$, has also recently been implemented (*11*). In all such calculations, the neglected terms are of the same leading order in α as the isospin splittings of interest (*10*). To have a calculation that fully includes QED effects to $O(\alpha)$ requires including electromagnetic effects in the quark sea. Three exploratory studies have attempted to include these effects. The first two used reweighting techniques in $N_f = 2 + 1$ QCD simulations (*12*, *13*). Beyond the difficulty of estimating the systematic error associated with reweighting, the computation in (*12*) was carried out with a single lattice spacing in a relatively small (3 fm)^3 spatial volume and the one in (*13*) on a single, much coarser and smaller lattice, with pion masses larger than their physical value. In the third study (*14*), real dynamical QCD and QED simulations were performed, albeit on a single lattice at unphysical quark mass values.

Here, we provide a fully controlled ab initio calculation for these isospin splittings. We used 1 + 1 + 1 + 1 flavor QCD+QED with 3 HEX (QCD) and 1 APE (QED) smeared clover improved Wilson quarks. Up to now, the most advanced simulations have included up, down, and strange quarks in the sea but neglected all electromagnetic and up-down mass difference effects. Such calculations have irreducible systematic uncertainties of $O(1/N_c/m_c^2, \alpha, m_d - m_u)$, where $N_c = 3$ is the number of colors in QCD. This limits their accuracy to the percent level. We reduced these uncertainties to $O(1/N_c/m_b^2, \alpha^2)$, where m_b is the bottom quark mass, yielding a complete description of the interactions of quarks at low energy accurate to the per mil level.

In our parameter set, we have four lattice spacings ranging from 0.06 to 0.10 fm. We observed very small cutoff effects in our results, which is in good agreement with our earlier spectrum determination (*15*, *16*). Nevertheless, these small cutoff effects are accounted for in our systematic error analysis as g^2a or a^2 corrections in the histogram method described in (*17*).

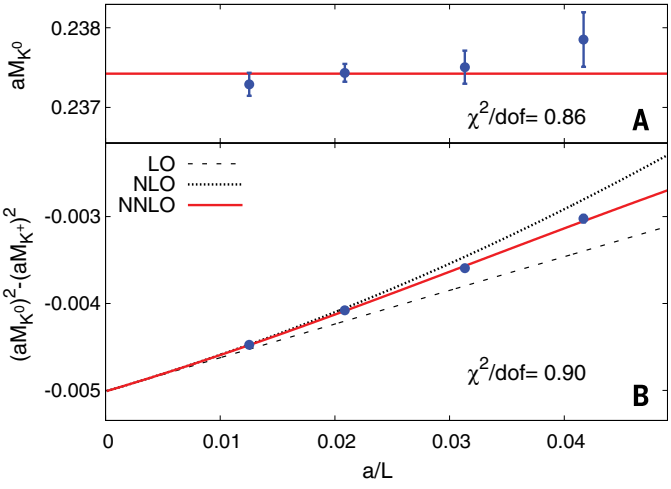

Fig. 1. Finite-volume behavior of kaon masses. (**A**) The neutral kaon mass, M_{K^0}, shows no significant finite volume dependence; L denotes the linear size of the system. (**B**) The mass-squared difference of the charged kaon mass, M_{K^+}, and M_{K^0} indicates that M_{K^+} is strongly dependent on volume. This finite-volume dependence is well described by an asymptotic expansion in $1/L$ whose first two terms are fixed by QED Ward-Takahashi identities (*17*). The solid curve depicts a fit of the lattice results (points) to the expansion up to and including a fitted $O(1/L^3)$ term. The dashed and dotted curves show the contributions of the leading and leading plus next-to-leading order terms, respectively. The computation was performed by using the following parameters: bare $\alpha \sim 1/10$, M_π = 290 MeV, and M_{K^0} = 450 MeV. The mass difference is negative because a larger-than-physical value of α was used. The lattice spacing a is ~0.10 fm.

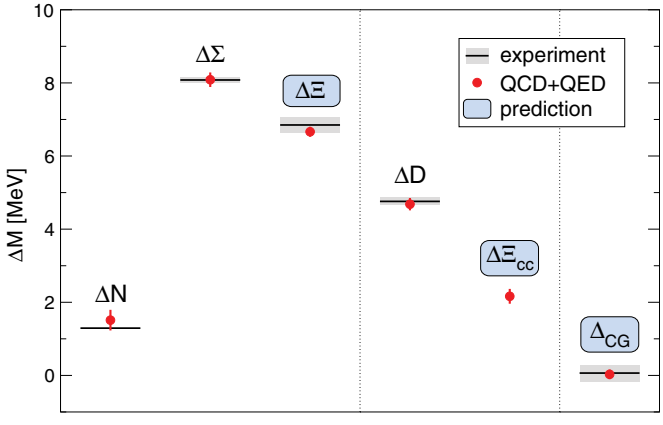

Fig. 2. Mass splittings in channels that are stable under the strong and electromagnetic interactions. Both of these interactions are fully unquenched in our 1+1+1+1 flavor calculation. The horizontal lines are the experimental values, and the gray shaded regions represent the experimental error (*2*). Our results are shown by red dots with their uncertainties. The error bars are the squared sums of the statistical and systematic errors. The results for the ΔM_N, ΔM_Σ, and ΔM_D mass splittings are post-dictions, in the sense that their values are known experimentally with higher precision than from our calculation. On the other hand, our calculations yield ΔM_Ξ, $\Delta M_{\Xi cc}$ splittings, and the Coleman-Glashow difference Δ_{CG}, which have either not been measured in experiment or are measured with less precision than obtained here. This feature is represented by a blue shaded region around the label.

We performed computations with four values of the bare fine structure constant: 0, a value close to the physical value of 1/137, and two larger values, approximately 1/10 and 1/6. Most of our runs were carried out at $\alpha = 0$ and ~1/10. Because QED effects in typical hadron masses are small (around or below the 1 ‰ level), statistical noise in the splittings can be reduced by interpolating between results obtained with the larger value of α and those obtained with $\alpha = 0$. We then confirmed and improved this interpolation with simulations near the physical value of the coupling. The actual interpolation to the physical point is performed in terms of a renormalized fine structure constant defined via the QED Wilson flow (*18*). Within the precision reached in our work, the splittings studied show no deviation from linear behavior in the range of couplings studied. Our largest value of the fine structure constant was chosen so as to increase the signal for the mass splittings, while keeping under control large finite-volume corrections of the kind discussed below.

Our smallest pion mass is ~195 MeV (with more than 20,000 trajectories), and our largest lattice has a spatial extent of 8 fm. These parameters were carefully chosen to allow for a determination of the neutron-proton mass splitting that is ~5 standard deviations (SDs) from 0, with currently available computing resources. This is a challenge because accounting for isospin breaking effects increases the cost (*17*) of the calculation compared with computations with two degenerate light flavors used typically in recent works (*19*–*27*).

We produced gauge configurations with an improved version of the Hybrid Monte Carlo algorithm and checked, a posteriori, that the probability weights are always positive in the region of the parameter space used in our simulations.

We used two previously suggested frameworks for the photon fields. These correspond to a nonlocal modification of the action that vanishes in the infinite-volume limit. As we argue in (*17*), these nonlocalities do not generate new ultraviolet divergences at one-loop order in α. The final analysis is performed in the framework of (*28*), which respects reflection positivity and has a well-defined, large time limit, unlike previously used techniques (*17*). Generically, the photon fields show very large autocorrelation times of several thousand trajectories. We designed a Fourier accelerated algorithm within this QCD+QED framework that dramatically reduces these large autocorrelation times.

The long-range nature of the electromagnetic interaction poses one of the most serious difficulties of the present work. It induces finite-volume corrections that only fall off like inverse powers of the linear extent of the system. These are far more severe than the QCD finite-volume corrections, which are exponentially suppressed in these dimensions. Exponential corrections can easily be included in large-scale spectrum studies (*16*). We performed an extensive study of the much larger power-suppressed finite-volume corrections using both one-loop analytical QED calculations and high-precision QED simulations (*17*). The size and volume behavior of these corrections in our full QCD+QED calculation are illustrated in Fig. 1.

Statistical errors on the mass splittings are calculated by using 2000 bootstrap samples. The systematic uncertainties on the final results are determined with our histogram method (*16*). We considered a wide range of analyses, each of which provides a valid approach to obtain the physical splittings from our simulation results, and calculated the associated goodness of fit. Because these procedures have different numbers of free parameters, we combined them using the Akaike information criterion (AIC) (*29*) and obtained a distribution for each splitting. The means of these distributions are our central values, whereas the widths of the distributions provide estimates of systematic uncertainties. This procedure yields conservative errors.

Our final results for the mass splittings are shown in Fig. 2. A comparison with the results of (*10*) indicates that the precision of the signal for ΔM_N (thus the splitting being nonzero) increased from ~1σ to 5σ. For the other channels, the improvement is even more pronounced. In addition, the present work represents a fully controlled approach, whereas (*10*) was based on the electroquenched approximation with degenerate light quarks in the sea. The nucleon, Σ, and Ξ splittings are consistent with the Coleman-Glashow relation $\Delta_{CG} \equiv \Delta M_N - \Delta M_\Sigma + \Delta M_\Xi = 0$ (*30*). According to our calculation, this relation is fulfilled with an accuracy of 130 keV. We also computed the individual contributions to the splittings coming from mass isospin breaking effects ($\alpha = 0$, $m_d - m_u \neq 0$) and electromagnetic effects ($m_d - m_u = 0$, $\alpha \neq 0$), as defined in (*17*). The numerical results for all of our results are given in Table 1. Because the precision of the experimental result for the nucleon is far greater than ours, we additionally give the QED and QCD separation obtained by using the experimental value of $M_n - M_p$: $(M_n - M_p)_{QCD}/(M_n - M_p)_{QED} = -2.49(23)(29)$. Last, we used

Table 1. Isospin mass splittings of light and charm hadrons. Also shown are the individual contributions to these splittings from the mass difference ($m_d - m_u$) (QCD) and from electromagnetism (QED). This separation requires fixing a convention, which is described in (*17*). The last line is the violation of the Coleman-Glashow relation (*30*), which is the most accurate of our predictions.

	Mass splitting [MeV]	QCD [MeV]	QED [MeV]
$\Delta N = n - p$	1.51(16)(23)	2.52(17)(24)	−1.00(07)(14)
$\Delta\Sigma = \Sigma^- - \Sigma^+$	8.09(16)(11)	8.09(16)(11)	0
$\Delta\Xi = \Xi^- - \Xi^0$	6.66(11)(09)	5.53(17)(17)	1.14(16)(09)
$\Delta D = D^+ - D^0$	4.68(10)(13)	2.54(08)(10)	2.14(11)(07)
$\Delta\Xi_{cc} = \Xi_{cc}^{++} - \Xi_{cc}^{+}$	2.16(11)(17)	−2.53 (11)(06)	4.69(10)(17)
$\Delta_{CG} = \Delta N - \Delta\Sigma + \Delta\Xi$	0.00(11)(06)	−0.00 (13)(05)	0.00(06)(02)

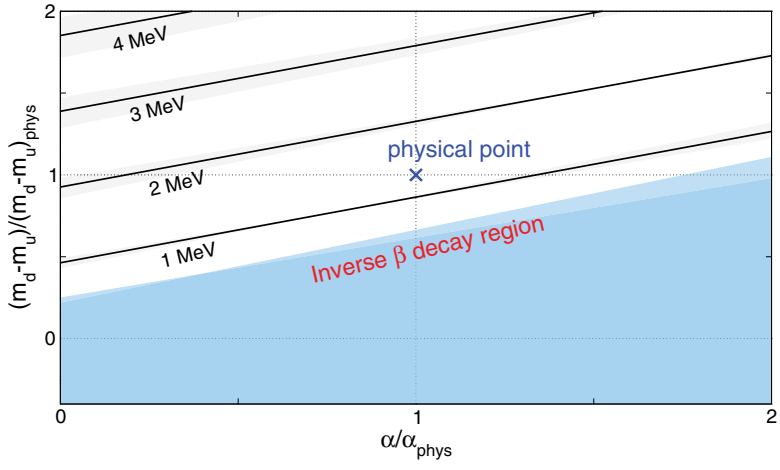

Fig. 3. Contour lines for the neutron-proton mass splitting. The contours are shown as a function of the quark mass difference and the fine structure constant, both normalized with their real-world, physical value. Because these two effects compete, by increasing α at fixed quark mass difference one can decrease the mass difference between the neutron and the proton to 0.511 MeV, at which inverse β-decay sets in, as depicted by the blue region. The blue cross shows the physical point. The shaded bands around the contours represent the total statistical and systematic uncertainties on these predictions. A constraint on the neutron-proton mass difference obtained from other considerations leads to a constraint on $m_d - m_u$ and/or α, which can be directly read off from the figure.

this number in Fig. 3 to plot the result of the neutron-proton mass splitting as a function of the quark-mass difference and electromagnetic coupling. In combination with astrophysical and cosmological arguments, this figure can be used to determine how different values of these parameters would change the content of the universe. This in turn provides an indication of the extent to which these constants of nature must be fine-tuned to yield a universe that resembles ours.

REFERENCES AND NOTES

1. A. Kronfeld, in *100 Years of Subatomic Physics*, E. Henley, S. Ellis, Eds. (World Scientific, Singapore, 2013), chap. 18.
2. J. Beringer *et al.*, *Phys. Rev. D Part. Fields Gravit. Cosmol.* **86**, 010001 (2012).
3. R. L. Jaffe, A. Jenkins, I. Kimchi, *Phys. Rev. D Part. Fields Gravit. Cosmol.* **79**, 065014 (2009).
4. D. J. Gross, F. Wilczek, *Phys. Rev. Lett.* **30**, 1343–1346 (1973).
5. H. D. Politzer, *Phys. Rev. Lett.* **30**, 1346–1349 (1973).
6. K. G. Wilson, *Phys. Rev. D Part. Fields* **10**, 2445–2459 (1974).
7. A. Duncan, E. Eichten, H. Thacker, *Phys. Rev. Lett.* **76**, 3894–3897 (1996).
8. T. Blum *et al.*, *Phys. Rev. D Part. Fields Gravit. Cosmol.* **82**, 094508 (2010).
9. S. Basak *et al.*, *Proc. Sci.* **12**, 30 (2013).
10. S. Borsanyi *et al.*, *Phys. Rev. Lett.* **111**, 252001 (2013).
11. G. de Divitiis *et al.*, *Phys. Rev. D Part. Fields Gravit. Cosmol.* **87**, 114505 (2013).
12. S. Aoki *et al.*, *Phys. Rev. D Part. Fields Gravit. Cosmol.* **86**, 034507 (2012).
13. T. Ishikawa *et al.*, *Phys. Rev. Lett.* **109**, 072002 (2012).
14. R. Horsley *et al.*, *Proc. Sci. Lattice* **2013**, 499 (2013).
15. S. Dürr *et al.*, *Phys. Rev. D Part. Fields Gravit. Cosmol.* **79**, 014501 (2009).
16. S. Dürr *et al.*, *Science* **322**, 1224–1227 (2008).
17. Materials and methods are available as supplementary materials on *Science* Online.
18. M. Lüscher, *J. High Energy Phys.* **1008**, 71 (2010).
19. S. Aoki *et al.*, *Phys. Rev. D Part. Fields Gravit. Cosmol.* **79**, 034503 (2009).
20. H. Ohki *et al.*, *Phys. Rev. D Part. Fields Gravit. Cosmol.* **78**, 054502 (2008).
21. H.-W. Lin *et al.*, *Phys. Rev. D Part. Fields Gravit. Cosmol.* **79**, 034502 (2009).
22. A. Bazavov *et al.*, *Rev. Mod. Phys.* **82**, 1349–1417 (2010).
23. S. Dürr *et al.*, *J. High Energy Phys.* **2011**, 148 (2011).
24. R. Baron *et al.*, *J. High Energy Phys.* **2010**, 111 (2010).
25. W. Bietenholz *et al.*, *Phys. Rev. D Part. Fields Gravit. Cosmol.* **84**, 054509 (2011).
26. R. Arthur *et al.*, *Phys. Rev. D Part. Fields Gravit. Cosmol.* **87**, 094514 (2013).
27. P. Fritzsch *et al.*, *Nucl. Phys. B* **865**, 397–429 (2012).
28. S. Uno, M. Hayakawa, *Prog. Theor. Phys.* **120**, 413–441 (2008).
29. H. Akaike, *IEEE Trans. Automat. Contr.* **19**, 716–723 (1974).
30. S. R. Coleman, S. L. Glashow, *Phys. Rev. Lett.* **6**, 423–425 (1961).

ACKNOWLEDGMENTS

This project was supported by the Deutsche Forschungsgemeinschaft grant SFB/TR55, the Partnership for Advanced Computing in Europe (PRACE) initiative, the Gauss Centre for Supercomputing e.V, a European Research Council grant (FP7/2007-2013/ERC No 208740), the Lendület program of the Hungarian Academy of Sciences (LP2012-44/2012), "Origines, Constituants et Évolution de l'Univers" (OCEVU) Labex (ANR-11-LABX-0060) and the A*MIDEX project (ANR-11-IDEX-0001-02) funded by the "Investissements d'Avenir" French government program and managed by the Agence Nationale de la Recherche (ANR), and the Grand Équipement National de Calcul Intensif–Institut du Développement et des Ressources en Informatique Scientifique (IDRIS) Grand Challenge grant 2012 "StabMat" as well as grant 52275. The computations were performed on JUQUEEN and JUROPA at Forschungszentrum Jülich (FZJ), on Turing at IDRIS in Orsay, on SuperMUC at Leibniz Supercomputing Centre in München, on Hermit at the High Performance Computing Center in Stuttgart, and on local machines in Wuppertal and Budapest. The data described in the paper are 60 TB and archived in FZJ.

SUPPLEMENTARY MATERIALS

www.sciencemag.org/content/347/6229/1452/suppl/DC1
Materials and Methods
Figs. S1 to S12
Tables S1 to S5
References (*31*–*74*)

6 June 2014; accepted 9 February 2015
10.1126/science.1257050

QUANTUM GASES

Crystallization in Ising quantum magnets

P. Schauß,[1]* J. Zeiher,[1] T. Fukuhara,[1] S. Hild,[1] M. Cheneau,[2] T. Macrì,[3] T. Pohl,[3] I. Bloch,[1,4] C. Gross[1]

Dominating finite-range interactions in many-body systems can lead to intriguing self-ordered phases of matter. For quantum magnets, Ising models with power-law interactions are among the most elementary systems that support such phases. These models can be implemented by laser coupling ensembles of ultracold atoms to Rydberg states. Here, we report on the experimental preparation of crystalline ground states of such spin systems. We observe a magnetization staircase as a function of the system size and show directly the emergence of crystalline states with vanishing susceptibility. Our results demonstrate the precise control of Rydberg many-body systems and may enable future studies of phase transitions and quantum correlations in interacting quantum magnets.

Quantum spin systems governed by interactions with a power-law dependence on distance are predicted to show intriguing physics very different from systems with at most next-neighbor interactions (*1*, *2*). Such interactions can lead, for example, to the realization of quantum spin glasses (*3*), quantum crystals (*4*), or strong modifications of the light-cone–like propagation of correlations (*5*, *6*). Rydberg atoms offer the possibility to realize such systems with neutral atoms because of the strong van der Waals interaction between them (*7*). The magnitude of the interactions between the Rydberg atoms is determined by the choice of the excited state, and it can exceed all other relevant energy scales on distances of several micrometers, thereby leading to an ensemble dominated by power-law interactions. The resulting Ising-type Hamiltonian is expected to support crystalline magnetic phases. To prepare the system in the crystalline phase, a dynamical approach based on controlled laser coupling has been suggested that adiabatically connects the ground state containing no Rydberg atoms (corresponding to all spins pointing downward) with the targeted crystalline state. At the heart of this dynamical crystallization technique is the coherent control of the many-body system (*8*–*14*). Here, we report on the deterministic ground-state preparation in quantum Ising spin systems composed of several hundred strongly interacting spins via coherently controlled coupling as proposed in (*8*–*10*). The physical system studied is a well-defined line- or disc-shaped atomic sample in an optical lattice with one atom per site. The ^{87}Rb atoms are coupled to the Rydberg state $43S_{1/2}$ with a controlled time-dependent Rabi frequency $\Omega(t)$ and detuning $\Delta(t) = \omega_l(t) - \omega_0$ of the laser frequency ω_l from the atomic resonance ω_0. The corresponding theoretical model describing this system is the so-called frozen Rydberg gas, in which only the internal electronic degrees of freedom are considered. This is justified by the short time scale of our experiments, during which the motion of the atoms in the lattice is negligible (*15*, *16*). Adopting a pseudo spin-1/2 description, the system maps to an Ising-type Hamiltonian

$$\hat{H} = \hbar\Omega(t)\sum_i \hat{\sigma}_x^{(i)} + \sum_i [\mathcal{I}_i - \hbar\Delta(t)]\hat{\sigma}_z^{(i)} + \sum_{i,j,(i\neq j)} \frac{V_{ij}}{2}\hat{\sigma}_z^{(i)}\hat{\sigma}_z^{(j)} \quad (1)$$

Here, the vectors $i = (i_x, i_y)$ label the position of the atoms on the lattice. The spin-1/2 operators on each site are defined as $\hat{\sigma}_x = (|\uparrow\rangle\langle\downarrow| + |\downarrow\rangle\langle\uparrow|)/2$ and $\hat{\sigma}_z = (|\uparrow\rangle\langle\uparrow| - |\downarrow\rangle\langle\downarrow|)/2$, where we omitted the site label to simplify the notation. The operators $|\uparrow\rangle\langle\downarrow|$ and $|\downarrow\rangle\langle\uparrow|$ describe a spin flip from the ground state $|\downarrow\rangle$ to the Rydberg state $|\uparrow\rangle$ and vice versa, whereas the operators $|\uparrow\rangle\langle\uparrow| = \hat{n}_\uparrow$ and $|\downarrow\rangle\langle\downarrow| = \hat{n}_\downarrow$ represent the local Rydberg and ground-state population, respectively. The first two terms of the Hamiltonian describe a transverse and longitudinal magnetic field, respectively. The former is controlled by the coherent

[1]Max-Planck-Institut für Quantenoptik, 85748 Garching, Germany. [2]Laboratoire Charles Fabry, Institut d'Optique Graduate School, CNRS, Université Paris Sud, 91127 Palaiseau, France. [3]Max-Planck-Institut für Physik Komplexer Systeme, 01187 Dresden, Germany. [4]Ludwig-Maximilians-Universität, Fakultät für Physik, 80799 München, Germany.
*Corresponding author. E-mail: peter.schauss@mpq.mpg.de

coupling between ground and Rydberg state with the time-dependent Rabi frequency $\Omega(t)$. The detuning $\Delta(t)$ determines the longitudinal field and can be used to counteract the energy offset $\mathcal{I}_i = \sum_{j,(i\neq j)} \frac{V_{ij}}{2}$ (positive for our parameters). The third term represents the van der Waals interaction potential between two atoms in the Rydberg state. For the $43S_{1/2}$ state, $V_{ij} = -C_6/r_{ij}^6$ is repulsive because the van der Waals coefficient $C_6 < 0$. Here, $r_{ij} = a_{\mathrm{lat}}|i-j|$ is the distance between two atoms on the lattice with period a_{lat}.

This system exhibits a rich variety of strongly correlated magnetic phases (*4*, *5*, *6*, *17*–*20*). In the classical limit ($\Omega = 0$) and for $\Delta > 0$, the many-body ground state corresponds to crystalline states with vanishing fluctuations in the total magnetization $M = 2N_\uparrow - N$, which, for fixed total atom number N, is determined by the spin-↑ component $N_\uparrow = \sum_i \langle \hat{n}_\uparrow^{(i)} \rangle$. In a one-dimensional (1D) chain of $\ell \gg N_\uparrow$ lattice sites, the number of spin-↑ atoms increases by one at the critical detunings $\ell^6\hbar\Delta_c \approx 7|C_6|N_\uparrow^6/a_{\mathrm{lat}}^6$ separating successive crystal states (*8*) (Fig. 1A). The laser coupling introduces quantum fluctuations that can destroy the crystalline order (*4*, *17*, *18*, *21*). Although finite-size effects naturally broaden the transitions in the (Ω, Δ) parameter space (the plot in Fig. 1A was calculated for $N = 7$), extended lobes corresponding to crystalline states can be identified.

The preparation of the crystalline states requires fast dynamical control because of the short lifetime of the Rydberg states of typically several tens of microseconds. The underlying idea is based on the well-known quantum optical technique of rapid adiabatic passage, here realized on a many-body level. Simultaneous temporal control of the Rabi frequency and laser detuning permits us to dynamically connect the many-body ground states in two distinct parameter regimes, while assuring a finite energy gap to the first excited state along the passage. Our initial state with all atoms in their electronic ground state ($N_\uparrow = 0$) coincides with the many-body ground state of the system for negative detuning and vanishing Rabi frequency. For a small coupling strength Ω, the energy gap to the first excited state closes at the transition points Δ_c between successive $N_\uparrow$ manifolds; thus, both Ω and Δ have to be varied to maximize the adiabaticity of the preparation scheme. An intuitive and simple choice of the path $(\Omega(t), \Delta(t))$ starts by slowly switching on the coupling $\Omega(t)$ at a large negative detuning $\Delta(t) = \Delta_{\mathrm{min}}$ (*8*–*10*). Next, the detuning is increased to the desired final blue-detuned value $\Delta_{\mathrm{max}} > 0$, followed by a gradual reduction of the coupling strength Ω to zero. Choosing Δ_{max} between the critical detunings Δ_c of adjacent $N_\uparrow$ manifolds thus yields a crystalline state with a well-defined and controllable magnetization. In the final stage of the last step, the energies of several many-body states become nearly degenerate, as illustrated in Fig. 1B for a representative system of five atoms. These lowest many-body excited states all belong to the same $N_\uparrow$ manifold but feature a finite density of dislocations with respect to the perfectly ordered classical ground state. In practice, this leads to unavoidable nonadiabatic transitions at the end of the laser pulse, which in 1D lead to a slight broadening of the characteristic spatial correlations.

Our experiment started from a 2D degenerate gas of 250 to 700 ^{87}Rb atoms confined to a single antinode of a vertical (z axis) optical lattice. The gas was driven deep into the Mott-insulating phase by adiabatically turning on a square optical lattice with period $a_{\mathrm{lat}} = 532$ nm in the xy plane (*22*). We used a deconfining beam to reduce the harmonic potential induced by the lattice beams and thereby enlarged the spatial extension of a single occupancy Mott insulating state (*23*). Next, we prepared the initial atomic density distribution precisely by cutting out the desired cloud shape from the initial Mott insulator using a spatial light modulator (Fig. 1, C and D) (*24*). For our measurements, we chose line- or disc-shaped atomic samples of well-controlled lengths or radii. The line had a width of three lattice sites and a variable length ℓ. Because this width was much smaller than the blockade radius of approximately nine sites, this geometry can theoretically be described by an effective 1D chain with a collectively enhanced Rabi frequency $\sqrt{3}\Omega$. The average filling was 0.8 atoms per site, and at the edge it dropped to below 0.1 atoms per site, within one lattice site. The coupling to the Rydberg state was realized by a two-photon process via the intermediate state $5P_{3/2}$, using laser wavelengths of 780 and 480 nm with σ^- and σ^+ polarizations, respectively (*25*). Detailed coupling beam parameters are summarized in table S1. Fast control of the Rabi frequency $\Omega(t)$ and the detuning $\Delta(t)$ was implemented by tuning intensity and frequency of the 780-nm coupling laser using a calibrated acousto-optical modulator (*24*). Finally, the Rydberg atoms were detected locally by fluorescence imaging after removing the ground-state atoms from the trap and depumping the Rydberg state back to the ground state (*24*, *25*). The spatial distribution of Rydberg atoms and, therefore, the magnetization profile were measured by averaging over at least 40 realizations (Fig. 1, E and F).

In a first series of experiments, we prepared crystalline states in the elongated geometry. For a fixed system size, the experimentally realizable number $N_\uparrow$ of spin-↑ atoms is limited by the interaction energy as the longitudinal magnetic

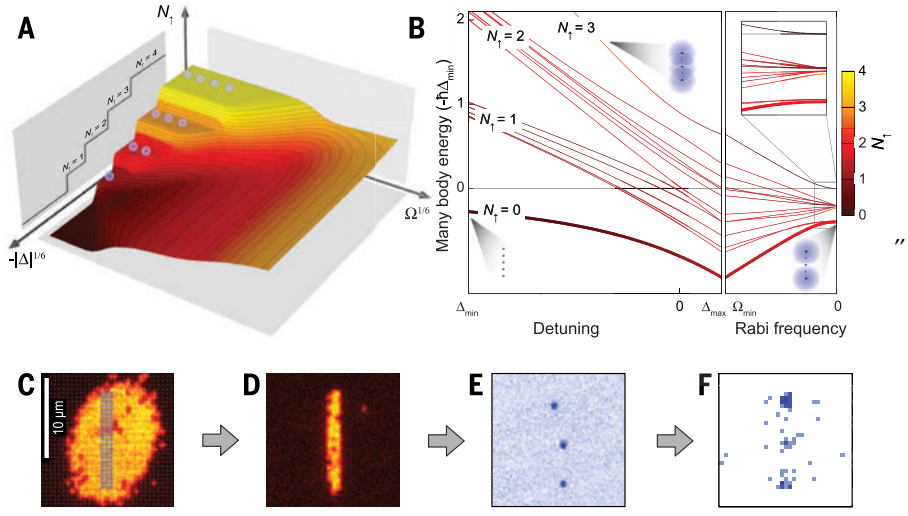

Fig. 1. Phase diagram, energy spectrum, and experimental sequence. (**A**) Phase diagram calculated for a 1D system of $N = 7$ atoms. The color scale indicates the number of spin-↑ atoms $N_\uparrow$ in the many-body ground state (also visualized in the crystalline phase by the small spheres). The detuning Δ and Rabi frequency Ω axes are rescaled by their sixth root. (**B**) Evolution of the many-body spectrum during a sweep, where coupling strength $\Omega(t)$ and detuning $\Delta(t)$ are controlled. The spectrum was calculated for a representative 1D system of five atoms. First, the detuning is changed from Δ_{min} to Δ_{max} at constant Rabi frequency Ω_{max}, with Δ_{max} chosen to prepare $N_\uparrow = 2$. Subsequently, the Rabi frequency is reduced from Ω_{max} to 0. The inset is a zoom into the end of the sweep highlighting the shrinking gap between the energy levels. The color of each line indicates the mean number of spin-↑ atoms in the many-body state. For strongly negative detuning, the four different manifolds correspond to the crystalline states with fixed magnetization given by $N_\uparrow$, as indicated in the figure. In three limiting cases in which the states become classical, the spatial distribution is shown schematically (blue circles, Rydberg atoms; gray circles, ground-state atoms). (**C** to **E**) Representative fluorescence pictures from different times in the experimental cycle. (C) Mott insulator with lattice sites (white dots) and spatial light modulator pattern (semitransparent overlay). (D) Initial atom configuration. (E) Single-shot Rydberg pattern. (**F**) Spatial Rydberg density (magnetization density) after averaging 40 experimental runs (darker color means more detected atoms).

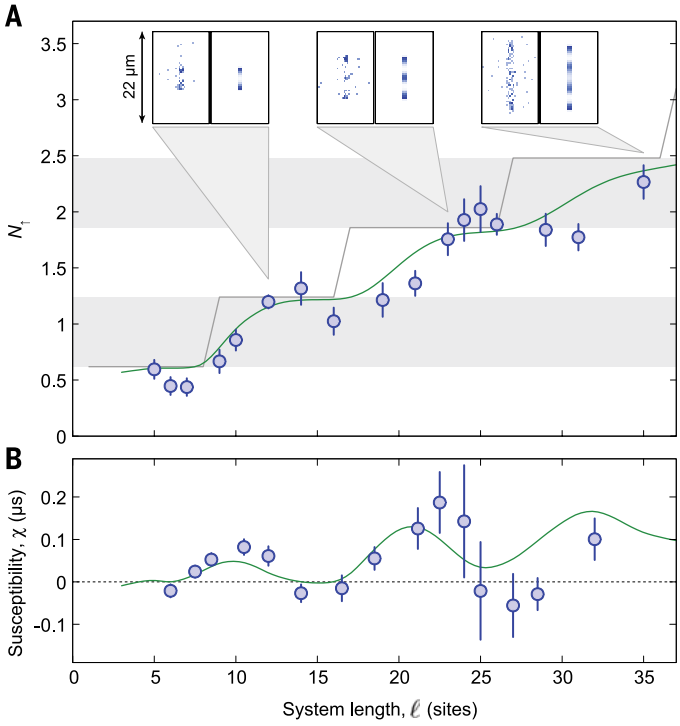

Fig. 2. Identification of the crystalline phase. (**A**) Mean spin-↑ number $N_\uparrow$ versus system length ℓ for an elongated system. Blue circles correspond to the experimental mean number of Rydberg atoms $N_\uparrow$ after the optimized sweep. The green line is the result of the numerical simulation for the experimental initial states, taking into account an initial state filling of 0.8 and length fluctuations on the order of one site. The gray line shows the classical ($\Omega = 0$) prediction. The only free parameter used to fit the theory to the experimental data is the detection efficiency $\alpha = 0.62$. (Insets) Measured spatial distribution of the magnetization (left) and corresponding theory (right) for system lengths ℓ of 12, 23, and 35 sites. The brightness (light to dark) translates to the normalized number of spin-↑ atoms. (**B**) Susceptibility χ of the prepared states. Blue circles are derived from the experimental data shown in (A), using a numerical central difference estimator for the derivative (*24*). The green line is a numerical calculation of $\chi = dN_\uparrow/d\Delta|_{\Delta\max}$ for a given system size ℓ. All error bars, mean ± SEM.

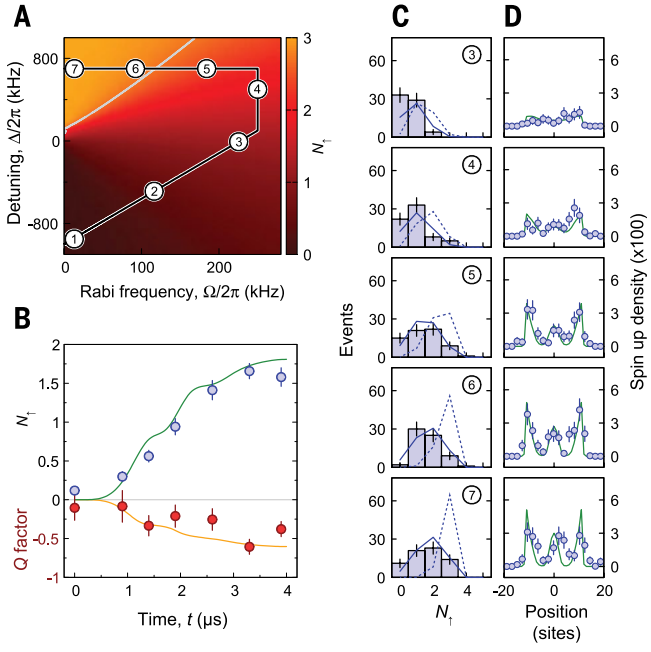

Fig. 3. Dynamical crystallization. (**A**) Illustration of the laser sweep. The black line shows the path of the sweep through the phase diagram; the numbered positions mark the measurements [see (C)]. The color scale indicates the number of spin-↑ atoms $N_\uparrow$ of the ground state for every pair (Ω, Δ). The gray line indicates the boundary of the crystalline lobes, where the Q factor drops below −0.9. The phase diagram was calculated for the experimental parameters. (**B**) Mean number of Rydberg atoms (blue circles) and Q factor (red circles) for the seven times marked in (A), together with the corresponding theoretical predictions (lines). Each of the seven data points is based on at least 65 independent experimental repetitions. (**C**) Experimental and theoretical probability distributions of the number of Rydberg atoms along the sweep [see (A)]. Blue boxes show experimental data, and the dashed and solid lines represent the theoretical result for detection efficiencies of $\alpha = 1$ and $\alpha = 0.62$, respectively. (**D**) Transversally averaged distributions (probability per site) of the spin-↑ atoms for the same times as in (C) with a binning of two sites (blue circles). The slight asymmetry toward the right might be due to a gradient in the Rabi frequency (*24*). The green line is the numerical result. All error bars, mean ± SEM.

field scales weakly with Δ. Hence, instead of varying the detuning, we changed the length ℓ of the initial system to explore the characteristics of the Rydberg crystals (*8*). We measured the mean number of Rydberg atoms $N_\uparrow$ for varying length ℓ using a numerically optimized sweep (*24*). In the optimization, the sweep duration was set to 4 μs, which is a reasonable compromise between the decreasing detection efficiency for longer sweeps and adiabaticity (fig. S1A). The results for the sweep to $\Delta_{\max} = 2\pi \cdot 700(200)$kHz (Fig. 2A) exhibit clear plateaus in $N_\uparrow$ and agree well with numerical predictions that take into account the measured initial atomic density, the laser sweep, and the detection efficiency; the latter is the only free parameter, with a fitted value of $\alpha = 0.62(5)$ (*24*). On the plateaus, the theory predicts strong overlap with states of fixed total magnetization (fig. S3). Using the fact that varying the system size ℓ is approximately equivalent to varying the detuning $\Delta_{\max}$, we extract the susceptibility $\chi \equiv \frac{\partial N_\uparrow}{\partial \Delta_{\max}} \approx \frac{\ell}{6\Delta_{\max}} \frac{\partial N_\uparrow}{\partial \ell}$ from our data (*24*). χ is found to vanish in the plateau regions (Fig. 2B), as expected for crystalline magnetic states. The finite values in between result from the small energy gaps between crystalline states of different magnetization around Δ_c, leading to the preparation of compressible superposition states.

The adiabatic preparation requires the crossing of a phase transition (*4*, *17*, *18*) and, thus, the system undergoes complex correlated quantum dynamics. To study the crystallization process along the sweep trajectory $(\Omega(t), \Delta(t))$, we abruptly switched off the coupling at different times, thereby projecting the many-body state onto the eigenstates of the uncoupled system ($\Omega = 0$). For the measurement, we chose the optimized sweep for the $N_\uparrow = 3$ crystalline manifold in a system of 3 by 23 sites. The path through the phase diagram is shown in Fig. 3A. For each evolution time, we measured the Rydberg number histogram, from which we extracted its mean $N_\uparrow$ and its normalized variance $Q = \frac{\langle(\sum_i \hat{n}_\uparrow^{(i)})^2\rangle - N_\uparrow^2}{N_\uparrow} - 1$ (Fig. 3B). During the sweep, $N_\uparrow$ increases until we observe a saturation behavior that we interpret as the onset of crystallization (fig. S2). Simultaneously, the Q factor decreases from the Poissonian value $Q \approx 0$ to $Q \approx -0.5(1)$, which reflects the approach to the crystalline state. The expected value $Q \approx -1$ is increased to $Q \approx -\alpha$ due to our detection efficiency. The measurement of the full counting statistics along the sweep trajectory allows for a more quantitative comparison with theory (Fig. 3C). However, the finite detection efficiency strongly affects the observed histograms and leads to a tail of the distributions toward lower spin-↑ atom numbers (*24*). Nevertheless, we find very good agreement between theory and experiment for the previously fitted $\alpha = 0.62$.

The high-resolution detection scheme allows for an even more detailed study of the dynamics via the spatial magnetization density, which is largely unaffected by the detection efficiency.

For these elongated finite-size systems, crystallization is directly apparent in the magnetization density and provides similar information as the correlation function $\langle \hat{n}_\uparrow^{(i)} \hat{n}_\uparrow^{(j)} \rangle$. This is because of a breakdown of the translational invariance: For $N_\uparrow > 1$ a spin-↑ atom localized at the edge is energetically favorable. At the beginning of the pulse, we observe delocalized Rydberg atoms throughout the cloud (Fig. 3D), characteristic for the magnetically disordered phase in this parameter regime. For longer times, the spin-↑ atoms start to accumulate at both ends of the line-shaped cloud and finally crystallize to the expected triple-peak configuration. The dynamics of this crystallization process match well with the theoretical prediction. The observed width of the peaks is compatible with the spatial resolution of one lattice site (*25*) (which was included in the theory).

In a different set of experiments, we investigated the adiabatic preparation in a disc-shaped spin system of up to 400 spins. We used the spatial light modulator to prepare the initial distribution with a controlled radius, whose value fluctuated by only one lattice site (*24*). Here, the dynamical preparation turned out to be more challenging, because the effects of the fluctuating boundary are much more pronounced in 2D than in the effective 1D geometry discussed above. Nevertheless, a proper frequency chirp of the coupling laser offers substantial control of the many-body dynamics and the preparation of energetically low-lying many-body states. This is demonstrated in Fig. 4, where we compare the magnetization density at a constant detuning to the result of a chirped coupling from $\Delta_{\mathrm{min}} < 0$ to Δ_{max} (fig. S1B). In the former case, the magnetization is almost uniformly distributed across the atomic sample, whereas in the latter, low-energy states with a localized magnetization density are prepared. The initial system size permits us to control the number of spin-↑ atoms. With increasing $N_\uparrow$, the configuration with all Rydberg atoms located along the circumference becomes energetically unfavorable compared to configurations with an extra Rydberg atom in the center. This structural change is directly visible in the observed patterns shown in Fig. 4.

In conclusion, we have prepared and studied the many-body ground state in a strongly interacting Ising model across the transition to the crystalline phase. This should be contrasted with (*25*), where the observation of ordered structures in highly excited many-body states relied on postselection of the pictures with above average Rydberg number. Such states can be realized by straightforward pulsed laser excitation, whereas preparation of the low-energy states requires precise coherent control of the many-body system via laser coupling and initial density engineering. In the future, our technique might be used to explore quantum phase transitions and the predicted intriguing dynamics when crossing them, such as two-stage melting via a floating crystal phase (*17*, *18*). More generally, our results enable studies of long-range quantum correlations and dissipative quantum magnets in Ising-type spin systems (*26*–*28*). The demonstrated level of control over Rydberg many-body systems is an important step toward the control of multi-atom correlations required for the quantum simulation of dynamical gauge theories (*29*).

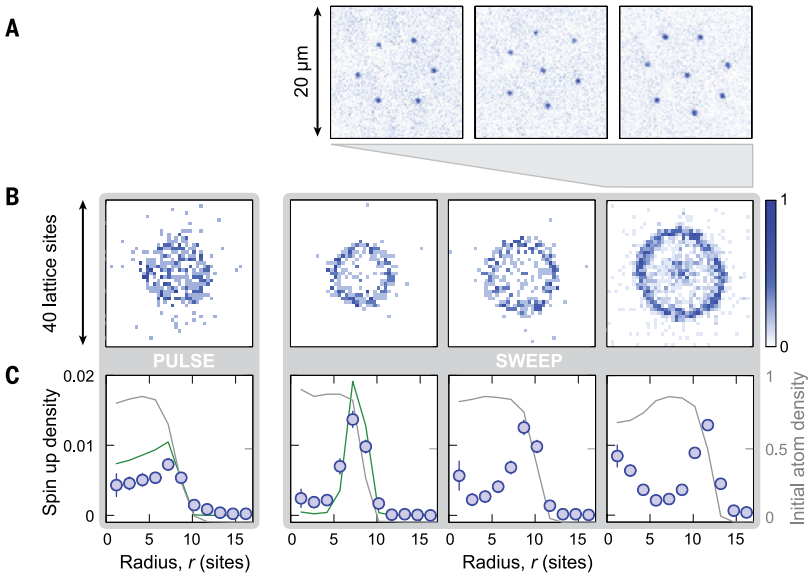

Fig. 4. Dynamical crystallization in disc-shaped samples. (**A**) Unprocessed experimental single shot pictures with 6, 7, and 8 Rydberg atoms from the rightmost data set. Each blue point corresponds to a single atom. (**B** and **C**) Rydberg densities for pulsed (left gray box) and sweeped laser coupling with increasing cloud size from left to right in the right gray box. The pulsed coupling was done with the same amplitude modulation as for the sweep (fig. S1B), but the detuning Δ was held constant (averaged data for $\Delta = 2\pi \cdot 260$ kHz and $\Delta = 2\pi \cdot 760$ kHz is shown). The cloud radius was 8.2(2), 8.3(1), 10.0(3), 11.8(2) lattice sites (left to right). (B) Measured 2D distribution of the magnetization. The color scale represents the normalized counts per site. (C) Azimuthally averaged density distribution (probability per site) of the data shown in (B) (blue dots) and comparison with theory (green line). The theoretical calculation was only feasible for small clouds and takes the atomic ground-state density distribution into account. The experimentally measured initial density is shown in gray on the right axis. Error bars, mean ± SEM.

REFERENCES AND NOTES

1. M. Baranov, *Phys. Rep.* **464**, 71–111 (2008).
2. K. R. A. Hazzard *et al.*, *Phys. Rev. A.* **90**, 063622 (2014).
3. W. Lechner, P. Zoller, *Phys. Rev. Lett.* **111**, 185306 (2013).
4. H. Weimer, R. Löw, T. Pfau, H. P. Büchler, *Phys. Rev. Lett.* **101**, 250601 (2008).
5. P. Richerme *et al.*, *Nature* **511**, 198–201 (2014).
6. P. Jurcevic *et al.*, *Nature* **511**, 202–205 (2014).
7. M. Saffman, T. G. Walker, K. Mølmer, *Rev. Mod. Phys.* **82**, 2313–2363 (2010).
8. T. Pohl, E. Demler, M. D. Lukin, *Phys. Rev. Lett.* **104**, 043002 (2010).
9. J. Schachenmayer, I. Lesanovsky, A. Micheli, A. J. Daley, *New J. Phys.* **12**, 103044 (2010).
10. R. M. W. van Bijnen, S. Smit, K. A. H. van Leeuwen, E. J. D. Vredenbregt, S. J. J. M. F. Kokkelmans, *J. Phys. At. Mol. Opt. Phys.* **44**, 184008 (2011).
11. I. I. Beterov *et al.*, *Phys. Rev. A* **84**, 023413 (2011).
12. R. T. Brierley, C. Creatore, P. B. Littlewood, P. R. Eastham, *Phys. Rev. Lett.* **109**, 043002 (2012).
13. D. Petrosyan, K. Mølmer, *Phys. Rev. A* **87**, 033416 (2013).
14. M. Ebert *et al.*, *Phys. Rev. Lett.* **112**, 043602 (2014).
15. W. R. Anderson, J. R. Veale, T. F. Gallagher, *Phys. Rev. Lett.* **80**, 249–252 (1998).
16. I. Mourachko *et al.*, *Phys. Rev. Lett.* **80**, 253–256 (1998).
17. H. Weimer, H. P. Büchler, *Phys. Rev. Lett.* **105**, 230403 (2010).
18. E. Sela, M. Punk, M. Garst, *Phys. Rev. B* **84**, 085434 (2011).
19. M. Viteau *et al.*, *Phys. Rev. Lett.* **107**, 060402 (2011).
20. P. Richerme *et al.*, *Phys. Rev. Lett.* **111**, 100506 (2013).
21. I. Lesanovsky, *Phys. Rev. Lett.* **106**, 025301 (2011).
22. J. F. Sherson *et al.*, *Nature* **467**, 68–72 (2010).
23. T. Fukuhara *et al.*, *Nature* **502**, 76–79 (2013).
24. Materials and methods are available as supporting material on *Science* Online.
25. P. Schauß *et al.*, *Nature* **491**, 87–91 (2012).
26. I. Lesanovsky, B. Olmos, J. P. Garrahan, *Phys. Rev. Lett.* **105**, 100603 (2010).
27. C. Ates, B. Olmos, J. P. Garrahan, I. Lesanovsky, *Phys. Rev. A* **85**, 043620 (2012).
28. D. Petrosyan, M. Höning, M. Fleischhauer, *Phys. Rev. A* **87**, 053414 (2013).
29. A. W. Glaetzle *et al.*, *Phys. Rev. X* **4**, 041037 (2014).

ACKNOWLEDGMENTS

We acknowledge funding by Max-Planck-Gesellschaft, Deutsche Forschungsgemeinschaft, European Union (UQUAM, SIQS, ITN-COHERENCE, and HAIRS, and a Marie Curie Fellowship to M.C.).

SUPPLEMENTARY MATERIALS

www.sciencemag.org/content/347/6229/1455/suppl/DC1
Supplementary Text
Figs. S1 to S3
Table S1
References (*30*, *31*)

4 July 2014; accepted 9 February 2015
10.1126/science.1258351

SUPERNOVAE

Distances with <4% precision from type Ia supernovae in young star-forming environments

Patrick L. Kelly,[1]* Alexei V. Filippenko,[1] David L. Burke,[2] Malcolm Hicken,[3] Mohan Ganeshalingam,[4] WeiKang Zheng[1]

The luminosities of type Ia supernovae (SNe), the thermonuclear explosions of white-dwarf stars, vary systematically with their intrinsic color and the rate at which they fade. From images taken with the Galaxy Evolution Explorer (GALEX), we identified SNe Ia that erupted in environments that have high ultraviolet surface brightness and star-formation surface density. When we apply a steep model extinction law, we calibrate these SNe using their broadband optical light curves to within ~0.065 to 0.075 magnitude, corresponding to <4% in distance. The tight scatter, probably arising from a small dispersion among progenitor ages, suggests that variation in only one progenitor property primarily accounts for the relationship between their light-curve widths, colors, and luminosities.

The disruption of a white dwarf by a runaway thermonuclear reaction can yield a highly luminous supernova (SN) explosion. The discovery that intrinsically brighter type Ia supernovae (SNe) have light curves that fade more slowly (*1*) and have bluer color (*2*) made it possible to determine the luminosity (intrinsic brightness) of individual SNe Ia with an accuracy of ~0.14 to 0.20 magnitude (mag) from only the SN color and the shape of the optical light curve. Through comparison between the intrinsic and apparent brightness of each SN Ia, the distance to each explosion can be estimated. With the precision afforded by light-curve calibration, measurements of distances to redshift $z \lesssim 0.8$ SNe Ia showed that the cosmic expansion is accelerating (*3*, *4*). Current instruments now regularly detect SNe Ia that erupted when the universe was only ≲4 billion years old (*5*).

A growing number of large-scale observational efforts, including wide-field surveys capable of discovering large numbers of SNe Ia, seek to identify the physical cause of the accelerating cosmic expansion (*6*). Recent analyses have identified a ~10% average difference between the calibrated luminosities of SNe Ia in low- and high-mass host galaxies (*7*–*10*), as well as a comparable difference between SNe Ia with and without strong local Hα emission within ~1 kpc (*11*). Study of the intrinsic colors of SNe Ia (*12*, *13*) has additionally found that the colors depend on the expansion velocities of the ejecta near maximum light. With accurate models that include possible evolution with redshift, corrections for these effects should improve cosmological constraints from SNe distances.

Sufficiently precise calibration of SNe Ia would sharply limit the impact of these potential systematic effects, as well as others, on cosmological measurements, so recent efforts have sought to improve calibration accuracy by examining features of SNe Ia spectra (*12*–*17*), infrared luminosities (*18*, *19*), and their host-galaxy environments (*7*–*9*, *11*). Flexible models for light curves, including principal components analysis, have also recently been applied to synthetic photometry of SNe spectral series (*20*). These several approaches that use additional data about the SN beyond its broadband optical light curve may enable calibration of luminosities to within ~0.10 to 0.12 mag (~5 to 6% in distance). Here we show that a subset of SNe Ia, identified only from photometry of a circular $r = 5$ kpc aperture at the SN position, yields distances from optical light-curve fitting with <4% precision. Our sample consists of SNe Ia with $0.02 < z < 0.09$ and is assembled from the Lick Observatory Supernova Search (LOSS), Harvard-Smithsonian Center for Astrophysics (CfA), and Carnegie Supernova Project (CSP) collections of published light curves given in table S1. Table S2 describes our light-curve sample selection criteria. The $0.02 < z < 0.09$ redshifts of the SNe place them in the Hubble flow, where galaxy peculiar velocities are substantially smaller than velocities arising from the cosmic expansion.

We computed distance moduli using the MLCS2k2 light-curve fitting algorithm (*21*), available as part of the SuperNova ANAlysis (SNANA; v10.35) (*22*) package. MLCS2k2 parameterizes light curves using a decline parameter Δ and an extinction to the explosion A_V and solves simultaneously for both. Model light curves with higher values of Δ fade more quickly and are intrinsically redder.

To model extinction by dust, MLCS2k2 applies the O'Donnell (*23*) law, parameterized by the ratio between the V-band extinction A_V and the selective extinction $E(B-V) = A_B - A_V$. Whereas this ratio $R_V = A_V/E(B-V)$ has a typical value of ~3.1 along Milky Way sight lines (*24*), lower values of R_V yield the smallest Hubble-residual scatter for nearby SNe Ia (*25*). A Hubble residual ($\mathrm{HR} \equiv \mu_{SN} - \mu_z$) is defined here as the difference between μ_{SN}, the distance modulus to the SN inferred from the light curve, and μ_z, the distance modulus expected from the SN redshift and the best-fitting cosmological parameters. SN Ia color variation that does not correlate with brightness (*26*) or reddening by dust different from that along Milky-Way sight lines (*27*) may explain why low values of R_V yield reduced HR scatter. We find that the value $R_V = 1.8$ minimizes the scatter of HRs of the SNe in our full $0.02 < z < 0.09$ sample, after fitting light curves with values of $1 \le R_V \le 4$ in $\Delta R_V = 0.1$ mag increments.

Using images taken by the GALEX satellite, we measured the host-galaxy surface brightnesses in the far- and near-ultraviolet (FUV and NUV) bandpasses within a circular $r = 5$ kpc aperture centered on the SN position. SNe Ia whose apertures have high NUV surface brightness (Fig. 1) exhibit an exceptionally small scatter among their HRs. Among the 17 SNe Ia in environments brighter than 24.45 mag arcsec^{-2}, the root-mean-square scatter in the HRs is 0.073 ± 0.012 mag. When we examine only the 10 SNe Ia with statistical uncertainty $\sigma_{\mu_{SN}} < 0.075$ mag for the distance modulus, the root-mean-square scatter is 0.065 ± 0.016 mag. The only SN we excluded when we computed the sample standard deviation is SN 2007bz, which

Table 1. The scatter among the SNe Ia HRs using $R_V = 1.8$ and $R_V = 3.1$. SB, surface brightness (mag arcsec^{-2}); Σ_{SFR}, star formation surface density [solar mass ($M_\odot$) year^{-1} kpc^{-2}]. We computed the standard deviation uncertainty through bootstrap resampling, after outliers with HRs of >0.3 mag were removed. A simulation found that the uncertainty of the standard deviation computed using bootstrap resampling is underestimated by ~25%, and we have corrected the estimates using this factor.

Criterion	σ_{HR} ($R_V = 1.8$)	σ_{HR} ($R_V = 3.1$)
UV and $\sigma_{\mu_{SN}} < 0.075$	0.128 ± 0.014 ($N = 50$)	0.131 ± 0.015 ($N = 46$)
NUV SB < 24.45	0.065 ± 0.016 ($N = 10$; $P = 1.1\%$)	0.094 ± 0.027 ($N = 8$; $P = 24\%$)
NUV SB < 24.7	0.074 ± 0.012 ($N = 13$; $P = 1.2\%$)	0.087 ± 0.019 ($N = 13$; $P = 17\%$)
Full UV sample	0.130 ± 0.010 ($N = 77$)	0.138 ± 0.008 ($N = 78$)
NUV SB < 24.45	0.073 ± 0.012 ($N = 17$; $P = 0.2\%$)	0.090 ± 0.014 ($N = 17$; $P = 1.1\%$)
NUV SB < 24.7	0.083 ± 0.012 ($N = 22$; $P = 0.3\%$)	0.089 ± 0.010 ($N = 24$; $P = 0.6\%$)
Full SFR sample	0.133 ± 0.012 ($N = 61$)	0.139 ± 0.012 ($N = 62$)
$\Sigma_{SFR} > -2.1$	0.075 ± 0.018 ($N = 11$; $P = 1.1\%$)	0.081 ± 0.016 ($N = 11$; $P = 1.3\%$)
$\Sigma_{SFR} > -2.25$	0.094 ± 0.015 ($N = 18$; $P = 1.8\%$)	0.102 ± 0.015 ($N = 18$; $P = 2.6\%$)

[1]Department of Astronomy, University of California, Berkeley, CA 94720-3411, USA. [2]SLAC National Accelerator Laboratory, 2575 Sand Hill Road, Menlo Park, CA 94025, USA. [3]Harvard-Smithsonian Center for Astrophysics, Cambridge, MA 02138, USA. [4]Lawrence Berkeley National Laboratory, 1 Cyclotron Road, Berkeley, CA 94720, USA.
*Corresponding author. E-mail: pkelly@astro.berkeley.edu

exploded in a region of high surface brightness and has an ~8σ offset from the redshift-distance relation (HR = 0.60 ± 0.07 mag). Although our R_V = 1.8 MLCS2k2 fit to the light curve of SN 2007bz yields A_V = 0.26 ± 0.07 mag, a published BAYESN fit instead favors a higher extinction of A_V = 0.81 ± 0.12 mag (*19*), which would correspond to a significantly reduced HR. The redshift-distance relation constructed using only SNe Ia in environments with high NUV surface brightness exhibits significantly smaller scatter than that for the entire SNe Ia sample (Fig. 2).

To determine the statistical significance of finding a sample of SNe with HR scatter σ_{HR}, we performed 10,000 simulations in which we randomly shuffled the HRs of the parent SN sample, after removing outliers with >0.3 mag. For each shuffled sample of SNe, we next simulated the selection of a NUV surface-brightness upper limit that minimizes the Hubble-residual scatter of the sample. Searching within ±0.2 mag of the 24.45 mag NUV analysis upper limit in 0.05 mag increments, we identify the upper limit that minimized the shuffled sample's HR scatter. The percentage of simulations that yielded a standard deviation smaller than σ_{HR} is the *P* value. As shown in Table 1, only 0.2% of simulated samples have a scatter smaller than the 0.073 ± 0.012 mag that we measured for SNe Ia in host environments with high UV surface brightness.

For the redshift distribution of the SNe that form the 24.45-mag NUV sample, we used Monte Carlo simulations to calculate the expected contributions of peculiar velocities to HR scatter. We computed σ_m = 0.050 ± 0.010 mag for σ_v = 200 km s^{-1}, and σ_m = 0.075 ± 0.015 mag for σ_v = 300 km s^{-1}. Because the expected scatter from peculiar motions is not much smaller than the HR scatter we measured, the intrinsic scatter in the calibrated luminosities of SNe Ia in host environments with high UV surface brightness is likely to be appreciably smaller than ~0.08 mag (~4% in distance).

We also estimated the average star-formation surface density [solar mass ($M_\odot$) year^{-1} kpc^{-2}] within each circular r = 5 kpc aperture, when both optical (*ugriz* or *BVRI*) and FUV and NUV imaging of the host galaxy were available. The star-formation rate is computed by comparing the observed fluxes with predictions for stellar populations having a broad range of star-formation histories. Although fewer host galaxies have the necessary imaging, Fig. 3 shows that the SNe having high–star-formation density environments also have comparably small scatter in their HRs. The 11 SNe Ia with average star-formation surface density values in their apertures greater than −2.1 dex exhibit σ_{HR} = 0.075 ± 0.018 mag. Among randomly shuffled samples, only 1.1% have a smaller standard deviation among their HRs, after searching within ±0.1 dex of the −2.1-dex limit.

The 10-kpc diameter of the host-galaxy aperture subtends an angle of 1.6″ at z = 0.5 and 1.3″ at z = 1. Therefore, for future cosmological analyses, the NUV surface brightnesses of high-redshift SNe Ia hosts within a circular r = 5 kpc aperture can be measured from the ground in conditions with sub–arcsecond seeing, making possible precise measurements of distances to high redshift.

The large UV surface brightnesses and star-formation densities of the environments of highly standardizable SNe Ia, as well as the star formation evident from Sloan Digital Sky Survey (SDSS) images, reveal the existence of young massive stars. A reasonable conclusion is that the delay between the birth of the SN precursor and its explosion as a white dwarf is comparatively short.

The SDSS composite images in fig. S6 show that the r = 5 kpc apertures include stellar populations of multiple ages, and the younger stellar populations are expected to dominate the measured NUV flux. Whereas O-type and early B-type stars of masses ≳15 $M_\odot$ are required to produce the ionizing radiation responsible for HII regions, stars with masses of ≳5 $M_\odot$ having lifetimes of ≲100 million years are responsible for the UV luminosity (*28*, *29*). A delay time of ~500 million years would be required for a SN Ia progenitor to travel ~5 kpc with a natal velocity of 10 km s^{-1}.

The total mass, metallicity, central density, and carbon-to-oxygen ratio of the white dwarf, as well as the properties of the binary companion, probably vary within the progenitor population

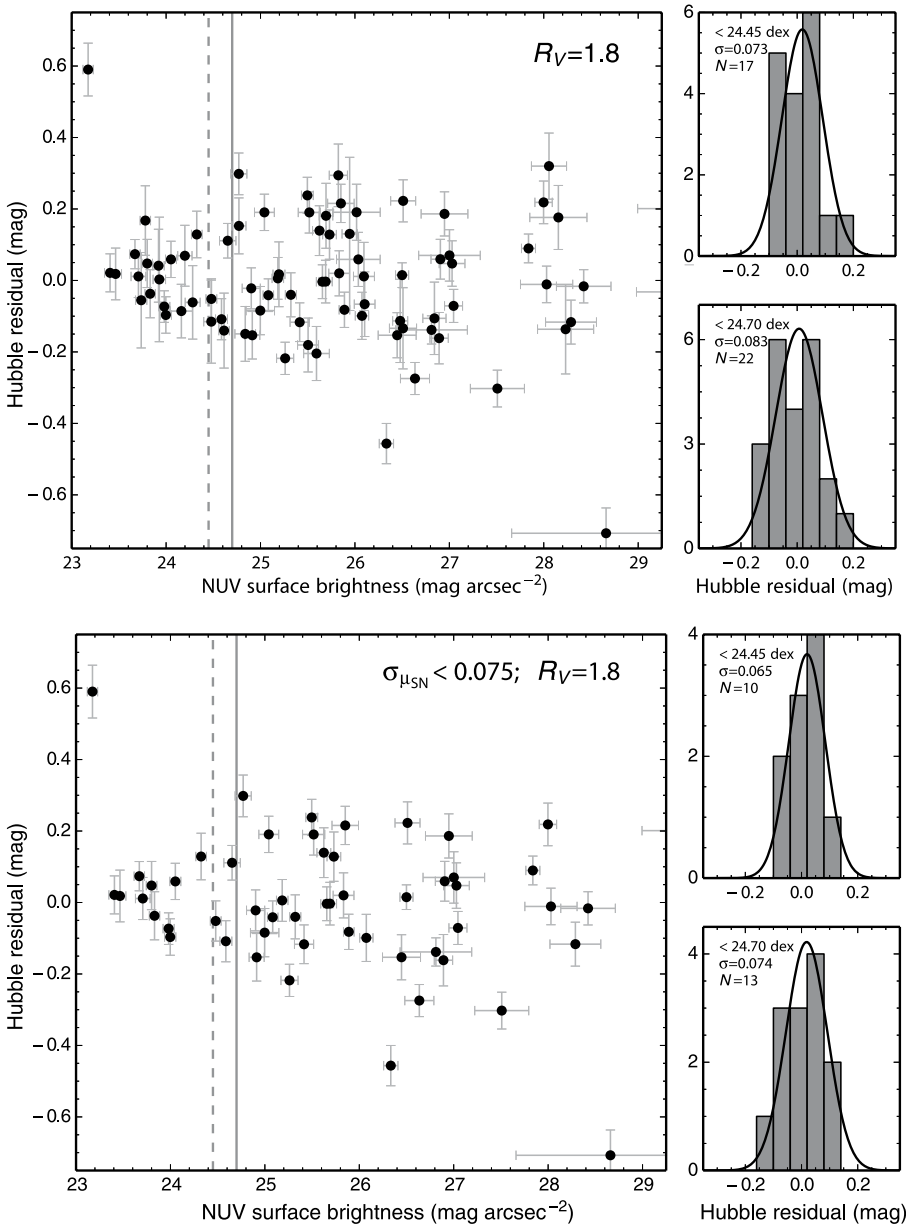

Fig. 1. HRs against NUV surface brightness within the r = 5 kpc aperture around SNe Ia. Top panels show all SNe in the sample, whereas bottom panels include only SNe with small statistical uncertainty ($\sigma_{\mu_{SN}}$ < 0.075 mag) in distance modulus. Panels on the right show the distributions of HRs for SNe in regions brighter than the 24.7 mag arcsec^{-2} marked by a solid vertical line in each figure. Dashed vertical lines show a more restrictive threshold of 24.45 mag arcsec^{-2}. Error bars shown above and in other plots correspond to 68% confidence intervals.

of SNe Ia. In theoretical simulations of both single-degenerate (*30*–*32*) and double-degenerate (*33*, *34*) explosions, the variation of many of these parameters can yield a correlation between light-curve decline rate and luminosity, but the normalization and slope of these predicted correlations generally show significant differences. Therefore, it is likely that variations in one, or possibly two, progenitor properties contribute significantly to the light-curve width/color/luminosity relation of the highly standardizable SNe Ia population. The asymmetry of the explosion, which is thought to increase random scatter around the light-curve width/color/luminosity relation, may be small within this population and may possibly indicate that most burning occurs during the detonation phase (*31*). A reasonable possibility is that the relatively young ages of the progenitor population correspond to a population with a smaller dispersion in their ages, leading to more uniform calibration.

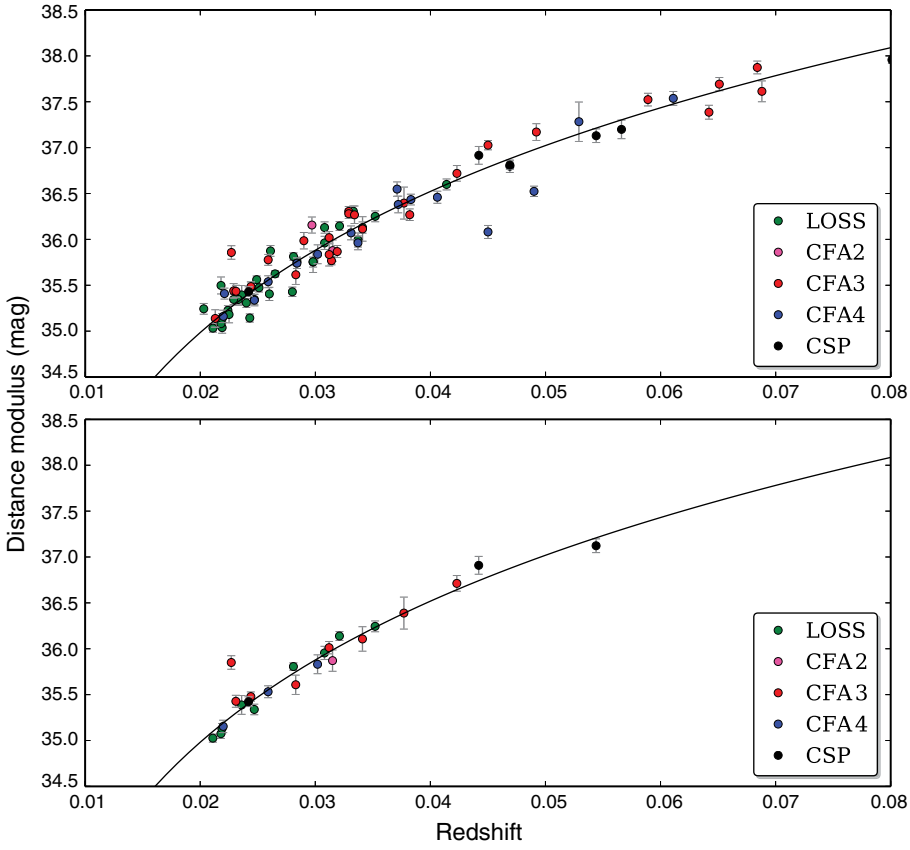

Fig. 2. The SNe Ia Hubble redshift-distance relations. Upper panel shows distance modulus μ versus redshift *z* for SNe Ia. Lower panel shows the same relation for SNe where the aperture NUV surface brightnesses are brighter than 24.7 mag arc sec^{-2}. The color of each point shows the source of the SN light curve. In the lower panel, SN 2007bz is the single object with an outlying distance modulus (0.60 ± 0.07 mag).

As we show in Table 1, for both the full sample and the SNe found in UV-bright environments, MLCS2k2 distances computed with R_V = 1.8 yield a smaller HR scatter than those computed with R_V = 3.1. Although the low apparent value of R_V may result in part from color variation unconnected to SN brightness (*26*), polarization data suggest that dust properties may also be important. For a handful of well-sampled SNe Ia where the extinction is large [$E(B - V) \gtrsim 0.4$ mag], the small intrinsic continuum polarization (≲0.3%) of SNe Ia (*35*) allows constraints on the wavelength-dependent polarization introduced by intervening dust (*27*). Analyses of SN 1986G, SN 2006X, SN 2008fp, and SN 2014J show evidence for low values of R_V and blue polarization peaks, which are consistent with a small grain size distribution (*27*). In these cases, the polarization vector is aligned with the apparent local spiral arm structure, suggesting that the dust is interstellar rather than circumstellar.

A possibility is that SN environments exhibiting intense star formation may generate outflowing winds that entrain small dust grains, which might explain the evidence for low R_V and the continuum polarization. Dust particles in the SN-driven superwind emerging from the nearby starburst galaxy

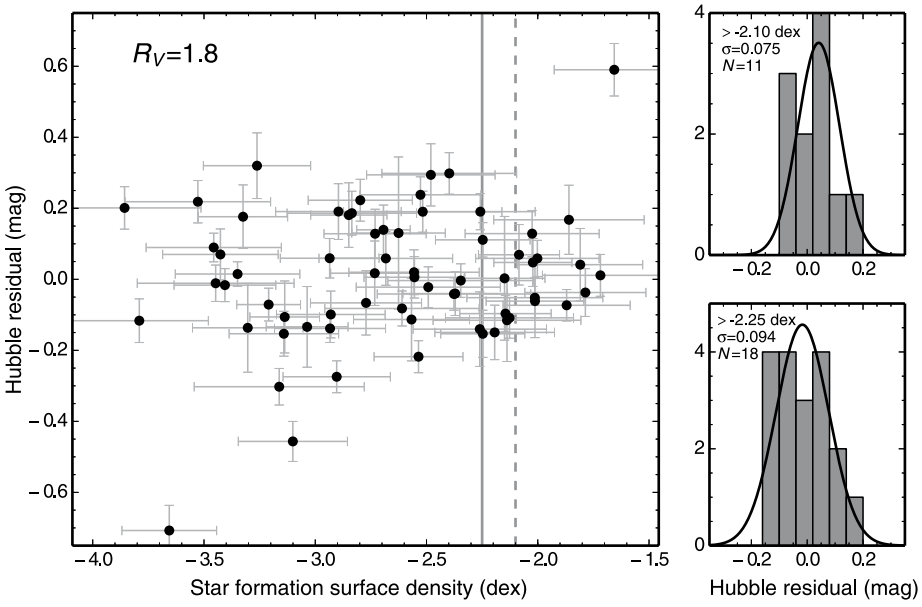

Fig. 3. HRs against star-formation surface density within the *r* = 5 kpc aperture around SNe Ia. Host-galaxy star-formation surface density measured within a circular *r* = 5 kpc aperture centered on the SN position. Panels on the right show the distributions of HRs for SNe in regions with higher star-formation surface density than the −2.25-dex limit marked by a solid vertical line and than the −2.1-dex limit marked by the vertical dashed line. As shown in Table 1, a smaller number of host galaxies have the optical broadband photometry necessary to estimate the star-formation surface density within the *r* = 5 kpc circular aperture.

M82 scatter light that originates in the star-forming disk, and the spectral energy distribution of the scattered light is consistent with a comparatively small grain size distribution (*36*).

REFERENCES AND NOTES

1. M. M. Phillips, *Astrophys. J.* **413**, L105 (1993).
2. A. G. Riess, W. H. Press, R. P. Kirshner, *Astrophys. J.* **473**, 88–109 (1996).
3. A. G. Riess *et al.*, *Astron. J.* **116**, 1009–1038 (1998).
4. S. Perlmutter *et al.*, *Astrophys. J.* **517**, 565–586 (1999).
5. D. O. Jones *et al.*, *Astrophys. J.* **768**, 166 (2013).
6. D. H. Weinberg *et al.*, *Phys. Rep.* **530**, 87–255 (2013).
7. P. L. Kelly, M. Hicken, D. L. Burke, K. S. Mandel, R. P. Kirshner, *Astrophys. J.* **715**, 743–756 (2010).
8. M. Sullivan *et al.*, *Mon. Not. R. Astron. Soc.* **406**, 782 (2010).
9. H. Lampeitl *et al.*, *Astrophys. J.* **722**, 566–576 (2010).
10. M. Childress *et al.*, *Astrophys. J.* **770**, 108 (2013).
11. M. Rigault *et al.*, *Astron. Astrophys.* **560**, A66 (2013).
12. X. Wang *et al.*, *Astrophys. J.* **699**, L139–L143 (2009).
13. R. J. Foley, D. Kasen, *Astrophys. J.* **729**, 55 (2011).
14. S. Bailey *et al.*, *Astron. Astrophys.* **500**, L17–L20 (2009).
15. S. Blondin, K. S. Mandel, R. P. Kirshner, *Astron. Astrophys.* **526**, A81 (2011).
16. J. M. Silverman, M. Ganeshalingam, W. Li, A. V. Filippenko, *Mon. Not. R. Astron. Soc.* **425**, 1889–1916 (2012).
17. K. S. Mandel, R. J. Foley, R. P. Kirshner, *Astrophys. J.* **797**, 75 (2014).
18. W. M. Wood-Vasey *et al.*, *Astrophys. J.* **689**, 377–390 (2008).
19. K. S. Mandel, G. Narayan, R. P. Kirshner, *Astrophys. J.* **731**, 120 (2011).
20. A. G. Kim *et al.*, *Astrophys. J.* **766**, 84 (2013).
21. S. Jha, A. G. Riess, R. P. Kirshner, *Astrophys. J.* **659**, 122–148 (2007).
22. R. Kessler *et al.*, *Publ. Astron. Soc. Pac.* **121**, 1028 (2009).
23. J. E. O'Donnell, *Astrophys. J.* **422**, 158 (1994).
24. E. L. Fitzpatrick, D. Massa, *Astrophys. J.* **663**, 320–341 (2007).
25. M. Hicken *et al.*, *Astrophys. J.* **700**, 1097–1140 (2009).
26. D. M. Scolnic *et al.*, *Astrophys. J.* **780**, 37 (2014).
27. F. Patat *et al.*, available at http://arxiv.org/abs/1407.0136 (2014).
28. S. G. Stewart *et al.*, *Astrophys. J.* **529**, 201–218 (2000).
29. S. M. Gogarten *et al.*, *Astrophys. J.* **691**, 115–130 (2009).
30. S. E. Woosley, D. Kasen, S. Blinnikov, E. Sorokina, *Astrophys. J.* **662**, 487–503 (2007).
31. D. Kasen, F. K. Röpke, S. E. Woosley, *Nature* **460**, 869–872 (2009).
32. S. A. Sim *et al.*, *Mon. Not. R. Astron. Soc.* **436**, 333–347 (2013).
33. D. Kushnir, B. Katz, S. Dong, E. Livne, R. Fernández, *Astrophys. J.* **778**, L37 (2013).
34. R. Moll, C. Raskin, D. Kasen, S. E. Woosley, *Astrophys. J.* **785**, 105 (2014).
35. L. Wang, J. C. Wheeler, *Annu. Rev. Astron. Astrophys.* **46**, 433–474 (2008).
36. S. Hutton *et al.*, *Mon. Not. R. Astron. Soc.* **440**, 150–160 (2014).

ACKNOWLEDGMENTS

We thank S. Sim, J. C. Wheeler, J. Silverman, A. Conley, M. Graham, D. Kasen, I. Shivvers, and R. Kessler for useful discussions and comments on the paper and J. Schwab for his help providing background about theoretical modeling. We are grateful to the staffs at Lick Observatory and Kitt Peak National Observatory (KPNO) for their assistance. The late Weidong Li was instrumental to the success of LOSS. A.V.F.'s supernova group at the University of California Berkeley has received generous financial assistance from the Christopher R. Redlich Fund, the TABASGO Foundation, and NSF grant AST-1211916. The Katzman Automatic Imaging Telescope and its ongoing operation were made possible by donations from Sun Microsystems, the Hewlett-Packard Company, AutoScope Corporation, Lick Observatory, NSF, the University of California, the Sylvia and Jim Katzman Foundation, and the TABASGO Foundation. The SLAC Department of Energy contract number is DE-AC02-76SF00515. GALEX data are available from http://galex.stsci.edu/GR6/, SDSS data may be obtained at www.sdss.org, the KPNO imaging is archived at http://portal-nvo.noao.edu, and the Lick Observatory images are available from http://astro.berkeley.edu/bait/public_html/iahostpaper/.

SUPPLEMENTARY MATERIALS

www.sciencemag.org/content/347/6229/1459/suppl/DC1
Materials and Methods
Figs. S1 to S7
Tables S1 to S4
References (*37*–*64*)

19 September 2014; accepted 12 February 2015
10.1126/science.1261475

DARK MATTER

The nongravitational interactions of dark matter in colliding galaxy clusters

David Harvey,[1,2]* Richard Massey,[3] Thomas Kitching,[4] Andy Taylor,[2] Eric Tittley[2]

Collisions between galaxy clusters provide a test of the nongravitational forces acting on dark matter. Dark matter's lack of deceleration in the "bullet cluster" collision constrained its self-interaction cross section $\sigma_{DM}/m < 1.25$ square centimeters per gram (cm^2/g) [68% confidence limit (CL)] (σ_{DM}, self-interaction cross section; m, unit mass of dark matter) for long-ranged forces. Using the Chandra and Hubble Space Telescopes, we have now observed 72 collisions, including both major and minor mergers. Combining these measurements statistically, we detect the existence of dark mass at 7.6σ significance. The position of the dark mass has remained closely aligned within 5.8 ± 8.2 kiloparsecs of associated stars, implying a self-interaction cross section $\sigma_{DM}/m < 0.47$ cm^2/g (95% CL) and disfavoring some proposed extensions to the standard model.

Many independent lines of evidence now suggest that most of the matter in the universe is in a form outside the standard model of particle physics. A phenomenological model for cold dark matter (*1*) has proved hugely successful on cosmological scales, where its gravitational influence dominates the formation and growth of cosmic structure. However, there are several challenges on smaller scales: The model incorrectly predicts individual galaxy clusters to have more centrally concentrated density profiles (*2*) and larger amounts of substructure (*3*, *4*) and anticipates that the Milky Way will have more satellites able to produce stars (*5*) than are observed. These inconsistencies could be resolved through astrophysical processes (*6*) or if dark matter particles are either warm (*7*) or self-interacting with cross section $0.1 < \sigma_{DM}/m < 1$ cm^2/g (*8*–*10*). Following (*11*), we define the momentum transfer cross section per unit mass σ_{DM}/m, integrating over all scattering angles and assuming that individual dark matter particles are indistinguishable.

Self-interaction within a hidden dark sector is a generic consequence of some extensions to the standard model. For example, models of mirror dark matter (*12*) and hidden-sector dark matter (*12*–*16*) all predict anisotropic scattering with $\sigma_{DM}/m \approx 1$ barn/GeV = 0.6 cm^2/g, similar to nuclear cross sections in the standard model. Note that couplings within the dark sector can be many orders of magnitude larger than those between dark matter and standard model particles, which are, at most, on the order of picobarns (*17*).

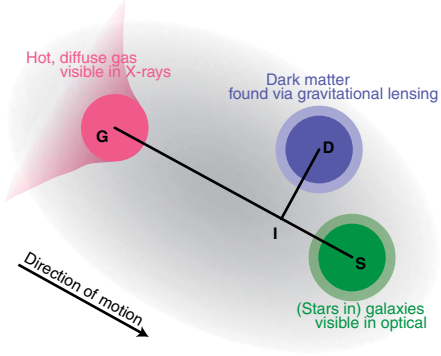

Fig. 1. Cartoon showing the three components in each piece of substructure and their relative offsets, illustrated by black lines. The three components remain within a common gravitational potential, but their centroids become offset due to the different forces acting on them, plus measurement noise. We assume the direction of motion to be defined by the vector from the diffuse, mainly hydrogen gas (which is stripped by ram pressure) to the galaxies (for which interaction is a rare event). We then measure the lag from the galaxies to the gas δ_{SG}, as well as to the dark matter in a parallel δ_{SI} and perpendicular δ_{DI} direction. G, hot, diffuse gas; D, dark matter; S, galaxies; I, the point along the vector joining the galaxies and gas that is closest to the location of the dark matter peak.

[1]Laboratoire d'Astrophysique, École Polytechnique Fédérale de Lausanne, Observatoire de Sauverny, 1290 Versoix, Switzerland. [2]Royal Observatory, University of Edinburgh, Blackford Hill, Edinburgh EH9 3HJ, UK. [3]Institute for Computational Cosmology, Durham University, South Road, Durham DH1 3LE, UK. [4]Mullard Space Science Laboratory, University College London, Dorking, Surrey RH5 6NT, UK.
*Corresponding author. E-mail: david.harvey@epfl.ch

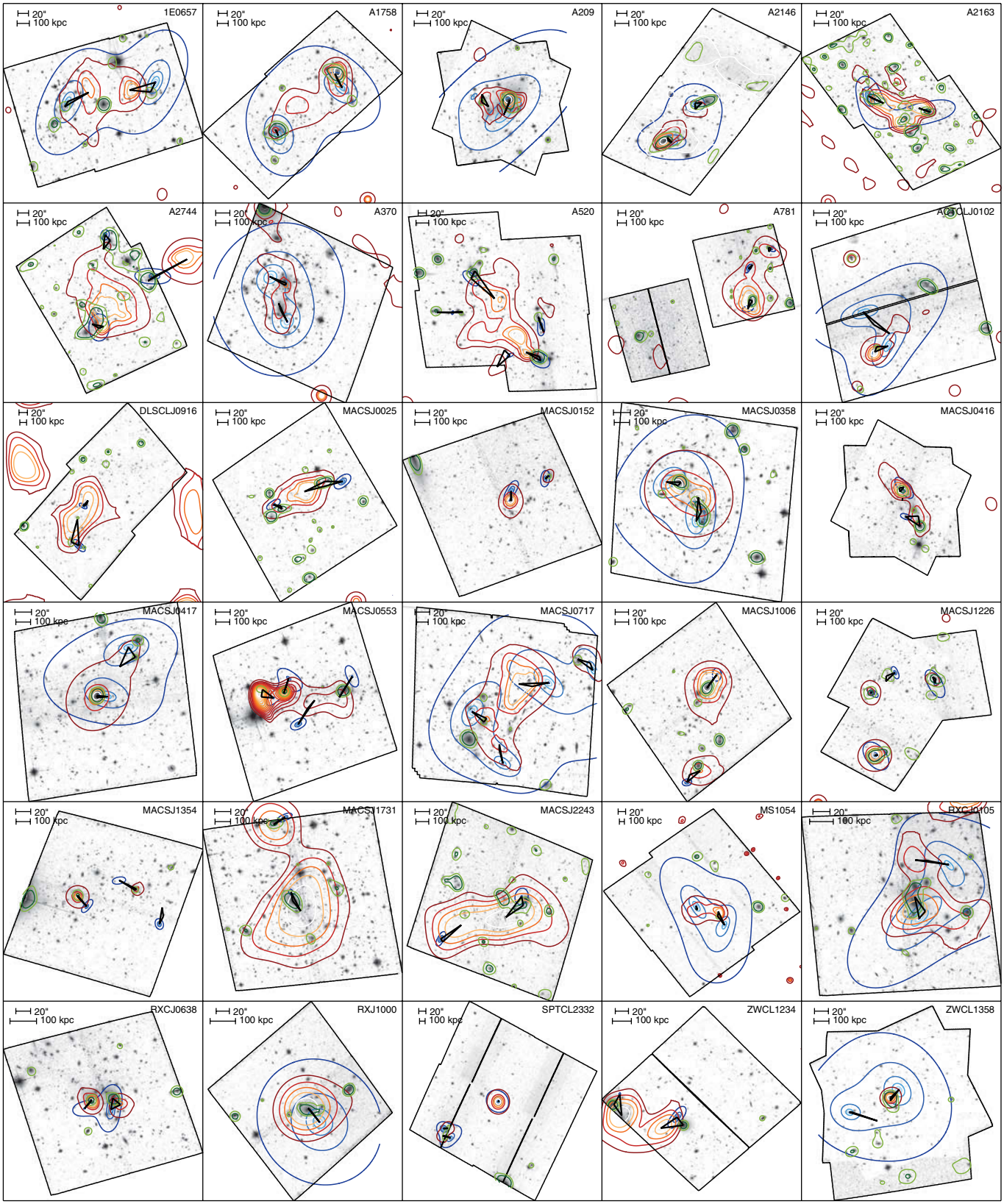

Fig. 2. Observed configurations of the three components in the 30 systems that we studied. The background shows the HST image, with contours showing the distribution of galaxies (green), gas (red), and total mass, which is dominated by dark matter (blue).

In terrestrial collider experiments, the forces acting on particles can be inferred from the trajectory and quantity of emerging material. Collisions between galaxy clusters contain dark matter and provide similar tests for dark sector forces. If dark matter's particle interactions are frequent but exchange little momentum (via a light mediator particle that produces a long-ranged force and anisotropic scattering), the dark matter will be decelerated by an additional drag force. If the interactions are rare but exchange a lot of momentum (via a massive mediator that produces a short-ranged force and isotropic scattering), dark matter will tend to be scattered away and lost (*11*, *18*, *19*).

The dynamics of colliding dark matter can be calibrated against that of accompanying standard model particles. The stars that reside within galaxies, which are visible in a smoothed map of their optical emission, have effectively zero cross section because they are separated by such vast distances that they very rarely collide. The diffuse gas between galaxies, which is visible in x-ray emission, has a large electroweak cross section; it is decelerated and most is eventually stripped away by ram pressure (*20*). Dark matter, which can be located via gravitational lensing (*21*), behaves somewhere on this continuum (Fig. 1).

The tightest observational constraints on dark matter's interaction cross section come from its behavior in the giant "bullet cluster" collision 1E0657-558 (*22*). A test for drag yields $\sigma_{DM}/m <$ 1.25 cm^2/g [68% confidence limit (CL)], and a test for mass loss yields $\sigma_{DM}/m <$ 0.7 cm^2/g (68% CL) (*18*). Half a dozen more galaxy cluster collisions have since been discovered, but no tighter constraints have been drawn. This is because the analysis of any individual system is fundamentally limited by uncertainty in the three-dimensional (3D) collision geometry (the angle of the motion with respect to our line of sight, the impact parameter, and the impact velocity) or the original mass of the clusters.

The same dynamical effects are also predicted by simulations in collisions between low-mass systems (*11*). Observations of low-mass systems produce noisier estimates of their mass and position (*23*–*25*), but galaxy clusters continually grow through ubiquitous minor mergers, and statistical uncertainty can be decreased by building a potentially very large sample (*26*, *27*). Furthermore, we have developed a statistical model to measure dark matter drag from many noisy observations, within which the relative trajectories of galaxies, gas, and dark matter can be combined in a way that eliminates dependence on 3D orientation and the time since the collision (*28*).

We have studied all galaxy clusters for which optical imaging exists in the Hubble Space Telescope (HST) (Advanced Camera for Surveys) data archive (*29*) and for which x-ray imaging exists in the Chandra Observatory data archive (*30*). We select only those clusters containing more than one component of spatially extended x-ray emission. Our search yields 30 systems, mostly between redshift $0.2 < z < 0.6$ plus two at $z > 0.8$, containing 72 pieces of substructure in total (table S1). In every piece of substructure, we measure the distance from the galaxies to the gas δ_{SG}. Assuming this lag defines the direction of motion, we then measure the parallel δ_{SI} and perpendicular δ_{DI} distance from the galaxies to the lensing mass (Fig. 2).

We first test the null hypothesis that there is no dark matter in our sample of clusters [a similar experiment was first carried out on the bullet cluster, finding a 3.4σ and 8σ detection (*31*)]. Observations that do not presuppose the existence of dark matter (*32*) show that 10^{14} $M_\odot$ clusters ($M_\odot$, solar mass) contain only 3.2% of their mass in the form of stars. We compensate for this mass, which pulls the lensing signal toward the stars and raises δ_{GI} by an amount typically 0.78 ± 0.30 kpc (computed using the known distances to the stars δ_{SG}; see supplementary materials and methods). The null hypothesis is that the remaining mass must be in the gas. However, we observe a spatial offset between that is far from the expected overlap, even in the presence of combined noise from our gravitational lensing and x-ray observations (Fig. 3A). A Kolmogorov-Smirnov test indicates that the observed offsets between gas and mass are inconsistent with the null hypothesis at 7.6σ, a P value of 3×10^{-14} (without compensation for the mass of stars, this is 7.7σ). This test thus provides direct evidence for a dominant component of matter in the clusters that is not accounted for by the luminous components.

Having reaffirmed the existence of dark matter, we attempt to measure any additional drag force acting on it, caused by long-range self-interactions. We measure the spatial offset of dark matter behind the stars, compensating as before for the 16% of mass in the gas (*33*) by subtracting a small amount from δ_{SI} (on average, 4.3 ± 1.6 kpc). We measure a mean dark matter lag of $\langle\delta_{SI}\rangle = -5.8 \pm 8.2$ kpc in the direction of motion (Fig. 3B) and $\langle\delta_{DI}\rangle = 1.8 \pm 7.0$ kpc perpendicularly. The latter is useful as a control test: Symmetry demands that it must be consistent with zero in the absence of systematics. We also use its scatter as one estimate of observational error in the other offsets.

We interpret the lag through a model (*28*) of dark matter's optical depth [similarly to previous studies (*19*, *23*)]. Gravitational forces act to keep gas, dark matter, and galaxies aligned, whereas any extra drag force on dark matter induces a fractional lag

$$\beta \equiv \frac{\delta_{SI}}{\delta_{SG}} = B\left\{1 - e^{\left[\frac{-(\sigma_{DM}-\sigma_{gal})}{\sigma^*}\right]}\right\} \qquad (1)$$

where σ_{gal} is the interaction cross section of the galaxies, coefficient B encodes the relative behavior of dark matter and gas, and σ* is the characteristic cross section at which a halo of given geometry becomes optically thick. We assume that stars do not interact, so $\sigma_{gal} \approx 0$. To ensure conservative limits on σ_{DM}/m, we also assume $B \approx 1$ and marginalize over $\sigma^*/m \approx 6.5 \pm 3$ cm^2/g, propagating this broad uncertainty to our final constraints (see materials and methods). Adopting the dimensionless ratio brings two advantages. First, it removes dependence on the angle of the collision with respect to the line of sight. Second, it represents a physical quantity

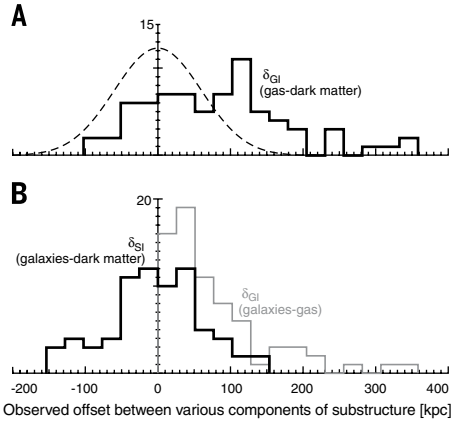

Fig. 3. Observed offsets between the three components of 72 pieces of substructure. Offsets δ_{SI} and δ_{GI} include corrections accounting for the fact that gravitational lensing measures the total mass, not just that of dark matter. (**A**) The observed offset between gas and mass, in the direction of motion. The smooth curve shows the distribution expected if dark matter does not exist; this hypothesis is inconsistent with the data at 7.6σ statistical significance. (**B**) Observed offsets from galaxies to other components. The fractional offset of dark matter toward the gas, δ_{SI}/δ_{SG}, is used to measure the drag force acting on the dark matter.

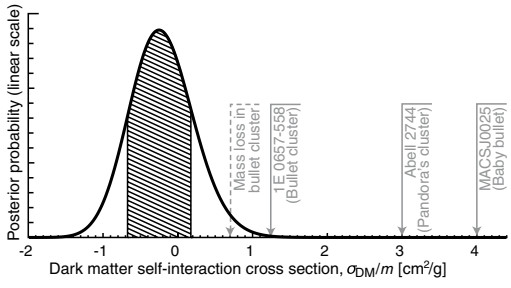

Fig. 4. Constraints on the self-interaction cross section of dark matter. These are derived from the separations $\beta = \delta_{SI}/\delta_{SG}$, assuming a dynamical model to compare the forces acting on dark matter and standard model particles (*28*). The hatched region denotes 68% CLs, to be compared to the 68% confidence upper limits from previous studies of the most-constraining individual clusters. Note that the tightest previous constraint is derived from a measurement of dark matter mass loss, which is sensitive to short-range self-interaction forces; all other constraints are measurements of a drag force acting on dark matter, caused by long-range self-interactions.

that is expected to be the same for every merger configuration, so measurements from the different systems can be simply averaged (with appropriate noise weighting, although in practice, the constraining power from weak lensing-only measurements comes roughly equally from all of the systems).

Combining measurements of all of the colliding systems, we measure a fractional lag of dark matter relative to gas $\langle\beta\rangle = -0.04 \pm 0.07$ (68% CL). Interpreting this through our model implies that dark matter's momentum transfer cross section is $\sigma_{DM}/m = -0.25^{+0.42}_{-0.43}$ cm^2/g (68% CL, two-tailed) or $\sigma_{DM}/m < 0.47$ cm^2/g (95% CL, one-tailed) (Fig. 4). This result rules out parts of model space of hidden-sector dark matter models [e.g., (*12*, *13*, *15*, *16*)] that predict $\sigma_{DM}/m \approx 0.6$ cm^2/g on cluster scales through a long-range force. The control test found $\langle\beta_\perp\rangle \equiv \langle\delta_{DI}/\delta_{SG}\rangle = -0.06 \pm 0.07$ (68% CL) ($\beta_\perp$, fractional displacement perpendicular to the vector connecting the galaxies and the gas), consistent with zero as expected. This inherently statistical technique can be readily expanded to incorporate much larger samples from future all-sky surveys. Equivalent measurements of mass loss during collisions could also test dark sector models with isotropic scattering. Combining observations, these astrophysically large particle colliders have potential to measure dark matter's full differential scattering cross section.

REFERENCES AND NOTES

1. M. Davis, G. Efstathiou, C. S. Frenk, S. D. M. White, *Astrophys. J.* **292**, 371–394 (1985).
2. J. Dubinski, R. G. Carlberg, *Astrophys. J.* **378**, 496–503 (1991).
3. A. Klypin, A. V. Kravtsov, O. Valenzuela, F. Prada, *Astrophys. J.* **522**, 82–92 (1999).
4. B. Moore *et al.*, *Astrophys. J.* **524**, L19–L22 (1999).
5. M. Boylan-Kolchin, J. S. Bullock, M. Kaplinghat, *Mon. Not. R. Astron. Soc.* **415**, L40–L44 (2011).
6. A. Pontzen, F. Governato, *Nature* **506**, 171–178 (2014).
7. J. M. Bardeen, J. R. Bond, N. Kaiser, A. S. Szalay, *Astrophys. J.* **304**, 15–61 (1986).
8. D. N. Spergel, P. J. Steinhardt, *Phys. Rev. Lett.* **84**, 3760–3763 (2000).
9. M. Rocha *et al.*, *Mon. Not. R. Astron. Soc.* **430**, 81–104 (2013).
10. J. Zavala, M. Vogelsberger, M. G. Walker, *Mon. Not. R. Astron. Soc.* **431**, L20–L24 (2013).
11. F. Kahlhoefer, K. Schmidt-Hoberg, M. T. Frandsen, S. Sarkar, *Mon. Not. R. Astron. Soc.* **437**, 2865–2881 (2014).
12. R. Foot, *Int. J. Mod. Phys. A* **29**, 1430013 (2014).
13. K. K. Boddy, J. L. Feng, M. Kaplinghat, T. M. P. Tait, *Phys. Rev. D Part. Fields Gravit. Cosmol.* **89**, 115017 (2014).
14. Y. Hochberg, E. Kuflik, T. Volansky, J. G. Wacker, *Phys. Rev. Lett.* **113**, 171301 (2014).
15. J. M. Cline, Z. Liu, G. D. Moore, W. Xue, *Phys. Rev. D* **90**, 015023 (2014).
16. S. Tulin, H.-B. Yu, K. M. Zurek, *Phys. Rev. Lett.* **110**, 111301 (2013).
17. D. S. Akerib *et al.*, *Phys. Rev. Lett.* **112**, 091303 (2014).
18. S. W. Randall, M. Markevitch, D. Clowe, A. H. Gonzalez, M. Bradac, *Astrophys. J.* **679**, 1173–1180 (2008).
19. M. Markevitch *et al.*, *Astrophys. J.* **606**, 819–824 (2004).
20. D. Eckert *et al.*, *Astron. Astrophys.* **570**, A119 (2014).
21. M. Bartelmann, P. Schneider, *Phys. Rep.* **340**, 291–472 (2001).
22. D. Clowe, A. Gonzalez, M. Markevitch, *Astrophys. J.* **604**, 596–603 (2004).
23. L. L. R. Williams, P. Saha, *Mon. Not. R. Astron. Soc.* **415**, 448–460 (2011).
24. D. Harvey *et al.*, *Mon. Not. R. Astron. Soc.* **433**, 1517–1528 (2013).
25. F. Gastaldello *et al.*, *Mon. Not. R. Astron. Soc.* **442**, L76–L80 (2014).
26. R. Massey, T. Kitching, D. Nagai, *Mon. Not. R. Astron. Soc.* **413**, 1709–1716 (2011).
27. J. G. Fernández-Trincado, J. E. Forero-Romero, G. Foex, T. Verdugo, V. Motta, *Astrophys. J.* **787**, L34 (2014).
28. D. Harvey *et al.*, *Mon. Not. R. Astron. Soc.* **441**, 404–416 (2014).
29. http://archive.stsci.edu/hst/.
30. http://cxc.harvard.edu/cda/.
31. D. Clowe *et al.*, *Astrophys. J.* **648**, L109–L113 (2006).
32. S. Giodini *et al.*, *Astrophys. J.* **703**, 982–993 (2009).
33. P. A. R. Ade *et al.*Planck Collaboration, *Astron. Astrophys.* **571**, A16 (2014).

ACKNOWLEDGMENTS

D.H. is supported by the Swiss National Science Foundation and Science and Technology Facilities Council. R.M. and T.K. are supported by the Royal Society. The raw HST and Chandra data are all publicly accessible from the mission archives (*29*, *30*). We thank the anonymous referees; S. Kay, E. Lau, D. Nagai, and S. Pike for sharing mock data on which we developed our analysis methods; R. Bowler for help stacking HST exposures; E. Jullo, J. Rhodes, and P. Marshall for help with shear measurement and mass reconstruction; D. Clowe, H. Dahle, and J. Jee for discussions of individual systems; and C. Boehm, F. Kahlhoefer, and A. Robertson for interpreting particle physics.

SUPPLEMENTARY MATERIALS

www.sciencemag.org/content/347/6229/1462/suppl/DC1
Materials and Methods
Supplementary Text
Figs. S1 to S8
References (*34*–*47*)

17 September 2014; accepted 12 February 2015
10.1126/science.1261381

NEURODEVELOPMENT

Human-specific gene *ARHGAP11B* promotes basal progenitor amplification and neocortex expansion

Marta Florio,[1] Mareike Albert,[1]* Elena Taverna,[1]* Takashi Namba,[1]* Holger Brandl,[1] Eric Lewitus,[1]† Christiane Haffner,[1] Alex Sykes,[1] Fong Kuan Wong,[1] Jula Peters,[1] Elaine Guhr,[1] Sylvia Klemroth,[2] Kay Prüfer,[3] Janet Kelso,[3] Ronald Naumann,[1] Ina Nüsslein,[1] Andreas Dahl,[2] Robert Lachmann,[4] Svante Pääbo,[3] Wieland B. Huttner[1]‡

Evolutionary expansion of the human neocortex reflects increased amplification of basal progenitors in the subventricular zone, producing more neurons during fetal corticogenesis. In this work, we analyze the transcriptomes of distinct progenitor subpopulations isolated by a cell polarity–based approach from developing mouse and human neocortex. We identify 56 genes preferentially expressed in human apical and basal radial glia that lack mouse orthologs. Among these, *ARHGAP11B* has the highest degree of radial glia–specific expression. *ARHGAP11B* arose from partial duplication of *ARHGAP11A* (which encodes a Rho guanosine triphosphatase–activating protein) on the human lineage after separation from the chimpanzee lineage. Expression of *ARHGAP11B* in embryonic mouse neocortex promotes basal progenitor generation and self-renewal and can increase cortical plate area and induce gyrification. Hence, *ARHGAP11B* may have contributed to evolutionary expansion of human neocortex.

Neocortex expansion is a hallmark of primate (especially human) evolution (*1*, *2*). The increased number of neurons generated during human cortical development results from increased proliferation of neural stem and progenitor cells (NPCs) (*3*–*8*). Three classes of cortical NPCs can be distinguished cell biologically: (i) apical progenitors, which undergo mitosis at the ventricular side of the ventricular zone (VZ)—i.e., apical radial glia (aRG) and apical intermediate progenitors; (ii) basal progenitors, which lack ventricular contact and undergo mitosis in the subventricular zone (SVZ)—i.e., basal (outer) radial glia (bRG) and basal intermediate progenitors (bIPs); and (iii) subapical progenitors, which undergo mitosis in the SVZ or basal VZ and retain ventricular contact (*9*).

Cortical expansion has been linked to increased generation of basal progenitors from aRG and their greater and prolonged proliferation, resulting in enlargement of the SVZ (*3*–*7*, *10*, *11*). Toward identifying the molecular basis of these processes, genome-wide transcriptome analyses of VZ and SVZ carried out in rodents (*12*, *13*) and primates (*14*), including humans (*13*, *15*), have provided insight. Further clues have come from transcriptome analyses of mouse NPC subpopulations (*16*) and retrospectively identified mouse and human NPC types (*17*–*19*). However, a rate-limiting step in understanding cortical expansion has been the lack of transcriptome analyses

[1]Max Planck Institute of Molecular Cell Biology and Genetics (MPI-CBG), Pfotenhauerstraße 108, D-01307 Dresden, Germany. [2]Technische Universität Dresden, Center for Regenerative Therapies Dresden, Fetscherstraße 105, D-01307 Dresden, Germany. [3]Max Planck Institute for Evolutionary Anthropology (MPI-EVA), Deutscher Platz 6, D-04103 Leipzig, Germany. [4]Technische Universität Dresden, Universitätsklinikum Carl Gustav Carus, Klinik und Poliklinik für Frauenheilkunde und Geburtshilfe, Fetscherstraße 74, D-01307 Dresden, Germany.
*These authors contributed equally to this work. †Present address: Département de Biologie, École Normale Supérieure, 46 Rue d'Ulm, 75005 Paris, France. ‡Corresponding author. E-mail: huttner@mpi-cbg.de

of human NPC subpopulations (in particular, of bRG) thought to have a key role in this process (*3*–*7*).

We therefore sought to isolate specific NPC types from fetal human neocortex and compare them with those from embryonic mouse neocortex. To this end, we exploited the differential apical-basal cell polarity of radial glia (*9*, *20*) (Fig. 1). Radial glia contacting the basal lamina

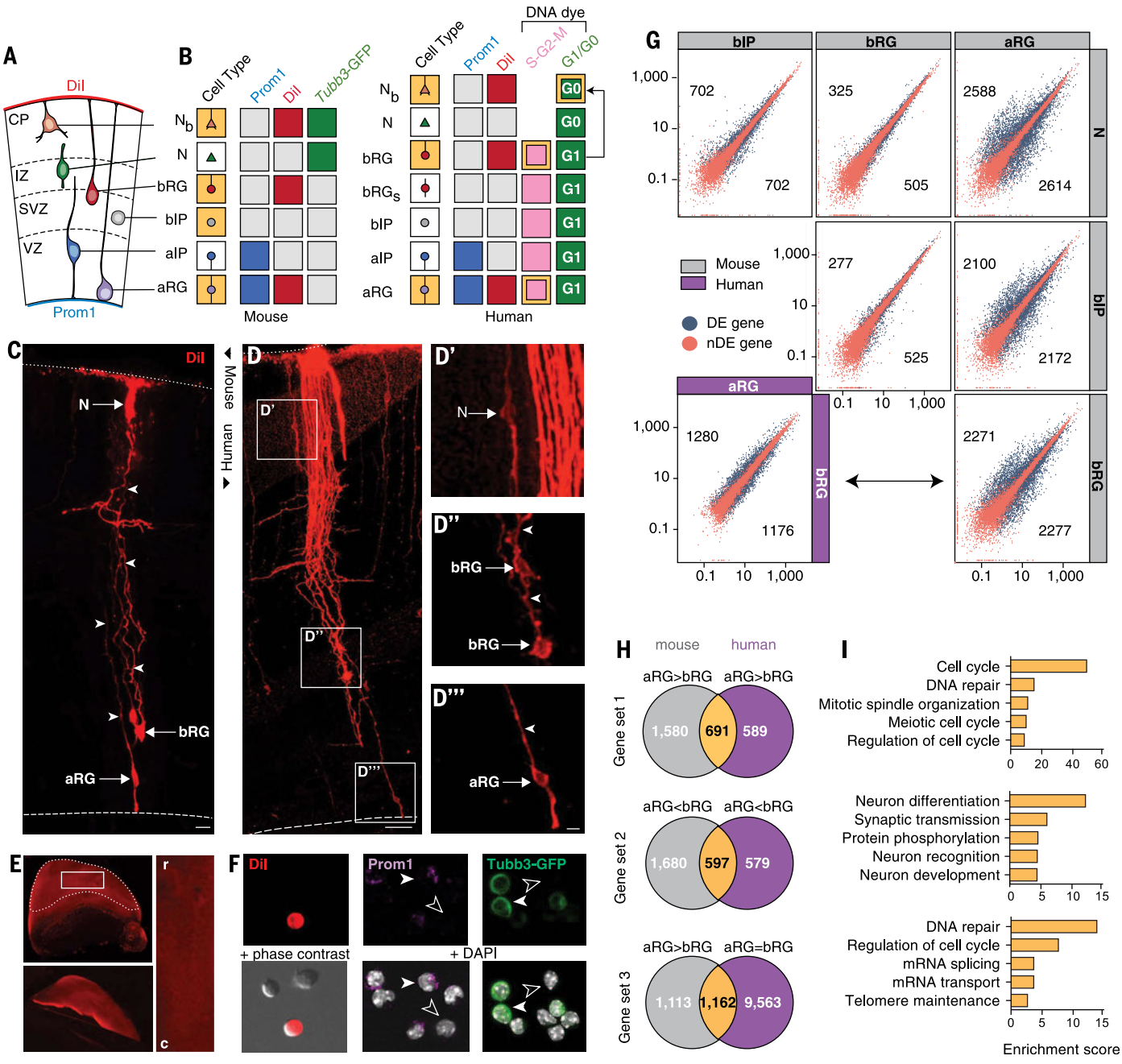

Fig. 1. Isolation of distinct NPC types from mouse and human neocortex and comparison of their transcriptomes. (**A**) NPC types labeled via their apical surface (Prom1) and/or basal lamina contact (DiI). N and N_b, neurons without and with basal contact, respectively; CP, cortical plate; IZ, intermediate zone. (**B**) Cell types isolated (yellow) from embryonic *Tubb3*-GFP mouse (left) and fetal human (right) neocortex based on the absence or presence of apical Prom1, basal DiI, neuronal *Tubb3*-GFP, G_1/G_0, and/or S-G_2-M. Human bRG with basal contact in G_1 are present in the N_b fraction (arrow). bRG_s, secondary bRG lacking basal contact. (**C** to **D**‴) Sparse DiI labeling of E14.5 mouse (C) and 13 weeks postconception (wpc) human (D to D‴) neocortex from basal lamina (dotted lines). Arrows, cell body; solid arrowheads, basal process; dashed lines, ventricular surface. DiI labeling is confined to aRG, bRG, and N_b. Scale bars, 20 μm. (**E**) Comprehensive basal DiI labeling of E14.5 *Tubb3*-GFP mouse hemisphere. r, rostral; c, caudal. The bottom left image shows dissected neocortex. (**F**) Dissociated DiI-labeled, Prom1 surface–labeled and *Tubb3*-GFP$^+$ cells from E14.5 *Tubb3*-GFP mouse neocortex. Solid and open arrowheads respectively indicate representative cells positive and negative for a given marker. (**G**) DESeq scatter plots showing pairwise comparisons of expression (FPKM) of protein-encoding genes between E14.5 mouse aRG, bRG, bIPs, and neurons (N) (gray; 12,897 genes in total) and between 13 wpc human aRG and bRG (purple; 14,302 genes in total). DE, differentially expressed (numbers); nDE, nondifferentially expressed. (**H**) Venn diagrams showing numbers of genes with indicated expression pattern in mouse and/or human aRG and bRG. (**I**) The five top-scoring clusters of significantly enriched ($P < 0.05$) GO terms (category: biological process) associated with the genes expressed in both mouse and human aRG and bRG with the indicated patterns [yellow in (B)].

via a basal process were labeled (along with basal lamina–contacting neurons) by basal application of the fluorescent membrane dye DiI (Fig. 1 and fig. S1) (see also supplementary materials and methods). This was followed by hemisphere culture to allow DiI to diffuse to the cell body of both bRG and aRG (Fig. 1 and fig. S1). NPCs that exhibited ventricular contact were labeled, after preparation of a cell suspension (Fig. 1 and fig. S1), by immunofluorescence for the apical plasma membrane marker prominin-1 (Prom1) (Fig. 1). To isolate neurons, we either used transgenic *Tubb3*–green fluorescent protein (GFP) mouse embryos (*21*) (Fig. 1) or, for fetal human neocortex, performed vital DNA staining of the cell suspension with a fluorescent dye to distinguish neurons (G_0) from NPCs (S-G_2-M) on the basis of their different DNA content (Fig. 1).

With these markers, we used fluorescence-activated cell sorting to isolate the following cell populations from embryonic mouse neocortex: aRG (DiI^+, $Prom1^+$, *Tubb3*-GFP^-), bRG (DiI^+, $Prom1^-$, *Tubb3*-GFP^-), neurons with basal lamina contact (DiI^+, *Tubb3*-GFP^+, $Prom1^-$), and bIPs (DiI^-, $Prom1^-$, *Tubb3*-GFP^-) (Fig. 1). Using the same $DiI^+/Prom1^{\pm}$ combination, we isolated aRG and bRG in S-G_2-M and neurons from fetal human neocortex (Fig. 1). The authenticity of the aRG, bRG, bIP, and neuron fractions was validated by quantitative polymerase chain reaction (qPCR) analyses of appropriate markers (figs. S2 and S3).

After RNA sequencing of each cell fraction (fig. S4), differential gene expression analysis indicated that in mice, bRG are very similar to bIPs and neurons but are distinct from aRG (Fig. 1 and fig. S5). In contrast, in humans, fewer genes were differently expressed between bRG and aRG (Fig. 2 and fig. S6). Hierarchical clustering corroborated these findings (fig. S7). Further evidence showing that bRG and aRG are distinct in mice but similar in humans was obtained by (i) transcriptome analyses, including comparison of proliferative (*Tis21*-GFP^-) versus differentiative (*Tis21*-GFP^+) mouse aRG (fig. S8), and (ii) quantitation of mRNA versus protein of the transcription factor *Eomes*/Tbr2 (figs. S3, S8, and S9).

We therefore searched for functional clues in the set of genes that have similar expression levels in human bRG and aRG but are down-regulated in mouse bRG compared with aRG (Fig. 1). The five clusters of gene ontology (GO) terms most enriched among these genes included DNA repair and telomere maintenance (Fig. 2C). This supports (i) the emerging concept (*16*, *22*) that proliferative NPCs invest more in DNA repair than neurogenic NPCs and (ii) the stem cell character of aRG and bRG in humans but only of aRG in mice (fig. S6). Conversely, the five GO term clusters most enriched among genes more highly expressed in both mouse and human bRG compared with aRG carried a strong neuronal differentiation signature (Fig. 1), consistent with bRG being neurogenic in both rodents and primates (*5*, *6*, *23*, *24*).

Next we searched for genes specifically expressed in human aRG and bRG, starting with two separate sets of differentially expressed human genes: (i) aRG>bRG>neurons (190 genes) and (ii) bRG≥aRG>neurons (394 genes) (Fig. 2 and tables S1 and S2). We then eliminated genes that had mouse orthologs that were expressed in mouse cortical NPCs or cortical germinal zones (*13*), and then genes with overt [fragments per

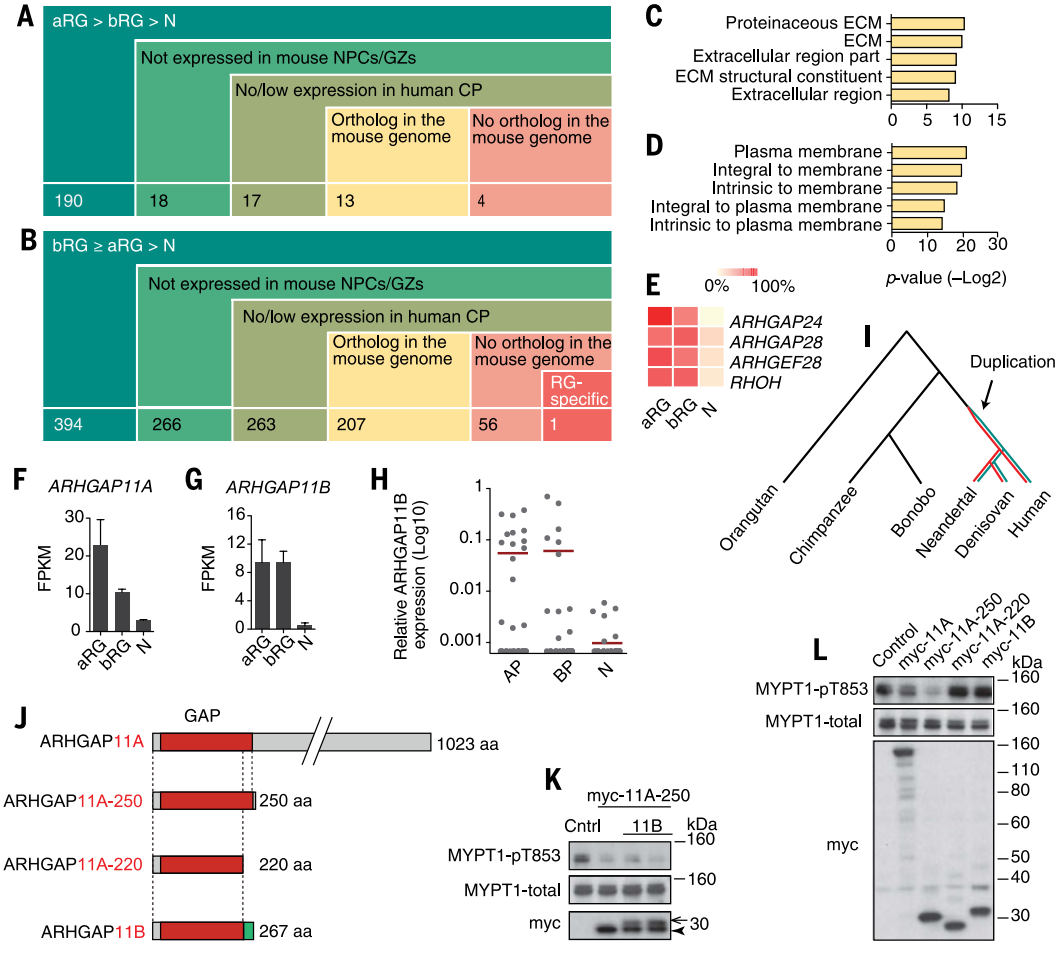

Fig. 2. Searching for genes specifically expressed in human radial glia reveals the hominin-specific gene *ARHGAP11B*. (**A** and **B**) Stepwise addition of exclusion parameters to the data sets of human genes with aRG>bRG>N (neuron) (A) and bRG≥aRG>N (B) expression at 13 wpc. GZs, germinal zones; CP, cortical plate. In (B), red color indicates that only one of the 56 human-specific, bRG≥aRG–enriched genes exhibits FPKM values bRG/N ≥ 10: *ARHGAP11B*. RG, radial glia. (**C** and **D**) The five most significantly enriched GO terms associated with the 13 aRG>bRG–enriched [(A), yellow] and 207 bRG ≥ aRG–enriched [(B), yellow] human genes with mouse orthologs. (**E**) Heat map showing relative expression levels in 13 wpc human aRG, bRG, and neurons (N) of the four Rho-related genes found in the 207 bRG≥aRG–enriched human genes with mouse orthologs [(B), yellow]. (**F** to **H**) *ARHGAP11A* (F) and *ARHGAP11B* (G) mRNA levels in 13 wpc human aRG, bRG, and neurons, and qPCR of retrospectively identified 12 wpc human apical progenitors (AP), basal progenitors (BP), and neurons. Error bars in (F) and (G) indicate SD; horizontal bars in (H) denote mean. (**I**) Phylogenetic tree showing duplication of *ARHGAP11B* (red) from *ARHGAP11A* (green). (**J**) Domain structure of ARHGAP11A, truncated ARHGAP11A versions, and ARHGAP11B. Red, GAP domain; green, unique sequence in ARHGAP11B. (**K** and **L**) Immunoblots showing Rho-GAP activity of myc-tagged ARHGAP11A, truncated ARHGAP11A versions, and ARHGAP11B, as revealed by dephosphorylation of myosin phosphatase target protein 1 (MYPT1-pT853). In (K), the arrow denotes ARHGAP11B, and the arrowhead indicates $ARHGAP11A_{1\text{-}250}$.

kilobase per million (FPKM) ≥ 5] expression in the human cortical plate (*13*). This reduced the number of human genes to 17 in the aRG>bRG>neurons gene set and to 263 in the bRG≥aRG>neurons gene set (Fig. 2). Each of these gene subsets was split into two groups: (i) human genes with orthologs in the mouse genome (which, however, are not expressed in mouse NPCs and germinal zones) and (ii) human genes without orthologs in the mouse genome.

The five most enriched GO terms associated with the 13 human genes with mouse orthologs identified in the aRG>bRG>neurons gene set point to a role of extracellular matrix (ECM), and the GO terms associated with the 207 human genes with mouse orthologs identified in the bRG≥aRG>neurons gene set point to a role of cell surface receptors (Fig. 2). These findings provide support for and extend the concept that endogenous production of ECM components and expression of ECM receptors by human aRG and bRG contribute to their greater proliferative potential when compared with that of mice (*6*, *13*, *16*).

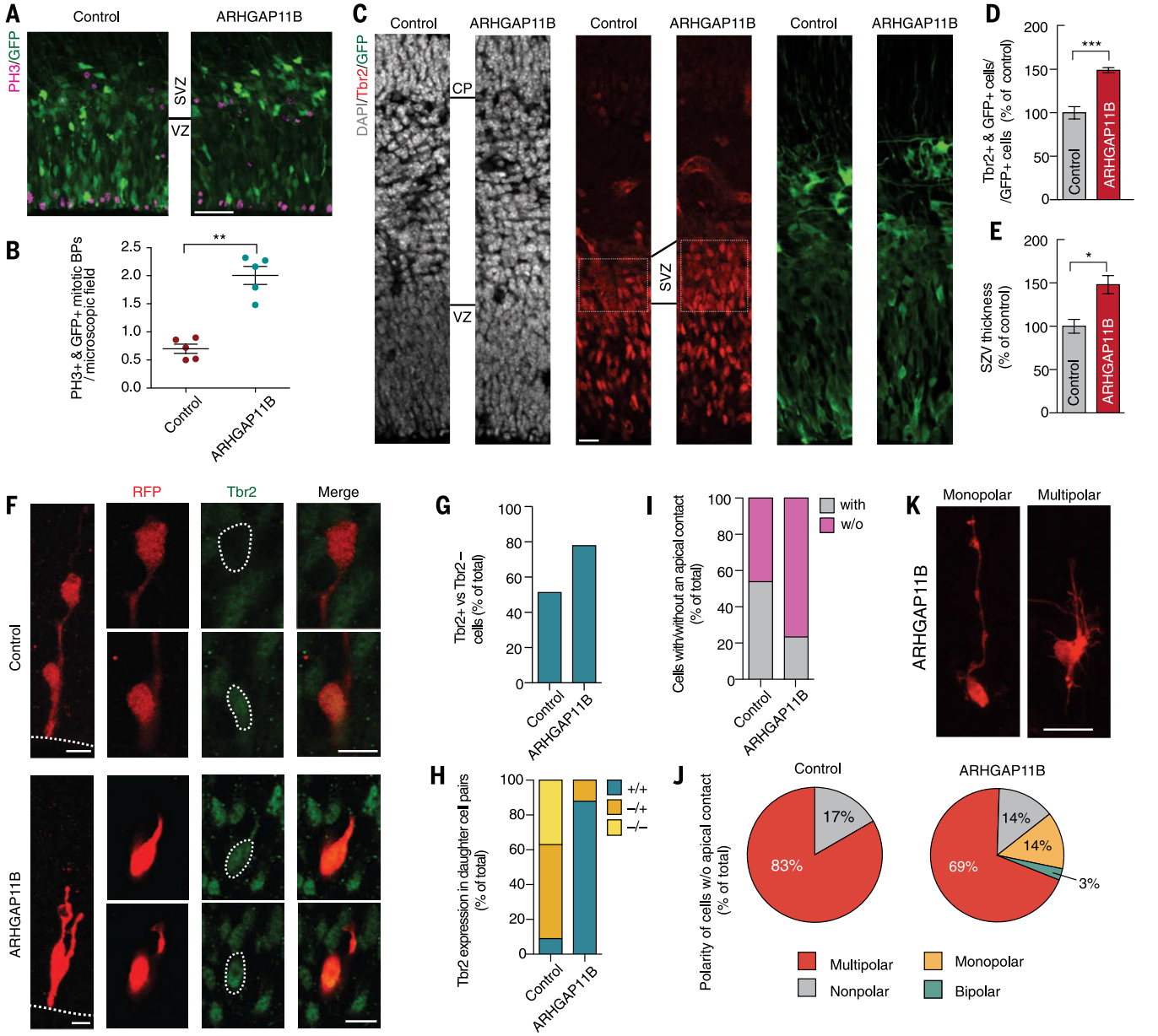

Fig. 3. *ARHGAP11B* expression in mouse aRG increases their symmetric differentiative division, basal progenitors abundance, and SVZ thickness. (**A** to **E**) Control and *ARHGAP11B* in utero electroporation of E13.5 mouse neocortex, followed by analysis at E14.5. (A) GFP and phosphohistone H3 (PH3) immunofluorescence. Scale bar, 50 μm. (B) Quantification of mitotic, $PH3^+$, and GFP^+ basal progenitors. Dots represent independent experiments; bars denote SD. $^{**}P < 0.01$. (C) 4′,6-diamidino-2-phenylindole (DAPI) staining and Tbr2 and GFP immunofluorescence. Scale bar, 20 μm. (D) Quantification of $Tbr2^+$ and GFP^+ basal progenitors. Error bars indicate SD. $^{***}P < 0.001$. (E) Quantification of SVZ thickness relative to cortical wall. Error bars represent SEM. $^{*}P < 0.05$. (**F** to **K**) Control and *ARHGAP11B* mRNA microinjection into aRG in E14.5 mouse neocortex slice culture, followed by red fluorescent protein (RFP) and Tbr2 immunofluorescence after 24 hours and 48 hours. (F) Examples of asymmetric $Tbr2^-/Tbr2^+$ (top) and symmetric $Tbr2^+/Tbr2^+$ (bottom) RFP^+ daughter cell pairs upon control and *ARHGAP11B* microinjection, respectively. Dotted lines, ventricular surface. Scale bars, 10 μm. (G) Quantification of $Tbr2^+$ and RFP^+ daughter cells. (H) Quantification of $Tbr2^-/Tbr2^-$, $Tbr2^-/Tbr2^+$, and $Tbr2^+/Tbr2^+$ RFP^+ daughter cell pairs. (I) Quantification of RFP^+ daughter cells with and without (w/o) apical contact after 48 hours. (J) Polarity of RFP^+ daughter cells without apical contact. (K) Examples of monopolar and multipolar RFP^+ daughter cells. Scale bar, 20 μm.

We then focused our attention on the 56 human genes without mouse orthologs in the human bRG≥aRG>neurons gene set, as these were prime candidates to include human-specific genes underlying bRG expansion. As bRG in G_1 were co-isolated along with neurons from fetal human neocortex by the protocol used (N_b fraction in Fig. 1), albeit at relatively low abundance (<20% of cells, as determined by Ki67 FPKM values), we concentrated on genes with FPKM values that were ≥10 times higher in bRG than in neurons to identify human genes that are truly specific for radial glia. Only one gene fulfilled this criterion: *ARHGAP11B*.

ARHGAP11B mRNA levels were found to be equally high in human aRG and bRG—as previously observed for human VZ, inner SVZ, and outer SVZ (*13*)—but virtually undetectable in human cortical neurons and cortical plate (Fig. 2). Single-cell qPCR of retrospectively identified human apical progenitors, basal progenitors, and neurons corroborated this finding (Fig. 2). A similar distribution across human cortical cell types (Fig. 2) and germinal zones (*13*) was observed for the mRNA of *ARHGAP11A*, the paralog of *ARHGAP11B*.

ARHGAP11B arose on the human evolutionary lineage after the divergence from the chimpanzee lineage by partial duplication of *ARHGAP11A* (*25*, *26*), which is found throughout the animal kingdom and encodes a Rho guanosine triphosphatase–activating protein (RhoGAP) (*27*, *28*). *ARHGAP11B* exists not only in present-day humans but also in Neandertals and Denisovans (*26*, *29*–*31*) (Fig. 2). ARHGAP11B contains 267 amino acids and is a truncated version of ARHGAP11A, comprising most of the GAP-domain (until Lys^{220}) followed by a unique C-terminal sequence but lacking the C-terminal 756 amino acids of ARHGAP11A (Fig. 2 and fig. S10).

In contrast to full-length ARHGAP11A and $ARHGAP11A_{1\text{-}250}$, ARHGAP11B (like $ARHGAP11A_{1\text{-}220}$) did not exhibit RhoGAP activity in a RhoA/Rho-kinase–based cell transfection assay (Fig. 2). This indicates that the C-terminal 47 amino acids of ARHGAP11B (after Lys^{220}) not only constitute a unique sequence, resulting from a frameshifting deletion (fig. S10), but also are functionally distinct from their counterpart in ARHGAP11A. In the present assay, coexpression of ARHGAP11B along with ARHGAP11A did not inhibit the latter's RhoGAP activity (Fig. 2).

The 207 human genes with mouse orthologs in the bRG≥aRG>neurons gene set included four additional genes related to Rho signaling: *ARHGAP24*, *ARHGAP28*, *ARHGEF28*, and *RHOH* (Fig. 2). This suggests a role for Rho proteins in human radial glia.

To explore the function of ARHGAP11B in corticogenesis, *ARHGAP11B* was expressed in mouse neocortex by in utero electroporation on E13.5 (embryonic day 13.5). This increased basal but not apical mitoses and $Tbr2^+$ basal progenitors at E14.5, with a similar proportion [≈30% (*16*)] of $Pax6^+$ basal progenitors as in control (fig. S11). It also resulted in thickening of the SVZ (Fig. 3). In contrast, overexpression of *ARHGAP11A* did not increase basal progenitors (fig. S12).

To further dissect the effects of ARHGAP11B, we microinjected (*32*) *ARHGAP11B* mRNA into single aRG in organotypic slice culture of E14.5 mouse neocortex. After 24 hours, the same proportion of aRG progeny was identifiable as daughter cell pairs upon control versus *ARHGAP11B* microinjection (fig. S13), indicating that ARHGAP11B did not affect aRG division as such. A greater percentage of aRG progeny showed Tbr2 immunoreactivity upon *ARHGAP11B* microinjection compared with control (Fig. 3), suggesting that ARHGAP11B promoted basal progenitor generation from aRG.

Analysis of daughter cell pairs of microinjected aRG showed that in the control, the vast majority of daughter cells were either both $Tbr2^-$ or one daughter cell was $Tbr2^-$ whereas the other was $Tbr2^+$ (Fig. 3). In contrast, upon *ARHGAP11B* mRNA microinjection, almost all daughter cell pairs observed were $Tbr2^+$ (Fig. 3). We conclude that ARHGAP11B induces aRG to switch from symmetric-proliferative and asymmetric-differentiative to symmetric-differentiative divisions yielding two basal progenitors, thereby increasing their generation.

Analysis of the loss of ventricular contact of the aRG progeny corroborated this conclusion. Whereas approximately half of the progeny of control-microinjected aRG still retained ventricular contact after 48 hours of culture, nearly 80% of the progeny of *ARHGAP11B*-microinjected aRG had lost ventricular contact (Fig. 3), indicating that ARHGAP11B increases delamination. Moreover, ARHGAP11B induced the appearance of bRG-like morphology in, and a more basal localization of, the delaminated progeny (Fig. 3 and fig. S13).

ARHGAP11B mRNA microinjection resulted in increased clone size of the aRG progeny (Fig. 4). Consistent with this finding, *ARHGAP11B* electroporation increased the proportion of cycling cells in the SVZ (Fig. 4). Together, this shows that ARHGAP11B promotes basal progenitor self-amplification.

Finally, in half of the cases analyzed, *ARHGAP11B* expression in the normally smooth (lissencephalic) mouse neocortex, induced at E13.5, resulted

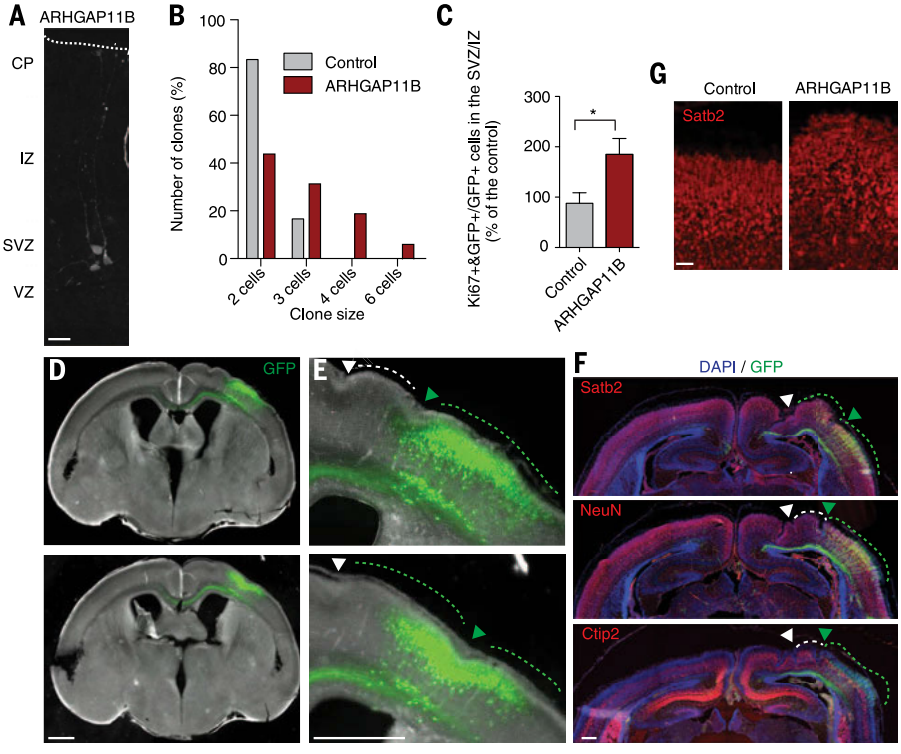

Fig. 4. *ARHGAP11B* expression in mouse neocortex increases basal progenitor proliferation and can induce cortical folding. (**A** and **B**) Control and *ARHGAP11B* mRNA microinjection into aRG in E14.5 mouse neocortex slice culture, followed by RFP immunofluorescence after 48 hours. (A) RFP fluorescence. Scale bar, 20 μm. (B) Quantification of daughter cell clones. (**C**) Control and *ARHGAP11B* in utero electroporation of E13.5 mouse neocortex, followed by quantification of $Ki67^+$ and RFP^+ basal progenitors at E15.5. Error bars indicate SEM. *$P < 0.05$. (**D** to **F**) Coronal sections of two independent E18.5 mouse telencephali in utero electroporated at E13.5 with *ARHGAP11B* and GFP expression plasmids. (D and E) Phase contrast and GFP fluorescence in two consecutive sections along the rostro-caudal axis. Scale bars, 500 μm. (E) Electroporated area. Green and white dashed lines and triangles indicate gyrus- and sulcus-like structures in and adjacent to the electroporated area, respectively. (F) Satb2, NeuN, and Ctip2 immunofluorescence combined with DAPI staining and GFP immunofluorescence in two consecutive sections along the rostro-caudal axis. Scale bar, 250 μm. (**G**) Satb2 immunofluorescence of the cortical plate areas of the gyrus-like structure of *ARHGAP11B*-expressing neocortex located between white and green triangles in (F), and of the corresponding contralateral, control side. Scale bar, 50 μm.

in neocortex folding at E18.5, reminiscent of gyrification, a hallmark of human neocortex (Fig. 4). Cortical plate area in the gyrus-like structures was increased compared with the contralateral smooth neocortex, with proper cortical lamination.

The methodology for isolation of cortical progenitor subpopulations established here can be applied to other mammalian species, including primates, opening avenues for comparative evolutionary studies. Furthermore, the present transcriptome data provide insight into molecular differences between the various types of cortical NPCs in developing mouse and human neocortex and constitute a resource for future studies. A very recent, independent analysis of human radial glia transcriptome (*19*) has concentrated on genes present in both mouse and human genomes but expressed only in human cortical progenitors, identifying a role for platelet-derived growth factor signaling (*16*) in human radial glia. In contrast, we focus here on genes present only in the human, but not mouse, genome and highly expressed in basal radial glia.

Thus, we identify *ARHGAP11B* as a human-specific gene that amplifies basal progenitors and is capable of causing neocortex folding in mice (*33*, *34*). This probably reflects a role for ARHGAP11B in development and evolutionary expansion of the human neocortex, a conclusion consistent with the finding that the gene duplication that created *ARHGAP11B* occurred on the human lineage after the divergence from the chimpanzee lineage but before the divergence from Neandertals, whose brain size was similar to that of modern humans.

Note added in proof: In work published after online publication of this paper, Johnson *et al.* (*35*) used a complementary approach to similarly isolate and compare the transcriptomes of human and mouse apical and basal radial glia.

REFERENCES AND NOTES

1. G. F. Striedter, *Principles of Brain Evolution* (Sinauer Associates, Sunderland, MA, 2005).
2. P. Rakic, *Nat. Rev. Neurosci.* **10**, 724–735 (2009).
3. J. H. Lui, D. V. Hansen, A. R. Kriegstein, *Cell* **146**, 18–36 (2011).
4. V. Borrell, I. Reillo, *Dev. Neurobiol.* **72**, 955–971 (2012).
5. M. Betizeau *et al.*, *Neuron* **80**, 442–457 (2013).
6. M. Florio, W. B. Huttner, *Development* **141**, 2182–2194 (2014).
7. V. Borrell, M. Götz, *Curr. Opin. Neurobiol.* **27**, 39–46 (2014).
8. T. Sun, R. F. Hevner, *Nat. Rev. Neurosci.* **15**, 217–232 (2014).
9. E. Taverna, M. Götz, W. B. Huttner, *Annu. Rev. Cell Dev. Biol.* **30**, 465–502 (2014).
10. I. H. Smart, C. Dehay, P. Giroud, M. Berland, H. Kennedy, *Cereb. Cortex* **12**, 37–53 (2002).
11. E. Lewitus, I. Kelava, A. T. Kalinka, P. Tomancak, W. B. Huttner, *PLOS Biol.* **12**, e1002000 (2014).
12. A. E. Ayoub *et al.*, *Proc. Natl. Acad. Sci. U.S.A.* **108**, 14950–14955 (2011).
13. S. A. Fietz *et al.*, *Proc. Natl. Acad. Sci. U.S.A.* **109**, 11836–11841 (2012).
14. M. L. Arcila *et al.*, *Neuron* **81**, 1255–1262 (2014).
15. J. A. Miller *et al.*, *Nature* **508**, 199–206 (2014).
16. Y. Arai *et al.*, *Nat. Commun.* **2**, 154 (2011).
17. A. Kawaguchi *et al.*, *Development* **135**, 3113–3124 (2008).
18. A. A. Pollen *et al.*, *Nat. Biotechnol.* **32**, 1053–1058 (2014).
19. J. H. Lui *et al.*, *Nature* **515**, 264–268 (2014).
20. S. A. Fietz, W. B. Huttner, *Curr. Opin. Neurobiol.* **21**, 23–35 (2011).
21. A. Attardo, F. Calegari, W. Haubensak, M. Wilsch-Bräuninger, W. B. Huttner, *PLOS ONE* **3**, e2388 (2008).
22. S. L. Houlihan, Y. Feng, *eLife* **3**, e03297 (2014).
23. A. Lukaszewicz *et al.*, *Neuron* **47**, 353–364 (2005).
24. X. Wang, J. W. Tsai, B. LaMonica, A. R. Kriegstein, *Nat. Neurosci.* **14**, 555–561 (2011).
25. B. Riley, M. Williamson, D. Collier, H. Wilkie, A. Makoff, *Genomics* **79**, 197–209 (2002).
26. F. Antonacci *et al.*, *Nat. Genet.* **46**, 1293–1302 (2014).
27. Y. Kagawa *et al.*, *PLOS ONE* **8**, e83629 (2013).
28. E. Zanin *et al.*, *Dev. Cell* **26**, 496–510 (2013).
29. P. H. Sudmant *et al.*, *Science* **330**, 641–646 (2010).
30. M. Meyer *et al.*, *Science* **338**, 222–226 (2012).
31. K. Prüfer *et al.*, *Nature* **505**, 43–49 (2014).
32. E. Taverna, C. Haffner, R. Pepperkok, W. B. Huttner, *Nat. Neurosci.* **15**, 329–337 (2012).
33. R. Stahl *et al.*, *Cell* **153**, 535–549 (2013).
34. B. G. Rash, S. Tomasi, H. D. Lim, C. Y. Suh, F. M. Vaccarino, *J. Neurosci.* **33**, 10802–10814 (2013).
35. M. B. Johnson *et al.*, *Nat. Neurosci.* 10.1038/nn.3980 (2015).

ACKNOWLEDGMENTS

We apologize to all researchers whose work could not be cited due to space limitation. We are grateful to the Services and Facilities of the MPI-CBG for the outstanding support provided, notably J. Helppi and his team of the Animal Facility, J. Peychl and his team of the Light Microscopy Facility, N. Lakshmanaperumal of the Bioinformatics Facility, and J. Jarrells and A. Eugster for support with single-cell analysis. We thank E. Perini for advice regarding RhoGAPs and all members of the Huttner lab for help and discussion, especially D. Stenzel for support in obtaining fetal human tissue, J. Paridaen and M. Wilsch-Bräuninger for advice, and N. Kalebic and K. Long for critical reading of the manuscript. We thank B. Höber and A. Weihmann of MPI-EVA for expert DNA sequencing; B. Habermann of Max Planck Institute of Biochemistry (MPI-B) for bioinformatics advice; and K. Kaibuchi and M. Amano (Nagoya University) for pCAGGS-myc-KK1, pCAGGS-HA, and anti-MYPT1 antibody. M.F. was a member of the International Max Planck Research School for Cell, Developmental and Systems Biology and a doctoral student at the Technische Universität Dresden. W.B.H. was supported by grants from the Deutsche Forschungsgemeinschaft (DFG) (SFB 655, A2) and the European Research Council (250197), the DFG-funded Center for Regenerative Therapies Dresden, and the Fonds der Chemischen Industrie. The supplementary materials contain additional data. RNA-seq raw data have been deposited with the Gene Expression Omnibus under accession codes GSE65000 and GSM1585634.

SUPPLEMENTARY MATERIALS

www.sciencemag.org/content/347/6229/1465/suppl/DC1

Materials and Methods
Figs. S1 to S14
Tables S1 to S4
References (*36*–*43*)

30 October 2014; accepted 17 February 2015
Published online 26 February 2015;
10.1126/science.aaa1975

PARASITOLOGY

The in vivo dynamics of antigenic variation in *Trypanosoma brucei*

Monica R. Mugnier, George A. M. Cross, F. Nina Papavasiliou*

***Trypanosoma brucei*, a causative agent of African Sleeping Sickness, constantly changes its dense variant surface glycoprotein (VSG) coat to avoid elimination by the immune system of its mammalian host, using an extensive repertoire of dedicated genes. However, the dynamics of VSG expression in *T. brucei* during an infection are poorly understood. We have developed a method, based on de novo assembly of VSGs, for quantitatively examining the diversity of expressed VSGs in any population of trypanosomes and monitored VSG population dynamics in vivo. Our experiments revealed unexpected diversity within parasite populations and a mechanism for diversifying the genome-encoded VSG repertoire. The interaction between *T. brucei* and its host is substantially more dynamic and nuanced than previously expected.**

The protozoan parasite *Trypanosoma brucei*, a major cause of human and animal Trypanosomiasis, lives extracellularly within its mammalian host, where it is constantly exposed to the host immune system. *T. brucei* has evolved a mechanism for antigenic variation during infection in which the parasite can turn on and off variant surface glycoprotein (VSG)–encoding genes from a genomic repertoire of ~2000 different genes (*1*). Each parasite expresses one VSG at a time, from one of ~15 telomeric expression sites (*2*); the rest (silent VSGs) sit in silent expression sites or in other genomic locations (*1*). The highly antigenic VSG is so densely packed on *T. brucei*'s surface that it obscures other cell-surface components from immune recognition. At any time, a few parasites in a population will stochastically switch their VSG. As previous variants are recognized by the immune system and cleared, newly switched variants emerge, giving rise to characteristic waves of parasitemia (*3*). These waves have long been interpreted as the sequential expression and clearance of one or a few VSGs, a notion supported by experimental evidence that relied on low-resolution approaches (*4*–*8*).

Despite attempts at modeling, little is known about the kinetics of VSG expression during infection (*9*–*12*). To assess this, we developed a targeted RNA sequencing (RNA-seq) approach, termed VSG-seq, in which VSG cDNA, amplified by using conserved sequences at the 5′ and 3′ end of every mature VSG mRNA (fig. S1), is sequenced and then assembled de novo by a transcriptome reconstruction method called Trinity (*13*). We validated

[1]Laboratory of Lymphocyte Biology, The Rockefeller University, New York, NY, USA. [2]Laboratory of Molecular Parasitology, The Rockefeller University, New York, NY, USA.
***Corresponding author. E-mail: papavasiliou@rockefeller.edu**

this approach using mixtures of *T. brucei* cell lines expressing specific VSGs in known proportions (Fig. 1 and fig. S1). We compared measured expression of each VSG in the control populations with the known input and found that we could accurately assemble a VSG sequence expressed in as few as nine cells in the control mixture. VSG-seq is capable of reliably detecting variants present on 0.01% of parasites and quantifying a variant's presence within the population, for variants present above 0.1% of the population (Fig. 1B and fig. S1). The apparent overestimation of minor VSGs in this control experiment is likely a result of low-level switching in the more abundant components of the mixture or low-level transcription of silent VSGs. The limits of detection and quantification for VSG-seq appear to be independent of starting cell number because control mixtures made from 10^6 or 10^7 cells show similar results (Fig. 1B and fig. S1).

To measure VSG expression within populations of *T. brucei*, we infected four mice with ~5 EATRO1125 parasites—originally expressing VSG AnTat1.1 (*14*, *15*) but now heterogeneous and each expressing a distinct VSG—and tracked VSG expression dynamics for 30 days. A few variants made up the majority of the population at each time, but surprisingly, each sample also contained many rare variants that would have been undetectable by using previous approaches (Fig. 2A and fig. S2). Infections showed great diversity even within parasitemic valleys. VSG-seq identified an average of 28 variants at each time point during the first 30 days of infection (Fig. 2C).

One mouse (mouse 3) survived much longer than did the other three (106 days, compared with 41 to 72 days). VSG identity has not been shown to affect growth rate or induction of the immune response (*16*, *17*), so the increased survival and lower diversity in this mouse are more likely due to the polyclonal germline B cell repertoire, which is unique to each mouse (*18*), rather than the initiating VSG. Although in the later stages of this infection, VSG dynamics did appear qualitatively different—with variants persisting longer before clearance (Fig. 2B), possibly owing to immune system exhaustion—parasite populations remained diverse, with 30 to 66 variants detectable at each sampling (Fig. 2C).

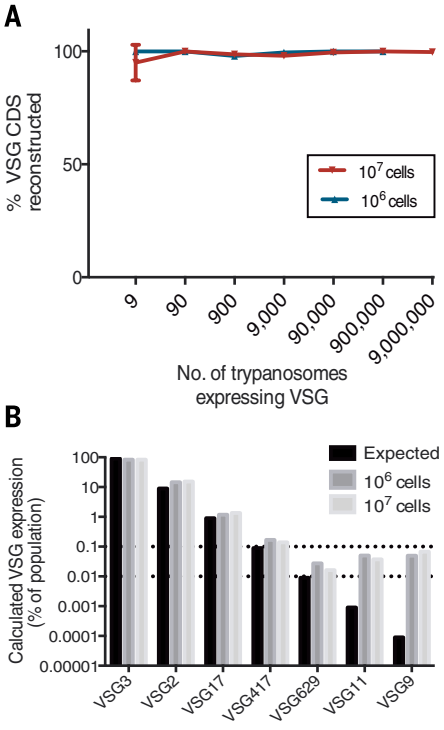

Fig. 1. VSG-seq for assembly of VSGs and quantification VSG expression in a population of African trypanosomes. (**A**) Efficiency of VSG assembly (mean ± SD). Control libraries made from a mixture of cell lines expressing different VSGs in known proportions were sequenced, and sequencing reads were assembled by using Trinity (*13*). Control mixtures were made from either 1 million or 10 million cells. (**B**) Quantification of VSG expression in control libraries (mean ± SD). The black bar ("Expected") represents the proportion of cells expressing that VSG in the control mixture, and the gray bars represent quantification for each library by use of VSG-seq.

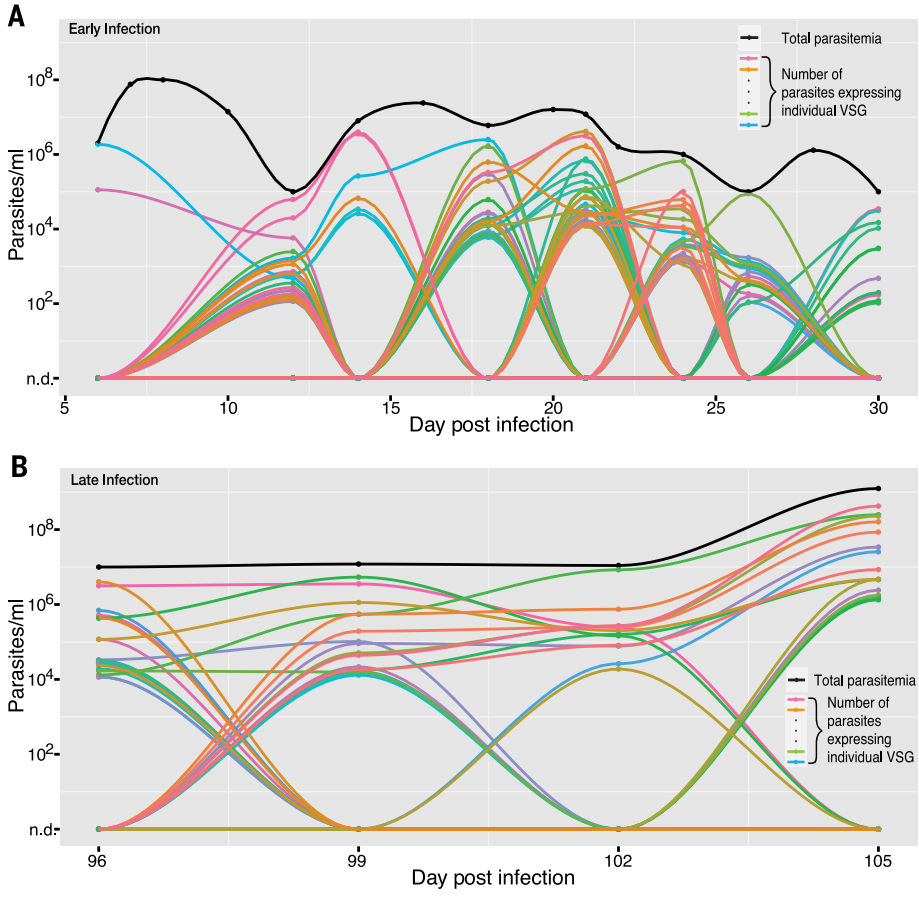

C

Number of VSGs expressed

Day	d6	d7	d12	d14	d18	d21	d24	d26	d30	d96	d99	d102	d105
Mouse 1	15		18	21	34	36	6	83	33				
Mouse 2	10		34	15	53	57	36	29	39				
Mouse 3		9	13	9	22	21	14	30	21	58	66	30	32
Mouse 4		7	23	17	79	39	12	39	25				

Fig. 2. Complex dynamics throughout *T. brucei* infection. (**A**) Dynamics of VSG expression during early infection (days 6 to 30). Each colored line represents an individual VSG's presence in the population, and the black line represents total parasitemia. Only variants present at >0.1% of the population at that time point are shown. When parasitemia could not be measured with a hemacytometer (<10^6/ml), parasitemia is artificially set at 10^5/ml in order to allow for visualization of the population. Because there are so many VSGs expressed during infection, colors are difficult to distinguish; overall, variants do not reappear later in the same infection. A smooth curve connects points at which expression or parasitemia was measured; these curves are for visualization and do not imply the actual kinetics of variant expression between points. This figure is representative of four infection experiments (mouse 2 is shown). (**B**) Dynamics of VSG expression during late infection (days 96 to 105) for mouse 3. (**C**) Number of VSGs present at each time point. Any variants quantified as >0.01% of the population are included.

To see whether these infections showed any bias or hierarchy in VSG expression (*6*, *8*, *19*, *20*), we compared the VSG repertoires of all four mice. During the first 30 days of infection, 192 VSGs were expressed. Although each infection initiated with a different major VSG, the majority of variants (86%) appeared in more than one infection, and nearly half (46%) appeared in all four infections (Fig. 3C). Ninety-seven VSGs were expressed in mouse 3 from days 96 to 105. We compared the later occurring VSGs with those expressed early in mice 1, 2, and 4 and found none in common, even though early variants from mouse 3 also appeared frequently in mice 1, 2, and 4 (Fig. 3D).

Our experiments revealed striking diversity within each infection, but surprisingly frequent occurrence of the same VSGs in different infections.

Within these diverse populations, many variants appeared transiently. We have termed these "minor" variants. By examining the fate of every variant, we found that at any time during the first 30 days of infection, about half (53%) of the variants present will never reach 1% of the population (Fig. 3A). Of the 48 VSGs that appeared in all four infections, few were consistently dominant, and few were only ever expressed as a minor variant (Fig. 3B). This implies that variant success is not determined only by the expressed VSG. Instead, variant success is likely to be determined by interactions between the parasite and the humoral immune response in each animal. Because of antigenic similarity among some VSGs and their consequent elimination by cross-reacting antibodies, the effective VSG repertoire will be smaller than the repertoire that the genome is capable of generating.

Besides losing variants to cross-reactivity, *T. brucei*'s genomic VSG repertoire consists of a high proportion of incomplete VSG genes or pseudogenes (*1*, *21*). Indeed, the 289 VSGs observed in our infections may represent more than half of the complete VSG repertoire [~400

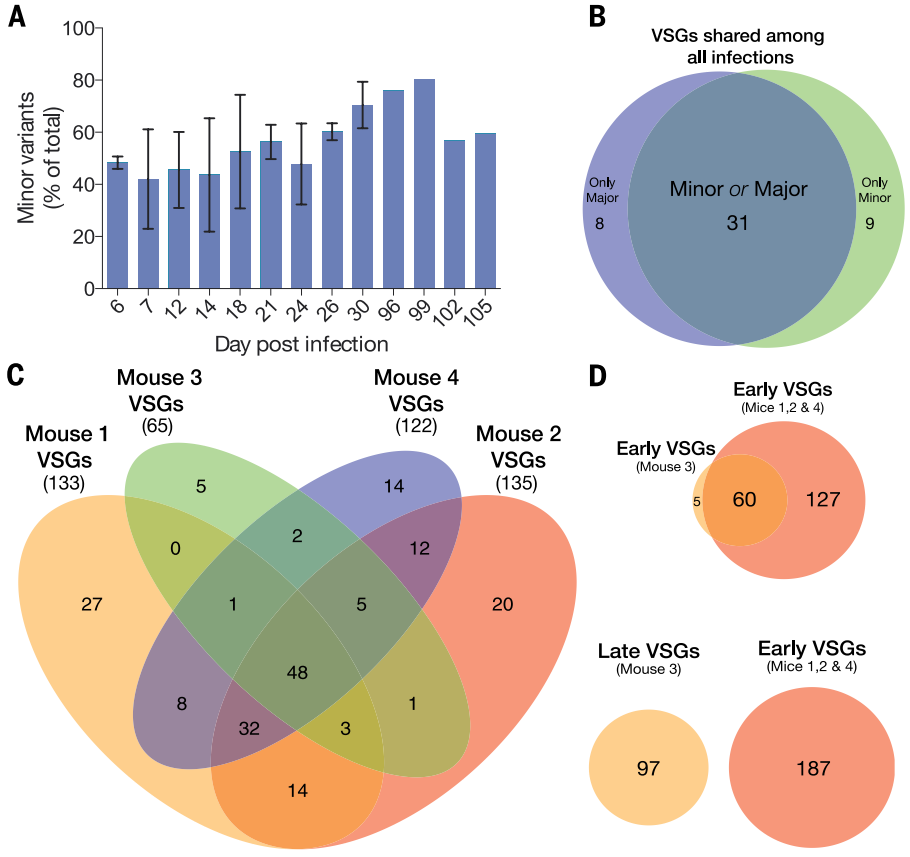

Fig. 3. Variant emergence during infection. (**A**) Minor variants present at each time point (mean ± SD). A minor variant is arbitrarily defined as any VSG that never exceeds 1% of the population during the course of infection in a single mouse. Major variants are any variant that exceeds 1% of the population at some point during infection. (**B**) Venn diagram comparing the fates of VSGs appearing in all four infections. (**C**) Intersection of sets of VSGs expressed during early infection (days 6 to 30). The total number of VSGs is listed in parentheses below the mouse number. (**D**) Venn diagrams showing intersection of VSGs expressed early in infection (VSGs from mouse 1, 2, or 4 versus VSGs from mouse 3, days 7 to 30) and intersection of VSGs expressed early in infection with VSGs expressed late in infection (VSGs from mouse 1, 2, or 4 versus VSGs from mouse 3, days 96 to 105).

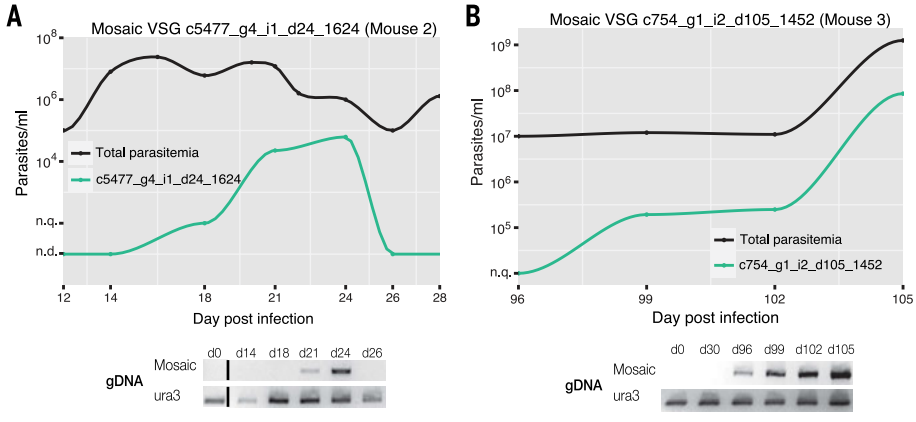

Fig. 4. Mosaic VSGs can be identified throughout infection. (**A**) Transient expression of a mosaic VSG in the population. PCR confirmation of the mosaic is shown below. The black line represents total parasitemia at each day after infection, and the green line represents the number of parasites expressing the mosaic VSG. "n.q." indicates that the VSG is detectable within the population, but not quantifiable. "n.d." indicates that the VSG is not detectable within the population. Below the graph are products from PCR of gDNA at each time point, by using either primers specific for the mosaic VSG or the control gene, *ura3*. This VSG could not be amplified when first detected with VSG-seq, likely because of low cell numbers in the DNA sample (probably less than 10 cells). (**B**) Mosaic from late infection, with PCR confirmation of the mosaic shown below.

complete and predicted to be functional VSGs for the Lister427 strain (*1*), although the VSG repertoire for the EATRO1125 strain has not been fully elucidated]. The 65 to 135 VSGs observed before day 30 could represent up to 35% of the preexisting repertoire. Given the sampling frequency in our experiment, these values almost certainly underestimate the expressed VSG diversity in vivo. Therefore, much of the intact VSG repertoire is likely to have been expended early in an infection, as a result of expression and subsequent recognition by the immune system. As a result, the preexisting repertoire of complete VSGs would appear to be insufficient to support the sometimes years-long infections observed in the field. Although parasitemia is much lower in natural hosts, preexisting immunity is common in native mammals (*22*), requiring constant VSG diversification to sustain infection.

Segmental gene conversion events have been demonstrated in both *Trypanosoma equiperdum* and *T. brucei* infections (*7*, *23*, *24*) generating "mosaic" VSGs that were not previously encoded in the genome. Previous studies had noted that mosaics tend to arise later in infection but have not determined when these variants are formed within the genome, or how. It is unknown whether mosaic VSGs form at the active expression site or within the silent repertoire before expression. To identify possible mosaics, we compared expressed VSG sequences to two independently assembled genomes for this parasite strain. Because of limitations in the amount of material available at each time point, we could choose only a few candidates for validation. To test that these were true mosaics and to determine when they formed within the genome, we used VSG-specific primers to confirm their absence from the genome of the parental strain and presence within genomic DNA (gDNA) collected during infection. We identified three mosaic VSGs using this approach. In each case, the mosaic VSG was only detectable by means of polymerase chain reaction (PCR) when it was also being expressed within the parasite population. This suggests that mosaic formation occurs, at least in these cases, shortly before expression, with subsequent transposition into the active expression site, or directly within the active expression site (Fig. 4 and fig. S3). Mosaic formation may be a mechanism for increasing repertoire diversity as infection progresses.

Our results indicate that VSG switching does not occur at a rate that we would have expected to be just sufficient for immune evasion, with only a few variants present at any time. This suggests that recombinatorial mechanisms that expand the preexisting VSG repertoire may be critical for sustaining the long infections observed in natural hosts. Recent work on samples collected from sleeping sickness patients shows higher-than-expected VSG diversity (*25*), indicating that complex VSG dynamics are likely to be clinically relevant. Our results provide a foundation for the study of VSG switching and diversification in vivo and demonstrate the potential of high-throughput approaches for studying antigenic variation, in trypanosomes and other parasitic diseases, in naturally infected humans and animals.

REFERENCES AND NOTES

1. G. A. M. Cross, H. S. Kim, B. Wickstead, *Mol. Biochem. Parasitol.* **195**, 59–73 (2014).
2. C. Hertz-Fowler *et al.*, *PLOS ONE* **3**, e3527 (2008).
3. R. Ross, D. Thomson, *Proc. R. Soc. London Ser. B* **82**, 411–415 (1910).
4. C. M. Turner, J. D. Barry, *Parasitology* **99**, 67–75 (1989).
5. C. M. Turner, *FEMS Microbiol. Lett.* **153**, 227–231 (1997).
6. E. N. Miller, M. J. Turner, *Parasitology* **82**, 63–80 (1981).
7. J. P. J. Hall, H. Wang, J. D. Barry, *PLOS Pathog.* **9**, e1003502 (2013).
8. L. J. Morrison, P. Majiwa, A. F. Read, J. D. Barry, *Int. J. Parasitol.* **35**, 961–972 (2005).
9. K. A. Lythgoe, L. J. Morrison, A. F. Read, J. D. Barry, *Proc. Natl. Acad. Sci. U.S.A.* **104**, 8095–8100 (2007).
10. P. MacGregor, N. J. Savill, D. Hall, K. R. Matthews, *Cell Host Microbe* **9**, 310–318 (2011).
11. S. A. Frank, *Proc. Biol. Sci.* **266**, 1397–1401 (1999).
12. E. Gjini, D. T. Haydon, J. D. Barry, C. A. Cobbold, *Proc. Biol. Sci.* **280**, 20122129–20122129 (2013).
13. M. G. Grabherr *et al.*, *Nat. Biotechnol.* **29**, 644–652 (2011).
14. N. Van Meirvenne, P. G. Janssens, E. Magnus, *Ann. Soc. Belg. Med. Trop.* **55**, 1–23 (1975).
15. F. Claes *et al.*, *PLOS Negl. Trop. Dis.* **3**, e486 (2009).
16. J. R. Seed, *J. Protozool.* **25**, 526–529 (1978).
17. A. R. Gray, *J. Gen. Microbiol.* **41**, 195–214 (1965).
18. J. Lu *et al.*, *Mol. Immunol.* **57**, 274–283 (2014).
19. P. J. Myler, A. L. Allen, N. Agabian, K. Stuart, *Infect. Immun.* **47**, 684–690 (1985).
20. A. Y. Liu, P. A. Michels, A. Bernards, P. Borst, *J. Mol. Biol.* **182**, 383–396 (1985).
21. M. Berriman *et al.*, *Science* **309**, 416–422 (2005).
22. L. Marcello, J. D. Barry, *J. Eukaryot. Microbiol.* **54**, 14–17 (2007).
23. S. M. Kamper, A. F. Barbet, *Mol. Biochem. Parasitol.* **53**, 33–44 (1992).
24. C. Roth, F. Bringaud, R. E. Layden, T. Baltz, H. Eisen, *Proc. Natl. Acad. Sci. U.S.A.* **86**, 9375–9379 (1989).
25. B. A. Eyford, R. Ahmad, J. C. Enyaru, S. A. Carr, T. W. Pearson, *PLOS ONE* **8**, e71463 (2013).

ACKNOWLEDGMENTS

We thank A. Ivens, K. Matthews, K. Gunasekera, and I. Roditi for generously sharing their independently assembled genome sequences and J. Scott for help with early optimization experiments. The work presented has been supported in part by the NIH/National Institute of Allergy and Infectious Diseases (AI085973) to F.N.P., by an NSF Graduate Research Fellowship (DGE-1325261) to M.R.M., and by a Rockefeller University Women in Science Fellowship to M.R.M. All raw data has been deposited to the National Center for Biotechnology Information's Sequence Read Archive under accession number SRP051697, along with all the methods used to generate the figures.

SUPPLEMENTARY MATERIALS

www.sciencemag.org/content/347/6229/1470/suppl/DC1
Materials and Methods
Figs. S1 to S3
References (*26*–*30*)
Databases S1 to S5

10 December 2014; accepted 19 February 2015
10.1126/science.aaa4502

GEOMICROBIOLOGY

Redox cycling of Fe(II) and Fe(III) in magnetite by Fe-metabolizing bacteria

James M. Byrne,[1]*† Nicole Klueglein,[1]† Carolyn Pearce,[2,3] Kevin M. Rosso,[3] Erwin Appel,[4] Andreas Kappler[1]

Microorganisms are a primary control on the redox-induced cycling of iron in the environment. Despite the ability of bacteria to grow using both Fe(II) and Fe(III) bound in solid-phase iron minerals, it is currently unknown whether changing environmental conditions enable the sharing of electrons in mixed-valent iron oxides between bacteria with different metabolisms. We show through magnetic and spectroscopic measurements that the phototrophic Fe(II)-oxidizing bacterium *Rhodopseudomonas palustris* TIE-1 oxidizes magnetite (Fe_3O_4) nanoparticles using light energy. This process is reversible in co-cultures by the anaerobic Fe(III)-reducing bacterium *Geobacter sulfurreducens*. These results demonstrate that Fe ions bound in the highly crystalline mineral magnetite are bioavailable as electron sinks and electron sources under varying environmental conditions, effectively rendering magnetite a naturally occurring battery.

Iron is critical to all living organisms, with many bacteria having developed pathways to access iron either as a nutrient or as an electron acceptor or donor, depending on its mobility, oxidation state, and bioavailability (*1*). Fe(III)-reducing bacteria, including *Geobacter sulfurreducens*, combine reduction of Fe(III) with oxidation of organic matter or H_2 for energy conservation (*2*), whereas phototrophic Fe(II)-oxidizing bacteria such as *Rhodopseudomonas palustris* TIE-1 grow in light with Fe(II) or H_2 as the electron donor (*3*). Bacteria of the *Geobacter* genus and photoferrotrophs have previously been shown to simultaneously occur in sediments (*4*, *5*). The mixed-valent magnetic mineral magnetite (Fe_3O_4), which contains both Fe(II) and Fe(III) in a 1:2 ratio, is often a byproduct of these Fe-metabolization

processes; however, despite its abundance and conductive properties (*6*), the potential use of magnetite in microbial iron and electron cycling is relatively underexplored.

Fe(III)-reducing bacteria readily use dissolved Fe(III) complexes or short-range–ordered minerals (e.g., ferrihydrite) and even magnetite as terminal electron acceptors (*7*–*9*). In contrast, growing cultures of phototrophic Fe(II)-oxidizers are seen to access Fe(II) only in dissolved [$Fe^{2+}_{(aq)}$] or complexed [e.g., Fe(II)-nitrilotriacetic acid] forms (*10*), thus making the bioavailability of magnetite as an electron donor unclear. Nevertheless, *c*-type cytochromes purified from a microaerophilic Fe(II)-oxidizing bacterium can oxidize the surface of magnetite, changing the ratio of iron oxidation states [Fe(II)/Fe(III)] (*11*), and *R. palustris* can accept electrons from a solid electrode (*12*), although direct interaction between living cells and magnetite has not been observed.

We investigated co-cultures of *R. palustris* and *G. sulfurreducens* incubated with magnetite nanoparticles to explore mineral-bound Fe redox cycling. We controlled light and organic matter supply (*13*) in order to investigate the microbially driven mineralogical and magnetic changes that occur within the magnetite due to its dependence on Fe(II)/Fe(III). The magnetite unit cell contains eight Fe(II) and eight Fe(III) octahedrally coordinated ions, which are coupled in antiparallel magnetic orientation to eight Fe(III) tetrahedral coordinated ions. The magnetic moments of the Fe(III) ions cancel one another out, leaving Fe(II) as the main factor in the mineral magnetization. Fe(II)/Fe(III) is based on the total distribution of iron in the formula unit [i.e., in stoichiometric magnetite, Fe(II)/Fe(III) = 0.5]. Indeed, Fe(II)/Fe(III) plays a crucial role in the magnetic properties of magnetite, with maghemite (the fully oxidized form of magnetite) having a lower bulk saturation magnetization (M_s) of ~75 A·m^2/kg (A·m, ampere meter) at room temperature, in comparison to M_s = 92 A·m^2/kg for stoichiometric magnetite (*14*). These experiments support our hypothesis that magnetite can serve as a battery through which bacteria store and withdraw electrons, regulated by changing redox and light conditions.

R. palustris was incubated in constant light with only magnetite (diameter ~12 nm; 10 mg) as an electron donor, leading to a decrease in Fe(II)/Fe(III) (Fig. 1A). After 14 days, Fe(II)/Fe(III) decreased from 0.59 ± 0.03 to 0.31 ± 0.02. Subsequent removal of *R. palustris* and the addition of *G. sulfurreducens* with 10 mM acetate as electron donor initiated magnetite reduction, with Fe(II)/Fe(III) increasing to 0.56 ± 0.02 over 2 days. $Fe^{2+}_{(aq)}$ in the supernatant remained low during oxidation (39 ± 16 μM), but increased to 113 ± 13 μM after *G. sulfurreducens* was added. Sterile controls showed only minor changes in Fe(II)/Fe(III) and $Fe^{2+}_{(aq)}$ over time. Using in situ volume-specific magnetic susceptibility (κ), we analyzed the cultures non-invasively without removing any sample (*15*). Cultures inoculated with *R. palustris* showed a clear decrease in κ by −8.7% (from 1508 ± 9 × 10^{-6} to 1378 ± 7 × 10^{-6} SI) after 9 days (Fig. 1B). κ rapidly increased again (+4.6%) after the addition of *G. sulfurreducens*. After day 10, we observed a decrease in κ, perhaps due to minor magnetite dissolution by *G. sulfurreducens*, as confirmed by a small increase in $Fe^{2+}_{(aq)}$ in the supernatant.

[1]Geomicrobiology, Center for Applied Geosciences, University of Tuebingen, Sigwartstrasse 10, 72076 Tuebingen, Germany. [2]School of Chemistry, University of Manchester, M13 9PL Manchester, UK. [3]Pacific Northwest National Laboratory, Richland, WA 99352, USA. [4]Geophysics, Center for Applied Geosciences, University of Tuebingen, Sigwartstrasse 10, 72076 Tuebingen, Germany.
*Corresponding author. E-mail: James.Byrne@uni-tuebingen.de
†These authors contributed equally to this work.

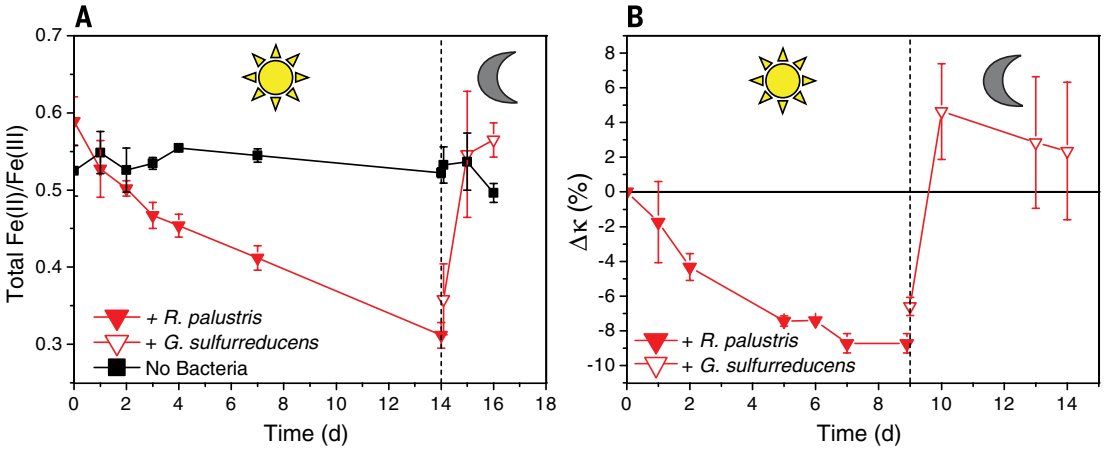

Fig. 1. Oxidation/reduction of magnetite nanoparticles by growing Fe-metabolizing bacteria. (**A**) Observed changes in Fe(II)/Fe(III) over time in magnetite nanoparticles in the presence of Fe-metabolizing bacteria. (**B**) Change in κ with respect to the starting value over time of magnetite nanoparticles in the presence of *R. palustris* and *G. sulfurreducens*. The dashed vertical lines indicate a change from light to dark incubation. Error bars indicate standard deviation of the mean.

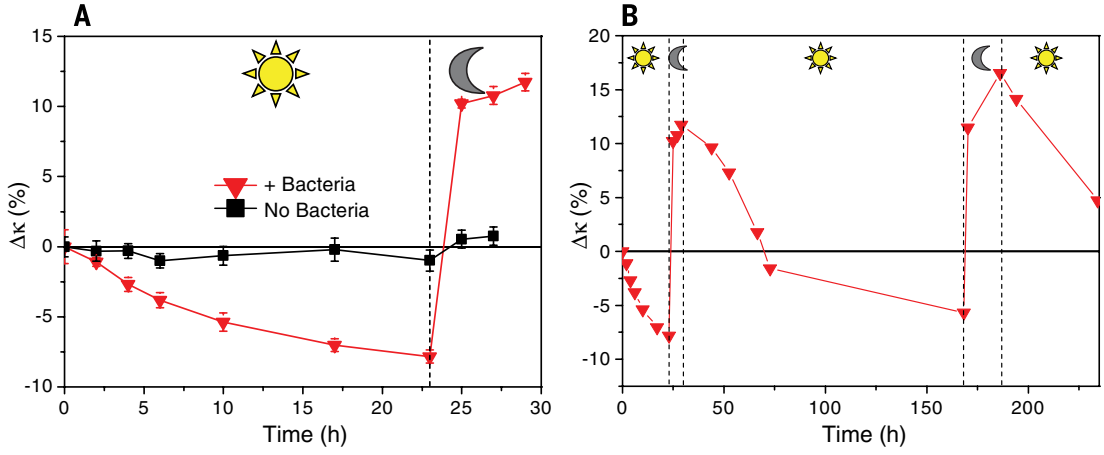

Fig. 2. Magnetite Fe cycling in a cell suspension of Fe-metabolizing bacteria. (**A**) Change in κ of magnetite over 28 hours in the presence of a co-culture of Fe-metabolizing bacteria. Error bars indicate standard deviation of the mean. (**B**) Continuous cycling of magnetite over 240 hours in the co-culture controlled by light and acetate amendment (1 mM).

We examined the consequences of the oxidation/reduction processes on the mineralogical and magnetic properties of the magnetite, using concentrated bacterial cell suspensions of co-cultures of *R. palustris* and *G. sulfurreducens*. These concentrated suspensions enhanced the reaction rate 10-fold, due to a ×10 increase in cell numbers. Over 23 hours in the light, κ decreased by –7.4% (from $1552 \pm 13 \times 10^{-6}$ SI to $1437 \pm 7 \times 10^{-6}$ SI) due to microbial Fe(II) oxidation by *R. palustris* (Fig. 2A). Without removing the media or Fe(II)-oxidizing bacteria, *G. sulfurreducens* and 1 mM acetate were added to the bottles to stimulate reduction with cultures placed in the dark to inhibit *R. palustris* activity. This stimulated a dramatic increase in κ (+11.7%; $P < 0.05$ at every time point except for $t = 0$ and $t = 2$ for which $P = 0.3$; see Fig. 2). Six hours later, the cultures were returned to light to stimulate *R. palustris*, resulting in κ decreasing by –5.7%. Subsequent acetate addition and incubation in the dark led κ to increase (+16.5%) before decreasing again in the light. Acetate addition without *G. sulfurreducens* (and incubation in the dark) did not affect κ (fig. S1). The concurrent changes in κ show that continuous cycling of iron within magnetite is possible by these bacteria, although the rate of change of κ appears to slow down over repeated cycles, perhaps due to saturation of the magnetite surface with bacteria and/or extracellular organic material (i.e., formation of a biofilm), blocking or at least limiting access to magnetite.

We analyzed the mineralogical properties of the incubated magnetite at three time points, including the starting material (T_{zero}), oxidized magnetite after 23 hours (T_{ox}), and the reduced sample after 6 hours of reduction (T_{red}). Spectrophotometric ferrozine analyses (table S4) showed T_{zero} to be slightly oxidized, with Fe(II)/Fe(III) = 0.45 ± 0.02 as compared to 0.41 ± 0.05 for T_{ox} and 0.52 ± 0.02 for T_{red}, which is comparable to the growth experiment results. Micro–x-ray diffraction (μ-XRD) patterns (fig. S2) showed the characteristic reflections of magnetite without any reflections corresponding to other mineral phases. The average crystallite sizes were calculated as 11.6, 11.6, and 11.5 nm for T_{zero}, T_{ox}, and T_{red}, respectively. Using the lattice parameters (table S4) (*16*), we determined the structural Fe(II)/Fe(III) of T_{zero}, T_{ox}, and T_{red} as 0.47, 0.42, and 0.47, respectively.

^{57}Fe Mössbauer (Fig. 3 and table S1) spectra collected at 295 K show the characteristic overlapping sextets of magnetite corresponding to tetrahedral (A-site) and octahedral (B-site) Fe, with almost no differences between samples and no indication of additional mineral phases. At 140 K, the samples show more pronounced differences. Although the center shifts and hyperfine fields of the A and B sites remained relatively comparable for all samples, the relative populations of each site showed differences,

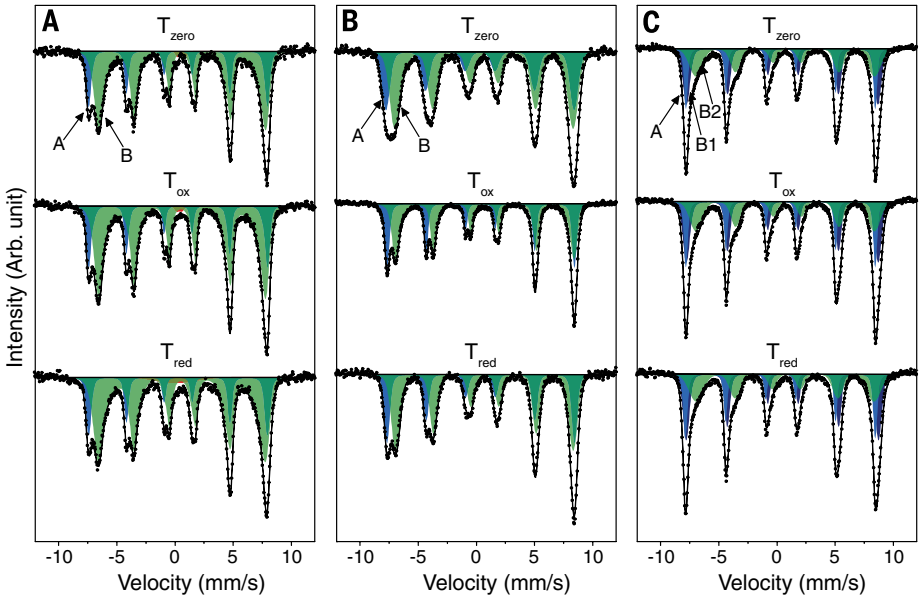

Fig. 3. Mössbauer spectroscopy of magnetite before and after reduction/oxidation. Spectra collected for T_{zero}, T_{ox}, and T_{red} at (**A**) 295 K, (**B**) 140 K, and (**C**) 77 K. All spectra are characteristic of magnetite with tetrahedral (blue) A and octahedral (green) B sites observable at all temperatures.

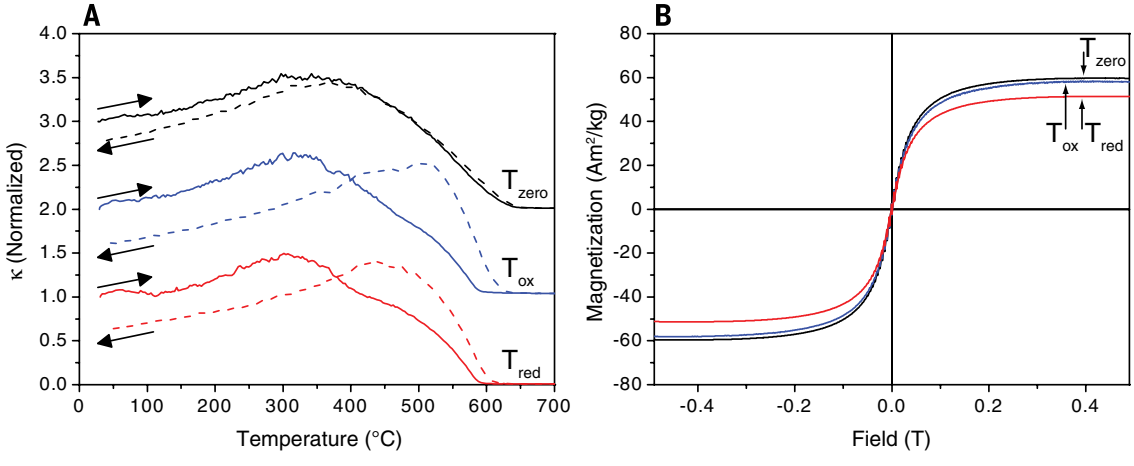

Fig. 4. Magnetic measurements of magnetite before and after reduction/oxidation. (**A**) Normalized high-temperature–dependent susceptibility (κ) curves for T_{zero}, T_{ox}, and T_{red}. Heating curves are shown as solid lines, with dashed lines indicating the cooling curves. Values are normalized to the starting susceptibility measured at the beginning of the heating run and displaced vertically for better comparison. (**B**) Magnetic hysteresis curves collected for T_{zero} (black), T_{ox} (blue), and T_{red} (red) at room temperature.

which were then used to calculate the Fe(II)/Fe(III) for each sample (*17*) (table S4). In accordance with the expected trend, Fe(II)/Fe(III) decreased from 0.46 ± 0.03 (T_{zero}) to 0.42 ± 0.01 (T_{ox}), before increasing to 0.46 ± 0.01 after reduction (T_{red}). At 77 K, the samples were again almost identical with no differences in Fe(II)/Fe(III), although the B site split into two separately ordered subsextets corresponding to Fe^{3+} (B_1) and Fe^{2+} (B_2). The fact that the spectral differences between samples are only observed at 140 K suggests a temperature-dependent effect, probably related to the Verwey transition (T_v ~ 119 K), which can suppressed by magnetite oxidation (*18*).

We also obtained high-temperature magnetic susceptibility (κ-*T*) data for all time points (Fig. 4A). A broad peak with an apex at ~330°C in the heating curve for T_{zero} indicates the presence of single-domain particles or particle clusters that become superparamagnetic at elevated temperatures. κ-*T* decreases to approximately meet the magnetite Curie temperature (T_c ~ 580°C). Apart from a small loss at room temperature (indicating destruction of some magnetite during heating), the cooling curve shows good reversibility. The T_{ox} heating curve looks similar to that of T_{zero}, but in the cooling curve the peak is clearly shifted to a higher temperature. This can be explained by a maghemitized shell that resulted from microbial Fe(II) oxidation that is transformed to hematite during heating due to the thermal instability of maghemite (*19*), leaving behind the magnetite core. The T_{red} heating curve shows similarities to that of T_{ox}; however, the relatively higher κ value at 450°C indicates a higher fraction of magnetite. The loss of susceptibility after cooling for T_{red} is less than for T_{ox} but still obvious; thus, much of the maghemitized volume fraction is obviously still present. The peak in the cooling curve of T_{red} is ~100°C lower than that of T_{ox} but ~100°C higher than that of T_{zero}, suggesting magnetic grain size differences.

Magnetic hysteresis loops (Fig. 4B and table S5) are characteristic of nanoparticulate ferrimagnetic magnetite, with near-zero coercivity (H_c) indicating superparamagnetic (SP) behavior. The saturation magnetization (M_s) of all samples is much lower than the theoretical 92 $A{\cdot}m^2/kg$ of bulk magnetite due to surface spin effects in SP particles (*20*, *21*). The small decrease in M_s of 1.5 $A{\cdot}m^2/kg$ between T_{zero} and T_{ox} is consistent with magnetite oxidation (*22*, *23*). The effect of re-reduction is much less clear, as T_{red} shows an even greater decrease of 8.3 $A{\cdot}m^2/kg$ as compared to T_{zero}. This is counterintuitive to the idea that *G. sulfurreducens* is able to re-reduce the oxidized magnetite to stoichiometric magnetite [i.e., Fe(II)/Fe(III) = 0.5]. One explanation may lie with consideration of the dissolved Fe^{2+} concentration that was detected in the supernatant after the reduction step (127.6 ± 21.2 μM). This dissolution of the particles could in fact have led to an overall decrease in the particle size (as seen from μ-XRD, table S4) leading to the observed decrease in M_s. Alternatively, re-reduction could lead to distortion of the magnetic spin ordering at the surface of the particles; i.e., the maghemitized surface layer is reduced but still forms a distinct shell layer that is not fully coupled to the magnetite core. A nonmagnetic shell in magnetite nanoparticles has previously been shown to form and increases in thickness, depending on the amount of Fe(II) (i.e., level of oxidation) present in the crystal lattice (*24*). Although our average magnetite crystallite size was larger, and therefore a smaller volume fraction was available for oxidation, the formation of a surface layer appears to be the most likely explanation for the impact of bacterial oxidation.

To examine whether our results apply to other systems, we performed further experiments with nitrate-reducing Fe(II)-oxidizing bacteria and other Fe(III)-reducing bacteria (*13*). *Paracoccus denitrificans* strain ATCC 19367, a nitrate-reducing bacterium that is known to indirectly oxidize Fe(II), resulted in a decrease in κ of ~ −10% (from $1885 \pm 81 \times 10^{-6}$ SI to $1693 \pm 49 \times 10^{-6}$ SI) of magnetite (fig. S3). In contrast, *Shewanella oneidensis* MR1, a Fe(III)-reducing bacterium found in anoxic sediments, led to an increase in κ of ~+22% (from $1689 \pm 6 \times 10^{-6}$ SI to $2059 \pm 5 \times 10^{-6}$ SI) (fig. S3). Additionally, the nitrate-reducing bacterium *Acidovorax* sp. BoFeN1 induced a decrease in κ of −8% (from $683 \pm 24 \times 10^{-6}$ SI to $627 \pm 6 \times 10^{-6}$ SI) after 15 days of incubation. This culture was then inoculated with *G. sulfurreducens*, leading to κ increasing to +4.5% ($713 \pm 15 \times 10^{-6}$ SI) (fig. S4), suggesting that the magnetite was re-reduced.

Collectively, these experiments show that magnetite can sustain a vast variety of different bacterial communities functioning as an electron sink, which gets "charged" under reducing conditions by Fe(III) reducers, storing up to 2.6×10^{21} electrons/g (*13*); and then "discharged" under conditions that support its being used as an electron source for Fe(II) oxidizers. In the environment, magnetite could therefore function for microbes as a battery: an environmentally relevant electron sink and source. Alternating oxidation/reduction processes within magnetite could potentially take place in anoxic, photic environments (such as littoral sediments), where environmental fluctuations drive the metabolic use of magnetite (*5*). For example, fluctuating water levels could lead to varying oxygen penetration depths and therefore fluctuating redox conditions, which in turn lead to oxidation and reduction at low and high water levels, respectively. These findings also have direct implications for environmental remediation, in which the reactivity of magnetite with organic contaminants is directly linked to the ratio of Fe(II) to Fe(III) (*25*). Moreover, for environmental magnetic susceptibility measurements, changes in κ are mainly attributed to changes in the amount of magnetite; however, we have shown that microbial activity directly influences the magnetic properties of magnetite without changing the concentration of the mineral. This implies that increasing or decreasing κ could be due to microbial activity rather than magnetite formation, which could have important but currently neglected effects on soil and sediment magnetic properties (*26*).

REFERENCES AND NOTES

1. E. D. Melton, E. D. Swanner, S. Behrens, C. Schmidt, A. Kappler, *Nat. Rev. Microbiol.* **12**, 797–808 (2014).
2. D. R. Lovley, E. J. P. Phillips, D. J. Lonergan, *Appl. Environ. Microbiol.* **55**, 700–706 (1989).
3. Y. Jiao, A. Kappler, L. R. Croal, D. K. Newman, *Appl. Environ. Microbiol.* **71**, 4487–4496 (2005).
4. E. D. Melton, C. Schmidt, S. Behrens, B. Schink, A. Kappler, *Geomicrobiol. J.* **31**, 835–843 (2014).
5. E. D. Melton, C. Schmidt, A. Kappler, *Front. Microbiol.* **3**, 10.3389/fmicb.2012.00197 (2012).
6. S. Kato, K. Hashimoto, K. Watanabe, *Proc. Natl. Acad. Sci. U.S.A.* **109**, 10042–10046 (2012).
7. R. S. Cutting, V. S. Coker, J. W. Fellowes, J. R. Lloyd, D. J. Vaughan, *Geochim. Cosmochim. Acta* **73**, 4004–4022 (2009).
8. H. Dong *et al.*, *Chem. Geol.* **169**, 299–318 (2000).
9. J. A. Smith, D. R. Lovley, P.-L. Tremblay, *Appl. Environ. Microbiol.* **79**, 901–907 (2013).
10. L. J. Bird, V. Bonnefoy, D. K. Newman, *Trends Microbiol.* **19**, 330–340 (2011).
11. J. Liu *et al.*, *J. Am. Chem. Soc.* **135**, 8896–8907 (2013).
12. A. Bose, E. J. Gardel, C. Vidoudez, E. A. Parra, P. R. Girguis, *Nat. Commun.* **5**, 3391 (2014).
13. Materials and methods are available on *Science* Online
14. D. J. Dunlop, Ö. Özdemir, *Rock Magnetism: Fundamentals and Frontiers* (Cambridge Univ. Press, Cambridge, 1997).
15. K. Porsch, U. Dippon, M. L. Rijal, E. Appel, A. Kappler, *Environ. Sci. Technol.* **44**, 3846–3852 (2010).
16. C. I. Pearce *et al.*, *J. Colloid Interface Sci.* **387**, 24–38 (2012).
17. C. A. Gorski, M. M. Scherer, *Am. Mineral.* **95**, 1017–1026 (2010).
18. Ö. Özdemir, D. J. Dunlop, B. M. Moskowitz, *Geophys. Res. Lett.* **20**, 1671–1674 (1993).
19. M. E. Evans, F. Heller, *Environmental Magnetism: Principles and Applications of Enviromagnetics* (Elsevier Science, Academic Press, San Diego, CA, 2003).
20. A. E. Berkowitz *et al.*, *J. Magn. Magn. Mater.* **196–197**, 591–594 (1999).
21. J. M. D. Coey, *Phys. Rev. Lett.* **27**, 1140–1142 (1971).
22. J.-P. Jolivet, E. Tronc, *J. Colloid Interface Sci.* **125**, 688–701 (1988).
23. P. J. Vikesland, A. M. Heathcock, R. L. Rebodos, K. E. Makus, *Environ. Sci. Technol.* **41**, 5277–5283 (2007).
24. R. L. Rebodos, P. J. Vikesland, *Langmuir* **26**, 16745–16753 (2010).
25. C. A. Gorski, M. M. Scherer, *Environ. Sci. Technol.* **43**, 3675–3680 (2009).
26. B. A. Maher, *Elements* **5**, 229–234 (2009).

ACKNOWLEDGMENTS

We thank G. Ojha for help with κ-*T* measurements and C. Berthold for advice on μ-XRD. This work was funded by the Deutsche Forschungsgemeinschaft. Part of this work was funded by the Pacific Northwest National Laboratory Science Focus Area, the Subsurface Biogeochemical Research program of the U.S. Department of Energy Office of Biological and Environmental Research. We thank J. Liu (Peking University) for providing TEM images, which were taken in the Environmental Molecular Science Laboratory (EMSL), a national user facility supported by the OBER and located at PNNL. All data associated with this publication are available at www.pangaea.de.

SUPPLEMENTARY MATERIALS

www.sciencemag.org/content/347/6229/1473/suppl/DC1
Materials and Methods
Figs. S1 to S5
Tables S1 to S5
References (*27*–*34*)

15 December 2014; accepted 20 February 2015
10.1126/science.aaa4834

NEUROTECHNIQUES

Wireless magnetothermal deep brain stimulation

Ritchie Chen,[1,2] Gabriela Romero,[2] Michael G. Christiansen,[1,2] Alan Mohr,[3] Polina Anikeeva[1,2]*

Wireless deep brain stimulation of well-defined neuronal populations could facilitate the study of intact brain circuits and the treatment of neurological disorders. Here, we demonstrate minimally invasive and remote neural excitation through the activation of the heat-sensitive capsaicin receptor TRPV1 by magnetic nanoparticles. When exposed to alternating magnetic fields, the nanoparticles dissipate heat generated by hysteresis, triggering widespread and reversible firing of TRPV1$^+$ neurons. Wireless magnetothermal stimulation in the ventral tegmental area of mice evoked excitation in subpopulations of neurons in the targeted brain region and in structures receiving excitatory projections. The nanoparticles persisted in the brain for over a month, allowing for chronic stimulation without the need for implants and connectors.

Stimulation of deep brain structures affected by treatment-resistant psychiatric and neurological disorders can ameliorate associated symptoms but is currently only achieved by permanently implanted electrodes (*1*). Second-generation neuromodulation technologies rely on acoustic (*2*), electromagnetic induction (*3*), or optical (*4*) signals. These fields are largely absorbed and scattered by tissue and similarly require a conduit for deep brain stimulation. In contrast, low-radiofrequency alternating magnetic fields (100 kHz to 1 MHz) can penetrate into the body without substantial attenuation and thus enable signal delivery into deep brain regions (*5*). Alternating magnetic fields can be converted into biological stimuli by magnetic nanoparticles (MNPs) that dissipate heat via hysteretic power loss (*6*). Although MNP heating has been investigated as a cell-destructive therapy in magnetic hyperthermia for 50 years (*7*), this effect has only recently been exploited for control of cell membrane depolarization and gene expression in engineered xenografts and invertebrates (*8*, *9*). Magnetothermal control of neural activity in vivo in a mammalian system remains to be demonstrated.

To achieve reversible neuronal activation with alternating magnetic fields, we developed an intracellular calcium control scheme by sensitizing cells to heat generated from MNPs (Fig. 1A). Earlier experiments relied on synthetic transgenes to target MNPs to the cell membrane and required tens to thousands of seconds to observe increased calcium ion (Ca^{2+}) influx, which exceeded temporal dynamics of neuronal firing by orders of magnitude. Recent studies suggest that MNP functionalization with proteins induces cell internalization and the formation of protein coronas that may reduce the effectiveness of targeting and heat dissipation in vivo (*10*, *11*). We reasoned that untargeted Fe_3O_4 MNPs optimized for efficient heat dissipation at clinically

[1]Department of Materials Science and Engineering, Massachusetts Institute of Technology, Cambridge, MA 02139, USA. [2]Research Laboratory of Electronics, Massachusetts Institute of Technology, Cambridge, MA 02139, USA. [3]Department of Chemical Engineering, Massachusetts Institute of Technology, Cambridge, MA 02139, USA.
*Corresponding author. E-mail: anikeeva@mit.edu

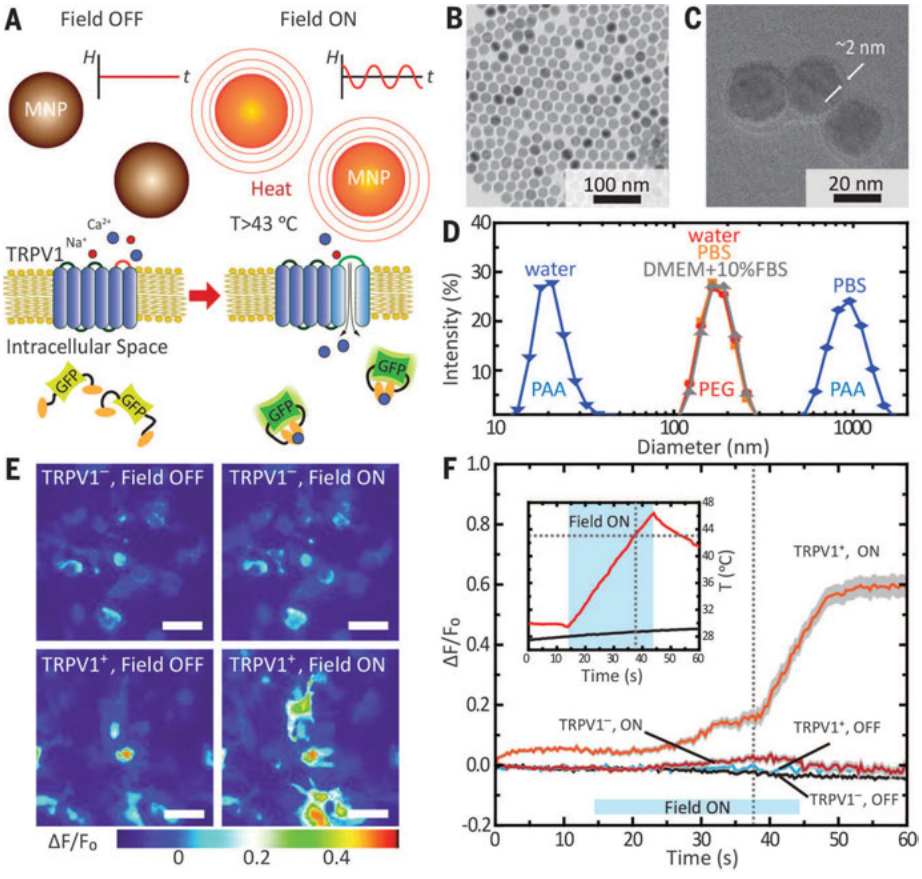

Fig. 1. Wireless ON switch for controlled magnetothermal membrane depolarization of TRPV1$^+$ cells. (**A**) Experimental scheme. Magnetic field stimulation ("Field ON") of TRPV1 from MNP heating is visualized by gCaMP6s fluorescence changes. (**B** and **C**) Transmission electron micrographs of MNPs: (B) as-synthesized and (C) after surface modification with a 2-nm PEG shell. (**D**) Size distribution plot for PAA- and PEG-coated MNPs observed by dynamic light scattering. Aggregation in physiological fluids is observed for PAA-coated MNPs but not for PEG-coated MNPs. (**E**) Color maps of fluorescence intensity changes for TRPV1$^-$ and TRPV1$^+$ HEK293FT cells before and during magnetic field stimulus. Scale bar, 50 μm. (**F**) Normalized fluorescence intensity change ($\Delta F/F_0$) as a function of time (solid lines indicate the mean, and shaded gray areas indicate standard error). Dashed line corresponds to the crossing of TRPV1 activation threshold temperature. Fluorescence increase was observed only in TRPV1$^+$ cells upon magnetic field application. (Inset) Temperature profile without (gray) and with (red) magnetic field application. In all experiments, field amplitude is H_o = 15 kA/m, and frequency is f = 500 kHz.

relevant alternating magnetic field conditions can (i) reduce the latency period for neural excitation, (ii) eliminate exogenous targeting transgenes, and (iii) have chronic utility in vivo because MNPs exhibit minimal cytotoxicity and remain intact several months after injection (*12*, *13*). Spherical Fe_3O_4 MNPs 22 nm in diameter possess some of the highest heating rates per gram, or specific loss power, measured for a synthetic material at a therapeutically relevant frequency f = 500 kHz and field amplitude H_o = 15 kA/m (*14*). We prepared these monodisperse MNPs via the thermal decomposition of an environmentally benign iron-oleate precursor (*15*) and dispersed them in water through high-temperature ligand exchange with poly(acrylic acid) (PAA) (Fig. 1B) (*14*). Grafting poly(ethylene glycol) (PEG) chains onto PAA-coated MNPs resulted in their steric dispersion, which improved colloidal stability (Fig. 1, C and D) and biocompatibility, as indicated by the increased viability of human embryonic kidney (HEK) 293FT cells over prolonged exposure (fig. S1) (*16*). These MNPs exhibited specific loss of power of 660 ± 50 W/g, which is sixfold greater than that of hyperthermia agents currently used in clinical settings (fig. S2). Magnetic fields were generated by a resonant coil custom designed for fluorescence imaging during stimulation (fig. S3, A to E). Although transient receptor potential cation channel subfamily V member 1 (TRPV1) is naturally expressed across the mammalian nervous system (*17*), we designed a transgene to establish sustained and uniform levels of TRPV1 expression for magnetothermal membrane depolarization across different cell lines (*18*). The TRPV1 transgene was placed under the excitatory neuronal promoter calmodulin kinase II α-subunit along with mCherry separated from TRPV1 by the posttranscriptional cleavage linker p2A (*CamKIIα::TRPV1-p2A-mCherry*) (*19*) and packed into the lentiviral vector so as to enable long-term in vitro and in vivo neural transfection (*20*). Cells were additionally transfected with the adeno-associated virus serotype 9 (AAV9) carrying GCaMP6s under the neuronal promoter human synapsin (*hSyn::GCaMP6s*) for measurement of intracellular Ca^{2+} changes as a proxy for membrane depolarization (*21*). Functionality of the two genes was confirmed by observing increased fluorescence intensity in response to capsaicin, a TRPV1 agonist, and temperature increase above 43°C in nonexcitable HEK293FT cells (fig. S4, A to C).

We first demonstrated magnetothermal control of intracellular Ca^{2+} influx in HEK293FT cells. Fluorescence intensity maps indicated that only cells expressing TRPV1 ($TRPV1^+$) responded to the field stimulus (f = 500kHz, H_o = 15 kA/m) when incubated in MNP solutions (2 mg/mL), whereas cells not expressing TRPV1 ($TRPV1^-$) as well as $TRPV1^+$ and $TRPV1^-$ cells without field stimulus did not exhibit changes in intracellular Ca^{2+} concentration (Fig. 1E). A field-induced temperature increase in excess of 43°C in MNP solutions triggered a GCaMP6s fluorescence increase of $\Delta F/F_0$ > 50% in 36.1 ± 4.3% (mean ± SD) of $TRPV1^+$ cells, whereas only 1.7 ± 1.6% (mean ± SD) of $TRPV1^-$ cells exhibited a similar response (Fig. 1F and fig. S5, A to D).

Magnetothermal membrane depolarization was sufficient to evoke trains of action potentials in primary hippocampal neurons expressing TRPV1 when exposed to 10-s field pulses at 60-s intervals. Viral transfection with *AAV9-hSyn::GCaMP6s*, which allows for fluorescence detection of single action potential events (*21*), and *Lenti-CamKIIα::TRPV1-p2A-mCherry* ($TRPV1^+$) or *Lenti-CamKIIα::mCherry* ($TRPV1^-$) yielded a coexpression efficiency of 57% after 5 days (Fig. 2A). In MNP solutions (10 mg/ml), 85 ± 14% of $TRPV1^+$ neurons exhibited synchronized firing within 5 s after stimulus, whereas only sporadic activity

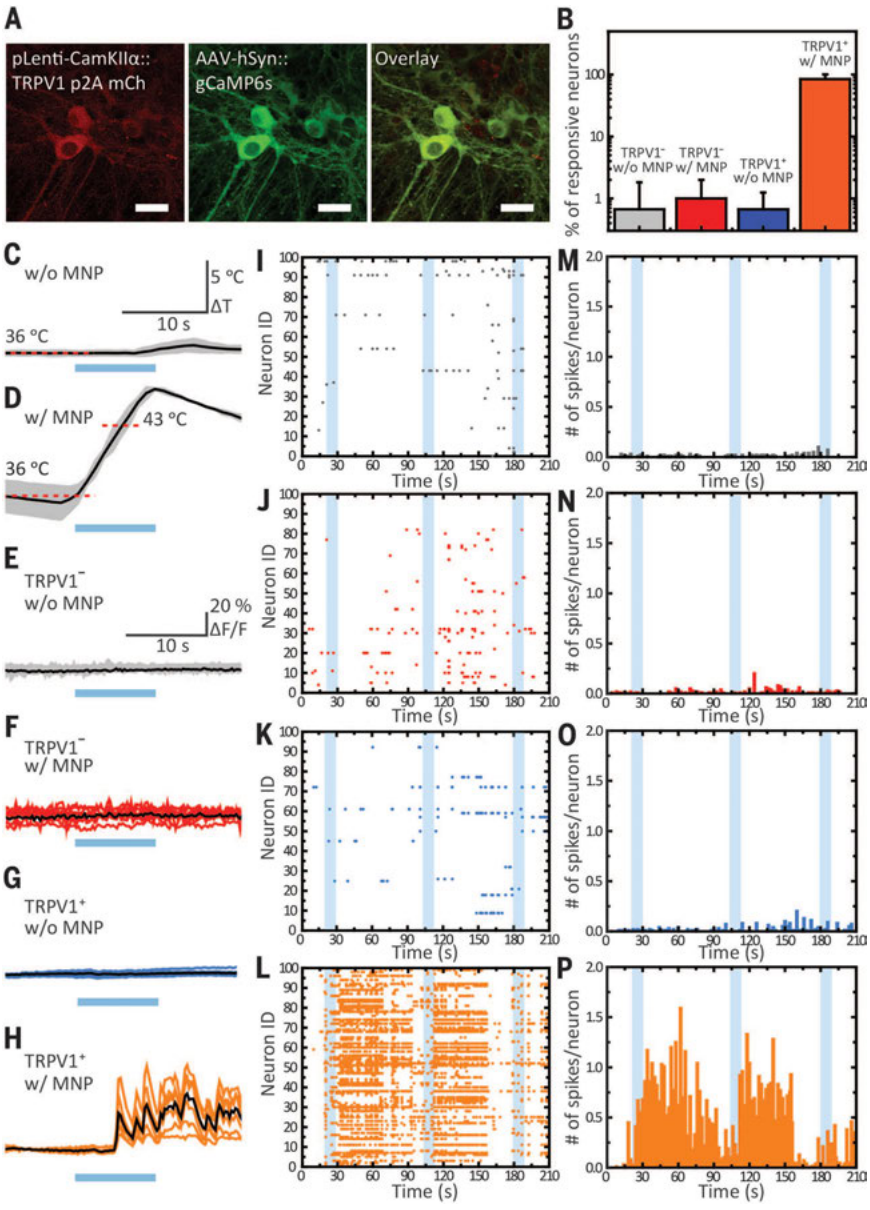

Fig. 2. Alternating magnetic field stimulus evokes correlated and repeated trains of action potentials. (**A**) Confocal fluorescent images of cotransfected hippocampal neurons. Scale bar, 25 μm. (**B**) Population study of 100 neurons from three trials counting the number of neurons that spike within a 5-s bin after magnetic field stimulus. (**C** and **D**) Temperature profiles during magnetic field application in Tyrode's solution (C) without and (D) with MNPs. Shaded area is the SD with average value overlaid (black). (**E** to **H**) Example fluorescence traces of 10 individual neurons with average overlaid (black). (**I** to **L**) Raster plots of 100 randomly selected neurons from three trials. Calcium spikes were counted according to an automated algorithm. (**M** to **P**) Peristimulus time histograms of the raster plots binned at 2 s. Color scheme for (E) to (P): $TRPV1^-$ neurons in Tyrode's solution without MNPs, gray; $TRPV1^-$ neurons in Tyrode's solution with MNPs, red; $TRPV1^+$ neurons in Tyrode's solution without MNPs, blue; $TRPV1^+$ neurons in Tyrode's with MNPs, orange. Shaded blue bars represent alternating magnetic field pulses (H_o = 15 kA/m, f = 500 kHz).

was observed in TRPV1$^-$ neurons (Fig. 2, B to H). This implies that the temperature increase (Fig. 2D) in MNP solutions exposed to alternating magnetic field was sufficient to trigger TRPV1 (Fig. 2H) while avoiding nonspecific thermal effects such as changes in membrane capacitance (Fig. 2F) (*22*). In the absence of MNPs, magnetic field did not induce appreciable solution heating (Fig. 2C), and no correlated response was observed in TRPV1$^+$ or TRPV1$^-$ neurons (Fig. 2, B, E, and G). We recorded neural activity from GCaMP6s temporal fluorescence traces (fig. S6, A to D, and movie S1) (*23*). Waves of Ca^{2+} spikes were repeatedly induced by field pulses only in TRPV1$^+$ neurons in the presence of MNPs (Fig. 2, I to P). The observed 5-s latency between the field application and the onset of neural activity is fivefold faster than previously described (*8*).

We next tested whether alternating magnetic field could activate a subpopulation of neurons in deep brain tissue in mice. We used finite element modeling corroborated with temperature recordings in brain phantoms to predict local temperature changes in response to field stimulus (fig. S7). Injections (2.5 μL) of MNP solution (100 mg/mL) delivered temperature gradients sufficient to reach the TRPV1 activation threshold within 5 s and cool back to 37°C over 60-s cycles (fig. S7, B to F), thus avoiding prolonged exposure to noxious heat (fig. S7G) (*24*).

With low endogenous expression of TRPV1 (*25*) and well-characterized projections (*26*), the ventral tegmental area (VTA) was an attractive deep brain target for initial demonstration of magnetothermal stimulation. Furthermore, phasic excitation in the VTA has therapeutic implications in the treatment of major depression (*27*). We sensitized excitatory neurons in the VTA to heat through the lentiviral delivery of TRPV1, which was followed by MNP injection into the same region 4 weeks later (Fig. 3, A and B, and fig. S8A). The anesthetized mice were exposed to the magnetic field conditions described above (fig. S8, B and C). Neuronal excitation was quantified by the extent of activity-dependent expression of the immediate early gene c-fos within a 250-μm vicinity of the MNP injection (Fig. 3, C to F) (*28*). Neural activity was only triggered by magnetic field in the VTA of mice transfected with TRPV1 in the presence of MNPs, resulting in a significantly higher proportion of c-fos–positive (c-fos$^+$) cells, as revealed by a two-way analysis of variance (ANOVA) with a Bonferroni post hoc test ($F_{1,13} = 47.5$, $P < 0.0001$) (Fig. 3G). Control subjects testing whether the MNP injection, heat dissipation with field stimulus, or TRPV1 expression alone can result in neural stimulation showed no significant c-fos expression (Fig. 3, C to E and G). Furthermore, the spatial extent of neuronal activation was largely collocated with TRPV1 expression in the VTA (Fig. 3, H and I).

We next investigated whether neurons in the VTA can be activated 1 month after MNP injection so as to explore its chronic utility (Fig. 3, J to O). We again observed increased c-fos expression in the VTA only in mice transfected with TRPV1 in the presence of MNPs and exposed to

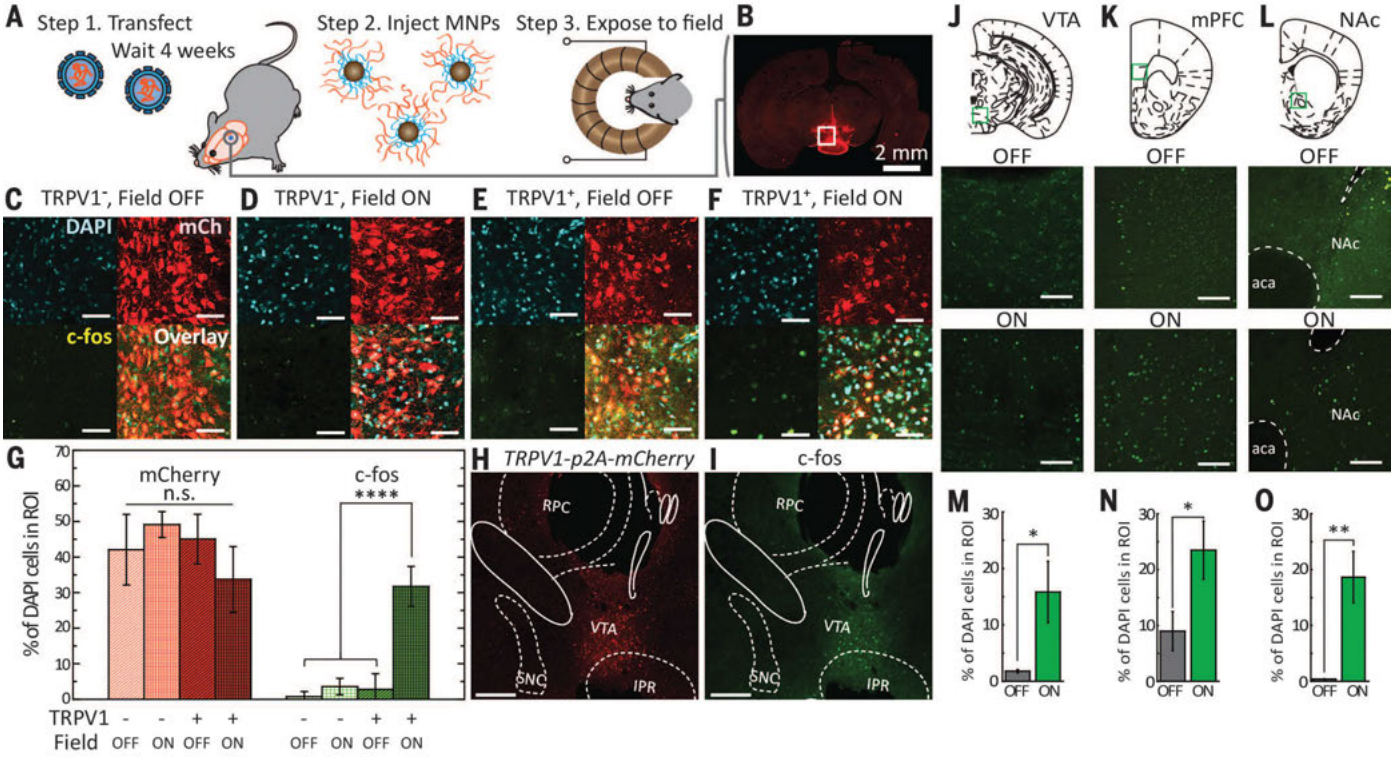

Fig. 3. Wireless magnetothermal stimulation in vivo. (**A**) In vivo experimental scheme. (**B**) Confocal image of a coronal slice representative of the *TRPV1-p2A-mCherry* expression profile in the VTA. (**C** to **F**) 4′,6-diamidino-2-phenylindole (DAPI) (blue), mCherry (red), and c-fos (green) and overlay confocal images of regions used for quantification of neural stimulation. Scale bar, 25 μm. All animals were injected with MNPs. Experimental conditions were (C) without (OFF) and (D) with (ON) magnetic field stimulation in TRPV1$^-$ VTA, and (E) OFF and (F) ON stimulation in TRPV1$^+$ VTA. (**G**) Percentage of mCherry-positive and c-fos–positive neurons within cell population indicated by DAPI corresponding to the four conditions presented in (C) to (F). Significance is confirmed by two-way ANOVA with Bonferroni post hoc test ($n = 4$ mice, $F_{1,13} = 47.5$, $P < 0.0001$). (**H** and **I**) Confocal images of the VTA after acute magnetothermal stimulation. c-fos expression is largely confined to the VTA in regions where TRPV1 is expressed. Scale bar, 100 μm. (**J** to **L**) Confocal images of the (J) VTA, (K) mPFC, and (L) NAc 1 month after MNP injection without (OFF) and with (ON) field treatment. Scale bar, 100 μm. (**M**) Percentage of c-fos$^+$ neurons in the VTA among DAPI-labeled cells with and without magnetic field stimulation. Increased c-fos expression is observed after field treatment (ON) as compared with unstimulated (OFF) controls ($n = 3$ mice OFF/ON; Student's t test, $P < 0.02$). (**N** and **O**) Similarly, up-regulation is observed in (N) the mPFC and (O) in the NAc with alternating magnetic field (ON) as compared with the same regions without (OFF) the field stimulus ($n = 3$ mice OFF/ON; Student's t test $^*P < 0.02$, $^{**}P < 0.002$).

the magnetic field protocol described above (Fig. 3, J and M, "ON") (Student's t test, $P < 0.02$). In these mice, we also found evidence of field-evoked up-regulation of c-fos in the medial prefrontal cortex (mPFC) (Fig. 3, K and N, "ON") (Student's t test, $P < 0.02$) and nucleus accumbens (NAc) (Fig. 3, L and O, "ON") (Student's t test, $P < 0.002$), which are known to receive excitatory inputs from VTA neurons (*26*, *29*). In the absence of stimulation, neurons in the VTA near the MNP injection site and the neurons in the mPFC and NAc did not exhibit increased c-fos expression (Fig. 3, J to O, "OFF").

We compared the biocompatibility of the MNP injection with a similarly sized stainless steel implant (fig. S9). The interface between the MNP injection and the tissue exhibited significantly lower glial activation and macrophage accumulation and higher proportion of neurons, as compared with that of the steel implant 1 week and 1 month after surgery (fig. S9, A to F). The improved tissue compatibility can likely be attributed to the mechanically pliable nature of the MNP injection and sequestration via endocytosis (*12*, *13*). No difference in neuronal or glial density was observed between brain tissue of stimulated and unstimulated mice, suggesting that the rapidly dissipated magnetothermal cycles cause minimal thermal damage to the surrounding tissue (fig. S9G).

We demonstrated widespread and repeatable control of cellular signaling in nonexcitable and electroactive cells using wireless magnetothermal stimulation in vitro and in vivo. Finer control over stimulation intensity to facilitate applications of this approach to problems in systems neuroscience can be achieved by further reducing the latency between field onset and evoked neural firing by developing MNPs with high specific loss powers (*30*) and by introducing heat-sensitive ion channels with lower thermal thresholds (*31*). Mechanosensitive potassium and chloride channels may serve as potential mediators of magnetothermal inhibition (*32*). Although demonstrated for chronic stimulation of targeted neural circuits, this magnetothermal paradigm may be formulated to trigger thermosensitive ion channels endogenously expressed in the peripheral nervous system (*17*), enabling wireless control in deep tissue regions that currently pose substantial challenges to bioelectronic medicines (*33*).

REFERENCES AND NOTES

1. J. S. Perlmutter, J. W. Mink, *Annu. Rev. Neurosci.* **29**, 229–257 (2006).
2. Y. Tufail *et al.*, *Neuron* **66**, 681–694 (2010).
3. V. Walsh, A. Cowey, *Nat. Rev. Neurosci.* **1**, 73–80 (2000).
4. E. S. Boyden, F. Zhang, E. Bamberg, G. Nagel, K. Deisseroth, *Nat. Neurosci.* **8**, 1263–1268 (2005).
5. J. H. Young, M. T. Wang, I. A. Brezovich, *Electron. Lett.* **16**, 358–359 (1980).
6. J. Carrey, B. Mehdaoui, M. Respaud, *J. Appl. Phys.* **109**, 083917–083921 (2011).
7. Q. A. Pankhurst, J. Connolly, S. K. Jones, J. Dobson, *J. Phys. D Appl. Phys.* **36**, R167–R181 (2003).
8. H. Huang, S. Delikanli, H. Zeng, D. M. Ferkey, A. Pralle, *Nat. Nanotechnol.* **5**, 602–606 (2010).
9. S. A. Stanley *et al.*, *Science* **336**, 604–608 (2012).
10. S. Tenzer *et al.*, *Nat. Nanotechnol.* **8**, 772–781 (2013).
11. A. Salvati *et al.*, *Nat. Nanotechnol.* **8**, 137–143 (2013).
12. F. K. H. van Landeghem *et al.*, *Biomaterials* **30**, 52–57 (2009).
13. C. Petters, E. Irrsack, M. Koch, R. Dringen, *Neurochem. Res.* **39**, 1648–1660 (2014).
14. R. Chen, M. G. Christiansen, P. Anikeeva, *ACS Nano* **7**, 8990–9000 (2013).
15. J. Park *et al.*, *Nat. Mater.* **3**, 891–895 (2004).
16. J. Xie, C. Xu, N. Kohler, Y. Hou, S. Sun, *Adv. Mater.* **19**, 3163–3166 (2007).
17. A. I. Basbaum, D. M. Bautista, G. Scherrer, D. Julius, *Cell* **139**, 267–284 (2009).
18. L. Naldini, U. Blömer, F. H. Gage, D. Trono, I. M. Verma, *Proc. Natl. Acad. Sci. U.S.A.* **93**, 11382–11388 (1996).
19. J. H. Kim *et al.*, *PLOS ONE* **6**, e18556 (2011).
20. E. Asante-Appiah, A. M. Skalka, *Antiviral Res.* **36**, 139–156 (1997).
21. T. W. Chen *et al.*, *Nature* **499**, 295–300 (2013).
22. M. G. Shapiro, K. Homma, S. Villarreal, C. P. Richter, F. Bezanilla, *Nat. Commun.* **3**, 736 (2012).
23. B. F. Grewe, D. Langer, H. Kasper, B. M. Kampa, F. Helmchen, *Nat. Methods* **7**, 399–405 (2010).
24. J. R. Lepock, *Int. J. Hyperthermia* **19**, 252–266 (2003).
25. D. J. Cavanaugh *et al.*, *J. Neurosci.* **31**, 5067–5077 (2011).
26. L. W. Swanson, *Brain Res. Bull.* **9**, 321–353 (1982).
27. K. M. Tye *et al.*, *Nature* **493**, 537–541 (2013).
28. S. P. Hunt, A. Pini, G. Evan, *Nature* **328**, 632–634 (1987).
29. L. A. Gunaydin *et al.*, *Cell* **157**, 1535–1551 (2014).
30. J. H. Lee *et al.*, *Nat. Nanotechnol.* **6**, 418–422 (2011).
31. E. O. Gracheva *et al.*, *Nature* **464**, 1006–1011 (2010).
32. S. Yoo, S. Hong, Y. Choi, J. H. Park, Y. Nam, *ACS Nano* **8**, 8040–8049 (2014).
33. K. Birmingham *et al.*, *Nat. Rev. Drug Discov.* **13**, 399–400 (2014).

ACKNOWLEDGMENTS

We thank K. Deisseroth, D. Julius, and F. Zheng for generous gifts of plasmids and cell lines; C. Ramakrishnan for molecular biology advice; the GENIE project and Howard Hughes Medical Institute Janelia Farm for *AAV9-hSyn::GCaMP6s* supplied by the University of Pennsylvania vector core; and D. Irvine and A. Jasanoff for their thoughtful comments on our manuscript. This work was funded in part by a Defense Advanced Research Projects Agency Young Faculty Award (D13AP00043), the McGovern Institute for Brain Research, and the NSF CAREER award (CBET-1253890). This work made use of the MIT Materials Research Science and Engineering Center Shared Experimental Facilities under award DMR-0819762. R.C. and M.G.C. are supported by the NSF Graduate Research Fellowship Program and National Defense Science and Engineering Graduate fellowships, respectively. Methods of analysis and additional data are included in the supplementary materials. P.A., M.G.C., and R.C. have filed a U.S. and international patent (application PCT/US14/67866) describing magnetically multiplexed heating of volumes, which is peripherally related to this work.

SUPPLEMENTARY MATERIALS

www.sciencemag.org/content/347/6229/1477/suppl/DC1
Materials and Methods
Supplementary Text
Figs. S1 to S9
Tables S1 and S2
References (*34*–*42*)
Movie S1

29 September 2014; accepted 29 January 2015
Published online 12 March 2015;
10.1126/science.1261821

SOCIAL SCIENCE

Intergenerational transmission of child abuse and neglect: Real or detection bias?

Cathy Spatz Widom,[1]* Sally J. Czaja,[1] Kimberly A. DuMont[2]

The literature has been contradictory regarding whether parents who were abused as children have a greater tendency to abuse their own children. A prospective 30-year follow-up study interviewed individuals with documented histories of childhood abuse and neglect and matched comparisons and a subset of their children. The study assessed maltreatment based on child protective service (CPS) agency records and reports by parents, nonparents, and offspring. The extent of the intergenerational transmission of abuse and neglect depended in large part on the source of the information used. Individuals with histories of childhood abuse and neglect have higher rates of being reported to CPS for child maltreatment but do not self-report more physical and sexual abuse than matched comparisons. Offspring of parents with histories of childhood abuse and neglect are more likely to report sexual abuse and neglect and that CPS was concerned about them at some point in their lives. The strongest evidence for the intergenerational transmission of maltreatment indicates that offspring are at risk for childhood neglect and sexual abuse, but detection or surveillance bias may account for the greater likelihood of CPS reports.

For years, the notion that abused children grow up to become abusive parents has been widely accepted in the field of child abuse and neglect (*1*–*3*). However, because many other factors in a person's life (such as natural abilities, biological or genetic predispositions, or intervening relationships) may mediate the effects of child abuse and neglect, assessing the intergenerational transmission of abuse and neglect is challenging. Although some studies have provided empirical support for the intergenerational transmission of child abuse (*4*–*10*),

[1]Psychology Department, John Jay College of Criminal Justice, and Graduate Center, City University of New York, New York, NY, USA. [2]William T. Grant Foundation, New York, NY, USA.
*Corresponding author. E-mail: cwidom@jjay.cuny.edu

Table 1. Child protective service agency records by childhood history of abuse or neglect. The percentages reported here are based on individuals known to have lived within the original state at some point in their lives (N = 1147; see the supplementary materials for more details). Numbers for the specific types of abuse and neglect add up to more than the total for the abuse/neglect group overall because there is a small percentage of the subjects (10%) who have more than one type of abuse or neglect.

	Type of abuse and/or neglect experienced in childhood by G2 participants								
	Comparison group (N = 497)	Abuse/Neglect (N = 650)		Physical abuse (N = 108)		Sexual abuse (N = 104)		Neglect (N = 511)	
Child protective service report	%	%	AOR (95% CI)	%	AOR (95% CI)	%	AOR (95% CI)	%	AOR (95% CI)
Any maltreatment	11.7	21.4	2.01 (1.42–2.85)***	18.5	2.03 (1.10–3.73)*	26.0	3.43 (1.86–6.34)***	21.1	1.88 (1.30–2.70)***
Physical abuse	5.4	6.9	1.26 (0.75–2.12)	5.6	1.11 (0.40–3.04)	4.8	1.13 (0.39–3.23)	7.4	1.30 (0.76–2.23)
Sexual abuse	3.4	7.7	2.31 (1.24–4.30)**	7.4	3.90 (1.39–10.92)**	10.6	4.49 (1.64–12.26)***	7.8	2.20 (1.15–4.19)*
Neglect	9.5	18.0	2.06 (1.42–3.01)***	13.9	1.89 (0.96–3.69)	22.1	3.40 (1.75–6.58)***	17.8	1.96 (1.32–2.91)***
Failure to provide	3.6	9.4	2.53 (1.45–4.39)***	7.4	2.56 (0.99–6.59)*	12.5	4.07 (1.63–10.16)***	8.8	2.25 (1.26–4.02)**
Lack of supervision	8.2	14.2	1.76 (1.18–2.65)**	9.3	1.37 (0.62–3.00)	15.4	2.55 (1.20–5.44)*	14.7	1.79 (1.17–2.73)**

*P < 0.05; **P < 0.01; ***P < 0.001

other researchers have found no evidence for transmission (*11*–*14*). Critical reviews have called attention to serious methodological limitations of research examining this question (*15*–*20*). To date, studies are primarily cross-sectional snapshots, rather than prospective longitudinal studies in which children are followed up and assessed in adulthood. Studies that work backward from a population of abusive parents and inquire about their childhood histories may lead to an inflated rate of transmission because individuals who were abused but did not become abusive as a parent are not represented (*8*, *18*, *20*). Finally, theoretical explanations (*21*, *22*) and empirical research have focused on the transmission of physical abuse, largely ignoring the role of childhood sexual abuse and neglect in the intergenerational transmission of child maltreatment.

The present study was designed to overcome many of the methodological limitations of previous work. We used a prospective cohorts design (*23*, *24*), in which both groups were free of the "outcome" (i.e., intergenerational transmission) at the time they were selected for the study. We used court-substantiated cases and thus avoided ambiguity and potential biases associated with retrospective recall (*19*, *20*). We included a comparison group matched as closely as possible for age, sex, race, and approximate social class because it is theoretically plausible that any relationship between child abuse or neglect and later outcomes is confounded or explained by social class differences. We ascertained outcomes using multiple sources of information (parent and nonparent self-reports, offspring report, and child protection agency records) and multiple measures from standardized instruments. Details of methods and materials are available as supplementary materials on *Science* Online. Although our primary focus was on the parent's behavior toward their biological offspring, we also included an assessment of abuse of other children (nonoffspring). We tested whether individuals who have documented histories of abuse or neglect in childhood continue the intergenerational transmission of child abuse toward their own offspring or someone else's children. We also examined whether different types of child maltreatment (physical abuse, sexual abuse, and neglect) are passed on from one generation to the next.

The simplest model of intergenerational transmission is illustrated by the direct relationship across generations: G1→ G2 → G3. The G1 individuals (the first generation) are the parents of the G2 individuals (second generation), who have been participants in our longitudinal study and are now adults. G2 individuals represent those with documented histories of childhood abuse or neglect and those who represent the comparison group without documented histories of abuse or neglect. The offspring of the G2 individuals are the G3, or third generation.

The original sample was composed of 908 G2 children with documented cases of abuse and neglect during the years 1967 through 1971 in a Midwestern county area and a matched comparison group of children (N = 667) from the same neighborhoods. The study was begun as an archival records check with a search of criminal histories for both groups (*25*). The first in-person interviews were conducted from 1989 to 1995, when G2 participants were on average 29 years old (N = 1196). Since that time, three additional interviews have been conducted with these participants (see table S1 for a chronology of the study and the supplementary materials and methods for details of the design of the study and participants). For the purpose of assessing the intergenerational transmission of abuse and neglect, we conducted interviews in 2009 and 2010 with 649 of the original G2 participants (mean age 47.0) and a subset of G3 offspring (N = 697, mean age 22.8). During 2011 to 2013, child protective service (CPS) agency records in the original state were searched for the entire sample and their children, and information was extracted and coded (*26*). Details of attrition and selection bias are provided in the supplementary materials. Despite attrition (see table S2), multiple analyses indicated that child maltreatment status was not a significant factor in nonparticipation in the last wave of the study. There was no difference between the abuse/neglect group and the comparison group in the prevalence of having children (at the first interview, 72.4% of the comparison group and 72.6% of the abuse/neglect group reported having at least one child; P = 0.94).

Because there is no single gold standard to assess child maltreatment, we used multiple sources of information, multiple measures to assess different types of maltreatment, and multiple time points when information was collected. Table 1 shows the percentage of G2 individuals in the abuse/neglect and comparison groups who have CPS agency records for any child maltreatment and specific types of physical abuse, sexual abuse, and neglect. G2 adults with documented histories of childhood abuse or neglect are twice as likely to be reported to CPS because their child was maltreated compared with matched comparisons. Overall, about a fifth of G2 individuals (21.4%) with documented histories of childhood abuse or neglect were reported to CPS agencies compared with 11.7% of matched comparisons [adjusted odds ratio (AOR) = 2.01; 95% confidence interval (CI) = 1.42 to 2.85; P < 0.001, controlling for G2 age, sex, and race, and childhood

Table 2. G2 parent and nonparent self-reports of perpetration of child abuse and neglect. The reference group is the Comparison group. CTS, Conflict Tactics Scale, severe/very severe violence; CEQ, Childhood Experiences Questionnaire; NA, not applicable. For reports of physical abuse, the unadjusted ORs are 1.14, 1.00, 1.33, and 1.14 for nonparent G2s with histories of abuse/neglect overall, physical abuse, sexual abuse, and neglect, respectively. Due to the effects of control variables and small sample sizes here, the AORs appear inconsistent with raw percentages for G2 nonparents' reports of physical abuse.

	Comparison group	Abuse/Neglect		Physical abuse		Sexual abuse		Neglect	
G2 parent self-reports									
N	257	304		42		49		244	
Type of abuse or neglect reported	%	%	AOR (95% CI)	%	AOR (95% CI)	%	AOR (95% CI)	%	AOR (95% CI)
Physical abuse (CTS)	23.9	26.4	1.01 (0.67–1.54)	31.7	1.49 (0.67–3.29)	31.3	1.14 (0.55–2.37)	24.9	0.95 (0.61–1.48)
Sexual abuse	1.9	3.3	1.69 (0.56–5.08)	2.4	1.48 (0.15–14.63)	0.0	NA	3.7	1.75 (0.57–58.40)
Neglect (CTS)	51.4	53.2	1.02 (0.72–1.45)	53.7	1.08 (0.53–2.17)	47.9	0.83 (0.42–1.64)	54.3	1.05 (0.72–1.52)
Neglect (CEQ)	29.0	41.7	1.83 (1.25–2.67)***	39.0	1.52 (0.73–3.20	34.0	1.65 (0.79–3.42)	42.7	1.92 (1.29–2.86)***
G2 nonparent self-reports									
N	34	54		12		5		42	
Type of abuse or neglect reported	%	%	AOR (95% CI)	%	AOR (95% CI)	%	AOR (95% CI)	%	AOR (95% CI)
Physical abuse	26.5	31.5	1.03 (0.37–2.87)	25.0	1.68 (0.29–9.69)	40.0	0.85 (0.04–18.68)	31.0	0.86 (0.28–2.63)
Sexual abuse	2.9	1.9	0.42 (0.01–21.27)	0.0	NA	0.0	NA	2.4	NA

*P < 0.05; **P < 0.01; ***P < 0.001

Table 3. G2 previous self-reports of trouble in relation to parenting. Excludes parents who did not report having children.

	Comparison group	Abuse/Neglect		Physical abuse		Sexual abuse		Neglect	
	%	%	AOR (95% CI)	%	AOR (95% CI)	%	AOR (95% CI)	%	AOR (95% CI)
Mean age 29.2									
During past year, child was placed in custody of courts	1.6	4.7	3.85 (1.44–10.29)**	2.6	2.76 (0.48–15.83)	2.6	3.03 (0.48–19.13)	5.7	4.53 (1.68–12.21)***
N	373	487		78		77		384	
Mean age 40.5									
During past year, child was placed in custody of courts	1.3	4.8	3.77 (1.25–1.35)*	1.6	1.19 (0.12–11.80)	3.8	3.02 (0.46–19.64)	5.6	4.29 (1.46–13.46)**
N	298	377		61		52		304	
Mean age 47.1									
During past year, child was placed in custody of courts	1.2	2.5	3.73 (0.76–18.33)	2.6	NA	0	NA	2.6	3.62 (0.73–18.02)
N	243	282		38		45		228	

*P < 0.05; **P < 0.01; ***P < 0.001

neighborhood advantage and disadvantage]. These rates vary by type of child maltreatment being perpetrated, with increased risk for sexual abuse (AOR = 2.31, 95% CI =1.24 to 4.30, P< 0.001) and neglect (AOR = 2.06; 95% CI = 1.42 to 3.01; P < 0.001) but not for physical abuse (AOR = 1.26, 95% CI = 0.75 to 2.12, not significant).

The intergenerational transmission hypothesis predicts that experiencing physical abuse in childhood will lead to increased risk for physically abusing one's own children. Table 1 also presents our results showing the extent to which the type of maltreatment experienced as a child by G2 predicts a differential likelihood of maltreating a child. G2 individuals with any childhood abuse and neglect were reported to CPS more often than comparisons for any maltreatment, sexual abuse, and neglect but not for physical abuse. In sum, these results indicate that G2 adults with histories of childhood abuse and neglect are at increased risk for being reported to CPS agencies for sexual abuse and neglect but not for physical abuse, compared with matched comparison group subjects.

In addition to any involvement with CPS, we examined the number of reports filed against a G2 individual and the chronicity of reports. Of those G2 with an official CPS report (N = 213), 50.2% (106) have one report, 22.3% (47) have two reports, 10.0% (21) have three reports, and 17.5%

Table 4. G3 offspring reports of experiencing child abuse and neglect. Comparisons are to the controls. LONGSCAN, LS; LS 0–11 refers to the time period from ages 0 to 11; LS 12–17 refers to ages 12 to 17; AH, Adolescent Health; LTVH, Lifetime Trauma and Victimization History; CTS, Conflict Tactics Scale; CEQ, Childhood Experiences Questionnaire.

		G2 parent histories							
	Comparison group (*N* = 209)	Abuse/Neglect (*N* = 245)		Physical abuse (*N* = 35)		Sexual abuse (*N* = 37)		Neglect (*N* = 197)	
G3 offspring report of abuse or neglect	%	%	AOR (95% CI)	%	AOR (95% CI)	%	AOR (95% CI)	%	AOR (95% CI)
Physical abuse (LS 0–11)	74.6	67.4	0.75 (0.49–1.16)	62.9	0.88 (0.38–2.01)	64.9	0.73 (0.31–1.71)	68.0	0.75 (0.47–1.18)
Physical abuse (LS 12–17)	49.8	54.5	1.29 (0.87–1.92)	51.4	1.37 (0.62–3.02)	45.9	1.13 (0.51–2.53)	55.2	1.34 (0.88–2.04)
Physical abuse (AH)	20.7	26.9	1.48 (0.93–2.36)	25.7	1.64 (0.68–3.95)	18.9	1.01 (0.39–2.63)	27.8	1.55 (0.95–2.52)
Physical abuse (LTVH)	22.9	27.1	1.25 (0.80–1.97)	32.4	1.65 (0.72–3.76)	27.0	1.16 (0.50–2.72)	26.0	1.23 (0.76–1.98)
Sexual abuse (LS 0–11)	15.8	24.1	1.46 (0.89–2.38)	25.7	2.03 (0.83–4.95)	24.3	1.54 (0.60–3.91)	24.4	1.40 (0.83–2.36)
Sexual abuse (LS 12–17)	12.9	16.3	1.06 (0.61–1.84)	17.1	1.76 (0.63–4.90)	10.8	0.50 (0.14–1.82)	17.3	1.09 (0.61–1.94)
Sexual abuse (AH)	4.0	13.0	3.03 (1.34–6.87)**	11.4	3.75 (0.92–15.34)	5.7	1.70 (0.29–9.92)	13.6	3.11 (1.34–7.21)**
Sexual abuse (LTVH)	14.7	22.9	1.55 (0.92–2.60)	23.3	1.82 (0.69–4.83)	22.2	1.45 (0.54–3.87)	23.1	1.51 (0.88–2.60)
Neglect (CTS)	59.0	69.0	1.58 (1.03–2.40)*	76.5	2.65 (1.10–6.39)*	75.7	3.07 (1.15–8.17)*	67.4	1.44 (0.92–2.26)
Neglect (AH)	59.8	65.0	1.42 (0.95–2.13)	62.9	1.55 (0.69–3.47)	70.3	1.81 (0.77–4.25)	64.6	1.38 (0.90–2.11)
Neglect (CEQ)	40.1	48.1	1.51 (1.0–2.30)*	34.4	0.77 (0.33–1.80)	47.2	1.51 (0.69–3.31)	47.6	1.49 (0.96–2.33)
Was CPS ever concerned?	7.4	16.7	2.51 (1.31–4.83)**	20.6	3.83 (1.32–11.16)**	18.9	4.76 (1.48–15.34)**	15.7	2.27 (1.14–4.52)*
Any of the above	90.0	90.2	1.13 (0.59–2.15)	91.4	1.54 (0.42–5.75)	89.2	1.12 (0.29–4.34)	90.9	1.23 (0.61–2.45)

*P < 0.05; **P < 0.01 ***P < 0.001

(37) have four or more reports. There were no differences between G2 individuals with histories of abuse and/or neglect and comparison group members in the chronicity or mean number of reports (abuse/neglect M = 2.64, SD = 2.96; comparison M = 2.37, SD = 2.35).

Because official agency records represent only a portion of child maltreatment that occurs—that is, only that which comes to the attention of the authorities—researchers depend heavily on self-reports by parents or other caregiving adults for information about whether they have abused or neglected their children or someone else's children. The top of Table 2 shows our results based on G2 parents' self-reports of perpetrating physical and sexual abuse and neglect. In contrast to the results in Table 1, Table 2 shows that G2 individuals with documented histories were not more likely to report that they had physically or sexually abused their children. G2 parents with histories of childhood abuse/neglect (and those with histories of neglect) reported that they had engaged in behaviors that are considered neglectful more often than comparison parents. This increased risk for neglect (based on one of the two measures used) was found for the maltreated group overall (41.7% versus 29.0%, respectively; AOR = 1.83, P < 0.001) and those with histories of neglect (42.7% versus 29.0%, AOR = 1.92, P < 0.001). The bottom part of Table 2 shows that there were no significant differences in the extent of physical and sexual abuse reported by G2 nonparents (abuse/neglect versus comparisons).

During earlier waves of the study, we asked G2 participants whether they had experienced a variety of stressful life events during the past year. This information was collected during interviews when the G2 abused/neglected individuals and matched comparisons were mean age 29.2 (1989 to 1995), mean age 40.5 (2003 to 2005), and mean age 47.1 (2009 to 2010). Table 3 shows that at approximate age 29, almost 5% of G2 individuals with documented histories of childhood abuse and/or neglect (AOR = 3.85, 95% CI = 1.44 to 10.29, P < 0.01) and 5.7% of G2 with histories of neglect (AOR = 4.53, 95% CI = 1.68 to 12.21, P < 0.001) reported having had a child placed in the custody of the courts during the past year, compared with 1.6% of the comparisons

Approximately 12 years later, G2 adults with histories of abuse/neglect overall and neglect specifically were again more likely to report having a child placed in custody of the courts within the past year (4.8%, AOR = 3.77, 95% CI = 1.25 to 1.35, P < 0.05, and 5.6%, AOR = 4.29, 95% CI = 1.46 to 13.46, P < 0.01, respectively), compared with 1.3% of the controls. In the last interview (mean age 47), the G2 groups did not differ significantly, although twice as many G2 individuals with histories of abuse/neglect and neglect in particular reported having a child placed in the custody of the courts.

Thus far, the information presented has focused on the G2 parent generation. Because one might be skeptical of abusive parents' willingness to report on their own behavior, it was important to have an additional assessment based on reports by G3 offspring of these individuals, along with official CPS reports. We used multiple self-report measures of physical abuse, sexual abuse, and neglect (see the supplementary materials for more detail) to ascertain whether the G3 offspring of individuals with documented histories of childhood abuse and neglect compared to offspring of nonmaltreated comparisons reported having been abused or neglected (see Table 4). G3 offspring of G2 parents with any history of abuse and/or neglect and neglect were significantly more likely to report having been sexually abused on one

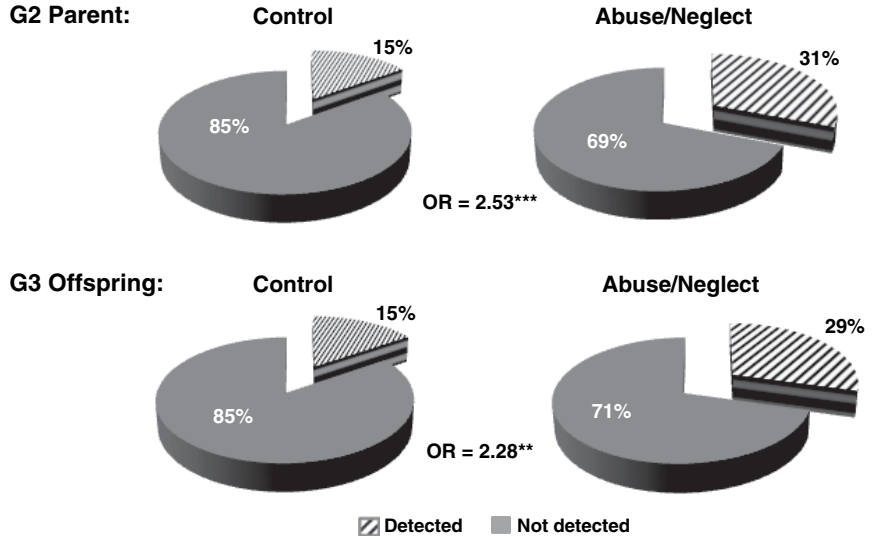

Fig. 1. Rates of child protective system detection among G2 parents who report engaging in, and G3 offspring who report being the victim of, child abuse and/or neglect.

of three measures, compared with reports by G3 offspring of parents without such histories. G3 offspring of G2 parents with histories of abuse/neglect overall and histories of physical and sexual abuse reported higher rates of being neglected than controls.

The bottom of Table 4 shows that more than twice as many of the G3 offspring of previously maltreated G2 individuals answered affirmatively to a question about whether "CPS was ever concerned about you" (16.7% of the G3 offspring of G2 abused/neglected individuals compared with 7.4% of the comparison group offspring, AOR = 2.51, 95% CI = 1.31 to 4.83, $P < 0.01$). G3 offspring of G2 parents with all three types of maltreatment were also more likely to report that CPS was concerned about them (G3 offspring of G2 parents with histories of physical abuse = 20.6%, sexual abuse = 18.9%, and neglect = 15.7% compared with 7.4% of the comparison group offspring).

Finally, because of concerns about a possible detection or surveillance bias that may occur with increased surveillance of families involved with CPS, we also examined the extent to which participants (G2 and G3) who self-report child maltreatment have a CPS report. Presumably, because these individuals have reported that they either engaged in child maltreatment (G2 parents) or were the victim of child maltreatment (G3 offspring), we should expect approximately equal rates of official CPS reports, even though the concordance between self-reports and CPS reports is expected to be low (*27*, *28*). Figure 1 shows that the detection rates for maltreatment are not equivalent across the groups. G2 parents with documented histories of childhood abuse and neglect are two and a half times more likely to have a CPS report than comparison parents (30.9% versus 15.0%, AOR = 2.53, 95% CI = 1.53 to 4.13, $P = 0.000$), suggesting a detection or surveillance bias. Similarly, among the G3 offspring who reported being abused or neglected, 29.3% of those whose parents had documented histories of childhood abuse or neglect were detected (that is, had an official CPS report), compared with 15.4% of the comparison group (whose parents did not have documented histories of childhood abuse or neglect), with an AOR = 2.28, 95% CI = 1.32 to 3.79, $P < 0.003$.

These findings suggest that our understanding of the intergenerational transmission of child abuse and neglect is more complex and challenging than expected. G2 parents with histories of childhood abuse or neglect are more likely to have G3 children who are reported to CPS agencies. Parents with histories of childhood abuse and neglect are more likely to report neglect of their offspring, but not physical or sexual abuse, compared to parents without documented histories of abuse and neglect. Offspring of parents with histories of childhood abuse and neglect are more likely to report being sexually abused and neglected. However, differences in these results make clear that the substance and extent of the intergenerational transmission of abuse and neglect depend in large part on the source of the information used to assess maltreatment. Having only one source of information may lead to incorrect conclusions.

The strongest evidence for the intergenerational transmission of maltreatment indicates that offspring are at risk for neglect and sexual abuse. Contrary to most theories, we found little evidence of the intergenerational transmission of physical abuse. Our findings were consistent across sources (G2 parent self-reports, G3 offspring reports, and CPS reports) that individuals with histories of child maltreatment were not at increased risk to physically abuse their children. Some have speculated that public education efforts to call attention to physical abuse and corporal punishment have had an effect on society and attitudes toward abuse (*29*) or, at a minimum, that these efforts have had an effect on willingness to report physical abuse. There is also trend data showing decreases in rates of physical abuse in national statistics (*30*). On the other hand, given that we found an increased risk for sexual abuse and neglect, it is not immediately apparent why these types of child maltreatment would not be subject to the same societal changes or attitudes.

Although there are numerous strengths associated with this research, several caveats need to be kept in mind. G2 abuse and neglect cases in this study were identified through official records from 40 years ago and represent children whose cases were processed through the courts. Many cases are not reported and never come to the attention of the authorities. Also, the abuse/neglect cases and comparisons in this study are predominantly from lower socioeconomic strata, and the association between poverty and child maltreatment (*31*) may in part explain the high rates of maltreatment in the sample in general. Thus, these findings may not be generalizable to unreported cases of abuse and neglect and to children from middle- or upper-class families who were abused or neglected. However, these results suggest the need for expanded prevention services and parent support within low-income communities. These findings are also not generalizable to abused and neglected children who were adopted in infancy or early childhood, because these cases were excluded from the sample. It is also possible that these findings represent an underestimate of the extent of child abuse and neglect perpetration, given that we may have missed older or sealed cases or cases that were lost over time. Finally, we are not able to report on the extent to which genetic factors may contribute to the intergenerational transmission of child abuse and neglect.

It is not easy to determine causality for any human behavior, especially in the natural environment, where, in contrast to the laboratory, comparisons are not easy to achieve. However, results based on this study's cohort design lead us to conclude that further research is needed to understand the mechanisms underlying the intergenerational transmission of neglect and sexual abuse. These findings also have implications for child protective service systems that may be disproportionately scrutinizing families with past histories of child maltreatment, while overlooking instances of child abuse and neglect among families in the broader public. Research is needed to understand whether these families present more opportunities for intervention (e.g., are using more services) or whether they are truly more dysfunctional.

REFERENCES AND NOTES

1. J. Garbarino, J., G. Gilliam, *Understanding Abusive Families* (Lexington Books, Lexington, MA, 1980).
2. R. S. Kempe, C. H. Kempe, *Child Abuse* (Fontana, London, 1978).
3. B. F. Steele, C. B. Pollock, in *The Battered Child Syndrome*, R. Helfer, C. Kempe, Eds. (Univ. of Chicago Press, Chicago, 1968), pp. 103–145.
4. L. J. Berlin, K. Appleyard, K. A. Dodge, *Child Dev.* **82**, 162–176 (2011).
5. L. Dixon, K. Browne, C. Hamilton-Giachritsis, *J. Child Psychol. Psychiatry* **46**, 47–57 (2005).

6. B. Egeland, D. Jacobvitz, K. Papatola, in *Child Abuse and Neglect: Biosocial Dimensions*, R. J. Gelles, J. B. Lancaster, Eds. (Transaction Publishers, Piscataway, NJ, 1987), pp. 255–276.
7. R. S. Hunter, N. Kilstrom, *Am. J. Psychiatry* **136**, 1320–1322 (1979).
8. K. C. Pears, D. M. Capaldi, *Child Abuse Negl.* **25**, 1439–1461 (2001).
9. R. Thompson, *J. Trauma Pract.* **5**, 57–72 (2006).
10. T. P. Thornberry, *Criminology* **47**, 297–325 (2009).
11. W. A. Altemeier, S. O'Connor, K. B. Sherrod, D. Tucker, P. Vietze, *Child Abuse Negl.* **10**, 319–330 (1986).
12. L. M. Renner, K. S. Slack, *Child Abuse Negl.* **30**, 599–617 (2006).
13. P. Sidebotham, J. Golding, ALSPAC Study Team, Avon Longitudinal Study of Parents and Children, *Child Abuse Negl.* **25**, 1177–1200 (2001).
14. C. S. Widom, *Am. J. Orthopsychiatry* **59**, 355–367 (1989).
15. I. O. Ertem, J. M. Leventhal, S. Dobbs, *Lancet* **356**, 814–819 (2000).
16. S. D. Herzberger, *Am. Behav. Sci.* **33**, 529–545 (1990).
17. L. Falshaw, K. D. Browne, C. R. Hollin, *Aggress. Violent. Behav.* **1**, 389–404 (1996).
18. J. Kaufman, E. Zigler, *Am. J. Orthopsychiatry* **57**, 186–192 (1987).
19. T. P. Thornberry, K. E. Knight, P. J. Lovegrove, *Trauma Violence Abuse* **13**, 135–152 (2012).
20. C. S. Widom, *Psychol. Bull.* **106**, 3–28 (1989).
21. A. Bandura, *Aggression: A Social Learning Analysis* (Prentice-Hall, Englewood Cliffs, NJ, 1973).
22. K. A. Dodge, J. E. Bates, G. S. Pettit, *Science* **250**, 1678–1683 (1990).
23. J. M. Leventhal, *Child Abuse Negl.* **6**, 113–123 (1982).
24. F. Schulsinger, S. A. Mednick, J. Knop, *Longitudinal Research: Methods and Uses in Behavioral Sciences* (Martinus Nijhoff Publishers, Boston, 1981).
25. C. S. Widom, *Science* **244**, 160–166 (1989).
26. CPS is the unit within a government agency that responds to reports of child abuse or neglect. It typically falls within a state's division of social services or department of children and family services. CPS units were first established in 1974 in response to the Federal Child Abuse Prevention and Treatment Act (CAPTA: Public Law 93-247) that provided funding for federal and state child maltreatment research and services. CAPTA mandated all states to establish procedures to investigate suspected incidents of child maltreatment in order to prevent, identify, and treat child abuse and neglect. A report must be made when an individual knows or has reasonable cause to believe or suspect that a child has been subjected to abuse or neglect.
27. J. Brown, P. Cohen, J. G. Johnson, S. Salzinger, *Child Abuse Negl.* **22**, 1065–1078 (1998).
28. M. D. Everson *et al.*, *Child Maltreat.* **13**, 14–26 (2008).
29. M. A. Straus, R. J. Gelles, *J. Marriage Fam.* **48**, 465–479 (1986).
30. D. Finkelhor, L. M. Jones, "Have sexual abuse and physical abuse declined since the 1990s?" (University of New Hampshire, Crimes Against Children Research Center, 2012).
31. A. J. Sedlak *et al.*, *Fourth National Incidence Study of Child Abuse and Neglect (NIS–4): Report to Congress, Executive Summary* (Administration for Children and Families, U.S. Department of Health and Human Services, Washington, DC, 2010).

ACKNOWLEDGMENTS

This research was supported in part by grants from the Eunice Kennedy Shriver National Institute of Child Health and Human Development (HD40774), the National Institute of Justice (86-IJ-CX-0033 and 89-IJ-CX-0007), the National Institute of Mental Health (MH49467 and MH58386), the National Institute on Drug Abuse (DA17842 and DA10060), the National Institute on Alcohol Abuse and Alcoholism (AA09238 and AA11108), and the Doris Duke Charitable Foundation. The opinions, findings, and conclusions or recommendations expressed in this paper are those of the authors and do not necessarily reflect those of the funding agencies.

SUPPLEMENTARY MATERIALS

www.sciencemag.org/content/347/6229/1480/suppl/DC1
Materials and Methods
Tables S1 to S4
References (*32*–*52*)

12 August 2014; accepted 18 February 2015
10.1126/science.1259917

SNARE PROTEINS

Spring-loaded unraveling of a single SNARE complex by NSF in one round of ATP turnover

Je-Kyung Ryu,[1,2]* Duyoung Min,[1,2]* Sang-Hyun Rah,[1,2]* Soo Jin Kim,[3] Yongsoo Park,[4] Haesoo Kim,[3] Changbong Hyeon,[5] Ho Min Kim,[3] Reinhard Jahn,[4]† Tae-Young Yoon[1,2]†

During intracellular membrane trafficking, *N*-ethylmaleimide-sensitive factor (NSF) and alpha-soluble NSF attachment protein (α-SNAP) disassemble the soluble NSF attachment protein receptor (SNARE) complex for recycling of the SNARE proteins. The molecular mechanism by which NSF disassembles the SNARE complex is largely unknown. Using single-molecule fluorescence spectroscopy and magnetic tweezers, we found that NSF disassembled a single SNARE complex in only one round of adenosine triphosphate (ATP) turnover. Upon ATP cleavage, the NSF hexamer developed internal tension with dissociation of phosphate ions. After latent time measuring tens of seconds, NSF released the built-up tension in a burst within 20 milliseconds, resulting in disassembly followed by immediate release of the SNARE proteins. Thus, NSF appears to use a "spring-loaded" mechanism to couple ATP hydrolysis and unfolding of substrate proteins.

Soluble *N*-ethylmaleimide-sensitive factor (NSF) attachment protein receptor (SNARE) proteins are the essential molecular machinery for intracellular membrane fusion in eukaryotic cells (*1*). Synaptic exocytosis is among the best studied, in which synaptic vesicle–associated VAMP2 engages with syntaxin-1A and SNAP-25 on the presynaptic membrane to form the neuronal SNARE complex (*2*, *3*). Although the formed SNARE complex is very stable after synaptic vesicle fusion (*4*–*6*), the complex must be disassembled for reuse of the SNARE proteins, requiring a specialized molecular machinery, consisting of NSF and alpha-soluble NSF attachment protein (α-SNAP) (*7*–*12*).

NSF belongs to the type II adenosine triphosphatase associated with various cellular activities (AAA+) family, which assembles into a homohexamer (*13*–*15*). Despite the fundamental role of NSF in synaptic transmission (*7*, *9*, *16*), surprisingly little is known about how its adenosine triphosphate (ATP) hydrolysis cycle is coupled to disassembly of the SNARE complex. The NSF hexamer may disassemble a SNARE complex by unwinding it in a processive manner, similar to translocation of AAA+ adenosine triphosphatases (ATPases) on DNA or peptide substrates (*17*, *18*). Alternatively, NSF may exploit a critical conformational transition to evoke the disassembly of the SNARE complex largely in one step (*19*). It is not clear how many cycles of ATP hydrolysis are needed and how these cycles are organized to disassemble the extraordinarily stable SNARE complex.

To gain insight into these questions, we first formed single SNARE complexes on surface-immobilized vesicles (*20*, *21*), which were observed as single-molecule fluorescence spots when viewed with total internal reflection (TIR) microscopy (Fig. 1, A and B, and fig. S1). Here the soluble part of VAMP2 was used and labeled with the Cy3 dye. We subsequently injected α-SNAP and then the NSF hexamers (*2*, *11*, *12*) along with ATP and Mg^{2+} ions (Fig. 1, A and C, and fig. S1A). After 5 min of reaction, we counted the number of fluorescence spots.

We observed that the fluorescence spots disappeared only when α-SNAP, NSF, ATP, and Mg^{2+} were added (Fig. 1, B and D). When any one component was missing or either nonhydrolyzable ATPγS or α-SNAP L294A mutant that abolished ATP hydrolysis in NSF (*22*) was used, no disappearance of Cy3-labeled spots was observed (Fig. 1D). Thus, the disappearance of Cy3 spots strictly depended on the presence of both α-SNAP and NSF and also on ATP hydrolysis by NSF, indicating that the disassembly of single SNARE complexes induced by NSF and α-SNAP was reconstituted on our single-molecule fluorescence microscope.

We next attempted to differentiate between NSF binding and ATP hydrolysis. This time, we introduced NSF with ATP and EDTA to induce ATP-dependent NSF binding but without hydrolysis of ATP molecules (Fig. 1E). Using labeled antibodies, we were able to confirm sequential binding of α-SNAP and NSF (Fig. 1, F and G, and fig. S2, A to C). After formation of the immobilized 20*S* complexes (NSF/α-SNAP/SNARE complex), we performed washing and injected Mg^{2+} and ATP. We observed disassembly of single SNARE complexes, indicating that single NSF-binding

[1]National Creative Research Initiative Center for Single-Molecule Systems Biology, Korea Advanced Institute of Science and Technology (KAIST), Daejeon 305-701, South Korea. [2]Department of Physics, KAIST, Daejeon 305-701, South Korea. [3]Graduate School of Medical Science and Engineering, KAIST, Daejeon 305-701, South Korea. [4]Department of Neurobiology, Max-Planck-Institute for Biophysical Chemistry, 37077 Göttingen, Germany. [5]Korea Institute for Advanced Study, Seoul 130-722, South Korea.
*These authors contributed equally to this work. **†Corresponding author. E-mail: rjahn@gwdg.de (R.J.); tyyoon@kaist.ac.kr (T.-Y.Y.)**

was sufficient for the disassembly (Fig. 1H). Moreover, we observed the SNARE complex disassembly when we injected only Mg^{2+} ions (Fig. 1H). Because free ATP molecules were completely removed before Mg^{2+} injection, the disassembly was exclusively mediated by hydrolysis of the ATP molecules already bound to NSF. By imaging disassembly with high temporal resolution (fig. S2, F and G), we confirmed that the disassembly using only one-round ATP turnover was as fast as that observed in the presence of excess NSF and ATP (Fig. 1I). Thus, binding of a single NSF hexamer and only one round of ATP hydrolysis in NSF was sufficient for disassembly of a single neuronal SNARE complex.

To explore how such a tight coupling between ATP hydrolysis and NSF activity can be achieved, we used single-molecule fluorescence resonance energy transfer (FRET) (*23*). We labeled either the N- or C-terminal end of the SNARE motif with the Cy3-Cy5 pair (Fig. 2A and fig. S3). We observed that α-SNAP induces destabilization of the C-terminal part of the SNARE complex, albeit to different extents for individual SNARE complexes (fig. S4) (*11*, *24*). Next, we added NSF and followed the protocol, allowing only one round of ATP hydrolysis (Fig. 2B). Notably, when we measured FRET at the C-terminal end ($E_{C\text{-term}}$), the donor and acceptor fluorescence signals initially remained stationary and then disappeared all of a sudden (Fig. 2, C and D, and fig. S5). Such behavior was found in more than 96% of the entire time-resolved traces even when the traces started

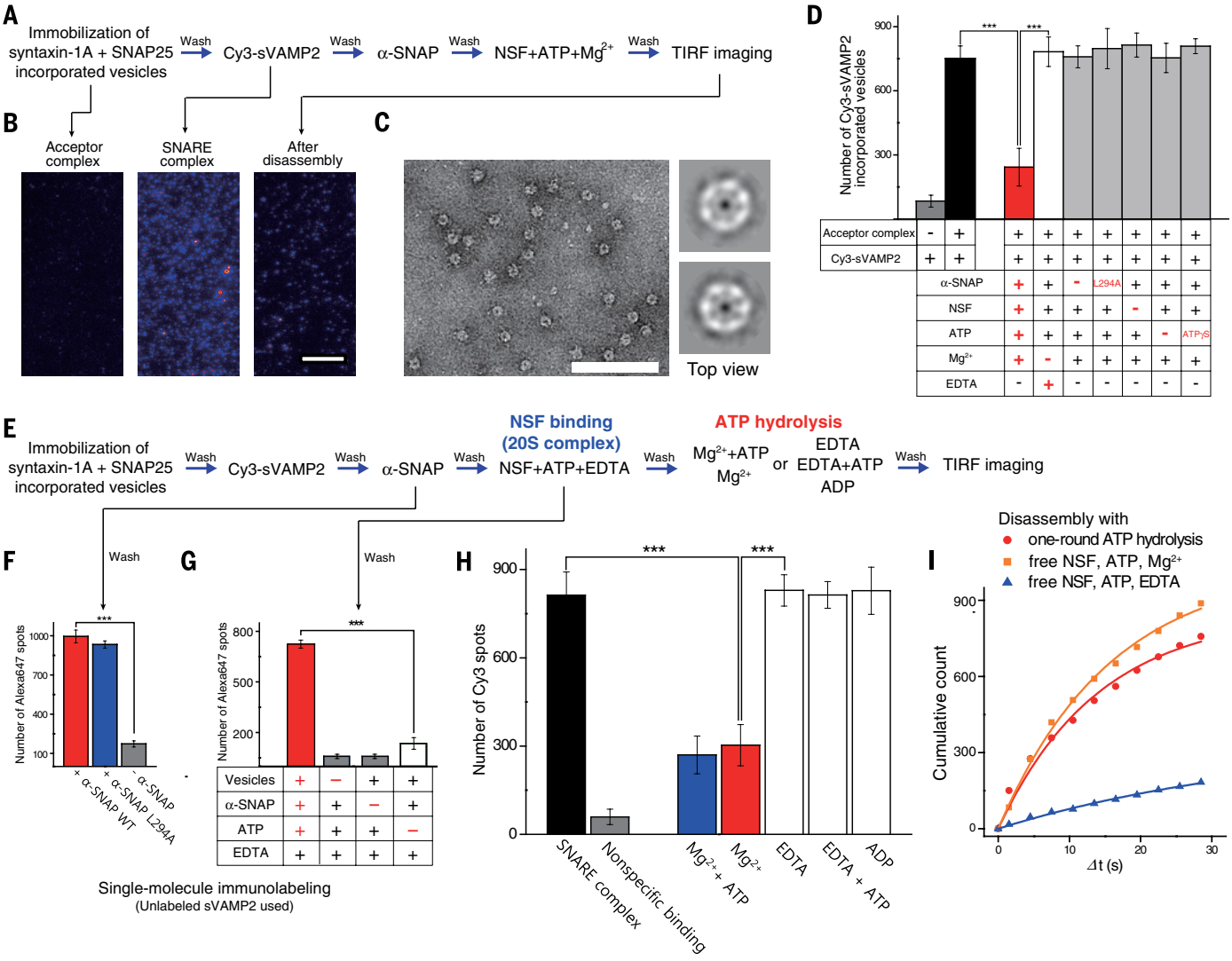

Fig. 1. Reconstitution of NSF-mediated SNARE complex disassembly on a single-molecule fluorescence microscope. (**A**) Procedure of the experiment. (**B**) Exemplary TIR microscopy images after immobilization of acceptor vesicles (left), after SNARE complex formation (middle), and after disassembly reaction (right). Scale bar, 10 μm. (**C**) NSF imaged using negative stain electron microscopy (left). Scale bar, 100 nm. Representative two-dimensional class averages (right). Top views are shown. (**D**) Number of surface vesicles containing Cy3-sVAMP2 measured with various components of the disassembly reaction. (Left) Nonspecific binding of sVAMP2 in the absence of acceptor vesicles (dark gray). Disassembly (loss of fluorescence) is observable only when all components required for disassembly are present (red bar). ***$P < 0.001$, assessed using the paired t test, and all the errors are SD ($n \geq 20$ TIR images) unless otherwise specified. (**E**) Procedure to allow for one-round ATP hydrolysis during the disassembly reaction. (**F** and **G**) Single-molecule immunolabeling assays for confirmation of α-SNAP-binding (F) and NSF-binding (G). Number of Alexa647 spots measured after incubation with the depicted components of the disassembly reaction. (**H**) Number of vesicles containing Cy3-sVAMP2 measured after SNARE complex formation (black), nonspecific binding of Cy3-sVAMP2 (gray), and after the experimental protocol in (E) with Mg^{2+} and ATP (blue) or with Mg^{2+} (red). Other bars indicate control experiments where, instead of Mg^{2+}, either EDTA only, EDTA and ATP, or ADP (white) were injected during the ATP hydrolysis step. (**I**) Cumulative distributions of Δt for disassembly under conditions of one round of ATP hydrolysis and in the presence of excess NSF, ATP, and Mg^{2+}. Δt was measured from $t = 0$ to the event of stepwise fluorescence decrease (fig. S2, F and G). Fitting of the distributions using a single exponential function gives time constants of 15.8 ± 1.1 s and 14.1 ± 1.9 s for disassembly with one-round ATP hydrolysis and free NSF, ATP, and Mg^{2+}, respectively.

from a high FRET state (Fig. 2E and fig. S6). Thus, after a quiescent waiting time, the SNARE complex was disassembled in one step, and the Cy3-labeled sVAMP2 was immediately released from the 20*S* complex after disassembly. We repeated the time-resolved measurements with the N-terminal FRET pair ($E_{N\text{-term}}$), and 95% of the real-time traces showed the one-step disassembly pattern (Fig. 2E and fig. S5). We also observed disassembly in the presence of free NSF and ATP. For both N- and C-terminal FRET pairs, the traces predominantly showed the one-step disassembly (Fig. 2E and fig. S5). Finally, we observed disassembly of the SNARE complexes in their native configuration, with both syntaxin-1A and full-length VAMP2 anchored to the same membrane (Fig. 2F and fig. S7). Once again, one-step disassembly comprised ~90% of the total traces obtained during both disassembly via one-round ATP hydrolysis and with free NSF and ATP (Fig. 2G and fig. S8). Thus, the NSF hexamer disassembled the entire SNARE complex in a single burst and released the disassembled, individual SNARE components immediately after disassembly.

Next, we wanted to gain more mechanistic insights into the disassembly reaction using single-molecule force spectroscopy (*4*, *25*–*27*). While pulling a single SNARE complex with 3.9 pN force, we introduced α-SNAP followed by a mixture of NSF, ATP, and Mg^{2+} ions (Fig. 3, A to C, and figs. S9 to S13). Upon addition of α-SNAP and NSF, the extension was largely maintained at the same level, although the distribution became broader and the extension peak was slightly shifted to higher values (Fig. 3D). Notably, in about half of all experiments, the connection was lost abruptly with a characteristic latency of 71.4 s. (Fig. 3A, red arrow, and fig. S14). Such abrupt disappearance of the signal indicates that the tweezed SNARE complex was disassembled within our time resolution (16.7 ms) and the disassembled SNARE proteins were immediately released from the 20*S* complex, concordant with our single-molecule FRET data. In the other half of the traces, the extension value showed a sudden increase and stayed there for a few seconds before complete release (Fig. 3B). The extension burst corresponded to disassembly up to the N-terminal end of the SNARE motif and was completed within 21.8 ms (Fig. 3E, pink distributions, and fig. S15). Thus, we conclude that virtually in all the observed traces, the SNARE complex was disassembled by NSF in one step even when resolved at a time resolution of 16.7 ms. Finally, we observed rare events where the SNARE complex showed repetitive unzipping and rezipping (Fig. 3C), giving a hint as to why it is important to instantly release the SNARE proteins after the disassembly. The repeated failures suggest either that some SNARE complexes are more difficult to unzip or that certain 20*S* complexes show a looser coupling between ATP hydrolysis in NSF and SNARE complex disassembly.

The question then arises how exactly the burst disassembly is coupled to the steps of the given, single ATP hydrolysis cycle. To answer this final question, we replicated our disassembly experiment with one difference: that free phosphate ions (Pis) or Pi analogs were added along with Mg^{2+} ions (Fig. 4A). Addition of free Pis up to 10 mM only minimally affected disassembly (Fig. 4B). However, a Pi analog, orthovanadate (VO_4^{3-}), significantly inhibited the disassembly at 1 μM concentration (Fig. 4C). Addition of a different Pi analog, 10 μM AlFx, also inhibited disassembly. In addition, 1 μM VO_4^{3-} impeded the disassembly of the SNARE complexes with full-length VAMP2 (Fig. 4, D and E). Given that the Pi analogs used here (but not Pi) selectively stabilize a transition state containing adenosine diphosphates (ADPs) (*28*, *29*),

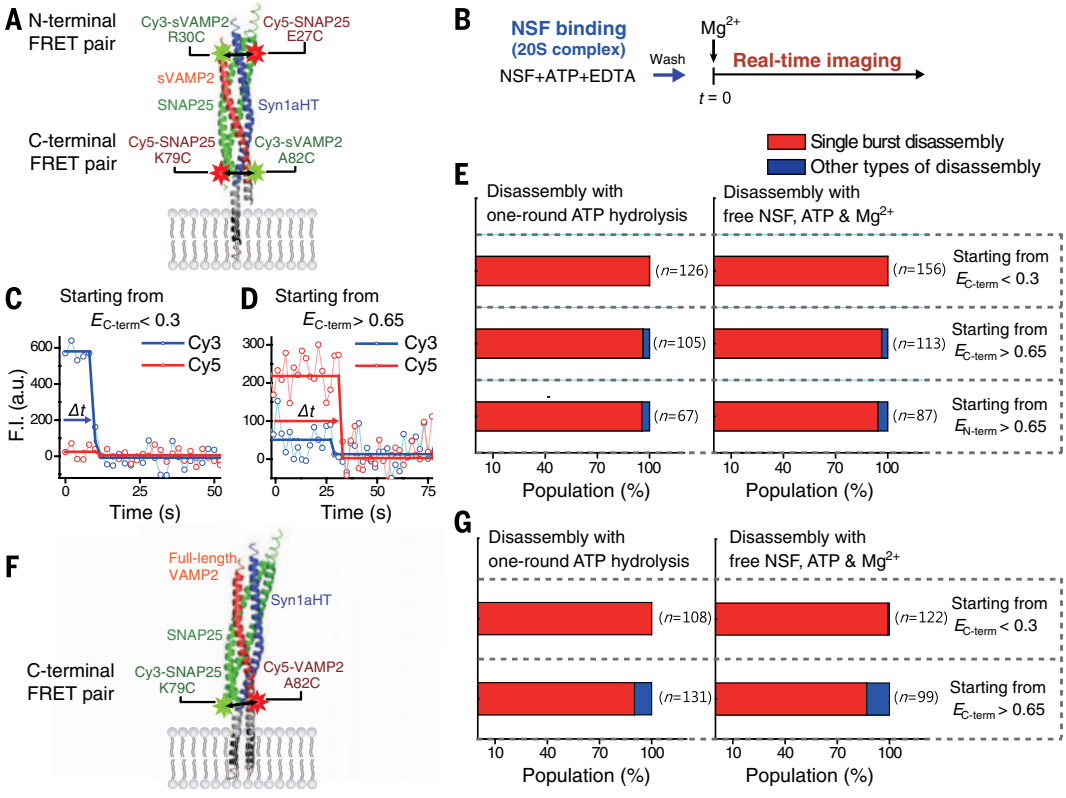

Fig. 2. Intermediates of NSF/α-SNAP disassembly of SNARE complex monitored by single-molecule FRET. (**A**) Labeling positions of Cy3 and Cy5 on either the N-terminal or the C-terminal end of the SNARE complex. According to the crystal structure (*3*), the expected distance between two dyes is less than 1.4 nm for both cases. (**B**) Experimental procedure. NSF, ATP, and EDTA were injected into the chamber containing α-SNAP-SNARE complexes. Movies were recorded starting at the same time as the injection of Mg^{2+}. (**C** and **D**) Representative disassembly traces of C-terminal FRET pairs starting from low FRET (<0.3) (C) and high FRET (>0.65) (D). (**E**) Relative abundance of disassembly events classified as single burst (red) and other types (blue). Disassembly was carried out under one-round ATP hydrolysis condition (left) or with excess NSF, ATP, and Mg^{2+} (right). (**F**) Labeling positions of Cy3 and Cy5 on the C-terminal end of the SNARE complex with full-length VAMP2. (**G**) Relative abundance of disassembly events classified as single burst (red) and other types (blue) using C-terminal FRET of SNARE complex with full-length VAMP2.

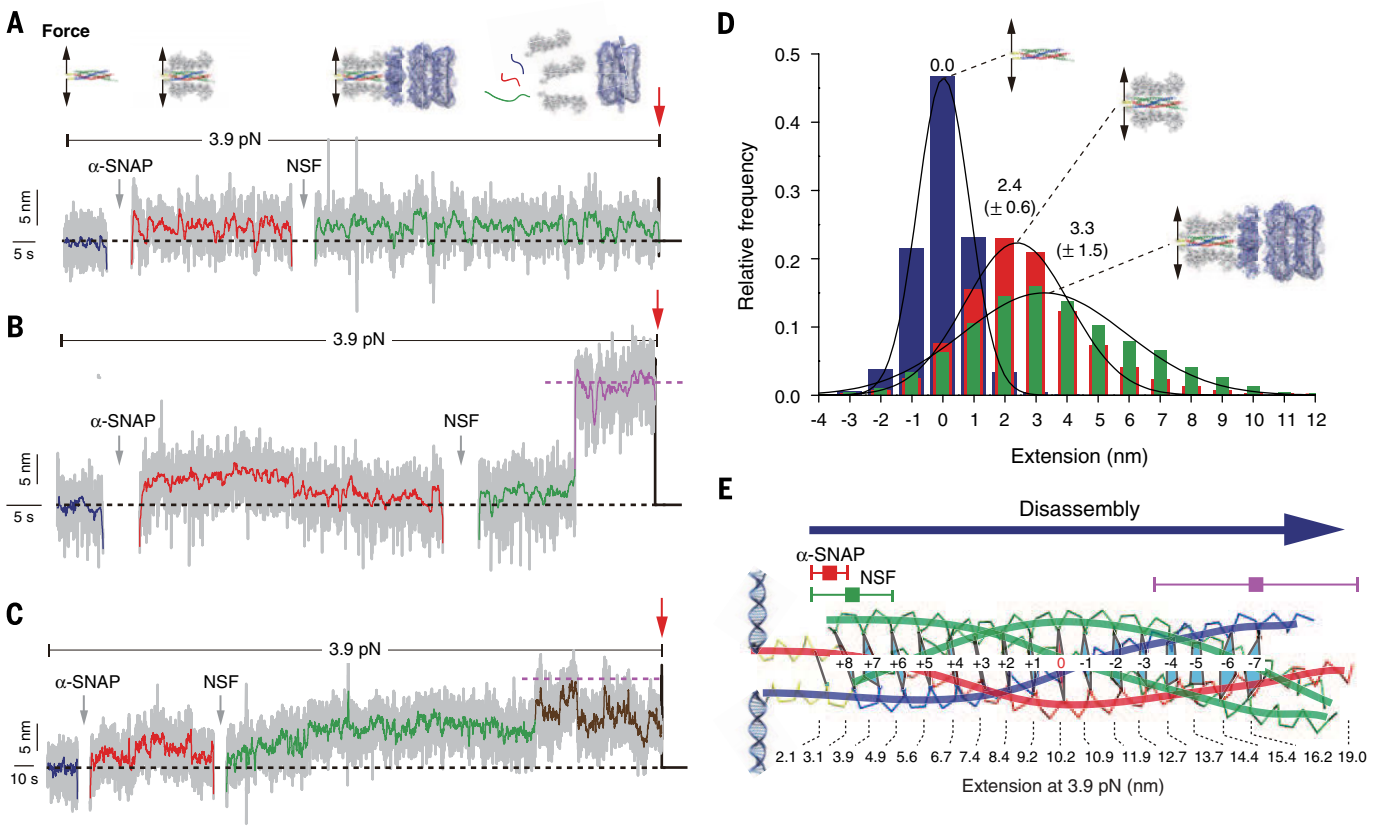

Fig. 3. Observation of NSF-mediated SNARE-complex disassembly with single-molecule magnetic tweezers. (**A** to **C**) Representative real-time traces showing destabilization and disassembly of SNARE complexes driven by α-SNAP and NSF. The traces are categorized according to the disassembly types: complete disassembly within a temporal resolution of 16.7 ms (A), almost complete disassembly but with a few seconds delay before the final release (B), and repetitive unzipping of almost full SNARE complex before the final release (C). Pink dotted lines in (B) and (C) denote the fully unzipped state up to the seventh layer. (**D**) Extension distributions of the sequential stages colored as blue, red, and green in the extension traces of (A) to (C) (n = 23 traces). (**E**) Structure diagram of the SNARE complex mapping the extension changes onto the corresponding positions in the structure. When a SNARE complex is unzipped to specific layers at 3.9 pN, the expected extension values are estimated with the wormlike chain model (shown at the bottom) (table S1). The positions of destabilizations (red for α-SNAP only and green for α-SNAP/NSF) and the position after the disassembly step (pink) are shown.

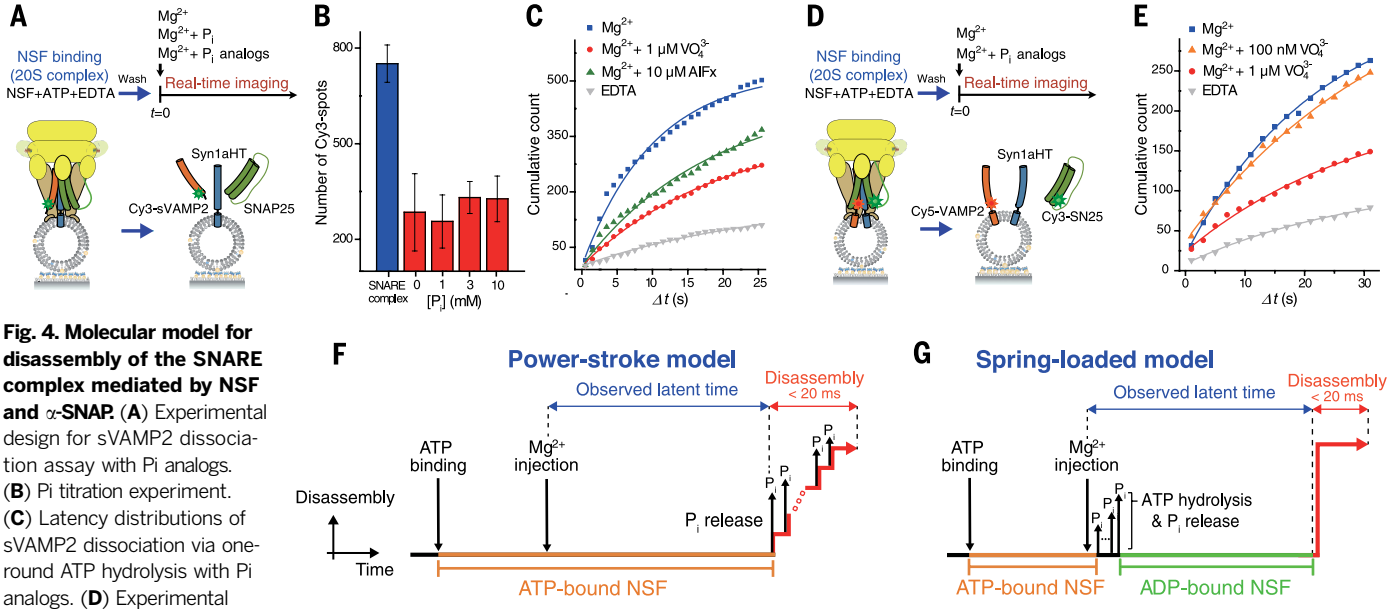

Fig. 4. Molecular model for disassembly of the SNARE complex mediated by NSF and α-SNAP. (**A**) Experimental design for sVAMP2 dissociation assay with Pi analogs. (**B**) Pi titration experiment. (**C**) Latency distributions of sVAMP2 dissociation via one-round ATP hydrolysis with Pi analogs. (**D**) Experimental design for SNAP-25 dissociation from the SNARE complex with full-length VAMP2 with Pi analogs. (**E**) Latency distributions of SNAP-25 dissociation with Pi analogs. (**F**) and (**G**) Mechanochemical model of the dwell-burst disassembly process for the power-stroke model (F) and the spring-loaded model (G).

we suggest that NSF is overall bound with ADP during the latent time before disassembly.

Our observations suggest two alternative models for the NSF function (fig. S16). First, the disassembly is precisely coupled to the release of Pis, which is also the force-generating step for the translocational motion of ClpXP and φ29 (*17*, *30*). In this "power-stroke" model, release of Pis from the subunits of NSF can occur in a predetermined order (*18*, *30*), which may be viewed as processive unwinding of the SNARE complex (Fig. 4F). The second model implies that ATP hydrolysis and Pi release need to be completed first to initiate disassembly. Because the SNARE complex resists disassembly, NSF is trapped in the conformation of the ATP-bound state while it is actually bound to ADP. Mechanical tension develops within the NSF hexamer and then is delivered to the SNARE complex. In this "spring-loaded" model, NSF tears the SNARE complex into individual SNARE proteins upon brief destabilization of the SNARE complex by thermal fluctuations (Fig. 4G).

These two models are distinguished by the type of nucleotides bound to NSF during the latent time before disassembly. In the power-stroke model, the NSF hexamer will remain in the ATP-bound state, whereas in the spring-loaded model, NSF will be essentially bound to ADP during the latent time (Fig. 4, F and G). Our experimental data, in particular those using Pi analogs, favor the spring-loaded model for the NSF function. With the spring-loaded model, NSF takes advantage of thermal fluctuations, eventually unraveling the target SNARE complex if a long latent time is given (fig. S17). We presume that the Pi analogs diminish the internal strain in the 20*S* complex and impede the disassembly process. We cannot rule out the possibility that the Pi analogs negatively affect the 20*S* particles in a way other than described here. Detailed conformational changes involved in disassembly remain unclear (*31*). Because the AAA domains are highly conserved, the spring-loaded mechanism elucidated here for NSF may be shared by many other AAA+ ATPases, which provides a way to tightly couple their ATP hydrolysis and unfolding of protein substrates.

REFERENCES AND NOTES

1. T. Söllner *et al.*, *Nature* **362**, 318–324 (1993).
2. P. I. Hanson, R. Roth, H. Morisaki, R. Jahn, J. E. Heuser, *Cell* **90**, 523–535 (1997).
3. R. B. Sutton, D. Fasshauer, R. Jahn, A. T. Brunger, *Nature* **395**, 347–353 (1998).
4. D. Min *et al.*, *Nat. Commun.* **4**, 1705 (2013).
5. Y. Gao *et al.*, *Science* **337**, 1340–1343 (2012).
6. F. Li *et al.*, *Nat. Struct. Mol. Biol.* **14**, 890–896 (2007).
7. D. W. Wilson *et al.*, *Nature* **339**, 355–359 (1989).
8. S. W. Whiteheart *et al.*, *Nature* **362**, 353–355 (1993).
9. T. Söllner, M. K. Bennett, S. W. Whiteheart, R. H. Scheller, J. E. Rothman, *Cell* **75**, 409–418 (1993).
10. U. Winter, X. Chen, D. Fasshauer, *J. Biol. Chem.* **284**, 31817–31826 (2009).
11. L. F. Chang *et al.*, *Nat. Struct. Mol. Biol.* **19**, 268–275 (2012).
12. A. Moeller *et al.*, *J. Struct. Biol.* **177**, 335–343 (2012).
13. C. U. Lenzen, D. Steinmann, S. W. Whiteheart, W. I. Weis, *Cell* **94**, 525–536 (1998).
14. R. C. Yu, P. I. Hanson, R. Jahn, A. T. Brünger, *Nat. Struct. Biol.* **5**, 803–811 (1998).
15. E. E. Nagiec, A. Bernstein, S. W. Whiteheart, *J. Biol. Chem.* **270**, 29182–29188 (1995).
16. C. Zhao, E. A. Matveeva, Q. Ren, S. W. Whiteheart, *J. Biol. Chem.* **285**, 761–772 (2010).
17. M. E. Aubin-Tam, A. O. Olivares, R. T. Sauer, T. A. Baker, M. J. Lang, *Cell* **145**, 257–267 (2011).
18. M. Sen *et al.*, *Cell* **155**, 636–646 (2013).
19. E. U. Weber-Ban, B. G. Reid, A. D. Miranker, A. L. Horwich, *Nature* **401**, 90–93 (1999).
20. A. V. Pobbati, A. Stein, D. Fasshauer, *Science* **313**, 673–676 (2006).
21. T. Y. Yoon, B. Okumus, F. Zhang, Y. K. Shin, T. Ha, *Proc. Natl. Acad. Sci. U.S.A.* **103**, 19731–19736 (2006).
22. R. J. Barnard, A. Morgan, R. D. Burgoyne, *J. Cell Biol.* **139**, 875–883 (1997).
23. T. Ha *et al.*, *Proc. Natl. Acad. Sci. U.S.A.* **93**, 6264–6268 (1996).
24. Y. Park *et al.*, *J. Biol. Chem.* **289**, 16326–16335 (2014).
25. W. J. Greenleaf, M. T. Woodside, S. M. Block, *Annu. Rev. Biophys. Biomol. Struct.* **36**, 171–190 (2007).
26. J. R. Moffitt, Y. R. Chemla, S. B. Smith, C. Bustamante, *Annu. Rev. Biochem.* **77**, 205–228 (2008).
27. I. De Vlaminck, C. Dekker, *Annu Rev Biophys* **41**, 453–472 (2012).
28. T. Shimizu, K. A. Johnson, *J. Biol. Chem.* **258**, 13833–13840 (1983).
29. D. R. Davies, W. G. J. Hol, *FEBS Lett.* **577**, 315–321 (2004).
30. Y. R. Chemla *et al.*, *Cell* **122**, 683–692 (2005).
31. M. Zhao *et al.*, *Nature* **518**, 61–67 (2015).

ACKNOWLEDGMENTS

We thank J. Jo and B. Choi for help with preparing illustrations and S. E. Lee for help with single-molecule analysis. This work was supported by the National Creative Research Initiative Program (Center for Single-Molecule Systems Biology to T.-Y.Y.) and a grant (NRF-2012R1A1A1010456 to H.M.K.) through the National Research Foundation of Korea (NRF) funded by the Korean government. Funding was also generously provided by the National Institutes of Health (3P01GM072694-05S1 to R.J.).

SUPPLEMENTARY MATERIALS

www.sciencemag.org/content/347/6229/1485/suppl/DC1
Materials and Methods
Supplementary Text
Figs. S1 to S17
Table S1
References (*32*–*69*)

18 December 2014; accepted 27 February 2015
10.1126/science.aaa5267

INTERNATIONAL COSMOS PRIZE

WHO WILL BE THE NEXT PRIZEWINNER?

We are now calling for recommendations for the 2015 International Cosmos Prize!

- International Cosmos Prize is awarded for excellent research and work that contributes to the development of the concept of Expo '90, "The Harmonious Coexistence between Nature and Mankind".
- The Prize is an annual academic prize presented by the Expo '90 Foundation in Osaka, Japan. The monetary prize is 40 million yen.

1993 Prizewinner
Sir Ghillean Prance
Director, Royal Botanic Gardens, Kew, U.K.
Specialty : Botany

1994 Prizewinner
Dr. Jacques François Barrau (deceased)
Professor, Paris National Museum of Natural History, France
Specialty : Ethnobiology

1995 Prizewinner
Dr. Tatuo Kira (deceased)
Professor Emeritus, Osaka City University, Japan
Specialty : Plant Ecology

1996 Prizewinner
Dr. George Beals Schaller
Director of Science, the Wildlife Conservation Society, U.S.A.
Specialty : Biology

1997 Prizewinner
Dr. Richard Dawkins
Professor, Oxford University, U.K.
Specialty : Evolutionary Biology

1998 Prizewinner
Dr. Jared Mason Diamond
Professor, University of California at Los Angeles, U.S.A.
Specialty : Geographic History

1999 Prizewinner
Dr. Wu Zheng-Yi (deceased)
Professor and Director Emeritus, Kunming Institute of Botany, China
Specialty : Botany

2000 Prizewinner
Sir David Attenborough
Producer, Naturalist, Zoologist, U.K.
Specialty : Zoology, Film producer

2001 Prizewinner
Prof. Anne Whiston Spirn
Professor, Massachusetts Institute of Technology, U.S.A.
Specialty : Landscape Architecture

2002 Prizewinner
The Charles Darwin Research Station
Puerto Ayora, Santa Cruz Island, Galapagos Islands, Ecuador
Specialty : Diverse activities in the Galapagos Islands

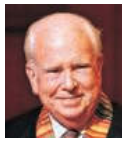

2003 Prizewinner
Dr. Peter Hamilton Raven
Director, Missouri Botanical Garden, U.S.A.
Specialty : Botany

2004 Prizewinner
Prof. Julia Carabias Lillo
Professor, National Autonomous University of Mexico, Mexico
Specialty : Environmental Science

2005 Prizewinner
Dr. Daniel Pauly
Professor and Director, Fisheries Centre, University of British Columbia, Canada
Specialty : Marine Biology

2006 Prizewinner
Dr. Raman Sukumar
Professor, Centre for Ecological Sciences, Indian Institute of Science, India
Specialty : Conservation Ecology

2007 Prizewinner
Dr. Georgina Mary Mace
Professor of Conservation Science and Director of NERC Centre for Population Biology, Imperial College, London, U.K.
Specialty : Conservation Ecology

2008 Prizewinner
Dr. Phan Nguyen Hong
Professor Emeritus, Hanoi National University of Education, Vietnam
Specialty : Conservation Ecology

2009 Prizewinner
Dr. Gretchen Cara Daily
Professor, Stanford University, U.S.A.
Specialty : Environmental Science

2010 Prizewinner
Dr. Estella Bergere Leopold
Professor Emeritus, University of Washington, U.S.A.
Specialty : Paleontology

2011 Prizewinner
Scientific Steering Committee of the Census of Marine Life
Secretariat: Washington, DC, U.S.A.
Specialty : Compiling the Ocean Biogeographic Information System

2012 Prizewinner
Dr. Edward Osborne Wilson
Pellegrino University Research Professor Emeritus at Harvard University, U.S.A.
Specialty : Biology

2013 Prizewinner
Dr. Robert Treat Paine
Professor Emeritus of Zoology, University of Washington, U.S.A.
Specialty : Conservation Ecology

2014 Prizewinner
Dr. Philippe Descola
Professor, the Collège de France, France
Specialty : Anthropology

If you have a candidate whom you would like to recommend, please e-mail us at the address below. We will send you a recommendation form (in Microsoft Word). The deadline for recommendations is April 15.

✔ **Expo '90 Foundation** **E-mail: rec-cosmos@expo-cosmos.or.jp**

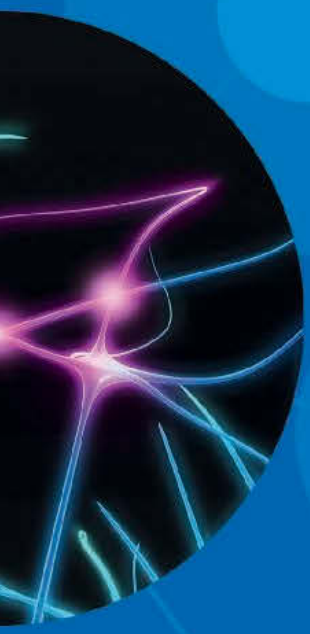

PRIX COUPS D'ÉLAN POUR LA RECHERCHE FRANÇAISE

Now in its 15th year, the Bettencourt Schueller Foundation "Prix Coups d'élan pour la recherche française" has been awarded to four top-performing French laboratories. The prize rewards teams specifically chosen for the promising nature of their research programs. It enables them to optimize their infrastructure (construction / renovation of their premises, the purchasing of new equipment) and to receive practical assistance when required. From the year 2000 onwards, 50 research laboratories, from both the Inserm (French National Institute of Health and Medical Research) and the CNRS (National Center for Scientific Research), have received € 250,000 each. As a direct result, over 500 researchers have been able to benefit from optimal physical working conditions.

Established in 1987 as a public interest foundation, the Bettencourt Schueller Foundation was set up by Liliane, André Bettencourt and their daughter Françoise Bettencourt Meyers, in memory of Eugène Schueller, a renowned researcher and chemist. Its mission is to "take talent to the top", in order to contribute to a stronger French society and boost France's influence on the international stage. This mission is focused on three main areas: life sciences, the arts and the promotion of an inclusive society. Driven by strong convictions, the Foundation's approach and actions serve the common good, thus demonstrating a firm commitment to social responsibility.

Bettencourt Schueller Foundation
27-29 rue des Poissonniers • 92200 Neuilly-sur-Seine • France
www.fondationbs.org • Contact: sciences@fondationbs.org

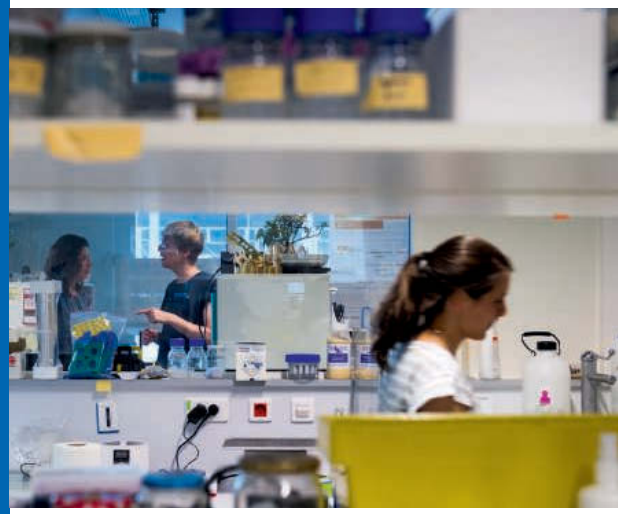

2014 PRIZE WINNER

Chantal Abergel
Giant viruses: Revisiting the concept of virus in the giant virus era

STRUCTURAL AND GENOMIC INFORMATION LABORATORY, MARSEILLE
CNRS / AIX-MARSEILLE UNIVERSITY
FRANCE

Valentina Emiliani
Exploring *in vivo* brain functioning by optogenetic and wavefront shaping

NEUROPHOTONICS LABORATORY, PARIS
CNRS / PARIS DESCARTES UNIVERSITY
FRANCE

Frédéric Saudou
Exploring neuronal mechanisms of Huntington disease

GRENOBLE INSTITUTE OF NEUROSCIENCE
INSERM / JOSEPH FOURIER UNIVERSITY / UNIVERSITY HOSPITAL CENTER OF GRENOBLE (CHUG)
FRANCE

Manuel Théry
Stem Cell Architecture (STAR)

SAINT-LOUIS HOSPITAL, PARIS
INSERM / THE FRENCH ALTERNATIVE ENERGIES AND ATOMIC ENERGY COMMISSION (CEA)
FRANCE

FONDATION BETTENCOURT SCHUELLER

Discovery Fast Track *Challenge*

The world is eager for new medicines. This is your chance to join GSK scientists—helping to put your novel drug discovery concept on the fast track.

Are you an academic researcher in Europe or North America? Do you have a drug discovery concept you're eager to explore?

The Discovery Fast Track Challenge could be just what you need.

Tell us about your idea. Our expert judges will select up to 12 researchers to win a collaboration with GSK. You'll work side-by-side with GSK scientists, discovering active compounds using our high-throughput screening capabilities and extensive compound library. In short, you and your concept will be on the fast track to success.

Submissions are being accepted March 23 - April 24.
Enter today at **gsk.com/discoveryfasttrack**

Seven leaders who have changed the world of biomedical science

inspired. dedicated. lauded.

Dr. Lewis C. Cantley
Director, Sandra and Edward Meyer Cancer Center at Weill Cornell Medical College and New York-Presbyterian Hospital

CANADA GAIRDNER INTERNATIONAL AWARD

Discovered a growth signaling molecule called phosphoinositide 3-kinase (PI3K) that is leading to treatments for cancer and diabetes.

Dr. Lynne E. Maquat
Director, Center for RNA Biology, University of Rochester School of Medicine and Dentistry

CANADA GAIRDNER INTERNATIONAL AWARD

Discovered and elucidated in humans Nonsense-Mediated mRNA Decay (NMD), which is a quality-control mechanism that detects many disease-associated mRNAs, such as in cystic fibrosis and Duchene muscular dystrophy, and also mistakes routinely made in our cells to derail the production of unwanted proteins that initiate disease. NMD is also regulated by our cells to better adapt to changing environmental conditions.

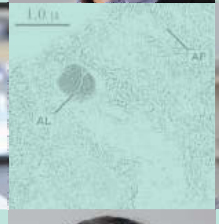

Dr. Michael N. Hall
Professor, Biozentrum, University of Basel

CANADA GAIRDNER INTERNATIONAL AWARD

Discovered the protein "target of rapamycin" (TOR) and its central role in cell growth control. Insights into TOR signaling pathways have led to new strategies for the treatment of cancer, diabetes, obesity, and cardiovascular disease.

Dr. Yoshinori Ohsumi
Honorary Professor of Tokyo Institute of Technology (Tokyo Tech)

CANADA GAIRDNER INTERNATIONAL AWARD

First to visually observe the function of autophagy (self-eating), whereby cells recycle nutrients and clean up the garbage and invaders within them keeping healthy cells. This discovery may aid in future developments to treat Alzheimer's, cancer, and many other diseases.

Dr. Shimon Sakaguchi
Vice Director, Immunology Frontier Research Center, Osaka University

CANADA GAIRDNER INTERNATIONAL AWARD

Discovered regulatory T (Treg) cells which help maintain order in the immune system. He demonstrated that increasing the number of Treg cells can prevent and treat autoimmune diseases and suppressing Treg cells has applications in cancer treatment.

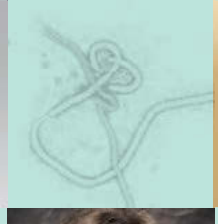

Dr. Peter Piot
Director, London School of Hygiene & Tropical Medicine

CANADA GAIRDNER GLOBAL HEALTH AWARD

Co-discovered the Ebola virus and also made major contributions to HIV/AIDS research, especially in Africa. He played an integral role in bringing the AIDS epidemic to the forefront of global attention, raising international commitments to its funding, control and treatment.

Dr. Janet Rossant
Chief of Research, The Hospital for Sick Children (SickKids)

CANADA GAIRDNER WIGHTMAN AWARD

Made major scientific contributions to developmental biology and has exceptional international leadership in stem cell biology and policy-making, and in advancing research programs for children's illnesses.

The Canada Gairdner Award winners for 2015

Find out more about the work of the Gairdner Foundation and this year's winners at www.gairdner.org

gairdner
LES PRIX CANADA GAIRDNER AWARDS

The Gairdner Symposia • Gairdner National Program • Gairdner Student Outreach Program • Gairdner Awardee Lecture Series

www.gairdner.org • @GairdnerAwards

eppendorf

Impress Yourself

The new Eppendorf Cell Culture Consumables

The all new product line of Eppendorf Cell Culture Consumables will truly delight your cells. Its outstanding design, reliability and purity is based on more than 50 years of experience.
Products created by experts, developed for perfectionists. Impress yourself!

> Unsurpassed quality, clarity, purity and sterility, providing reliable cell culture conditions
> Significantly improved design for more safety and consistency
> Maximum safety and confidence during storage and transportation

www.eppendorf.com/ccc

Remote Access Blot and Gel Imager

The new T:Genius imaging system allows high-performance, walk-away imaging of gels and blots on a smartphone or tablet. What makes the new T:Genius outperform other commercial imagers is the amazing ability to quickly and easily access stunning quality images anywhere from a tablet, computer, or smartphone. Using the T:Genius' StatusLink feature, researchers can stay updated and even share image results with colleagues in labs around the world. This is a great time saver when, for instance, scientists are developing a long exposure chemi blot and want to see how it's doing while having lunch or busying themselves with something else in the lab. The new T:Genius is both stylish and practical, comes in a choice of exciting colors and features a fantastic, sensitive camera that will give high-res images of even the biggest gels and blots as well as tricky applications such as stain-free protein gel imaging.

Syngene
For info: +44-(0)-1223-727123
www.syngene.co.uk/t-genius

GPC Column

The SecurityGuard family of products has been extended to include a cartridge-based system that protects any nonaqueous gel permeation chromatography (GPC) column. The cartridge system replaces traditional guard columns, offering a more convenient and cost-effective system for protecting expensive GPC columns from the damaging effects of contaminants and microparticulates. The unique cartridge design enables the user to visually inspect the surface of the column's packing material at any time and monitor contaminant buildup. The visual inspection allows for cartridge changes at the right time to maintain optimal column protection and performance. This is the only guard cartridge system on the market for GPC columns and it offers many advantages over traditional guard columns. SecurityGuard is compatible with any manufacturer's GPC column of any particle or pore size. The SecurityGuard is easy to use and connects directly into the column without the use of additional fittings that can decrease column performance.

Phenomenex
For info: 310-212-0555
www.phenomenex.com

Stereo Microscopes

Two new compact Greenough stereo microscopes are available for educational uses, lab routines, and industrial inspections: ZEISS Stemi 305 and ZEISS Stemi 508. Users are able to observe their samples in true color, 3-D, with high contrast, and free of distortion or color fringes. ZEISS Stemi 305 offers a 5:1 zoom. The microscope is easy to use and everything is integrated: LED illumination, reflected and transmitted light illuminations, and documentation. Users choose between the phototube to have access to all ZEISS microscope cameras or the integrated 1.2 megapixel Wi-Fi camera to connect several microscopes via wireless Internet. This enables them to share images and documentation with colleagues or students. The optics and mechanics of ZEISS Stemi 508 are designed for a heavy workload. The microscope is equipped with a large 8:1 zoom and offers a 35 mm large object field. Thanks to the changeable optics, users can observe specimens up to 120 mm in size as a whole.

ZEISS
For info: 800-233-2343
www.zeiss.com

Aspiration Controller

BrandTech is introducing the new VACUUBRAND VHC^{PRO} handheld fluid aspiration controller for cell and tissue culture. Its ergonomic design accommodates several different hand positions for comfortable fluid aspiration using Pasteur pipettes or pipette tips. All aspirated liquid is contained in the tubing for easy decontamination and minimizing air leakage. An optional eight-channel manifold with tip ejector is available. Supplied with the VACUUBRAND® BVC line of fluid aspiration systems, it can easily be fitted to aspiration systems from major manufacturers.

BrandTech
For info: 888-522-2726
www.brandtech.com

System Control Software

Unicorn 7.0 system control software has been designed for planning and controlling runs as well as analyzing results. The software controls protein purification runs as well as cell culture and preparation. Specifically designed to support the levels of collaboration required today, Unicorn 7.0 delivers a simplified user interface and enhanced features. Unicorn 7.0 provides a new evaluation module for quick insights to complex data, the ability to securely share developed methods, and an easy copy/paste function for preparation of reports. The software supports both simple and advanced tasks for both ÄKTA chromatography and ReadyToProcess WAVE 25 bioreactor systems. Fully scalable, the Unicorn platform is suitable for use within small-scale research all the way to full-scale manufacturing. Unicorn 7.0 offers the following features: easy-to-use intuitive interface to get started quickly with minimal training; secure data handling in a robust database; enhanced efficiency with network setup and collaborative features; and quick evaluation of results through single-click operations.

GE Healthcare Life Sciences
For info: 800-526-3593
www.gelifesciences.com/unicorn

Electronically submit your new product description or product literature information! Go to www.sciencemag.org/products/newproducts.dtl for more information.

Newly offered instrumentation, apparatus, and laboratory materials of interest to researchers in all disciplines in academic, industrial, and governmental organizations are featured in this space. Emphasis is given to purpose, chief characteristics, and availability of products and materials. Endorsement by *Science* or AAAS of any products or materials mentioned is not implied. Additional information may be obtained from the manufacturer or supplier.

Japan launches multimillion dollar program to internationalize university education

The inception of the Top Global University Project was precipitated by the perception amongst university administrators that Japan is losing ground in the globalization of education and research. The Japanese government is now undertaking a program to improve world rankings, increase international student ratios, and change the mindset of faculty and staff at select universities.

By Adarsh Sandhu

In September 2014, Japan's Ministry of Education, Culture, Sports, Science and Technology (MEXT) announced the selection of 37 Japanese universities for the 10-year, multimillion dollar Top Global University (TGU) Project, with the goal of "enhancing the international compatibility and competitiveness of higher education in Japan" (see Top Global University Project designations). Notably, the funding for this project is aimed at internationalizing education at Japanese universities, in contrast to funding for research-based reforms that was the aim of the 10-year Program for Promoting the Enhancement of Research Universities launched in the fall of 2013 (*1*).

The annual funding for the chosen universities is divided into Type A (¥420 million, US$3.5 million) for those that have the potential to be ranked as one of the top 100 in the world, and Type B (¥172 million, US$1.4 million) to support "innovative universities" in their efforts to internationalize.

With a view to openness and accountability, MEXT has posted the original 37 winning proposals for this project on its website (*2*). An examination of the proposals reveals many common goals and aspirations as well novel initiatives based on the history of each institute. Several universities are planning to introduce a new quarterly semester system to align Japan's academic calendar with the rest of the world, thereby enabling the launch of new English language dual-degree programs. Another common theme is a commitment to growing the number of international students. Many universities have promised the construction of new "international dormitories" to house overseas and domestic students in the same space as well as an expansion of the powers of university presidents to hire new faculty and set competitive salaries.

Sense of crisis within Japan's university administration

The TGU Project highlights a sense of crisis among Japan's university administrators who feel that the country is slow in coming to terms with the globalization of education. Some recent statistics published by MEXT that compare the performances of Japanese universities with those in the United States and Europe underscore these concerns. For example, only 2.9% of students enrolled at Japanese universities are from overseas and in Japan only 5.1% of teaching staff are from abroad, compared with 29.5% at Harvard University (U.S.) and 41.4% at Cambridge University (U.K.).

Another, and perhaps equally important issue, is encouraging Japanese students to study abroad. According to MEXT, only approximately 57,500 Japanese students went abroad in 2011, compared with around 83,000 in 2004. The consensus amongst Japan's academia to explain this trend is that there is no real need for Japanese students to go overseas because they can find everything they need for their studies and careers in Japan. A major concern is that such inward-looking students will not readily become part of the global network of scientists, thus further isolating Japan in terms of research and education in the future.

Paying for education

There are 775 universities in Japan: 86 national, 86 public, and 603 private, with approximately 5% of the 2.8 million students studying at national or public institutes. So why are Japan's university administrators spending so much time and energy on internationalization? There are two main reasons.

The first is the realization that the dramatic fall in Japan's birth rate—in 2014 there were 1.001 million births and 1.269 million deaths according to the health ministry—will lead to excess capacity, with the possibility of serious financial problems for both national and private universities. The drive to recruit more international students is intended to fill those places not taken by domestic students.

In terms of public sector university financing, national universities have had to justify their existence following passage of the National University Corporation Law in 2004 that gave Japan's national universities much greater autonomy to manage their own affairs, but importantly, required them by law to submit strategies and plans to the government in order to receive subsidies. Another significant change in government funding support was the introduction of a 2005 policy that reduced the annual government subsidy by 1% each year. In 2007, the government also began to reduce subsidies to private universities by 1% annually. In general, government subsidies cover approximately 80% of the running costs of national universities and about 10% of private institutes.

Tuition fees are an important source of income for universities. The annual tuition fee at Japan's national universities is approximately ¥550,000 (US$4,600), while at private universities it is between ¥1,000,000 (US$8,400)

for arts, sciences, and engineering and over ¥3,000,000 (US$25,200) for medicine and other medical degrees. Since this income is insufficient to cover the running costs for most universities, they must compete for government funding.

The second reason that projects to internationalize Japan's universities are being supported is the poor showing of these universities in world ranking tables. University presidents are puzzled and irritated in equal measure to find that only the University of Tokyo and Kyoto University were in the top 100 of the 2014 *Times Higher Education World University Rankings*. This contrasts with three each from China and South Korea, and two from the tiny nation of Singapore. The performance of Japan's top universities appears to reflect the large disconnect between how universities are evaluated within Japan when compared with the criteria used internationally. The president of one of Japan's top institutes confides, "We ignored the rankings for many years. However, the recent world rankings were a trigger that led us to devise new initiatives to improve our global competitiveness."

The search for new career paths for university graduates

Another driving force behind the TGU Project is that Japanese companies have a greater presence overseas now than a decade ago, especially in Asia. They are increasingly global in their outlook and operations, and need employees with a multidisciplinary education and the ability to work globally. In response to the demands of Japan's industrial sector, the proposals submitted by the 37 selected universities contain plans to give students opportunities to study interdisciplinary undergraduate courses and go abroad on industrial internships as well as to provide internships for overseas students at companies in Japan.

The next 10 years and beyond

Only time will tell whether Japan's top 37 universities will achieve their project goals, in particular whether they are able to improve their world university ranking. It seems theoretically possible to achieve all these aims given innovative management, financing, and strategic global networking. However, some prominent academics in Japan have lingering concerns about just how far such internationalization should go, with some saying that the ultimate question will be whether Japan's taxpayers want to support universities that are educating so many overseas students.

Adarsh Sandhu is a freelance writer based in Tokyo.

REFERENCES

1. *Japanese Universities Gain a Competitive Edge*, *Science* **343**, 1524 (2014) www.sciencemag.org/site/products/advertorials/Japanese_Univ_low_20140408.pdf.
2. www.jsps.go.jp/j-sgu/h26_kekka_saitaku.html (in Japanese).

Top Global University Project designations

Type A Universities

Hokkaido University
Tohoku University
University of Tsukuba National
The University of Tokyo
Tokyo Medical and Dental University National
Tokyo Institute of Technology
Nagoya University National
Kyoto University
Osaka University National
Hiroshima University National
Kyushu University
Keio University*
Waseda University*

Type B Universities

Tokyo University of the Arts National
Nagaoka University of Technology
Kanazawa University National
Toyohashi University of Technology
Kyoto Institute of Technology
Nara Institute of Science and Technology
Okayama University
Kumamoto University
Akita International University (Public)
The University of Aizu (Public)
Hosei University*
International Christian University*
International University of Japan*
Kwansei Gakuin University*
Meiji University*
Rikkyo University*
Ritsumeikan University*
Ritsumeikan Asia Pacific University*
Shibaura Institute of Technology*
Soka University*
Sophia University*
Toyo University*

*Indicates private university; all others are national universities.

Osaka University—Modernizing Japanese strategies for internationalization

Osaka University envisions *World Tekijuku* boosting diversity and internationalization in academics for the 21st century.

Osaka University is of one of Japan's top-tier research-based comprehensive universities. Its roots grew out of the philosophy on which *Tekijuku* was built, explains Toshio Hirano, president of Osaka University. *Tekijuku*—a private school established in 1838 by Ogata Koan during the Edo period—was based on the Dutch educational system, or *Rangaku* (literally, "Dutch learning"), and exposed students to Western concepts. The curriculum primarily focused on medicine and used a rare collection of Dutch dictionaries and encyclopedias owned by Ogata, a prominent physician and scholar of the time.

During that time, Japan was isolated from the rest of the world, but the unique, global education enabled "graduates to play pivotal roles in the modernization of Japan during the Meiji Restoration in the late 19th century," says Hirano. "The *Tekijuku* evolved into the forerunner of Osaka Medical School, and then, following the strong financial, administrative, and logistical support from the people of Osaka, in 1931 the Japanese government formally established what is now the modern Osaka University as Japan's sixth Imperial University."

Toshio Hirano

Tekijuku goes global

Humans have faced a number of unique challenges over the past century—including the rapid proliferation of information technology, unprecedented growth in the world's population, and increased mobility of people. "We launched the idea of *World Tekijuku* to help advance global efforts of finding

Demographics

Schools, Faculties, and Institutes at Osaka University

Osaka University encompasses 11 undergraduate schools, 16 graduate schools, 28 research institutes and centers, two university hospitals. In 2007, the university merged with Osaka University of Foreign Studies, which provides majors in 25 different languages.

Main Campuses: (area in square meters)

Suita (997,071), Toyonaka (445,851), Minoh (140,400), and Nakanoshima Center (1,000)

Budget

¥151.826 billion (2014) (US$1.28 billion)

People

23,429 students, 2012 international students, 3,460 academic staff members, 2,822 nonacademic staff members, and 860 international researchers.

Student exchange programs

Osaka University's Short-Term Nondegree Programs

www.isc.osaka-u.ac.jp/en/education/student_exchange_programs.html

Osaka University Short-Term Student Exchange Program (OUSSEP)

www.osaka-u.ac.jp/en/international/inbound/exchange_program/oussep/oussepguide

FrontierLab@OsakaU

www.osaka-u.ac.jp/jp/international/iab/e/Frontierlab.html

Japanese Short-Stay In-Session Pogram (J-ShIP)

ex.ciee.osaka-u.ac.jp/shortstay-programs/JShIP/index.html

solutions to some of the major issues facing humankind in the 21st century," says Hirano, an internationally respected immunologist and a recipient of the Crafoord Prize for his discovery of interleukin 6, an important mediator of inflammation. One of the goals of *World Tekijuku* is reforming Osaka University to become a research-based, globally recognizable institute that ranks as one of the top 10 universities in the world by its centenary in 2031. "The world is full of diversity," says Hirano. "Our ultimate goal is to eliminate barriers due to diversity and prevent conflict by mutual understanding and respect of people with different cultures and religions through the common human language of scholarship. That is the meaning of creating 'harmonious diversity through scholarship,' building on the philosophy and spirit of free scholarship and inquiry taught by Ogata Koan at the *Tekijuku*."

The university's Institute for Academic Initiatives (IAI), which plays a key role in initiating interdisciplinary and global research, is in charge of promoting initiatives to support *World Tekijku*. "The IAI was established in 2012 and is managed directly under the leadership of university president Hirano," says Yasuyuki Okamura, executive vice president in charge of international strategies. "The institute offers five doctoral programs and has world-class research divisions which focus on drug development, cognitive neuroscience robotics, photon science and technology, and global history." Importantly, students enrolled in these courses will have the opportunity to establish international collaborations to both enhance the quality of their research and gain first hand insights into the global socio-economic issues being faced by their research partners in other countries. This direct exposure will improve their understanding of other cultures and expose them to different ways of thinking, engendering cooperation rather than conflict—the central goal of *Tekijuku*.

In 2014, Japan's Ministry of Education, Culture, Sports, Science and Technology (MEXT) selected Osaka University for the Top Global University (TGU) Project as a Type A institution (see editorial on page 1492), based on the university's proposal to advance *World Tekijuku*. "The funding from the highly competitive TGU Program will be used to continue reforms at Osaka University to realize the goals of [this initiative]," says Hirano.

"The original *Tekijuku* successfully nurtured scholars who led the modernization of Japan and the birth of the Meiji era," continues Hirano. "This was an epoch-making period in Japan's history. We are confident that the concept of the *World Tekijuku* will play an important role in the resolution of diversity engendered conflicts by creating harmonious diversity through scholarship."

World Tekijuku strategies

- Establish a new generation of World Tekijuku graduate schools by 2017 to accelerate international, interdisciplinary research projects and related personnel management systems initiated by the Institute for Academic Initiatives (IAI).
- Introduce a new quarter-based configuration for the academic year, consisting of three terms and a summer vacation, not widely used in Japan, but commonly used internationally. This will enable more students to study overseas and more international student to enroll in the university's summer programs, such as the Osaka University Short-Term Student Exchange Program (OUSSEP), FrontierLab @OsakaU, and J-ShIP (see student exchange programs box).
- Create a new entrance examination system that can increase the number of international students accepted and improve their Japanese language proficiency.
- Quadruple the number of international joint research laboratories in which established scientists from overseas can conduct research at an Osaka University campus.
- Introduce highly competitive salary systems and a "cross-appointments" system with institutes around the world to double the number of international faculty within three years.
- Offer high-quality courses to students globally as part of the massive open online course (MOOC) platform, founded by the Massachusetts Institute of Technology and Harvard University in 2012. (Osaka University joined the consortium of top universities offering classes via edX in 2014.)
- Construct the Osaka University "Global Village" using a private, finance initiative to build 2,600 new student housing units for both domestic and international students as well as faculty and staff.
- Invite the University of California to set up an overseas office on the Osaka University campus to enhance the interaction between the institutions' researchers and initiate new summer programs.
- Enhance Osaka's global presence by collaborating with other universities via international frameworks and initiatives (for example, in June 2015, Osaka University will organize and host the annual meeting of the Association of Pacific Rim Universities, an organization of 45 universities from across the globe).

Prizes

Winner	Prize	Achievement
Hideki Yukawa	Nobel Prize in Physics 1949	Theoretical prediction of the existence of mesons
Hidesaburo Hanafusa	Lasker Award in 1982	Demonstration of how RNA tumor viruses cause cancer
Tadamitsu Kishimoto and Toshio Hirano	Crafoord Prize in 2009	Isolation of interleukins
Shizuo Akira	Gairdner International Award in 2011	Discovery of proteins that play a key role in innate immunity
Tadamitsu Kishimoto and Toshio Hirano	Japan Prize in 2011	Discovery of interleukin 6
Osamu Hayashi	Wolf Prize in Medicine in 1986	Discovery of oxygenase enzymes
Mikio Sato	Wolf Prize in Mathematics in 2002–2003	Foundation of algebraic analysis

Toyohashi University of Technology—Creating an international campus to nurture global technology architects

Established in 1976, Toyohashi University of Technology (Toyohashi Tech) is one of the smallest and youngest national universities in Japan with around 2,000 students and 200 faculty members.

"About 80% of our students are from Japan's technical colleges who enroll as third year undergraduates, and the majority of them continue on to do a Master's degree," says President Takashi Onishi, an expert on urban regional development and president of the Science Council of Japan. "Our graduates continue to make important contributions to society as industry engineers, university educators, and researchers at institutes all over the world."

Toyohashi Tech's research and education success has been recognized by being selected for four major program awards from Japan's Ministry of Education, Culture, Sports, Science and Technology (MEXT), including the Program for Promoting the Enhancement of Research Universities; the Program for Leading Graduate Schools on "Brain Information Architect," a joint project with Universiti Sains Malaysia (USM) to establish an overseas education base in Penang, Malaysia; and, most recently, the Top Global University (TGU) Project launched in October 2014.

Takashi Onishi

Takaaki Takashima

Education centers at Toyohashi Tech

Institute for Global Network Innovation in Technology Education (IGNITE)
Accelerates the university's globalization and human resources efforts.
ignite.tut.ac.jp/english/index.html

International Cooperation Center for Engineering Education Development (ICCEED)
Facilitates international exchange and alliances with the university.
ignite.tut.ac.jp/icceed/english/about/index.html

Center for International Relations
Contributes to the internationalization of the campus by serving as a meeting place for students.
ignite.tut.ac.jp/cir/english/

Center for International Education/TUT-USM Technology Collaboration Center in Penang Malaysia
Serves as an overseas education base.
ignite.tut.ac.jp/cie/penang/english/

Top Global University Project

"Selection for the Top Global University Project Type B [see editorial on page 1492] will enable us to increase our efforts to raise our global profile," explains Onishi. "Over the next 10 years, we want to create a multicultural campus for students from Japan and overseas befitting the title of our program, 'Creative Campus for Nurturing Global Technology Architects.'"

The main features of the Toyohashi Tech TGU Project include the introduction of bilingual language education at the undergraduate level and industrial internship opportunities for foreign students of the Global Technology Architects course at leading technology companies in Aichi Prefecture, where Toyohashi Tech is located, as well as across Japan. Notably, Aichi is the home to the headquarters and manufacturing base of Toyota Motor Corporation and affiliated companies. Additionally, it has the third largest gross domestic product in Japan after Tokyo and Osaka.

"We will also support foreign students who graduate from this course by helping them to find jobs in Japan," says Takaaki Takashima, who is responsible for implementing and managing the TGU Project and was one of the first graduates of Toyohashi Tech. "We have many close links with companies in Aichi and in other parts of Japan. We are confident that students from this course will be able to embark on career paths of their choice."

Takashima graduated in 1982 and immediately joined IBM, he explains. His initial role required him to communicate in English—a task that his time at Toyohashi Tech helped facilitate. "I was lucky to have had opportunities to travel overseas during my student days," explains Takashima. "Also, around 50% of the course textbooks were in English, so I gained confidence in my ability to communicate in English. This experience was important for my role at IBM because my first boss was not a native Japanese speaker."

Since then, Takashima has had a productive 32-year career at IBM and has worked on projects related to personal computer development, hard disk business sales engineering, intellectual property business development, and sales and contract management.

Takashima commutes to Toyohashi from his home approximately 250 km away near Yokohama—approximately 100

minutes on the *Kodama Shinkansen* (bullet train) from Odawara Station. "I come here on Mondays and return on Fridays almost every week, staying locally during the weekdays," says Takashima. "I would not have moved away from my home to the rather remote location of the Toyohashi campus if I had not been a graduate of this university. I am looking forward to managing this project to a successful conclusion over the next 10 years."

Milestones for the Top Global University Project

The first group of undergraduates accepted for the "Global Technology Architects Course" will be graduates from technical colleges who will enroll as third-year students in 2017. Thereafter, the first group of graduating high school students will enroll as first-year entrants in 2018. A total of 440 students (240 domestic and 200 international) are expected to enroll in the course over the subsequent 10 years of the project. The aim is to boost the total percentage of international students from the current 10.3% to 27.2%. Toyohashi Tech is making major changes to its curricula, with the ultimate goal of making all courses bilingual within 10 years. The university will introduce new tutoring systems incorporating mentors to strengthen language skills in English and Japanese, with the aim of nurturing students to achieve the best scores possible in language proficiency tests for both languages.

The construction of a new multicultural boarding house is one of the flagship projects of the Toyohashi Tech program. The boarding house will be built with private financing and consist of several buildings, with a total of 200 shared rooms. "The aim is to have 42% of all students living, eating, and studying in an international environment on campus, where 25% are international students," says Takashima.

The university also plans to increase the number of Japanese students with international experience from 0.3% to 20.5% by sending them on overseas internships and dual-degree programs.

There are also plans to increase international exchanges between nonacademic staff with overseas partner universities, increase foreign nonacademic staff from 1.4% to 7.1%, and increase the number of nonacademic staff attaining top language proficiency scores to at least 30%. Regarding faculty members, the university plans to have at least 50% of academic staff showing excellent language proficiency and to increase overseas staff from 16.8% to 23.4% and female staff from 5.2% to 12.9%.

Toyohashi Tech TGU Project overview
www.tut.ac.jp/english/docs/tgup2014-overview.pdf

Toyohashi Tech TGU Project concept description
www.tut.ac.jp/english/docs/tgup2014-concept.pdf

Research centers at Toyohashi Tech

Electronics-Inspired Interdisciplinary Research Institute (EIIRIS)
Research flagship established in October 2010 to fuse strengths in electronics, life sciences, medical care, agricultural science, environment, telecommunications, and robotics.
eiiris.tut.ac.jp

Venture Business Laboratory
Develops innovative technology and training programs for the electronics industry.
www.vbl.tut.ac.jp

Incubation Center for Venture Business
Offers space and facilities for growing ideas from the bench to the market place.
www.vbl.tut.ac.jp/icvb

Research Center for Collaborative Area Risk Management
Improves the disaster prevention capacity of the Higashi Mikawa region.
www.carm.tut.ac.jp/index_eng.html

Research Center for Agrotechnology and Biotechnology
Introduces information and sensing technology into agriculture.
www.recab.tut.ac.jp/contents/intro.html

Center for Human-Robot Symbiosis Research
Develops robot applications for rehabilitation and nursing, support in daily life, and education and human resource development.
robot.tut.ac.jp/english/index.html

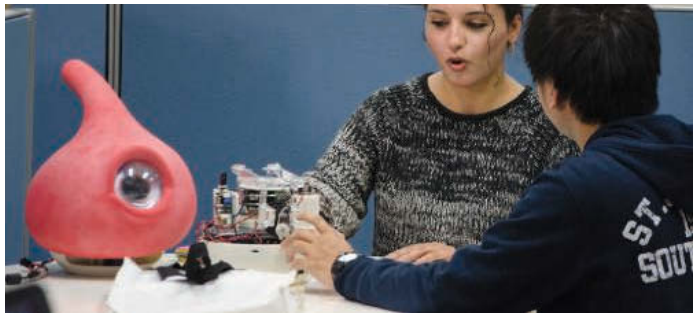

Hiroshima University—Knowledge creation for the prosperity of humankind

Hiroshima University is one of the largest comprehensive academic institutes in Japan with an annual income of ¥85.9 billion (US$732 million). It offers courses in subjects ranging from law, economics, and education to science, engineering, and medicine. The university has approximately 11,000 undergraduate students, 4,200 graduate school students, and 1,100 international students from 66 countries as well as 1,700 faculty and 1,600 nonacademic staff.

Masaki Sakakoshi

Hajime Nishitani

Fusahito Yoshida

"The founding principles of Hiroshima University are embodied in its motto: 'a single unified university, free and pursuing peace,'" says Masaki Sakakoshi, executive and vice president responsible for international education and peace. "The university is committed to nurturing students in a stimulating, international environment where scholars pursue cutting-edge research for the prosperity of humankind. Our mission is to be a base for knowledge creation."

The roots of Hiroshima University go back to 1874 with the establishment of the Hakushima School. The modern university was formed in 1949 by combining Hakushima with six other schools. "The university worked closely with the city of Hiroshima to rebuild after the devastation of the first atomic bomb attack in history," says Sakakoshi. "We decided to move out of central Hiroshima and by 1995, had merged and relocated 9 of our 11 faculties to the Higashi-Hiroshima campus. The faculties of Medicine and Dentistry, and Hiroshima University Hospital are located at the Kasumi campus, while some departments of the faculties of Law, Economics, and the Graduate School of Social Sciences and the Law School are at the Higashi Senda campus.

Top Global University Project

In 2014, Hiroshima University was selected by the Ministry of Education, Culture, Sports, Science and Technology (MEXT) as one of Japan's top 13 universities for the Type A (see editorial on page 1492) Top Global University (TGU) Project.

"The selection of Hiroshima University by MEXT for this highly competitive project underscores our accomplishments providing world-class research and education to date," says Hajime Nishitani, vice president for internationalization. "Some of our ambitious goals over the 10-year duration of the project include increasing the number of international students to 20%, offering 50% of courses in English, and increasing international faculty members to 50%."

Objective assessment of the quality of education is a high priority at Hiroshima University. One of the measures that will be implemented as part of the TGU Project is peer review of the new educational programs by representatives from the international universities involved in the Student Experience in the Research University consortium.

Research is an integral part of the university's strategy for globalization. Internationally renowned research facilities include the Research Institute for Radiation Biology and Medicine (RIRBM)—set up in 1961 to provide medical care for survivors of the August 1945 atomic bomb—and the Institute for Amphibian Biology, which holds unique expertise in rearing amphibians for studying the development, inheritance, and evolution of inbred strains of tropical clawed frogs.

"Our excellence in research was acknowledged in 2013 when we were selected by MEXT for the Program for Promoting the Enhancement of Research Universities," explains Fusahito Yoshida, executive and vice president for research. "We are an open-minded university that welcomes the global community of students and scholars to join us to solve challenging problems of the 21st century." Notably, researchers at the RIRBM are now studying the effects of radiation on people affected by the Fukushima nuclear reactor accident caused by the earthquake and tsunami in March 2011.

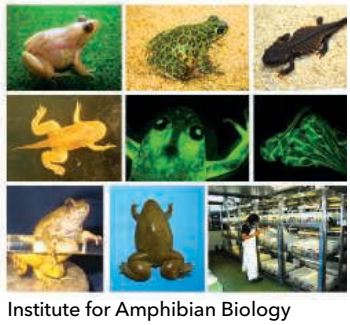

Institute for Amphibian Biology

Session on radiation emergency medicine in a Ph.D. program

Aiming for the top

Hiroshima University is committed to creating knowledge on a global scale. "We offer a wide range of innovative educational programs, run unique research programs, and have launched highly successful industry-academia partnerships," explains Sakakoshi. "We want to improve our global visibility over the next 10 years to enhance our presence on the international stage. One of the goals of the TGU Project is to improve our international standing and be one of the top 100 universities in the world within 10 years."

Hiroshima University
www.hiroshima-u.ac.jp/index.html

Nara Institute of Science and Technology—Creating new career paths through interdisciplinary education and research

Naotake Ogasawara

Mikio Kataoka

Nara Institute of Science and Technology (NAIST) is Japan's new national graduate school university. Located in Japan's first capital city, Nara, NAIST was established in 1991 and focuses on information, biology, and materials science. By implementing the concept of "education through research," NAIST has been consistently recognized among Japan's top-ranked universities in quality of research (Thomson Reuters' Essential Science Indicators). To date, approximately 6,300 Master's level students and 1,200 doctoral students have graduated from NAIST and taken up leading positions both in Japan and overseas.

Notably, NAIST has nurtured internationally renowned scientists including Shinya Yamanaka, director of the Center for iPS Cell Research and Application in Kyoto and 2012 Nobel laureate in physiology or medicine, who conducted his early research at NAIST. "With the extremely high level of both its research environment and faculty, NAIST is one of the top research universities in Japan," explains Yamanaka. "Although I am now researching iPS cells at Kyoto University, most of the core members supporting me in my lab are colleagues and former students from my time at NAIST who came to Kyoto to work with and support me. Nara is really an excellent place to conduct research."

Interdisciplinary education and research

"The institute's selection for the Top Global University [TGU] Project by the Japanese government in 2014 and for the Research University Enhancement Promotion Project in 2013 acknowledges the high quality of our graduate school education and cutting-edge research," says Naotake Ogasawara, president of NAIST.

The TGU Project is a 10-year initiative funded by Japan's Ministry of Education, Culture, Sports, Science and Technology (MEXT) with the aim of strengthening the international competiveness of Japan's academic institutes. The objectives of NAIST during the decade-long TGU Project include: (1) launching new joint degree programs with foreign universities to enhance its portfolio of doctoral course programs; (2) reforming the university's governance for more flexibility in hiring staff in new research fields; (3) creating a global campus environment to support interdisciplinary education and cultural diversity; and (4) reorganizing the current three graduate schools into a single entity to establish a unique and massive interdisciplinary platform to meet the needs of the information society of the 21st century.

NAIST Global[3]

Forging new career paths

"Society is changing at a rapid pace," says Ogasawara. "In an increasingly cyber-based society, scientists of the 21st century will require a greater understanding of diverse topics such big data, information and communication technology, and data sciences. Indeed, the scope of science is expanding rapidly, while at the same time its role in society is also changing dramatically. To meet such challenges, we are transforming our three divisions of information, biology, and materials into a single platform to prepare our students for new career paths in the interdisciplinary world of the future where knowledge of a wide range of specialties will be essential."

Specific targets during the 10-year TGU Project include increasing the number of foreign doctoral students from the current 30% to 50%, and sending NAIST students for one-year stays overseas at partner universities such as Paul Sabatier University in France and the University of California, Davis in the United States.

"Creating new career paths is an important part of the project," says Mikio Kataoka, executive director and vice president of NAIST. "We want to extend the abilities of our graduates so that they can become not only research scientists, but also have choices of other careers, such as in government policy and journalism."

The goals of the project are formidable and achieving them will require the full support of the staff at NAIST. "One of the key issues will be changing the mindset of staff at NAIST," stresses Ogasawara. "We are entering an era where academics and university administrators must think globally and outside of the box."

2015 MRS® FALL MEETING & EXHIBIT

November 29 – December 4, 2015 | Boston, Massachusetts

CALL FOR PAPERS

Abstract Submission Opens May 18, 2015 | Abstract Submission Deadline June 18, 2015

A Engaged Learning of Materials Science and Engineering in the 21st Century

BIOMATERIALS AND SOFT MATERIALS

B Stretchable and Active Polymers and Composites for Electronics and Medicine
C Tough, Smart and Printable Hydrogel Materials
D Biolological and Bioinspired Materials in Photonics and Electronics—Biology, Chemistry and Physics
E Engineering and Application of Bioinspired Materials
F Biomaterials for Regenerative Engineering
G Plasma Processing and Diagnostics for Life Sciences
H Multifunctionality in Polymer-Based Materials, Gels and Interfaces
I Nanocellulose Materials and Beyond—Nanoscience, Structures, Devices and Nanomanufacturing
J Wetting and Soft Electrokinetics
K Materials Science, Technology and Devices for Cancer Modeling, Diagnosis and Treatment
L Nanofunctional Materials, Nanostructures and Nanodevices for Biomedical Applications

NANOMATERIALS AND SYNTHESIS

M Micro- and Nanoscale Processing of Materials for Biomedical Devices
N Magnetic Nanomaterials for Biomedical and Energy Applications
O Plasmonic Nanomaterials for Energy Conversion
P Synthesis and Applications of Nanowires and Hybrid 1D-0D/2D/3D Semiconductor Nanostructures
Q Nano Carbon Materials—1D to 3D
R Harsh Environment Sensing—Functional Nanomaterials and Nanocomposites, Materials for Associated Packaging and Electrical Components and Applications

MECHANICAL BEHAVIOR AND FAILURE OF MATERIALS

S Mechanical Behavior at the Nanoscale
T Strength and Failure at the Micro- and Nanoscale—From Fundamentals to Applications
U Microstructure Evolution and Mechanical Properties in Interface-Dominated Metallic Materials
V Gradient and Laminate Materials
W Materials under Extreme Environments (MuEE)
Y Shape Programmable Materials

ELECTRONICS AND PHOTONICS

Z Molecularly Ordered Organic and Polymer Semiconductors—Fundamentals and Devices
AA Organic Semiconductors—Surface, Interface and Bulk Doping
BB Innovative Fabrication and Processing Methods for Organic and Hybrid Electronics
CC Organic Bioelectronics—From Biosensing Platforms to Implantable Nanodevices
DD Diamond Electronics, Sensors and Biotechnology—Fundamentals to Applications
EE Beyond Graphene—2D Materials and Their Applications
FF Integration of Functional Oxides with Semiconductors
GG Emerging Materials and Platforms for Optoelectronics
HH Optical Metamaterials—From New Plasmonic Materials to Metasurface Devices
II Phonon Transport, Interactions and Manipulations in Nanoscale Materials and Devices—Fundamentals and Applications
JJ Multiferroics and Magnetoelectrics
KK Materials and Technology for Non-Volatile Memories

ENERGY AND SUSTAINABILITY

LL Materials and Architectures for Safe and Low-Cost Electrochemical Energy Storage Technologies
MM Advances in Flexible Devices for Energy Conversion and Storage
NN Thin-Film and Nanostructure Solar Cell Materials and Devices for Next-Generation Photovoltaics
OO Nanomaterials-Based Solar Energy Conversion
PP Materials, Interfaces and Solid Electrolytes for High Energy Density Rechargeable Batteries
QQ Catalytic Materials for Energy
RR Wide-Bandgap Materials for Energy Efficiency—Power Electronics and Solid-State Lighting
SS Progress in Thermal Energy Conversion—Thermoelectric and Thermal Energy Storage Materials and Devices

THEORY, CHARACTERIZATION AND MODELING

TT Topology in Materials Science—Biological and Functional Nanomaterials, Metrology and Modeling
UU Frontiers in Scanning Probe Microscopy
VV *In Situ* Study of Synthesis and Transformation of Materials
WW Modeling and Theory-Driven Design of Soft Materials
XX Architected Materials—Synthesis, Characterization, Modeling and Optimal Design
YY Advanced Atomistic Algorithms in Materials Science
ZZ Material Design and Discovery via Multiscale Computational Material Science
AAA Big Data and Data Analytics for Materials Science
BBB Liquids and Glassy Soft Matter—Theoretical and Neutron Scattering Studies
CCC Integrating Experiments, Simulations and Machine Learning to Accelerate Materials Innovation
DDD Lighting the Path towards Non-Equilibrium Structure-Property Relationships in Complex Materials

X Frontiers of Material Research

www.mrs.org/fall2015

The **MRS/E-MRS Bilateral Conference on Energy** *will be comprised of the energy-related symposia at the 2015 MRS Fall Meeting.*

Meeting Chairs

T. John Balk University of Kentucky
Ram Devanathan Pacific Northwest National Laboratory
George G. Malliaras Ecole des Mines de St. Etienne
Larry A. Nagahara National Cancer Institute
Luisa Torsi University of Bari "A. Moro"

Don't Miss These Future MRS Meetings!

2016 MRS Spring Meeting & Exhibit
March 28 - April 1, 2016
Phoenix, Arizona

2016 MRS Fall Meeting & Exhibit
November 27 - December 2, 2016
Boston, Massachusetts

MRS MATERIALS RESEARCH SOCIETY®
Advancing materials. Improving the quality of life.
506 Keystone Drive • Warrendale, PA 15086-7573
Tel 724.779.3003 • Fax 724.779.8313
info@mrs.org • www.mrs.org

NEW ENGLAND BioLabs® Inc.

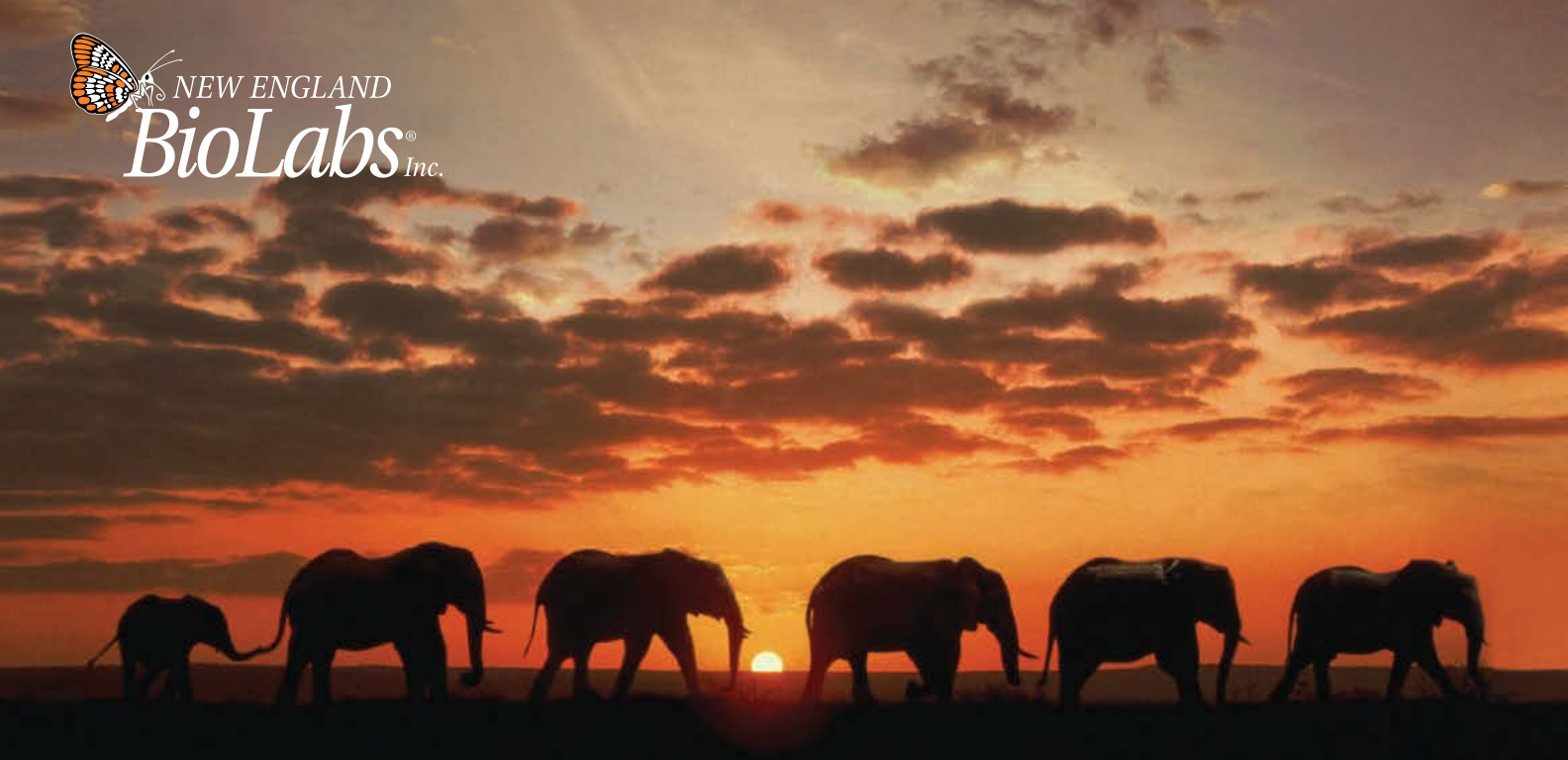

The Next Generation of DNA Assembly and Cloning

NEBuilder® HiFi DNA Assembly

The next generation of DNA assembly and cloning has arrived. With NEBuilder HiFi DNA Assembly, you'll enjoy virtually error-free joining of DNA fragments. More efficient assembly is now possible, even with larger fragments, low inputs, or 5´- and 3´-end mismatches. Additionally, use NEBuilder HiFi to bridge two dsDNA fragments with a ssDNA oligo. Save time with less screening or re-sequencing, and benefit from no licensing fee requirements from NEB when choosing NEBuilder products.

Request a free sample*
at www.NEBuilderHiFi.com

NEBuilder HiFi DNA Master Mix offers improved fidelity over Gibson Assembly Master Mix

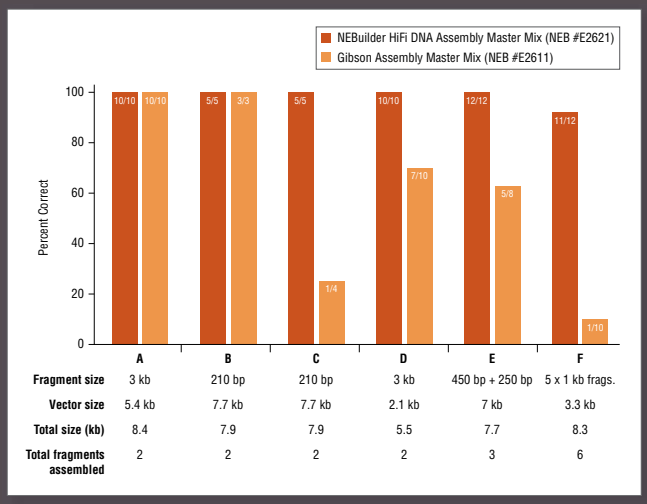

	A	B	C	D	E	F
Fragment size	3 kb	210 bp	210 bp	3 kb	450 bp + 250 bp	5 x 1 kb frags.
Vector size	5.4 kb	7.7 kb	7.7 kb	2.1 kb	7 kb	3.3 kb
Total size (kb)	8.4	7.9	7.9	5.5	7.7	8.3
Total fragments assembled	2	2	2	2	3	6

Fidelity of assembled products was compared between NEBuilder HiFI DNA Assembly Master Mix (NEB #E2621) and Gibson Assembly Master Mix (NEB #E2611). Experiments were performed using the various fragment and vector sizes, following suggested protocols. Experiments B and C vary because sequences of fragments are different. Experiments D and F were performed with fragments containing 3´-end mismatches.

* While supplies last. Offer valid in the US only. Limit one sample per customer.

There's only one Science

Science Careers Advertising

For full advertising details, go to ScienceCareers.org and click For Employers, or call one of our representatives.

Tracy Holmes
Worldwide Associate Director
Science Careers
Phone: +44 (0) 1223 326525

THE AMERICAS

E-mail: advertise@sciencecareers.org
Fax: 202 289 6742

Tina Burks
Phone: 202 326 6577

Nancy Toema
Phone: 202 326 6578

Marci Gallun
Sales Administrator
Phone: 202 326 6582

Online Job Posting Questions
Phone: 202 312 6375

EUROPE / INDIA / AUSTRALIA / NEW ZEALAND / REST OF WORLD

E-mail: ads@science-int.co.uk
Fax: +44 (0) 1223 326532

Axel Gesatzki
Phone: +44 (0) 1223 326529

Sarah Lelarge
Phone: +44 (0) 1223 326527

Kelly Grace
Phone: +44 (0) 1223 326528

JAPAN

Katsuyoshi Fukamizu (Tokyo)
E-mail: kfukamizu@aaas.org
Phone: +81 3 3219 5777

Hiroyuki Mashiki (Kyoto)
E-mail: hmashiki@aaas.org
Phone: +81 75 823 1109

CHINA / KOREA / SINGAPORE / TAIWAN / THAILAND

Ruolei Wu
Phone: +86 186 0082 9345
E-mail: rwu@aaas.org

ScienceCareers
FROM THE JOURNAL SCIENCE AAAS

ScienceCareers.org

For recruitment in science, there's only one Science

What makes *Science* the best choice?

- Read and respected by 570,400 readers around the globe
- 78% of readers read *Science* more often than any other journal
- Your ad sits on specially labeled pages to draw attention to the ad
- Your ad dollars support AAAS and its programs, which strengthens the global scientific community.

Why choose this microbiology section for your advertisement?

- Relevant ads lead off the career section with special Microbiology banner
- Bonus distribution to:

  American Society for Microbiology (ASM)
  May 30–June 2, 2015 New Orleans, LA.

Expand your exposure. Post your print ad online to benefit from:

- Link on the job board homepage directly to microbiology jobs
- Dedicated landing page for jobs in microbiology
- Additional marketing driving relevant job seekers to the job board.

* Ads accepted until May 11 on a first-come, first-served basis.

SCIENCECAREERS.ORG

Science Careers
AAAS

To book your ad: **advertise@sciencecareers.org**

The Americas
202-326-6582

Europe/RoW
+44(0)1223-326500

Japan
+81-3-3219-5777

China/Korea/Singapore/Taiwan
+86-186-0082-9345

Pro-Science Stimulus to Revitalize Japan's R&D

Today, after two decades of economic stagnation, Japan's vitality and dynamism is almost palpable. As part of Prime Minister Shinzō Abe's Japan Revitalization Strategy, the country has set its sights on strengthening efforts in research and development, improving health technology and services, and elevating the status of its universities as well as reaching out globally for knowledge sharing and talent circulation. **By Julian Tang**

Science and technology research has been a reliable pillar of the Japanese economy. The steadily increasing national research budget acknowledges the importance of research and development (R&D) for the country as well as its role in finding solutions to Japan's urban, environmental, and economic challenges. For instance, in August 2014 the Ministry of Education, Culture, Sports, Science and Technology (MEXT)—the leading official body in coordinating and funding science and technology initiatives in Japan—requested US$11.1 billion for science and technology spending in its proposed budget for the next fiscal year. This represents an 18% increase from the previous year. At the same time, MEXT is targeting US$2.4 billion—a 5.8% increase—to grants-in-aid for scientific research to fund individuals, universities, and research centers.

Areas of focus for R&D efforts

Providing sufficient research funding will enable Japanese scientists to respond to the country's changing landscape. As part of the Japan Revitalization Strategy, officially approved by the Cabinet in June 2013, the government aims to position Japan as the "world's most innovation-friendly country." The government has identified five main goals to achieve by 2030: a clean and economical energy system, a healthy and active aging society, a framework of next generation infrastructures, substantial economic benefits through regional and international collaborations, and a complete recovery from the Great East Japan Earthquake of 2011. To meet these goals, the government has set a target of at least 4% of GDP for total R&D investment by the public and private sectors, and at least 1% of GDP invested in R&D by the government.

Promoting international, interdisciplinary research

In 2007, MEXT established the World Premier International (WPI) Research Center Initiative to attract top-flight researchers from around the world to the initial five—now nine—designated centers. These centers, which include the Kavli Institute for the Physics and Mathematics of the Universe (Kavli IPMU), are granted a significant level of autonomy to encourage revolutionary and innovative research. "Access to world-class facilities, and the opportunity to interact and collaborate with researchers across various disciplines, are some of the many appealing aspects of conducting research at a WPI center," says **Hitoshi Murayama**, Kavli IPMU director, who has extensive overseas research experience and understands the importance of global talent circulation. "In addition to allowing our researchers to go overseas to gain ample international exposure, we invite world-leading researchers here regularly to share their ideas and knowledge."

Kavli IPMU's interdisciplinary approach, which bridges the gap among mathematics, physics, and astronomy, is helping researchers in these fields to achieve new advances. The Subaru Measurements of Images and Redshifts (SuMIRe) project, which involves collaborations with Princeton University, the California Institute of Technology, the Max Planck Institutes, and other research organizations from Japan, Taiwan, and Brazil, has already completed its first instrument—a three-ton imaging camera—that will allow for a "cosmic census" of each galaxy. The next stage is to build an US$80 million spectrograph to extend the census. "Just like a population census, a large-scale cosmic census allows us to get the full picture of how a system works and behaves," explains Murayama. "We would be able to determine distances to the galaxies and study the physical properties of stellar and gas compositions in each galaxy." continued>

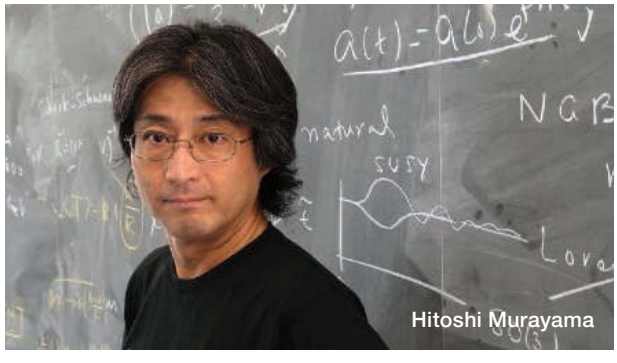
Hitoshi Murayama

PHOTOS: (FROM TOP) © XTOCK/SHUTTERSTOCK.COM; YUJIKO ENOMOTO

Upcoming Features

Postdocs—August 28 ■ *Faculty II—September 18* ■ *Faculty III—October 9*

"Under [the Brain/MINDS] project, we will address a fundamental question in neuroscience: How does the human mind work?"
— Akira Yoshida

Featured Participants

Kavli Institute for the Physics and Mathematics of the Universe
www.ipmu.jp

Okinawa Institute of Science and Technology Graduate University
www.oist.jp

National Child Health and Development
www.ncchd.go.jp

RIKEN
www.riken.jp

To maintain its foothold in large-scale, world-class research, Japan has launched its own Brain Mapping by Integrated Neurotechnologies for Disease Studies (Brain/MINDS) project, in line with the increasing interest in brain-mapping projects around the world, such as the Brain Research through Advancing Innovative Neurotechnologies (BRAIN) Initiative project in the United States and the Human Brain Project (HBP) in Europe. The Brain Science Institute (BSI) at RIKEN, Japan's largest research organization, and the Okinawa Institute of Science and Technology Graduate University (OIST), an interdisciplinary graduate university located at the southernmost tip of Japan, have been collaborating with the HBP since 2013 and applying their expertise in supercomputer-based models and simulations. Recently, BSI RIKEN and OIST were also invited by MEXT to be part of the 17-institute Brain/MINDS project, with BSI RIKEN as the core administrative and research facility. "Under this project, we will address a fundamental question in neuroscience: How does the human mind work?" reveals **Akira Yoshida**, research coordinator at BSI RIKEN. "The project's goal is to accelerate the development of technologies for mapping the brain's circuitry in animal models, specifically in the marmoset monkey, whose neural circuits are much closer to human compared with rodent models, and to connect the results to the diagnosis and treatment of human neurological disorders and mental illness."

Amid these dynamic developments, Japanese universities are not being overlooked. MEXT has launched the Program for Promoting the Enhancement of Research Universities, choosing 22 universities to lead the country's efforts in advancing science and technology. The financial support ranges from US$2 million to US$4 million annually for 10 years. The selected institutes include well-established former Imperial Universities such as The University of Tokyo, Kyoto University, and Osaka University, and private institutes such as Keio University and Waseda University. Despite the differences, the chosen universities have all made *kokusaika* ("internationalization") one of their highest priorities. They share an impressive track record of increasing the number of overseas researchers and students, improving international collaborations, introducing English language courses for students, training administration staff to produce bilingual documents, and introducing new salary scales to commensurate with institutes in Western countries.

Global collaborations

To support globalization projects, MEXT further selected 37 Japanese universities in September 2014 to become Super Global Universities, providing an annual subsidy from US$100 million to US$400 million to each of the chosen institutes over the next 10 years for personnel training, recruitment of international researchers, and improvement of university facilities. In parallel, MEXT has launched personnel exchange programs such as Research in Japan and Japan-Asia Youth Exchange Program in Science as well as joint research initiatives with East Asian nations and the Association of Southeast Asian Nations (ASEAN). Under MEXT's exchange programs, Japan has hosted over 30,000 international researchers in the last few years, while 150,000 local researchers have had the opportunity to pursue their studies overseas. "Under the forward-thinking leadership of MEXT, Japanese research organizations and academic institutions are certainly progressing towards globalization," notes **Jonathan Dorfan**, president of OIST. "When people free themselves from their traditional boundaries and come together to share ideas and information, big things can happen."

In a move to promote global health, the Department of Health Policy at The National Center for Child Health and Development (NCCHD), the largest maternal and pediatric hospital in the country, has been collaborating with the World Health Organization and the Japanese branch of the Cochrane Collaboration to improve clinical practice guidelines and maternal and child health in developing countries such as Mongolia and Sri Lanka. The hospital welcomes researchers from developing nations to share their research know-how. In return, these researchers, who usually face a shortage of technology and physical infrastructures, have access to the sophisticated instruments and facilities in Japan.

Meanwhile, in the private sector, Japan has also become the first nation to approve commercialization of a first-line drug for psoriasis vulgaris and psoriatic arthritis from the Swiss pharmaceutical company Novartis. The drug, sold under the name Cosentyx, is considered by experts to have a market value of US$1–2.5 billion annually. The city of Yokohama is also anticipating the construction of Apple's new, large-scale R&D facility, one that Prime Minister Abe pointed out would provide significant employment opportunities and is comparable to the company's largest existing R&D facilities in Asia.

Translational research and initiatives for a healthier future

Globally, the areas of maternal health and pediatrics are often overlooked, with too little funding being allocated and too few trials conducted. However, to safeguard the well-being of future generations, it is crucial to tackle genetic continued>

PHOTO: COURTESY OF AKIRA YOSHIDA

筑波大学 University of Tsukuba

www.tsukuba.ac.jp
1-1-1 Tennodai, Tsukuba, Ibaraki
305-8577, Japan

The University of Tsukuba campus is located at the heart of Tsukuba Science City, about 45 minutes north of Tokyo on the Tsukuba Express train. The modern structure of the university was established in 1973 after the reorganization of its predecessor, the Tokyo University of Education, whose roots go back to 1872. The huge campus—similar in size to New York's Central Park—is home to approximately 16,500 students and 4,000 faculty and administrative staff. The university offers a comprehensive curriculum including arts and social sciences, physical education and sports sciences, physical sciences and engineering, and medicine. Distinguished scholars affiliated with the university include Nobel Laureates Leo Esaki (Physics, 1973), Hideki Shirakawa (Chemistry, 2000), and Sin-Itiro Tomonaga (Physics, 1965).

The University is nominated as one of the top eleven research universities named RU11 in Japan. The university has been supported by "The program for promoting the enhancement of research universities" and "Top Global University Project", which are national projects aimed at the world's top-level research university.

Tsukuba Science City is the Center of Research and Development

Tsukuba is one of the world's largest science and knowledge-based regions in the world. It has 32 research and academic institutions, approximately 20,000 researchers, and more than 7,000 foreign workers.

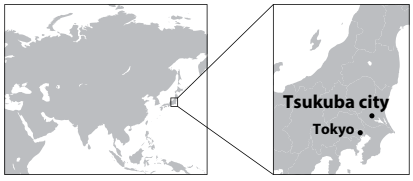

45mins ride of Tsukuba Express from downtown Tokyo to Tsukuba

■ Number of Students and Staffs

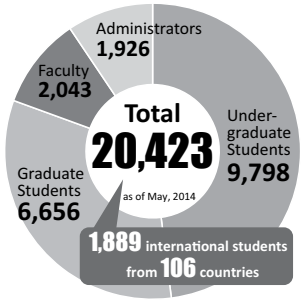

9 Undergraduate Schools
- Humanities and Culture
- Social and International Studies
- Human Sciences
- Life and Environmental Sciences
- Sciences and Engineering
- Informatics
- Medicine and Medical Sciences
- Health and Physical Education
- Art and Design

8 Graduate Schools
- Education
- Humanities and Social Sciences
- Business Sciences
- Pure and Applied Sciences
- Systems and Information Engineering
- Life and Environmental Sciences
- Comprehensive Human Sciences
- Library, Information and Media Studies

1 Integrative School
- School of Integrative and Global Majors (SIGMA)

International Institute for Integrative Sleep Medicine (IIIS)

Faculty Position:

☑ **WPI-IIIS Postdoctoral Fellows**
☑ **Junior Principal Investigators**

IIIS, founded in December 2012, is one of nine institutions in the World Premier International Research Center Initiative (WPI) supported by the Ministry of Education, Culture, Sports, Science and Technology of Japan. The implementation period as a WPI institution is 10 years.

The ultimate research goal of IIIS is
- To elucidate the fundamental mechanism of sleep/wakefulness
- To develop strategies to regulate sleep
- To contribute to the enhancement of world health through combatting sleep disorders and associated diseases

All applicants must have obtained a Ph.D. degree. We offer enough start-up funds for Junior Principal Investigators, a high degree of work autonomy, and a highly international research environment with new state-of-the-art equipment and facilities.Candidates are

encouraged to have a strong background in one or more of the following areas: Neuroscience, Physiology, Behavioral Neurobiology, Molecular Genetics, Cell Biology, Biochemistry, Medicinal Chemistry, Organic Chemistry, Bioinformatics, Clinical and Social Medicine, Psychiatry, Sleep Medicine.

Candidates should send a curriculum vitae, bibliography, statement of research interests and a list of references to iiis-career@un.tsukuba.ac.jp. Only electronic submissions will be accepted.

Applications and Details
http://wpi-iiis.tsukuba.ac.jp/position/

Numerous other positions are available

tsukuba.ac.jp/english/update/jobs.html

IMAGINE THE FUTURE. *University of Tsukuba*

"It is crucial for every child to be followed up annually until the age of 21 by a pediatrician—as is done in the United States—to detect hereditary disorders and pediatric diseases as early as possible. We are working towards implementing a similar system here in Japan."

— Takashi Igarashi

conditions and diseases in the pediatric population. NCCHD understands the importance of establishing a research-intensive hospital to address these issues. **Takashi Igarashi**, president and chief executive officer of NCCHD, strives to bring together clinicians and basic scientists both at the domestic and international level. "We believe that medicine and basic research are complementary to each other. Clinicians are well-versed with the human body and the delicate use of surgeries and drugs, while scientists understand the intricacies of how the body functions at the molecular and cellular level," he explains. "Tackling childhood diseases at an early stage allows for a healthier general population in the long run." NCCHD is the only hospital in the country that performs fetal surgery, particularly for cases with twin-to-twin transfusion syndrome, a rare condition in which the blood supply in the shared placenta is unequally distributed, leading to one twin lacking the necessary nutrients for normal growth and survival. The Ministry of Health, Labour and Welfare (MHLW) has designated NCCHD as the principal center to establish a national registry of rare pediatric diseases.

Further, NCCHD is leading the effort to introduce "Bright Futures," a national children's health promotion initiative that has been adopted by the American Academy of Pediatrics for well-child care, in Japan. "It is crucial for every child to be followed up annually until the age of 21 by a pediatrician—as is done in the United States—to detect hereditary disorders and pediatric diseases as early as possible," notes Igarashi. "We are working towards implementing a similar system here in Japan."

The journey ahead

Over the next 15–20 years, Japan must tackle key economic, human power, and demographic issues such as a declining birth rate, an aging population, and the challenge of sustaining a sufficiently skilled labor force. Furthermore, Japan is facing rising competition from regional nations in terms of attracting foreign talent and boosting research output. According to the Organization for Economic Co-operation and Development's (OECD) Science, Technology and Industry Outlook 2014, a review of key trends in science, technology, and innovation policies, and performance in more than 45 economies, South Korea and China are now the primary destinations for researchers from the United States and experienced a net "brain gain" over the period 1996–2011. South Korea also became the world's most R&D-intensive country in 2012, spending 4.36% of its GDP on R&D, versus an OECD average of 2.4%. The 2013 SCImago Journal and Country Rank list shows that Japan is also lagging behind China in terms of the number of scientific publications.

Nonetheless, the Abe government expects a prompt return on its investment in research. About a quarter of the science stimulus in the Japan Revitalization Strategy—some US$1.8 billion—is allocated for commercialization of university research. Much of the rest is for projects with industrial or clinical applications. The stimulus, for instance, will also aid in the renovation of the RIKEN SPring-8 synchrotron, one of the top photon science research facilities in the world, and the construction of data links between Japan's universities and RIKEN's K supercomputer, the world's fastest computer in 2011 and still ranked fourth today.

As MEXT's Program for Promoting the Enhancement of Research Universities moves forward, improving global rankings and attracting top-class foreign researchers are two of the main challenges. Despite having the honor of producing the largest number of Nobel Prize laureates in Asia, Japan is not well represented in the ranking tables for global universities. With only two universities listed in the top 100 2014–2015 Times Higher Education World University Rankings, Japan is on par with Singapore, China, and Hong Kong, but behind South Korea, which has three. Many of the universities have declared that part of the MEXT program's funding will be used to push their institutes higher in the rankings by the end of the 10-year program.

To nurture the next generation of researchers and health professionals, NCCHD has acquired funding from the MHLW to provide new training opportunities. "It is important to equip younger members of our community with up-to-date knowledge and training. We need to adopt new ideas and system reforms to cater to the demands of this evolving world, especially in a country like Japan where we experience many dynamic changes and challenges," states Igarashi, who emphasizes the importance of maintaining R&D and science education funding to make research careers attractive to young clinicians and scientists in Japan and around the world.

How and whether the Japanese government's effort will pay off remains to be seen. However, one thing is certain: Globalization is inevitable and Japan realizes it. Murayama sums it up, "We need to make a conscious effort to expand our horizons and stay connected globally. Looking at Japan in the context of this global community is like looking at the universe with the most powerful camera, we gain a new perspective by seeing the big picture."

Julian Tang is a medical editor and freelance science writer based in Tokyo, Japan
DOI: 10.1126/science.opms.r1500154

Job Announcement for Academic Staff(s) (full time, female and/or foreign nationality) at Institute of Space and Astronautical Science, The Japan Aerospace Exploration Agency

JAXA

Japan Aerospace Exploration Agency (JAXA) considers diversity to be one of the crucial factors for sustaining vitality in its basic research environment, and thus seeks to recruit one or two full-time female and/or foreign-nationality Academic staff(s). Successful applicant(s) will work as an associate and/or assistant professor at Institute of Space and Astronautical Science (ISAS), as described below;

Title and Number of position(s):
One or two in total, associate and/or assistant professor(s), to be selected from female and/or foreign-nationality applicants.

Summary of the Position (Contents of Work and Required Ability):
An applicant may either think of enhancing a research theme that is already dealt at ISAS or propose to set-up a new research theme that will expand the research horizon of ISAS. While being productive in academic research, a successful applicant is also expected to participate in space science projects conducted at ISAS.

Please see < **http://global.jaxa.jp/about/employ/index.html** > for further details.

ÉCOLE POLYTECHNIQUE
FÉDÉRALE DE LAUSANNE

Faculty Position in Microbiota

at the Ecole polytechnique fédérale de Lausanne (EPFL)

The School of Life Sciences at EPFL is expanding and invites applications for a faculty position in **the field of microbiota with relevance to nutrition, metabolism, gut-brain axis, or other aspects relevant to human health & disease.** We are primarily seeking candidates for a **tenure track assistant professor position** but in exceptional cases more experienced candidates will be considered.

Successful candidates will develop an independent and dynamic research program, participate in both undergraduate and graduate teaching, and supervise PhD students and postdoctoral fellows.

Significant start-up resources, research budget and state-of-the-art research infrastructure are available, within the framework of a campus that fosters very strong interactions between life sciences, basic science, informatics and engineering. Translational research is encouraged. Salaries and benefits are internationally competitive.

Candidates should upload their application as PDF files at the address
https://academicjobsonline.org/ajo/jobs/5418

and should include: cover letter, curriculum vitae, publication list, brief statement of research and teaching interests, names and e-mail addresses of 3 references. Interviews will start from **June 1, 2015.**

Further questions can be addressed to:

Prof. Stewart Cole
Director of the Global Health Institute
Email: GHI-recruit@epfl.ch

For additional information on EPFL, please consult
http://www.epfl.ch http://sv.epfl.ch/

EPFL is committed to increasing the diversity of its faculty, and strongly encourages women to apply.

WestVirginiaUniversity.

The Department of Microbiology, Immunology and Cell Biology
West Virginia University School of Medicine
invites applications for the
Open Rank Faculty Position in Neural Injury-Related Inflammatory Disease Research

The Department of Microbiology, Immunology and Cell Biology (http://medicine.hsc.wvu.edu/micro/) seeks a distinguished immunologist as tenure-track faculty (rank open) to further its scientific exploration and discovery that targets prevention and treatment of inflammatory diseases associated with neural injury or neurodegeneration. The successful applicant will hold a primary faculty appointment in the Department of Microbiology, Immunology and Cell Biology as well as membership in the WVU Center for Neuroscience (http://www.hsc.wvu.edu/wvucn/) in the WVU School of Medicine.

This joint recruitment with the Center for Neuroscience provides an exceptional opportunity to participate in robust, interdisciplinary basic and translational research and training programs in a highly collaborative atmosphere. The appointed faculty will be expected to conduct research on neuroinflammatory disease and teach immunology to medical, graduate and undergraduate students. The successful candidate will be an investigator with a PhD in a biomedical discipline or MD/PhD degree with the PhD in a biomedical discipline and at least two years of postdoctoral experience. The successful candidate will also have an accomplished track record of independent research, demonstrated by high quality publications in peer reviewed journals. Applicants with expertise and interest in the role of regulatory and/or non-coding RNA in neuroinflammation are encouraged to apply. Dedicated laboratory space and competitive operating funds will be made available.

Founded in Morgantown, WV in 1867, West Virginia University is 1 of only 11 research intensive land grant institutions offering a single health sciences campus with accredited Schools of Medicine, Dentistry, Nursing, and Pharmacy and a formative School of Public Health. WVU is West Virginia's major research and development center, and its only comprehensive doctoral granting institution. Our faculty conduct research totaling over $138 million in sponsored contracts and grants per year. The Carnegie Foundation for the Advancement of Teaching classifies WVU as a comprehensive doctoral institution with medical programs – placing it among only 50 such public and 28 private institutions nationwide.

Nominations, applications (including a cover letter, vitae, statement of research interests, and list of 3 professional references), expressions of interest, requests for information, or confidential inquiries should be directed (preferably electronically) to:

Christopher F. Cuff, Ph.D., Chair, Search Committee
c/o Barbara Pritt (bpritt@hsc.wvu.edu)
Department of Microbiology, Immunology and Cell Biology
West Virginia University School of Medicine
Morgantown, WV 26506-9177

The position remains open until filled.

West Virginia University is an EEO/Affirmative Action Employer-Minority/Female/Disability/Veteran.
West Virginia University is the recipient of an NSF ADVANCE award for gender equity.

POSITIONS OPEN

POSTDOCTORAL ASSOCIATE

The Gobler Laboratory within the School of Marine and Atmospheric Sciences (SoMAS) at Stony Brook University (**website: http://www.somas.stonybrook.edu/~gobler/index.html**) seeks to hire a full-time post-doctoral associate with expertise in the application of high throughput sequencing and other molecular techniques to answer questions related to the ecology and the physiology of aquatic plankton and microbes. Applicants must have a PhD and background in analyzing high throughput sequencing data sets (transcriptomic, genomic, metatranscriptomic, metagenomic). Preference will be given to appropriate candidates with background in comparative genomics, experimental approaches with plankton, and/or harmful algal blooms. This one year appointment is renewable after the first year pending satisfactory performance.

For additional information and to apply, please see website: **https://stonybrooku.taleo.net/careersection/2/jobdetail.ftl?job=1500155**

Equal Opportunity Employer, females, minorities, disabled, veterans.

NYU School of Medicine
NYU LANGONE MEDICAL CENTER

Institute Director, Computational Biology

The NYU School of Medicine announces its search for the Director of the Institute for Computational Biology. The Dean and faculty consider this an exceptional opportunity to lead a preeminent institute in the City of New York in close collaboration with the other schools and colleges of New York University.

The Institute Director for Computational Biology will drive the vision, strategy and development of the Institute. Responsibilities will include leading research and recruitment efforts. The selected Director should have a distinguished record of scientific achievements, ability to foster collaborations and promote innovation and creativity. The successful candidate will have a PhD and/or MD degree and will have demonstrated leadership experience in a university, medical center or research institute setting.

For additional information regarding the Institute for Computational Biology at NYU please visit: **http://www.nyuinformatics.org/**

Applications and nominations should include a *curriculum vitae and narrative discussing areas of clinical (if applicable), research, education, administration, and leadership*. All materials should be sent electronically, for confidential review by the search committee, to: **Andrea Botta, Project Manager for Education, Faculty and Academic Affairs, andrea.botta@nyumc.org**

The NYU School of Medicine was founded in 1841 and is an equal opportunity, affirmative action employer and provides a drug-free and smoke-free workplace.

AAAS is here –

helping scientists achieve career success.

Every month, over 400,000 students and scientists visit ScienceCareers.org in search of the information, advice, and opportunities they need to take the next step in their careers.

A complete career resource, free to the public, *Science* Careers offers hundreds of career development articles, webinars and downloadable booklets filled with practical advice, a community forum providing answers to career questions, and thousands of job listings in academia, government, and industry. As a AAAS member, your dues help AAAS make this service freely available to the scientific community. If you're not a member, join us. Together we can make a difference.

To learn more, visit aaas.org/plusyou/sciencecareers

AAAS + U = Δ

ETH zürich

Professor of Climate and Weather Risks

→ The Department of Environmental Systems Science (www.usys.ethz.ch) at ETH Zurich invites applications for the above-mentioned professorship.

→ The position will be jointly at the Swiss Federal Office of Meteorology and Climatology (MeteoSwiss) and the Department of Environmental Systems Science. This framework provides a wide range of opportunities for collaboration in the areas of climate variability and uncertainty, as well as climate impact scenarios, Earth system science, the interpretation of climate model data, engineering and societal risks and others.

→ The successful candidate is expected to develop an innovative research program that makes important scientific contributions to methodologies managing climate and weather risks associated with both climate variability and climate change. The research portfolio should include quantitative methodologies using probabilistic approaches to address climate and weather risks, and include stakeholder involvement. The core research activity could be in one or more fields related to climate change adaptation, treatment of uncertainties in risk assessment, or linking climate and weather predictions and climate change scenarios to decision making. Candidates should have an excellent international track record in disciplinary as well as system-oriented multidisciplinary research, and be able to effectively lead a research team. Furthermore, the new professor is expected to develop classes for students focusing on the development of quantitative methods, and interdisciplinary courses introducing students to the challenges and successful practices in applied policy areas. Undergraduate level courses are taught in German or English, and graduate level courses in English.

→ **Please apply online at www.facultyaffairs.ethz.ch**

→ Applications should include a curriculum vitae, a list of publications, and a statement of future research and teaching interests. The letter of application should be addressed **to the President of ETH Zurich, Prof. Dr. Lino Guzzella. The closing date for applications is 15 May 2015.** ETH Zurich is an equal opportunity and family friendly employer and is further responsive to the needs of dual career couples. We specifically encourage women to apply.

By **Sharon Ann Holgate**

Strength in disability

Ken O'Neill earned his Ph.D. in mathematics from the University of Strathclyde in 2012. Today, he is assistant statistician in the input-output statistics branch of the Office of the Chief Economic Adviser in the Scottish government. In his spare time, O'Neill, who has been profoundly deaf since birth, heads a project aimed at expanding the representation of mathematical and statistical terminology in British Sign Language (BSL). This interview has been edited for brevity and clarity.

Q: What are the most important barriers for deaf students?
A: Hearing teachers have little understanding of the broad impact of deafness and how to meet the needs of deaf children. For example, deaf students often have poor access to English, so it's more difficult for them to write answers to questions. Also, the insufficient specialist vocabulary within BSL makes it difficult for deaf students (and interpreters) to learn and communicate technical details.

Q: Tell us about your efforts to expand the BSL Glossary for mathematics.
A: A friend led me to the Scottish Sensory Centre in Edinburgh. I initiated discussions geared toward expanding the signs available for mathematics and statistics, and in 2014 the center put me in charge of these efforts. We have secured funding and are about to have a workshop where deaf mathematicians and scientists will work with linguists to create signs and terms based on the national math curriculum.

Q: When you were being recruited for your current job, at what stage did you reveal your deafness?
A: On the application form, the Scottish government invited applicants to claim a guaranteed interview or assessment under the Positive About Disabled People scheme. I made the claim and was treated positively.

Q: How would you advise scientists with a disability to respond to interview questions about performing the essential functions of a job?
A: I'd advise them to do it honestly, without dwelling on their disabilities. The focus should be on the job and how they can do it. If they do things differently for any reason, that's fine as long as it's explained clearly and realistically. Interviewers will be reassured when there are positive solutions.

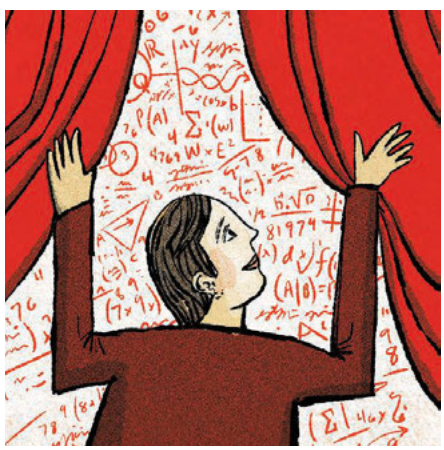

"The focus should be on the job and how they can do it."

It is perfectly possible to make a disability come across as a positive contribution to one's work. I have excellent visual skills due to my use of sign language, which are helpful in mathematics. When asked about communicating with colleagues, I respond that my experience with both deaf and hearing cultures—the deaf community views itself positively as a linguistic and cultural minority—means that I'm bilingual and bicultural. I appreciate the importance of different languages and how messages need to be targeted toward a specific audience.

It is important to not emphasize how disabilities affect our jobs negatively. This sends false messages to employers that we are not confident in doing our jobs, and employers will often fear what they do not know.

Q: What skills can scientists bring to the workplace as a result of their disabilities?
A: We have encountered problems or barriers in the workplace due to our disabilities and found ways to remove them. As a result, we tend to have a greater understanding and awareness of problems and how to deal with them than do scientists who have no disabilities. We also view the world differently, so we can provide a different perspective on real-world problems and models.

It is up to us to explain this clearly. We have to project confidence that we know what we are doing and talking about.

So we have to deal with any underlying issues we have, including our own attitudes toward our disabilities. If we accept our disabilities, then we will inevitably be better equipped to go about our daily lives and work comfortably. ■

Sharon Ann Holgate is a science writer in the United Kingdom. For more on life and careers, visit sciencecareers.org.

ILLUSTRATION: ROBERT NEUBECKER